Fluctuation-induced order and thermal transport in frustrated quantum magnets

by

Alexander Hickey

A thesis
presented to the University of Waterloo
in fulfillment of the
thesis requirement for the degree of
Doctor of Philosophy
in
Physics

Waterloo, Ontario, Canada, 2025

© Alexander Hickey 2025

Examining Committee Membership

The following served on the Examining Committee for this thesis. The decision of the Examining Committee is by majority vote.

External Examiner:	Arun Paramekanti Professor, Dept. of Physics, University of Toronto
Supervisor(s):	Michel J. P. Gingras Professor, Dept. of Physics and Astronomy, University of Waterloo
	Anton A. Burkov Professor, Dept. of Physics and Astronomy, University of Waterloo
Internal Member:	David G. Hawthorn Professor, Dept. of Physics and Astronomy, University of Waterloo
Internal-External Member:	Adam Wei Tsen Associate Professor, Dept. of Chemistry University of Waterloo
Other Member(s):	Roger G. Melko Professor, Dept. of Physics and Astronomy, University of Waterloo

Author's Declaration

This thesis consists of material all of which I authored or co-authored: see Statement of Contributions included in the thesis. This is a true copy of the thesis, including any required final revisions, as accepted by my examiners.

I understand that my thesis may be made electronically available to the public.

Statement of Contributions

This thesis is presented in the format of a manuscript-based ("sandwich") thesis, containing three first-author papers.

Chapter 3 contains a publication in Physical Review B [1], co-authored by Daniel Lozano-Gómez and Michel J. P. Gingras. For this project, Daniel Lozano-Gómez contributed the classical calculations, while I contributed the quantum calculations. Daniel Lozano-Gómez and I wrote the initial draft of the paper together, Michel J. P. Gingras supervised the project, and edited the manuscript.

Chapter 4 contains a preprint [2] co-authored by Jeffrey G. Rau, Subhankar Khatua, and Michel J. P. Gingras. I worked in collaboration with Jeffrey G. Rau and Subhankar Khatua to complete a proof presented in this paper that relates the fluctuation-induced gap to linear spin wave theory. Michel J. P. Gingras supervised the project and drafted the introduction. I wrote the remainder of the initial draft, and my co-authors edited the manuscript.

Chapter 5 contains a recently written manuscript, co-authored by Michel J. P. Gingras. I wrote the initial draft, and Michel J. P. Gingras supervised the project and edited the manuscript.

I am the sole author of Chapters 1, 2, 6, and the preface to Chapters 3-5.

Abstract

Order-by-disorder is a mechanism of "fluctuation-induced" ordering that occurs in many frustrated magnetic systems where magnetic moments, or spins, are subject to competing interactions. So far, this phenomenon has been discussed in systems where the quantum ground state is not a "classical" product state. In such a case, both thermal and quantum fluctuations act to lift the accidental classical degeneracy, raising the question of whether one mechanism of order-by-disorder is possible without the other.

In this thesis, we present results exposing a novel route to order-by-disorder, one without quantum zero-point fluctuations, in the ferromagnetic pyrochlore Heisenberg model with the Dzyaloshinskii-Moriya (DM) interaction as the leading perturbation. We show that any collinear ferromagnetic state is an *exact* eigenstate even in the presence of the anisotropic DM interaction, while thermal fluctuations give rise to a preferred magnetization direction. Using linear spin wave theory, we find that the anisotropy appears at lowest order as a sub-leading term in the low-temperature expansion of the free energy, proportional to $T^{7/2}$. Our results thus show that the phenomenon of thermal order-by-disorder can, in principle, occur even in the absence of quantum zero-point fluctuations driving quantum order-by-disorder. By extending our calculations to non-linear spin wave theory, we find that the ferromagnetic ground state becomes unstable for a spin-$\frac{1}{2}$ system when the DM interaction is large.

Next, we ask the question of how to adequately characterize order-by-disorder in real materials, and how to distinguish it from conventional energetic ordering. Currently, the only clear and universal signature that has been proposed is a characteristic temperature dependence of the fluctuation-induced *pseudo-Goldstone gap*. Thus far, this temperature dependence of the pseudo-Goldstone gap has only been characterized in the classical ($S \to \infty$) limit. Here, we use non-linear spin wave theory to characterize the pseudo-Goldstone gap in quantum magnets at low temperature, to leading order in $1/S$. Using exact sum-rules for the magnon spectral functions, we find that the gap exhibits a distinct power-law temperature dependence, scaling as either T^{d+1} or $T^{d/2+1}$ depending on whether the PG mode is linearly or quadratically gapless at the harmonic level, respectively. We examine the implications of our results for several candidate materials.

The final part of this thesis examines the thermodynamic and transport properties of the ferromagnetic pyrochlore $Lu_2V_2O_7$. Over the last decade, there has been immense interest in magnetic materials that host topologically non-trivial excitations. In ordered magnetic insulators, features analogous to those of topological insulators and semimetals can arise in the magnon band structure, and the associated Berry phases can manifest in observable heat and spin transport phenomena. This was unambiguously observed in $Lu_2V_2O_7$ in the form of a magnon thermal Hall signal, and proposed to arise from the DM interaction. A precise value of the DM interaction is not

known, as the values obtained from fitting both thermal transport and inelastic neutron scattering data, as well as from density functional theory, are all mutually inconsistent. Motivated by this, we investigate the effect of additional symmetry allowed perturbations to the spin Hamiltonian of $Lu_2V_2O_7$ in an attempt to reconcile the different experimental probes of this material. We find that the thermal transport and neutron scattering measurements are consistent with the addition of a small second-nearest-neighbour DM interaction to the model. Conversely, we argue that existing specific heat measurements are inconsistent with neutron scattering experiments and cannot be reconciled with any additional exchange couplings to the bilinear spin-model in the perturbative regime. Our results motivate future thermal transport and specific heat measurements of this material.

Acknowledgements

I am grateful to my PhD co-supervisors Michel Gingras and Anton Burkov for their consistent support and guidance throughout the course of my graduate studies. I am incredibly fortunate to have had the opportunity to learn from both of you.

Thank you to the remaining members of my committee for your constructive feedback during my committee meetings, your thoughtful questions on my comprehensive examination, and your time and effort in preparing for my thesis defence.

I appreciate the fruitful collaborations with Daniel Lozano-Gómez, Jeffrey Rau, and Subhankar Khatua on some of the work presented in this thesis.

Over the years, I have had the privilege of working alongside and learning from a remarkable group of fellow students and postdocs. Thank you to Daniel, Itamar, Kai, Subhankar, Xuzhe, Naman, Felipe, Varun, Michael, Griffin, Pranav, and everyone else whom I have pestered with questions over countless coffee breaks.

Finally, I would like to thank my family for their endless support over the course of my graduate studies.

Dedication

To Sophie and Micah.

Table of Contents

Examining Committee ii

Author's Declaration iii

Statement of Contributions iv

Abstract v

Acknowledgements vii

Dedication viii

List of Figures xiii

List of Tables xv

List of Abbreviations xvi

List of Symbols xvii

1 Introduction 1

2 Spin wave theory 7

2.1 Magnons 7

2.2 Perturbation theory 14

3 Order-by-disorder without quantum zero-point fluctuations **20**
3.0 Preface . . . 20
3.1 Introduction . . . 23
3.2 Model . . . 26
3.3 Methods . . . 28
3.3.1 Classical low-temperature expansion . . . 28
3.3.2 Classical Monte Carlo . . . 29
3.3.3 Quantum spin waves . . . 30
3.3.4 Non-linear spin waves . . . 32
3.4 Results . . . 34
3.4.1 Classical selection . . . 34
3.4.2 Quantum selection at $0^+ < T \ll T_c$ . . . 41
3.4.3 Quantum selection at $T = 0^+$ . . . 45
3.4.4 Limit of Stability . . . 46
3.5 Discussion and Conclusion . . . 49
Appendices . . . 51
3A Pyrochlore lattice convention . . . 51
3B Monte Carlo calculation of M_4, δM_4 and M_6 . . . 52
3C Perturbative calculation of the free energy . . . 54
3D Energy versus entropy as the mechanism for selection . . . 58
3E Magnetization direction in a field . . . 61
3F Calculation of the magnon self-energy . . . 64

4 Fluctuation-induced gaps in quantum magnets **67**
4.0 Preface . . . 67
4.1 Introduction . . . 69
4.2 Spin-wave theory . . . 72
4.3 Curvature formula . . . 74

4.4 Models . . . 76
4.5 Discussion . . . 77
End Matter . . . 79
4.EI Material candidate, $Er_2Ti_2O_7$ . . . 79
4.EII Material candidate, $Yb_2Ge_2O_7$ . . . 80
4.EIII Material candidate, $Lu_2V_2O_7$ . . . 82
Supplemental Material . . . 83
4.SI Details of spin wave theory . . . 83
4.SII Curvature formula . . . 89

5 Excess thermal conductivity and specific heat in $Lu_2V_2O_7$ 97
5.0 Preface . . . 97
5.1 Introduction . . . 99
5.2 Magnon Hall effect . . . 102
5.3 Specific heat . . . 107
5.4 Discussion . . . 108
Supplemental Material . . . 110
Pyrochlore lattice convention . . . 110
Details of spin wave theory . . . 112
Gauge-invariant calculation of the Berry Curvature . . . 115
Second nearest-neighbour Heisenberg model . . . 117

6 Conclusion and outlook 119

References 121

APPENDICES 146

A Evaluation of the magnon self-energy 147

B Non-linear spin wave theory of the Heisenberg ferromagnet **152**

Isotropic model 152

Anisotropic Ferromagnet 155

List of Figures

1.1 Schematic depicting the thermal Hall effect 4
1.2 The pyrochlore lattice 5

3.1 Classical ground state configurations of the ferromagnetic Heisenberg model with Dzyaloshinskii-Moriya interactions 25
3.2 Diagrams contributing to the magnon self-energy at $O(S^0)$ in the Holstein-Primakoff expansion 32
3.3 Phase diagram from classical Monte Carlo 35
3.4 Entropy distribution from the classical low-temperature expansion about a ferromagnetic ground state 36
3.5 Comparison of the classical entropy 38
3.6 Distribution of the magnetization direction from classical Monte Carlo simulations 39
3.7 Temperature dependence of moments of the magnetization, computed using classical Monte Carlo 40
3.8 Free energy distribution from linear spin wave theory 43
3.9 Phase diagram from linear spin wave theory 44
3.10 Zero-temperature magnon spectral function 47
3.11 Distribution of the global magnetization direction from classical Monte Carlo . . 52
3.12 Temperature dependence of the specific heat and moments of the magnetization from classical Monte Carlo 55
3.13 Free energy difference in linear spin wave theory and perturbation theory 58
3.14 Comparison of the thermodynamic free energy, energy, and entropy in linear spin wave theory 60

3.15 Magnetization direction as a function of temperature and magnetic field 63

4.1 Schematic picture depicting the spectrum of a pseudo-Goldstone mode 71
4.2 Pseudo-Goldstone gap for the Heisenberg-compass model 76
4.3 Pseudo-Goldstone gap for the pyrochlore oxides (a) $Er_2Ti_2O_7$, (b) $Yb_2Ge_2O_7$, and (c) $Lu_2V_2O_7$ 81

5.1 Crystal field splitting of the V^{4+} orbitals in $Lu_2V_2O_7$ 98
5.2 Thermal Hall conductivity as a function of the nearest-neighbour Dzyaloshinskii-Moriya interaction 103
5.3 Thermal Hall conductivity as a function of the two additional nearest-neighbour interactions 105
5.4 Thermal Hall conductivity as a function of the second nearest-neighbour Dzyaloshinskii-Moriya interaction 106
5.5 Low-temperature specific heat of $Lu_2V_2O_7$ 109
5.6 Thermal Hall conductivity as a function of the Heisenberg exchange 118

B.1 Relative spin-wave gap of the simple cubic Heisenberg ferromagnet with single-ion anisotropy 158
B.2 Spontaneous magnetization of the simple cubic Heisenberg ferromagnet with single-ion anisotropy 159

List of Tables

3.1 Expected values of the anisotropic cubic parameters in for various magnetization directions 53

5.1 Second nearest-neighbour Dzyaloshinskii–Moriya vectors for the pyrochlore lattice 112

List of Abbreviations

BZ first Brillouin zone 73, 86, 95, 104, 115

CLTE classical low-temperature expansion 28, 34–38, 40–42, 46, 52

DFT density functional theory 98, 99, 101, 103, 104, 106–108

DM Dzyaloshinskii-Moriya v, vi, 20–22, 24–27, 33, 38, 41, 45, 46, 48–50, 52, 53, 57, 62, 82, 99–108, 110, 112, 117, 119, 120

FCC face-centred cubic 29, 31, 51, 59, 110

FM ferromagnetic 34–36

GL Ginzburg-Landau 29, 30

GLW Ginzburg-Landau-Wilson 49

INS inelastic neutron scattering 67, 68, 80, 82, 98, 99, 101, 103, 104, 106–108, 117, 118, 120

MC Monte Carlo 29, 30, 34, 37, 38, 46, 49

ObD order-by-disorder 2, 3, 6, 19–21, 23–25, 27, 28, 30, 32, 34, 35, 40–42, 44–46, 48, 50, 52, 67–72, 75, 77–80, 82, 90, 119, 120

PG pseudo-Goldstone 3, 67–69, 71–78, 80–82, 87–93, 95, 96, 119, 120

List of Symbols

N_A Avogadro number 107

O(n) Orthogonal group of degree n 26, 27, 49, 77, 81, 82

SU(n) Special unitary group of degree n 77

T_c Critical temperature 24, 30, 35, 37–40, 42, 49, 53, 77, 78, 80–82, 100, 107

U(n) Unitary group of degree n 1, 26, 77, 80, 81, 102, 115

$\hbar$ Reduced Planck constant 4, 29, 101, 102, 114, 117

k_B Boltzmann constant 3, 13–15, 39, 43, 52, 75, 85, 86, 92–95, 102, 103, 107, 108, 114, 147, 148

Chapter 1

Introduction

A central objective in condensed matter physics is to understand how macroscopic order emerges from the collective behaviour of a very large number of simple constituents, such as electrons, ions, or magnetic moments, when subject to interactions. In many ordered phases, such as crystals, magnets, and superfluids, the order is described by spontaneous symmetry breaking, where the order lacks some of the symmetries present in the system [3]. In a crystalline solid, the periodic arrangement of ions arises from electrostatic interactions and breaks the continuous translational and rotational symmetries of free space. In many conventional magnets, the magnetic moments break rotational symmetry in spin space, together with time-reversal symmetry. In a superfluid, the definite phase of the macroscopic condensate breaks the U(1) symmetry associated with the conservation of particle number. In such cases, Goldstone's theorem provides a fundamental connection between the breaking of a continuous symmetry and the existence of gapless excitations, corresponding to long-wavelength fluctuations of the order parameter [4].

While spontaneous symmetry breaking has provided a central organizing principle for understanding ordered phases of matter—the so-called "Landau paradigm"—order does not *need* to arise solely from symmetry principles. In fact, a somewhat counterintuitive scenario exists where the development of long-range order is assisted by the presence of quantum or thermal fluctuations. This situation is broadly referred to as *order-by-disorder*, occurring when competing interactions result in a set of "accidentally" degenerate ground-states that are not related by symmetries. These accidental modes may still manifest as low-energy excitations, although their robustness and physical origin differ markedly from those mandated by symmetry breaking. Analogous to the gapless Nambu-Goldstone modes arising from continuous symmetry breaking, accidental degeneracies give rise to nearly gapless *pseudo-Goldstone* modes when these degeneracies are weakly lifted by fluctuations [5].

Another circumstance, falling outside the scope of the Landau paradigm, is the emergence of topological order. These topological phases of matter develop non-local order described by topological invariants that remain robust to local deformations of the system at hand. These so-called topological phases of matter can exhibit peculiar transport properties, localized edge states, fractionalized excitations, and long-range entanglement [6–9]. While initially considered in the context of electronic systems, interest has recently grown in understanding how topology manifests in the collective excitations of materials. One particular manifestation is the thermal Hall effect, a transverse thermal conductivity κ_{xy} in the presence of a temperature gradient, analogous to the well-known electronic Hall effect.

Over the last several decades, frustrated magnetic systems have proven to be fruitful ground in the study and realization of non-conventional order. The inherent competition between interactions in such systems often prevents the selection of a unique ground state, leading to degeneracies and enhanced fluctuations. In addition, deviations of the local magnetic order, known as *spin waves* (or *magnons*), can acquire nontrivial topological character due to the complex interplay between lattice geometry and spin-orbit coupling.

In this thesis, we will use frustrated magnetic systems as a platform to study order-by-disorder and the magnon Hall effect. This chapter provides a brief overview of order-by-disorder and the magnon Hall effect in these systems, motivating the projects presented in the remainder of this thesis.

Order-by-disorder

In many frustrated magnetic systems, the classical ground state is not uniquely determined by the Hamiltonian. Instead, a continuous manifold of degenerate configurations may emerge, owing to the competing interactions and geometric constraints that prevent the simultaneous minimization of energy on local bonds. In cases where this degeneracy is *accidental*, i.e., the states are not related by symmetry, the conventional approach of energetic selection mechanisms fails to distinguish a preferred ordered state, whereas fluctuations serve to stabilize a particular subset of configurations. This phenomenon is known as order-by-disorder (ObD),[1] originally proposed by Villain [10].

ObD comes from the idea that some degenerate configurations support more low-energy excitations than others. Operationally, the selected configurations minimize the free energy, which includes both entropic contributions at finite temperature *and* the quantum zero-point

[1]The "disorder" part of order-by-disorder comes from the association of thermal fluctuations with entropy; however, it should really be thought of as "order-by-fluctuations".

energy. Perhaps the simplest magnetic model that exhibits ObD is a ferromagnetic square-lattice compass model, defined by the Hamiltonian [11]

$$H = -JS^2 \sum_{\boldsymbol{r}} \left(\sigma^x_{\boldsymbol{r}} \sigma^x_{\boldsymbol{r}+\hat{\boldsymbol{e}}_x} + \sigma^z_{\boldsymbol{r}} \sigma^z_{\boldsymbol{r}+\hat{\boldsymbol{e}}_z} \right), \tag{1.1}$$

where $\boldsymbol{\sigma}_{\boldsymbol{r}}$ are Pauli operators and $J > 0$. The classical ground states of Eq. (1.1) are highly degenerate, corresponding to any collinear ferromagnetic configuration in the square lattice plane, with energy $-JNS^2$. Notably, however, this model does not have any continuous symmetry. To leading order in a $1/S$ expansion, the magnon dispersion is [11]

$$\epsilon_{\boldsymbol{k}}(\phi) = 4J\sqrt{1 - \cos^2\phi \cos k_x - \sin^2\phi \cos k_y}, \tag{1.2}$$

with ϕ representing the in-plane angle of the configuration, from which we can compute the corresponding free energy

$$F(\phi) = -JNS(S+1) + \sum_{\boldsymbol{k}} \left[\frac{S}{2} \epsilon_{\boldsymbol{k}}(\phi) + k_{\mathrm{B}} T \ln\left(1 - e^{-S\epsilon_{\boldsymbol{k}}(\phi)/k_{\mathrm{B}}T}\right) \right], \tag{1.3}$$

which notably, depends on the configuration angle ϕ. The free energy expression is minimized for the four angles $\phi = n\pi/2$, lifting the accidental degeneracy. The first term in Eq. (1.3) represents the quantum zero-point energy, while the second term is the "thermal" contribution to the free energy. While it is often the case that both the thermal and quantum zero-point fluctuations select the same subset of configurations, these two mechanisms of fluctuations may instead favour distinct long-range order. Chapter 3 of this thesis focuses on the relationship between thermal and quantum zero-point fluctuations in magnetic systems.

Although there are a large number of magnetic models that exhibit order-by-disorder, a natural question arises of what the experimental signatures of such an effect would be. A quick inspection of Eq. (1.2) indicates that the magnons are gapless, despite the lack of a continuous symmetry. This gapless magnon corresponds to the pseudo-Goldstone (PG) mode associated with the accidental degeneracy. Mediated by ObD, this PG mode must acquire a gap, serving as a signature that can, in principle, be observed in an inelastic neutron scattering experiment. Formally, this gap appears due to magnon-magnon interactions, which are not accounted for in Eq. (1.2). The topic of Chapter 4 is the signatures of these PG gaps in frustrated quantum magnets that exhibit ObD at finite temperatures. A more comprehensive overview of ObD is provided in Sections 3.0 and 4.0.

The magnon Hall effect

Magnons, the basic excitations in magnetic materials, have a well-defined spectrum and corresponding Bloch wavefunctions when translational symmetry is present. It was first predicted by

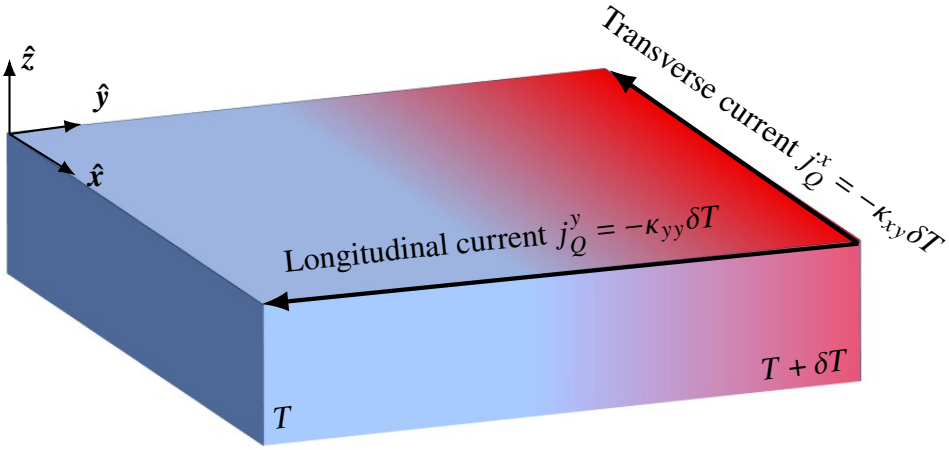


Figure 1.1: Schematic depicting the thermal Hall effect. A temperature gradient δT produces a heat current $\boldsymbol{j}_Q$ in the material with both longitudinal and transverse components.

Katsura *et al.* that magnons can acquire nontrivial topological order due to intrinsic spin-orbit interactions of magnetic ions [12]. In many instances, the consequence of this topological order is an associated anomalous Hall effect. While magnons are electrically neutral, such an effect is observable in thermal transport measurements, as a transverse heat current in response to a thermal gradient ∇T, known as the *thermal Hall effect*.[2] In such an experiment, the heat current density $\boldsymbol{j}_Q$ is related to the thermal gradient by the linear-response

$$\boldsymbol{j}_Q = -\boldsymbol{\kappa}\nabla T, \tag{1.4}$$

where $\boldsymbol{\kappa}$ is the thermal conductivity matrix. In this context, the thermal Hall effect arises from the antisymmetric components of the linear-response matrix (e.g. κ_{xy}). In practice, the topological character of the magnon band structure is encoded in the momentum space *Berry curvature* $\mathcal{F}_{xy}^{(a)}(\boldsymbol{k})$ that induces an anomalous velocity to the magnons. Matsumoto and Murakami showed that the intrinsic thermal Hall conductivity of magnons is [13, 14]

$$\kappa_{xy} = -\frac{k_B^2 T}{\hbar N_c} \sum_{\boldsymbol{k},a} c_2[n_B(\epsilon_{\boldsymbol{k},a})]\mathcal{F}_{xy}^{(a)}(\boldsymbol{k}), \tag{1.5}$$

where c_2 is a weighting function that captures the thermal population of magnons. A schematic of the thermal Hall effect is depicted in Fig. 1.1.

[2]The thermal Hall effect of magnons is often shortened to the "magnon Hall effect".

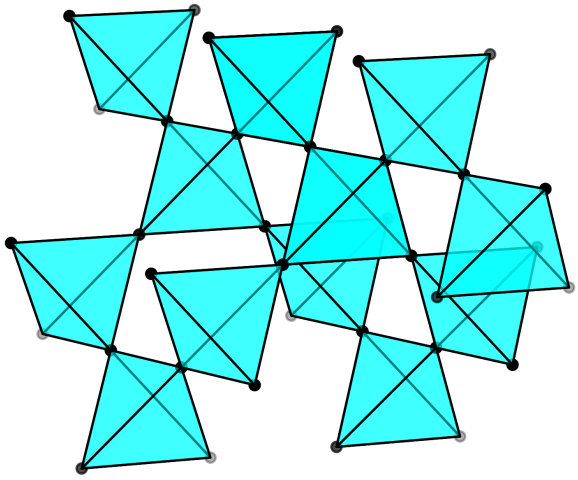


Figure 1.2: The pyrochlore lattice, consisting of a network of corner-sharing tetrahedra.

The magnon Hall effect was first measured by Onose *et al.* in a single crystal of the pyrochlore ferromagnet $Lu_2V_2O_7$ [15]. Following this discovery, the magnon Hall effect has been measured in a growing number of materials [16–18] and theoretically proposed to occur in a large number of other magnetic systems [19]. The magnon Hall effect exemplifies how topological band theory can be extended to charge-neutral bosonic excitations, with implications for both fundamental physics and the development of energy-efficient technologies [20]. Chapter 5 of this thesis focuses on the magnon Hall effect in the pyrochlore ferromagnet $Lu_2V_2O_7$, with more comprehensive details about this material discussed in Section 5.0.

The pyrochlore oxides

Pyrochlore oxides, with chemical formula $A_2B_2O_7$, are a family of materials that have emerged as a versatile platform for the study of geometric frustration and exotic collective phenomena. A defining feature of these compounds is that both the A and B cations form interpenetrating pyrochlore lattices, consisting of corner-sharing tetrahedra (see Fig. 1.2). When one (or both) of the cations is magnetic, this geometry tends to frustrate simple magnetic ordering, giving rise to a wide variety of unconventional magnetic phases (see Refs. [21–23] and references therein).

Among the most studied subclasses are the rare-earth pyrochlores, where A is a trivalent rare-earth ion and B is typically a transition metal. These systems often evade conventional magnetic order down to millikelvin temperatures due to competing dipolar, exchange, and anisotropic

couplings, which arise due to strong spin–orbit coupling and crystal electric field effects. The most prominent of these materials is arguably the classical spin ices $Ho_2Ti_2O_7$ and $Dy_2Ti_2O_7$ [24–33].

Each project presented in this thesis is unified by its focus on pyrochlore oxide materials, of which there are several candidate materials that exhibit ObD and/or topological magnons. A detailed overview of the remainder of this thesis is presented in the following section.

Overview of this thesis

In this thesis, three original research projects are presented on the topics of ObD and the thermal Hall effect in frustrated magnetic systems. The main method used throughout this thesis is spin wave theory, the topic of Chapter 2, which discusses many of the technical details that are employed in the later chapters. Chapters 3 and 4 focus on some fundamental theoretical questions about ObD in frustrated magnets. The topic of Chapter 3 is the role of quantum versus thermal fluctuations in magnetic systems that exhibit ObD. Here, a detailed example of a system that exhibits ObD in the absence of any quantum zero-point fluctuations, a novel situation that has not been discussed previously, is presented. Chapter 4 focuses on the physical characterization of ObD in real materials, and how to distinguish it from conventional energetic ordering. We argue here that a universal temperature-dependent gap in the magnon spectrum can serve as such a signature, and we provide several examples of pyrochlore oxides that can serve as candidate materials. Chapter 5 studies the thermodynamic and anomalous transport properties of the pyrochlore oxide $Lu_2V_2O_7$, which, as noted previously, exhibits the magnon Hall effect. It is argued that the currently accepted magnetic model for this material fails to be simultaneously consistent with several experimental observations, leading to an excess of thermal conductivity and specific heat. Finally, Chapter 6 consists of a summary and outlook on the work presented in this thesis.

Chapter 2

Spin wave theory

Elementary excitations in solid state physics are the key to understanding the low-temperature properties of matter. Indeed, their energy and lifetime are deduced from the real and imaginary parts of the complex pole of the related Green's function (propagator) that can be experimentally investigated through its relationship with correlation functions via linear response theory. In systems with conventional magnetic order, these elementary excitations are spin waves, corresponding to coherent fluctuations of the localized magnetic moments, or "spins", that propagate through a material, mediated by magnetic interactions, such as exchange interactions, dipolar forces, and external magnetic fields. The quantum of such an excitation is referred to as a magnon.[3]

While some content is repeated in the self-contained appendices/supplemental material of Chapters 3, 4, and 5, the purpose of this chapter is to provide an overview of the general methods in quantum many-body physics used in the remainder of the thesis in a manner that is more detailed and complete than the remaining chapters. In this spirit, the chapter is written in a somewhat technical manner. Spin wave theory is first formalized by introducing the Holstein-Primakoff expansion and linear spin wave theory in Section 2.1. In Section 2.2, linear spin wave theory is extended to include magnon-magnon interactions perturbatively at finite temperature.

2.1 Magnons

The concept of magnons (spin waves) was first introduced by Bloch in 1930 [34], shortly after the advent of quantum mechanics, to explain the thermal reduction of spontaneous magnetization in

[3] Throughout this thesis, the terms spin wave and magnon are used interchangeably.

ferromagnets. This was formalized by Holstein and Primakoff [35], and later by Dyson and Maleev [36, 37], who introduced bosonic representations of spin operators that we now know as spin wave theory. A key advantage of representing spin operators as bosons is that the resulting commutation relations involve complex numbers, rather than operators, which is crucial for building a series expansion of the Green's function in a systematic way. These representations describe the low-energy properties of systems with a magnetic ordered ground state by systematically embedding quantum and thermal fluctuations onto a classical product state, from which we may subsequently calculate physical observables of interest. Over the decades, spin wave theory has evolved into a central tool in quantum magnetism, offering deep insights into the thermodynamic, transport, and dynamical response of a wide variety of magnetic materials. It has also played a pivotal role in our understanding of dynamics and the statistical mechanics of magnetic excitations in insulating magnets [38].

For the remainder of this chapter, we discuss magnons in the context of a generic bilinear spin-S model

$$H = \frac{1}{2} \sum_{\boldsymbol{r}\boldsymbol{r}'} \sum_{ab} \boldsymbol{S}^{\intercal}_{\boldsymbol{r},a} \, \boldsymbol{J}_{\boldsymbol{r}-\boldsymbol{r}',ab} \boldsymbol{S}_{\boldsymbol{r}',b}, \tag{2.1}$$

where $\boldsymbol{r}$ represents the position of a magnetic unit cell, a is a sublattice index, and the matrices $\boldsymbol{J}_{\boldsymbol{\delta},ab}$ describe the magnetic exchange interactions. It is worth noting that the form of Eq. (2.1) describes the most general case of a non-Bravais lattice, such as the pyrochlore lattice.

The Holstein-Primakoff representation

The most widely used approach to spin wave theory is the Holstein-Primakoff transformation, where spin operators are represented as

$$\boldsymbol{S}_{\boldsymbol{r},a} = \left(S - n_{\boldsymbol{r},a}\right) \hat{\boldsymbol{e}}_{a,0} + \sqrt{S} \left[\left(1 - \frac{n_{\boldsymbol{r},a}}{2S}\right)^{1/2} a_{\boldsymbol{r},a} \hat{\boldsymbol{e}}_{a,-} + a^{\dagger}_{\boldsymbol{r}a} \left(1 - \frac{n_{\boldsymbol{r},a}}{2S}\right)^{1/2} \hat{\boldsymbol{e}}_{a,+} \right]. \tag{2.2}$$

Here, $n_{\boldsymbol{r},a} = a^{\dagger}_{\boldsymbol{r},a} a_{\boldsymbol{r},a}$ and the vectors $\hat{\boldsymbol{e}}_{a,\pm} \equiv (\hat{\boldsymbol{e}}_{a,x} \pm i\hat{\boldsymbol{e}}_{a,y})/\sqrt{2}, \hat{\boldsymbol{e}}_{a,0}$ define a local reference frame with respect to the classical ordering direction $\hat{\boldsymbol{e}}_{a,0}$ (i.e. $\hat{\boldsymbol{e}}_{a,x} \times \hat{\boldsymbol{e}}_{a,y} = \hat{\boldsymbol{e}}_{a,0}$), typically chosen to be a classical ground state. The Holstein-Primakoff transformation, as written in Eq. (2.2), is exact, and one can check that the bosonic commutation relations are obeyed

$$\left[a_{\boldsymbol{r},a}, a_{\boldsymbol{r}',b}\right] = 0, \qquad \left[a_{\boldsymbol{r},a}, a^{\dagger}_{\boldsymbol{r}',b}\right] = \delta_{ab}\delta_{\boldsymbol{r}\boldsymbol{r}'}. \tag{2.3}$$

Using the exact representation in Eq. (2.2), however, proves challenging as the transformation is non-linear, owing to the terms proportional to $\left(1 - \frac{n_{\boldsymbol{r},a}}{2S}\right)^{1/2}$. These terms are important, as they

enforce the "spin-length" constraint, requiring that the spectrum of the spin operators is bounded between $-S$ and S, which restricts the boson subspace to $n_{\boldsymbol{r},a} \leq 2S$. In practice, the term under the square root is expanded in a power series and truncated at some order. The spin-length constraint then produces a series of effective magnon-magnon interactions which can be included as perturbations to a single-magnon Hamiltonian. Formally, this is an expansion in inverse spin quantum number $1/S$, leading to a series representation $H = S^2 \sum_{n=0}^{\infty} S^{-n/2} H_n$. To $O(S^0)$, the (normal-ordered) magnon interactions are given by

$$H_0 = N\left(1 + \frac{1}{S}\right)\epsilon_{\mathrm{cl}}, \tag{2.4}$$

$$H_1 = \sqrt{N_c}\sum_a \left[L^a a^\dagger_{\boldsymbol{0},a} + \overline{L}^a a_{\boldsymbol{0},a}\right], \tag{2.5}$$

$$H_2 = \frac{1}{2}\sum_{\boldsymbol{k}}\sum_{ab}\left[A^{ab}_{\boldsymbol{k}} a^\dagger_{\boldsymbol{k},a} a_{\boldsymbol{k},b} + A^{ba}_{-\boldsymbol{k}} a_{-\boldsymbol{k},a} a^\dagger_{-\boldsymbol{k},b} + B^{ab}_{\boldsymbol{k}} a^\dagger_{\boldsymbol{k},a} a^\dagger_{-\boldsymbol{k},b} + \overline{B}^{ab}_{\boldsymbol{k}} a_{-\boldsymbol{k},b} a_{\boldsymbol{k},a}\right], \tag{2.6}$$

$$H_3 = \frac{1}{2!\sqrt{N_c}}\sum_{\boldsymbol{k}\boldsymbol{q}}\sum_{abc}\left[T^{abc}_{\boldsymbol{k},\boldsymbol{q}} a^\dagger_{\boldsymbol{k},a} a^\dagger_{\boldsymbol{q},b} a_{\boldsymbol{k}+\boldsymbol{q},c} + \overline{T}^{abc}_{\boldsymbol{k},\boldsymbol{q}} a^\dagger_{\boldsymbol{k}+\boldsymbol{q},c} a_{\boldsymbol{q},b} a_{\boldsymbol{k},a}\right], \tag{2.7}$$

$$H_4 = \frac{1}{N_c}\sum_{\boldsymbol{k}\boldsymbol{q}\boldsymbol{Q}}\sum_{abcd}\left[\frac{1}{(2!)^2} V^{abcd}_{\boldsymbol{k},\boldsymbol{q},\boldsymbol{Q}} a^\dagger_{\boldsymbol{k}+\boldsymbol{Q},a} a^\dagger_{\boldsymbol{q}-\boldsymbol{Q},b} a_{\boldsymbol{q},c} a_{\boldsymbol{k},d} + \frac{1}{3!}\left(D^{abcd}_{\boldsymbol{k},\boldsymbol{q},\boldsymbol{Q}} a^\dagger_{\boldsymbol{k},a} a^\dagger_{\boldsymbol{q},b} a^\dagger_{\boldsymbol{Q},c} a_{\boldsymbol{k}+\boldsymbol{q}+\boldsymbol{Q},d} + \mathrm{H.c.}\right)\right], \tag{2.8}$$

where $N = N_c N_s$ is the number of spins in a system with N_c primitive unit cells and N_s spins per unit cell, $S^2\epsilon_{\mathrm{cl}}$ is the energy per spin of the classical configuration, and the Fourier transform is defined as $a_{\boldsymbol{k},a} \equiv (N_c)^{-1/2}\sum_{\boldsymbol{r}} e^{i\boldsymbol{k}\cdot\boldsymbol{r}} a_{\boldsymbol{r},a}$.

In order to simplify the perturbation theory that will be introduced later, it is convenient to require that the interaction vertices must be symmetrized to appropriately match the commutator relations of the quasiparticle operators. For example, the three-body term is proportional to $T^{abc}_{\boldsymbol{k},\boldsymbol{q}} a^\dagger_{\boldsymbol{k},a} a^\dagger_{\boldsymbol{q},b} a_{\boldsymbol{k}+\boldsymbol{q},c}$. The two creation operators $a^\dagger$ commute, which implies that the three-body vertex must satisfy

$$T^{abc}_{\boldsymbol{k},\boldsymbol{q}} = T^{bac}_{\boldsymbol{q},\boldsymbol{k}}. \tag{2.9}$$

In a similar manner, the four-particle vertices have the symmetrization properties:

$$V^{abcd}_{\boldsymbol{k},\boldsymbol{q},\boldsymbol{Q}} = V^{abdc}_{\boldsymbol{q},\boldsymbol{k},\boldsymbol{Q}+\boldsymbol{k}-\boldsymbol{q}} = V^{bacd}_{\boldsymbol{k},\boldsymbol{q},\boldsymbol{q}-\boldsymbol{k}-\boldsymbol{Q}} = V^{badc}_{\boldsymbol{q},\boldsymbol{k},-\boldsymbol{Q}} = \left[V^{dcba}_{\boldsymbol{k}+\boldsymbol{Q},\boldsymbol{q}-\boldsymbol{Q},-\boldsymbol{Q}}\right]^*, \tag{2.10}$$

$$D^{abcd}_{\boldsymbol{k},\boldsymbol{q},\boldsymbol{Q}} = D^{acbd}_{\boldsymbol{k},\boldsymbol{Q},\boldsymbol{q}} = D^{bacd}_{\boldsymbol{q},\boldsymbol{k},\boldsymbol{Q}} = D^{cabd}_{\boldsymbol{Q},\boldsymbol{k},\boldsymbol{q}} = D^{bcad}_{\boldsymbol{q},\boldsymbol{Q},\boldsymbol{k}} = D^{cbad}_{\boldsymbol{Q},\boldsymbol{q},\boldsymbol{k}}. \tag{2.11}$$

The symmetrized interaction vertices that satisfy Eqs. (2.9)-(2.11) are found to be

$$\epsilon_{\text{cl}} = \frac{1}{2N_s}\sum_{ab}\mathcal{J}^{00}_{\mathbf{0},ab}, \tag{2.12}$$

$$L^a = \sum_b \mathcal{J}^{+0}_{\mathbf{0},ab}, \tag{2.13}$$

$$A^{ab}_{\boldsymbol{k}} = \mathcal{J}^{+-}_{\boldsymbol{k},ab} - \delta_{ab}\sum_c \mathcal{J}^{00}_{\mathbf{0},ac}, \tag{2.14}$$

$$B^{ab}_{\boldsymbol{k}} = \mathcal{J}^{++}_{\boldsymbol{k},ab}, \tag{2.15}$$

$$T^{abc}_{\boldsymbol{kq}} = -\delta_{bc}\mathcal{J}^{+0}_{\boldsymbol{k},ab} - \delta_{ac}\mathcal{J}^{+0}_{\boldsymbol{q},ba}, \tag{2.16}$$

$$\begin{aligned} V^{abcd}_{\boldsymbol{k},\boldsymbol{q},\boldsymbol{Q}} = {} & \frac{1}{2}\delta_{ac}\delta_{bd}\left(\mathcal{J}^{00}_{\boldsymbol{k}-\boldsymbol{q}+\boldsymbol{Q},ab} + \mathcal{J}^{00}_{-\boldsymbol{k}+\boldsymbol{q}-\boldsymbol{Q},ba}\right) + \frac{1}{2}\delta_{ad}\delta_{bc}\left(+\mathcal{J}^{00}_{\boldsymbol{Q},ab} + \mathcal{J}^{00}_{-\boldsymbol{Q},ba}\right) \\ & - \frac{1}{2}\left(\delta_{bc}\delta_{bd}\mathcal{J}^{+-}_{\boldsymbol{k}+\boldsymbol{Q},ab} + \delta_{ac}\delta_{ad}\mathcal{J}^{+-}_{\boldsymbol{q}-\boldsymbol{Q},ba} + \delta_{ab}\delta_{ad}\mathcal{J}^{+-}_{\boldsymbol{q},ac} + \delta_{ab}\delta_{ac}\mathcal{J}^{+-}_{\boldsymbol{k},ad}\right), \end{aligned} \tag{2.17}$$

$$D^{abcd}_{\boldsymbol{k},\boldsymbol{q},\boldsymbol{Q}} = -\frac{1}{2}\left(\delta_{cb}\delta_{db}\mathcal{J}^{++}_{\boldsymbol{k},ab} + \delta_{ac}\delta_{ad}\mathcal{J}^{++}_{\boldsymbol{q},ba} + \delta_{ab}\delta_{ad}\mathcal{J}^{++}_{\boldsymbol{Q},ca}\right), \tag{2.18}$$

where the Fourier transform of the local exchange matrices is defined as

$$\mathcal{J}^{\mu\nu}_{\boldsymbol{k},ab} \equiv \sum_{\boldsymbol{\delta}} e^{i\boldsymbol{k}\cdot\boldsymbol{\delta}}\mathcal{J}^{\mu\nu}_{\boldsymbol{\delta},ab}, \tag{2.19}$$

with $\mu, \nu = 0, \pm$ and the sum is taken over all bond vectors $\boldsymbol{\delta}$ connecting sites of type a to sites of type b. Note that the one-magnon vertex L^a vanishes so long as the classical configuration energy ϵ_{cl} is at a local minimum.

The Dyson-Maleev representation

Another bosonic representation of spin operators introduced by Dyson [36] and Maleev [37] is given by

$$\boldsymbol{S}_{\boldsymbol{r},a} = \left(S - n_{\boldsymbol{r},a}\right)\hat{\boldsymbol{e}}_{a,0} + \sqrt{S}\left[\left(1 - \frac{n_{\boldsymbol{r},a}}{2S}\right)a_{\boldsymbol{r},a}\hat{\boldsymbol{e}}_{a,-} + a^{\dagger}_{\boldsymbol{r}a}\hat{\boldsymbol{e}}_{a,+}\right], \tag{2.20}$$

with the restriction that physical states must satisfy $n_{\boldsymbol{r},a} \leq 2S$. This transformation avoids the use of a square root and therefore remains exact without the need for an infinite power series expansion of the number operator $n_{\boldsymbol{r},a}/2S$, producing at most a three-magnon interaction for a general bilinear spin Hamiltonian. The downside to this transformation is that it is non-Hermitian,

as we can see from Eq. (2.20), the raising and lowering operators $S^{\pm}_{\boldsymbol{r},a} = \sqrt{2}\hat{\boldsymbol{e}}^{\intercal}_{a,\pm}\boldsymbol{S}_{\boldsymbol{r},a}$ are no longer hermitian conjugates of each other.

Dyson showed that although Eq. (2.20) turns the spin Hamiltonian into a non-hermitian operator, the matrix elements between physical spin states are preserved when restricted to the physical subspace $n_{\boldsymbol{r},a} \leq 2S$. Furthermore, Dyson argued that relaxing the constraint to allow for unphysical states ($n_{\boldsymbol{r},a} > 2S$) does not modify the leading power-law contributions to observables at low temperatures. In particular, he showed that for a Heisenberg model, the effect of unphysical boson states is always less than $e^{-gT_{\mathrm{C}}/T}$, where T_{C} is the Curie temperature and g is a constant independent of temperature [39], while a similar statement cannot be extended to the Holstein-Primakoff representation.

Historically, the Dyson-Maleev representation was used extensively in the study of two-magnon bound states [36, 40–47]. This representation is particularly well suited for the study of Heisenberg models, which can be written in an exact form that contains only a four-magnon interaction using Eq. (2.20) [39]. Nonetheless, this representation will not be employed further in this thesis, as the Holstein–Primakoff representation is sufficient for the scope of the work presented here.

Linear spin-wave theory

The linear spin wave Hamiltonian results from truncating the Holstein-Primakoff expansion at $O(S)$ [Eqs. (2.4)-(2.6)] about a configuration corresponding to a classical ground state

$$H = NS^2\epsilon_{\mathrm{cl}} + S\sum_{\boldsymbol{k}}\sum_{ab}\left[A^{ab}_{\boldsymbol{k}}a^{\dagger}_{\boldsymbol{k},a}a_{\boldsymbol{k},b} + \frac{1}{2}\left(B^{ab}_{\boldsymbol{k}}a^{\dagger}_{\boldsymbol{k},a}a^{\dagger}_{-\boldsymbol{k},b} + \mathrm{H.c.}\right)\right] + O(S^{1/2}). \tag{2.21}$$

It is then convenient to rearrange the coefficients into matrix form

$$H = NS(S+1)\epsilon_{\mathrm{cl}} + \frac{S}{2}\sum_{\boldsymbol{k}}\begin{pmatrix}[\boldsymbol{a}^{\dagger}_{\boldsymbol{k}}]^{\intercal} & \boldsymbol{a}^{\intercal}_{-\boldsymbol{k}}\end{pmatrix}\begin{pmatrix}\boldsymbol{A}_{\boldsymbol{k}} & \boldsymbol{B}_{\boldsymbol{k}}\\ \boldsymbol{B}^{\dagger}_{\boldsymbol{k}} & \boldsymbol{A}^{\intercal}_{-\boldsymbol{k}}\end{pmatrix}\begin{pmatrix}\boldsymbol{a}_{\boldsymbol{k}}\\ \boldsymbol{a}^{\dagger}_{-\boldsymbol{k}}\end{pmatrix} + O(S^{1/2}). \tag{2.22}$$

We may diagonalize Eq. (2.22) by introducing a new set of bosons $b_{\boldsymbol{k},a}$, such that

$$\begin{pmatrix}\boldsymbol{a}_{\boldsymbol{k}}\\ \boldsymbol{a}^{\dagger}_{-\boldsymbol{k}}\end{pmatrix} = \mathcal{T}_{\boldsymbol{k}}\begin{pmatrix}\boldsymbol{b}_{\boldsymbol{k}}\\ \boldsymbol{b}^{\dagger}_{-\boldsymbol{k}}\end{pmatrix}. \tag{2.23}$$

Note that we have allowed for the new operators $b_{\boldsymbol{k},a}$ to be constructed from linear combinations of both $a_{\boldsymbol{k},a}$ and $a^{\dagger}_{-\boldsymbol{k},a}$, which is the most general linear transformation that conserves momentum.

By requiring $\left[b_{\boldsymbol{k},a}, b_{\boldsymbol{k},b}\right] = 0$ and $\left[b_{\boldsymbol{k},a}, b^\dagger_{\boldsymbol{k},b}\right] = \delta_{ab}$, we obtain the defining "para-unitary" condition for the boson Bogoliubov transformation [48]

$$\mathcal{T}_{\boldsymbol{k}}^{-1} = \boldsymbol{\sigma}_3 \mathcal{T}_{\boldsymbol{k}}^\dagger \boldsymbol{\sigma}_3, \tag{2.24}$$

where $\boldsymbol{\sigma}_3 = \mathrm{diag}(\mathbb{I}, -\mathbb{I})$ is a block Pauli matrix. Combining Eqs. (2.22)-(2.24), we find

$$H = NS(S+1)\epsilon_{\mathrm{cl}} + \frac{S}{2}\sum_{\boldsymbol{k}} \begin{pmatrix} [\boldsymbol{b}^\dagger_{\boldsymbol{k}}]^\intercal & \boldsymbol{b}^\intercal_{-\boldsymbol{k}} \end{pmatrix} \boldsymbol{\sigma}_3 \mathcal{T}_{\boldsymbol{k}}^{-1} \boldsymbol{\sigma}_3 \begin{pmatrix} \boldsymbol{A}_{\boldsymbol{k}} & \boldsymbol{B}_{\boldsymbol{k}} \\ \boldsymbol{B}^\dagger_{\boldsymbol{k}} & \boldsymbol{A}^\intercal_{-\boldsymbol{k}} \end{pmatrix} \mathcal{T}_{\boldsymbol{k}} \begin{pmatrix} \boldsymbol{b}_{\boldsymbol{k}} \\ \boldsymbol{b}^\dagger_{-\boldsymbol{k}} \end{pmatrix} + O(S^{1/2}). \tag{2.25}$$

The linear spin wave energies and corresponding wavefunctions are therefore determined by diagonalizing the $2N_s \times 2N_s$ boson Bogoliubov-de Gennes matrix [49]

$$\boldsymbol{\sigma}_3 \boldsymbol{M}_{\boldsymbol{k}} \equiv \begin{pmatrix} \boldsymbol{A}_{\boldsymbol{k}} & \boldsymbol{B}_{\boldsymbol{k}} \\ -\boldsymbol{B}^\dagger_{\boldsymbol{k}} & -\boldsymbol{A}^\intercal_{-\boldsymbol{k}} \end{pmatrix}, \tag{2.26}$$

with the columns of $\mathcal{T}_{\boldsymbol{k}}$ being made up of the eigenvectors of $\boldsymbol{\sigma}_3 \boldsymbol{M}_{\boldsymbol{k}}$, a generally non-Hermitian matrix. Based on the definitions in Eqs. (2.14) and (2.15), this matrix satisfies

$$\boldsymbol{\sigma}_1 \boldsymbol{M}_{\boldsymbol{k}} \boldsymbol{\sigma}_1 = \boldsymbol{M}^\intercal_{-\boldsymbol{k}}, \qquad \boldsymbol{\sigma}_1 \equiv \begin{pmatrix} \boldsymbol{0} & \mathbb{I} \\ \mathbb{I} & \boldsymbol{0} \end{pmatrix} \tag{2.27}$$

This can be viewed as an effective "particle-hole" symmetry, in analogy with electronic systems, and guarantees that the eigenvectors of Eq. (2.26) come in pairs $\boldsymbol{V}_{\boldsymbol{k},a}$ and $\boldsymbol{W}_{\boldsymbol{k},a} = \boldsymbol{\sigma}_1 \overline{\boldsymbol{V}}_{-\boldsymbol{k},a}$ [50], with eigenvalues $\pm\epsilon_{\pm\boldsymbol{k},a}$.[4,5] These make up the columns of the transformation matrix, i.e.

$$\mathcal{T}_{\boldsymbol{k}} = \begin{pmatrix} | & & | & | & & | \\ \boldsymbol{V}_{\boldsymbol{k},1} & \cdots & \boldsymbol{V}_{\boldsymbol{k},N_s} & \boldsymbol{W}_{\boldsymbol{k},1} & \cdots & \boldsymbol{W}_{\boldsymbol{k},N_s} \\ | & & | & | & & | \end{pmatrix}. \tag{2.28}$$

[4] Here, $\overline{\boldsymbol{V}}_{-\boldsymbol{k},a}$ represents the complex conjugate of $\boldsymbol{V}_{-\boldsymbol{k},a}$.

[5] To see this, multiply the complex conjugate of the eigenvalue equation $\boldsymbol{\sigma}_3 \boldsymbol{M}_{-\boldsymbol{k}} \boldsymbol{V}_{-\boldsymbol{k},a} = \epsilon_{-\boldsymbol{k},a} \boldsymbol{V}_{-\boldsymbol{k},a}$ by $\boldsymbol{\sigma}_1$ on the left, to obtain

$$-\boldsymbol{\sigma}_3 \boldsymbol{\sigma}_1 \boldsymbol{M}^\intercal_{-\boldsymbol{k}} \boldsymbol{\sigma}_1 \boldsymbol{\sigma}_1 \overline{\boldsymbol{V}}_{-\boldsymbol{k},a} = \epsilon_{-\boldsymbol{k},a} \boldsymbol{\sigma}_1 \overline{\boldsymbol{V}}_{-\boldsymbol{k},a},$$

where we have used the anticommutator relations $\{\boldsymbol{\sigma}_i, \boldsymbol{\sigma}_j\} = 2\delta_{ij}$. Using Eq. (2.27), we find

$$\boldsymbol{\sigma}_3 \boldsymbol{M}_{\boldsymbol{k}} \boldsymbol{\sigma}_1 \overline{\boldsymbol{V}}_{-\boldsymbol{k},a} = -\epsilon_{-\boldsymbol{k},a} \boldsymbol{\sigma}_1 \overline{\boldsymbol{V}}_{-\boldsymbol{k},a}.$$

To satisfy Eq. (2.24), the eigenvectors are chosen to satisfy the para-orthogonality conditions

$$\boldsymbol{V}_{\boldsymbol{k},a}^{\dagger}\boldsymbol{\sigma_3}\boldsymbol{V}_{\boldsymbol{k},b} = +\delta_{ab}, \tag{2.29}$$

$$\boldsymbol{W}_{\boldsymbol{k},a}^{\dagger}\boldsymbol{\sigma_3}\boldsymbol{W}_{\boldsymbol{k},b} = -\delta_{ab}, \tag{2.30}$$

$$\boldsymbol{V}_{\boldsymbol{k},a}^{\dagger}\boldsymbol{\sigma_3}\boldsymbol{W}_{\boldsymbol{k},b} = 0. \tag{2.31}$$

It follows that the spectral decomposition for the matrix $\boldsymbol{M}_{\boldsymbol{k}}$ is

$$\boldsymbol{M}_{\boldsymbol{k}} = \sum_a \boldsymbol{\sigma}_3 \left(\epsilon_{\boldsymbol{k},a} \boldsymbol{V}_{\boldsymbol{k},a} \boldsymbol{V}_{\boldsymbol{k},a}^{\dagger} + \epsilon_{-\boldsymbol{k},a} \boldsymbol{W}_{-\boldsymbol{k},a} \boldsymbol{W}_{-\boldsymbol{k},a}^{\dagger} \right) \boldsymbol{\sigma}_3. \tag{2.32}$$

The linear spin wave Hamiltonian then takes the diagonal form

$$H = NS(S+1)\epsilon_{\mathrm{cl}} + NS\epsilon_{\mathrm{qu}} + S\sum_{\boldsymbol{k}}\sum_{a=1}^{N_s} \epsilon_{\boldsymbol{k},a} b_{\boldsymbol{k},a}^{\dagger} b_{\boldsymbol{k},a} + O(S^{1/2}), \tag{2.33}$$

where the quantum zero-point energy (per spin) is

$$S\epsilon_{\mathrm{qu}} \equiv \frac{S}{2N}\sum_{\boldsymbol{k}}\sum_{a=1}^{N_s} \epsilon_{\boldsymbol{k},a}. \tag{2.34}$$

We may subsequently calculate the free energy (per spin) to $O(S)$ at temperature T as

$$f(T) = S(S+1)\epsilon_{\mathrm{cl}} + S\epsilon_{\mathrm{qu}} + \frac{k_{\mathrm{B}}T}{N}\sum_{\boldsymbol{k}}\sum_{a=1}^{N_s} \ln\left(1 - e^{-S\epsilon_{\boldsymbol{k},a}/k_{\mathrm{B}}T}\right) + O(S^{1/2}). \tag{2.35}$$

Some other quantities of interest in linear spin wave theory include the internal energy (per spin)

$$\langle H \rangle = S(S+1)\epsilon_{\mathrm{cl}} + S\epsilon_{\mathrm{qu}} + \frac{S}{N}\sum_{\boldsymbol{k}}\sum_{a=1}^{N_s} \frac{\epsilon_{\boldsymbol{k},a}}{\exp\left(\frac{S\epsilon_{\boldsymbol{k},a}}{k_{\mathrm{B}}T}\right) - 1} + O(S^{1/2}), \tag{2.36}$$

the specific heat (per spin)

$$C_V = \frac{\partial \langle H \rangle}{\partial T} = \frac{k_{\mathrm{B}}}{N}\sum_{\boldsymbol{k}}\sum_{a=1}^{N_s} \frac{\left(\frac{S\epsilon_{\boldsymbol{k},a}}{k_{\mathrm{B}}T}\right)^2 \exp\left(\frac{S\epsilon_{\boldsymbol{k},a}}{k_{\mathrm{B}}T}\right)}{\left[\exp\left(\frac{S\epsilon_{\boldsymbol{k},a}}{k_{\mathrm{B}}T}\right) - 1\right]^2} + O(S^{1/2}), \tag{2.37}$$

and the reduction of the ordered moment (per spin)

$$\frac{1}{N}\sum_{\boldsymbol{r},a}\left\langle \hat{\boldsymbol{e}}_{0,a}^{\intercal}\boldsymbol{S}_{\boldsymbol{r},a}\right\rangle = \frac{\partial\left\langle H\right\rangle}{\partial T} = S - \frac{1}{N}\sum_{\boldsymbol{k}}\sum_{a=1}^{N_s}\frac{1}{\exp\left(\frac{S\epsilon_{\boldsymbol{k},a}}{k_{\mathrm{B}}T}\right)-1} + O(S^{-1/2}). \tag{2.38}$$

While linear spin wave theory often provides a useful description of the excitations of quantum magnets at low temperature, it neglects interactions between magnons (e.g., Eqs. (2.7) and (2.8)) that become increasingly important at finite temperature or in low-spin systems. In the following section, we develop a perturbative framework to systematically include these corrections to leading order in $1/S$.

2.2 Perturbation theory

A particularly powerful approach for modelling finite-temperature quantum many-body systems is the imaginary-time (Matsubara) formalism [51], which reformulates the partition function in terms of a path integral evaluated along an imaginary time axis. This framework naturally encodes thermal effects in the calculation of physical correlation functions. In this formalism, the imaginary-time single-magnon *Green's function* (or *propagator*) is defined as

$$\mathcal{G}(\boldsymbol{k},\tau) \equiv \begin{pmatrix} \mathcal{G}^{-+}(\boldsymbol{k},\tau) & \mathcal{G}^{--}(\boldsymbol{k},\tau) \\ \mathcal{G}^{++}(\boldsymbol{k},\tau) & \mathcal{G}^{+-}(\boldsymbol{k},\tau) \end{pmatrix}, \tag{2.39}$$

with components

$$\mathcal{G}_{ab}^{-+}(\boldsymbol{k},\tau-\tau') = \left\langle \mathbb{T}_\tau a_{\boldsymbol{k},a}(\tau)a_{\boldsymbol{k},b}^{\dagger}(\tau')\right\rangle, \tag{2.40}$$

$$\mathcal{G}_{ab}^{+-}(\boldsymbol{k},\tau-\tau') = \left\langle \mathbb{T}_\tau a_{-\boldsymbol{k},a}^{\dagger}(\tau)a_{-\boldsymbol{k},b}(\tau')\right\rangle, \tag{2.41}$$

$$\mathcal{G}_{ab}^{++}(\boldsymbol{k},\tau-\tau') = \left\langle \mathbb{T}_\tau a_{-\boldsymbol{k},a}^{\dagger}(\tau)a_{\boldsymbol{k},b}^{\dagger}(\tau')\right\rangle, \tag{2.42}$$

$$\mathcal{G}_{ab}^{--}(\boldsymbol{k},\tau-\tau') = \left\langle \mathbb{T}_\tau a_{\boldsymbol{k},a}(\tau)a_{-\boldsymbol{k},b}(\tau')\right\rangle, \tag{2.43}$$

where $\langle\cdots\rangle \equiv \mathrm{Tr}\left[(\cdots)e^{-H/k_{\mathrm{B}}T}\right] / \mathrm{Tr}\left[e^{-H/k_{\mathrm{B}}T}\right]$ is the ensemble average and $\mathbb{T}_\tau$ is the imaginary time ordering operator, with time increasing from right to left [52]. For example, Eq. (2.40) is calculated as

$$\mathcal{G}_{ab}^{-+}(\boldsymbol{k},\tau-\tau') = \theta(\tau-\tau')\left\langle a_{\boldsymbol{k},a}(\tau)a_{\boldsymbol{k},b}^{\dagger}(\tau')\right\rangle + \theta(\tau'-\tau)\left\langle a_{\boldsymbol{k},b}^{\dagger}(\tau')a_{\boldsymbol{k},a}(\tau)\right\rangle. \tag{2.44}$$

The Fourier transform over the imaginary time variable is defined as

$$\mathcal{G}^{\mu\nu}_{ab}(\boldsymbol{k}, i\omega_n) \equiv \int_0^{(k_\mathrm{B}T)^{-1}} \mathrm{d}\tau\; e^{i\omega_n\tau}\mathcal{G}^{\mu\nu}_{ab}(\boldsymbol{k},\tau), \qquad \mathcal{G}^{\mu\nu}_{ab}(\boldsymbol{k},\tau) = k_\mathrm{B}T\sum_{\omega_n} e^{-i\omega_n\tau}\mathcal{G}^{\mu\nu}_{ab}(\boldsymbol{k}, i\omega_n), \tag{2.45}$$

where $\omega_n = 2\pi n k_\mathrm{B}T$ are the bosonic Matsubara frequencies.

Green's functions in linear spin wave theory

For the purpose of perturbation theory, we first solve for the propagators in linear spin wave theory, from which we can subsequently calculate corrections due to magnon-magnon interactions. For this task, it is useful to express the Bogoliubov transformation $\boldsymbol{\mathcal{T}}_{\boldsymbol{k}}$ of Eq. (2.23) as a block matrix [49]

$$\boldsymbol{\mathcal{T}}_{\boldsymbol{k}} \equiv \begin{pmatrix} \boldsymbol{X}_{\boldsymbol{k}} & \overline{\boldsymbol{Y}}_{-\boldsymbol{k}} \\ \boldsymbol{Y}_{\boldsymbol{k}} & \overline{\boldsymbol{X}}_{-\boldsymbol{k}} \end{pmatrix}, \tag{2.46}$$

This allows us to express the Bogoliubov quasiparticles as

$$a_{\boldsymbol{k},a} = \sum_c \left[X^{ac}_{\boldsymbol{k}} b_{\boldsymbol{k},c} + \overline{Y}^{ac}_{-\boldsymbol{k}} b^\dagger_{-\boldsymbol{k},c} \right]. \tag{2.47}$$

We define the bare Green's functions[6] as

$$g^{-+}_{ab}(\boldsymbol{k}, \tau-\tau') = \left\langle \mathbb{T}_\tau a_{\boldsymbol{k},a}(\tau) a^\dagger_{\boldsymbol{k},b}(\tau') \right\rangle_0, \tag{2.48}$$

$$g^{+-}_{ab}(\boldsymbol{k}, \tau-\tau') = \left\langle \mathbb{T}_\tau a^\dagger_{-\boldsymbol{k},a}(\tau) a_{-\boldsymbol{k},b}(\tau') \right\rangle_0, \tag{2.49}$$

$$g^{++}_{ab}(\boldsymbol{k}, \tau-\tau') = \left\langle \mathbb{T}_\tau a^\dagger_{-\boldsymbol{k},a}(\tau) a^\dagger_{\boldsymbol{k},b}(\tau') \right\rangle_0, \tag{2.50}$$

$$g^{--}_{ab}(\boldsymbol{k}, \tau-\tau') = \left\langle \mathbb{T}_\tau a_{\boldsymbol{k},a}(\tau) a_{-\boldsymbol{k},b}(\tau') \right\rangle_0, \tag{2.51}$$

where $\langle\cdots\rangle_0$ refers to the ensemble average with respect to the linear spin wave Hamiltonian in Eq. (2.22). A direct calculation of the propagators in the energy eigenbasis leads to

$$\int_0^{(k_\mathrm{B}T)^{-1}} \mathrm{d}\tau\; e^{i\omega_n\tau} \left\langle \mathbb{T}_\tau b_{\boldsymbol{k},a}(\tau) b^\dagger_{\boldsymbol{k},b}(0) \right\rangle_0 = \frac{\delta_{ab}}{-i\omega_n + S\epsilon_{\boldsymbol{k},a}}, \tag{2.52}$$

$$\int_0^{(k_\mathrm{B}T)^{-1}} \mathrm{d}\tau\; e^{i\omega_n\tau} \left\langle \mathbb{T}_\tau b^\dagger_{-\boldsymbol{k},a}(\tau) b_{-\boldsymbol{k},b}(0) \right\rangle_0 = \frac{\delta_{ab}}{i\omega_n + S\epsilon_{-\boldsymbol{k},a}}, \tag{2.53}$$

[6] Here, bare means "without interactions".

while $\left\langle \mathbb{T}_\tau b^\dagger_{-\boldsymbol{k},a}(\tau) b^\dagger_{\boldsymbol{k},b}(0) \right\rangle_0 = \left\langle \mathbb{T}_\tau b_{\boldsymbol{k},a}(\tau) b_{-\boldsymbol{k},b}(0) \right\rangle_0 = 0$. It follows that the bare Green's functions are

$$g^{-+}_{ab}(\boldsymbol{k}, i\omega_n) = \sum_c \left[\frac{X^{ac}_{\boldsymbol{k}} \bar{X}^{bc}_{\boldsymbol{k}}}{-i\omega_n + S\epsilon_{\boldsymbol{k},c}} + \frac{\bar{Y}^{ac}_{-\boldsymbol{k}} Y^{bc}_{-\boldsymbol{k}}}{i\omega_n + S\epsilon_{-\boldsymbol{k},c}} \right], \tag{2.54}$$

$$g^{+-}_{ab}(\boldsymbol{k}, i\omega_n) \equiv \sum_c \left[\frac{Y^{ac}_{\boldsymbol{k}} \bar{Y}^{bc}_{\boldsymbol{k}}}{-i\omega_n + S\epsilon_{\boldsymbol{k},c}} + \frac{\bar{X}^{ac}_{-\boldsymbol{k}} X^{bc}_{-\boldsymbol{k}}}{i\omega_n + S\epsilon_{-\boldsymbol{k},c}} \right], \tag{2.55}$$

$$g^{++}_{ab}(\boldsymbol{k}, i\omega_n) \equiv \sum_c \left[\frac{Y^{ac}_{\boldsymbol{k}} \bar{X}^{bc}_{\boldsymbol{k}}}{-i\omega_n + S\epsilon_{\boldsymbol{k},c}} + \frac{\bar{X}^{ac}_{-\boldsymbol{k}} Y^{bc}_{-\boldsymbol{k}}}{i\omega_n + S\epsilon_{-\boldsymbol{k},c}} \right], \tag{2.56}$$

$$g^{--}_{ab}(\boldsymbol{k}, i\omega_n) \equiv \sum_c \left[\frac{X^{ac}_{\boldsymbol{k}} \bar{Y}^{bc}_{\boldsymbol{k}}}{-i\omega_n + S\epsilon_{\boldsymbol{k},c}} + \frac{\bar{Y}^{ac}_{-\boldsymbol{k}} X^{bc}_{-\boldsymbol{k}}}{i\omega_n + S\epsilon_{-\boldsymbol{k},c}} \right]. \tag{2.57}$$

$$\tag{2.58}$$

Organizing these into a matrix, we find

$$\boldsymbol{g}(\boldsymbol{k}, i\omega_n) \equiv \begin{pmatrix} \boldsymbol{g}^{-+}(\boldsymbol{k}, i\omega_n) & \boldsymbol{g}^{--}(\boldsymbol{k}, i\omega_n) \\ \boldsymbol{g}^{++}(\boldsymbol{k}, i\omega_n) & \boldsymbol{g}^{+-}(\boldsymbol{k}, i\omega_n) \end{pmatrix} = \sum_c \left(\frac{\boldsymbol{V}_{\boldsymbol{k},c} \boldsymbol{V}^\dagger_{\boldsymbol{k},c}}{-i\omega_n + S\epsilon_{\boldsymbol{k},c}} + \frac{\boldsymbol{W}_{-\boldsymbol{k},c} \boldsymbol{W}^\dagger_{-\boldsymbol{k},c}}{i\omega_n + S\epsilon_{-\boldsymbol{k},c}} \right) \tag{2.59}$$

Comparing Eq. (2.59) to Eq. (2.32), we see that the bare Green's function takes the simple form

$$\boldsymbol{g}(\boldsymbol{k}, i\omega_n) = \left(-i\omega_n \boldsymbol{\sigma}_3 + S\boldsymbol{M}_{\boldsymbol{k}}\right)^{-1}. \tag{2.60}$$

To "dress" the Green's function and incorporate interactions, we introduce the self-energy operator.

Magnon self-energy

In non-linear spin wave theory, the magnon-magnon interactions are encoded perturbatively in the imaginary time self-energy $\boldsymbol{\Sigma}(\boldsymbol{k}, i\omega_n)$. This arises from a generalization of the Dyson equation to systems where particle number is not conserved, relating the full Green's function to the bare versions, to include both normal and anomalous blocks.[7] The Dyson-Gor'kov equation is [49]

$$\boldsymbol{\mathcal{G}}(\boldsymbol{k}, i\omega_n) = \boldsymbol{g}(\boldsymbol{k}, i\omega_n) \left[\boldsymbol{1} - \boldsymbol{\Sigma}(\boldsymbol{k}, i\omega_n) \boldsymbol{\mathcal{G}}(\boldsymbol{k}, i\omega_n)\right], \tag{2.61}$$

[7] Here, *normal* refers to the number-conserving blocks of Eq. (2.22) (i.e. terms proportional to $a^\dagger a$ and $aa^\dagger$) and *anomalous* refers to the number-non-conserving blocks (i.e. terms proportional to $a^\dagger a^\dagger$ and aa).

where we have defined the self-energy to have the same block structure as the Green's function

$$\boldsymbol{\Sigma}(\boldsymbol{k}, i\omega_n) = \begin{pmatrix} \boldsymbol{\Sigma}^{-+}(\boldsymbol{k}, i\omega_n) & \boldsymbol{\Sigma}^{--}(\boldsymbol{k}, i\omega_n) \\ \boldsymbol{\Sigma}^{++}(\boldsymbol{k}, i\omega_n) & \boldsymbol{\Sigma}^{+-}(\boldsymbol{k}, i\omega_n) \end{pmatrix}. \tag{2.62}$$

The Dyson-Gor'kov equation Eq. (2.61) arises directly from the equations of motion of the Green's function and perturbation theory, effectively summing an infinite series of interaction processes into a compact form that captures how quasiparticles propagate while being renormalized by interactions [49, 53]. Solving Eq. (2.61) for the full Green's function, we find

$$\boldsymbol{\mathcal{G}}(\boldsymbol{k}, i\omega_n) = \left[\boldsymbol{g}(\boldsymbol{k}, i\omega_n)^{-1} + \boldsymbol{\Sigma}(\boldsymbol{k}, i\omega_n)\right]^{-1} = \left[-i\omega_n \boldsymbol{\sigma}_3 + S\boldsymbol{M}_{\boldsymbol{k}} + \boldsymbol{\Sigma}(\boldsymbol{k}, i\omega_n)\right]^{-1}. \tag{2.63}$$

Interactions may therefore be included by calculating the self-energy perturbatively in the limit $1/S \to 0$. To do this, it is useful to introduce diagrammatic representations of the Green's functions and self-energy. In this context, the bare propagators are represented as lines with directed arrows:

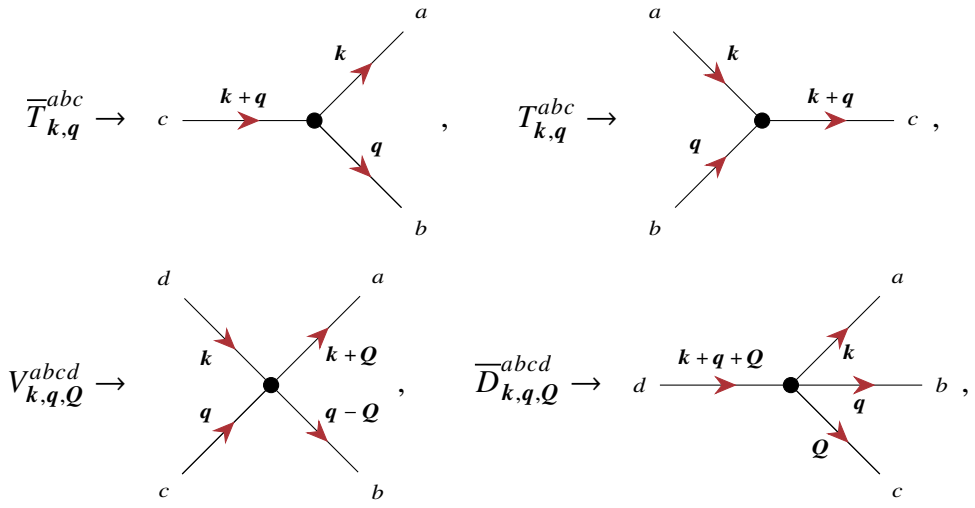
$$g^{-+}_{ab}(\boldsymbol{k}, i\omega_n) \;\to\; a \xrightarrow{\boldsymbol{k}, i\omega_n} b\,, \tag{2.64}$$

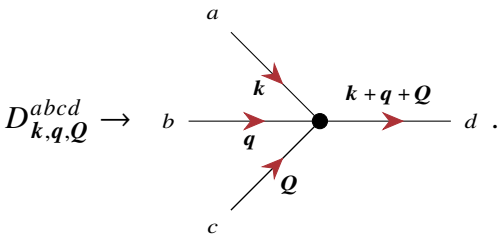
$$g^{+-}_{ab}(\boldsymbol{k}, i\omega_n) \;\to\; a \xleftarrow{\boldsymbol{k}, i\omega_n} b\,, \tag{2.65}$$

$$g^{++}_{ab}(\boldsymbol{k}, i\omega_n) \;\to\; a \xleftarrow{\boldsymbol{k}, i\omega_n} b\,, \tag{2.66}$$

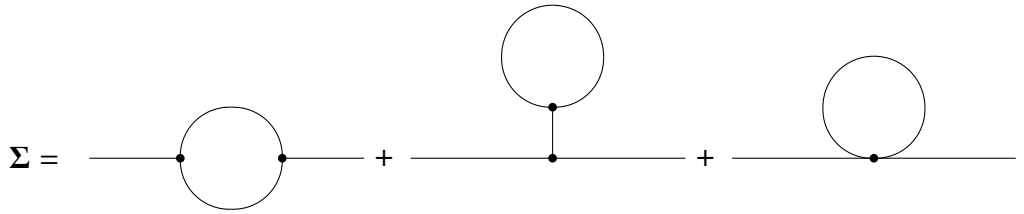
$$g^{--}_{ab}(\boldsymbol{k}, i\omega_n) \;\to\; a \xrightarrow{\boldsymbol{k}, i\omega_n} b\,, \tag{2.67}$$

while each of the vertices in Eqs. (2.7) and (2.8) are represented as





The self-energy then corresponds to the sum of all one-particle irreducible[8] diagrams with two external legs [53]. As one expects in perturbation theory, we can truncate this infinite sum to some finite order of the expansion parameter at hand. In the case of spin wave theory, the leading $O(S^0)$ contribution to the self-energy can be represented as the sum of three classes of diagrams [53]



(2.68)

constructed from both three- and four-magnon interaction vertices. In general, these diagrams carry a conserved wavevector and frequency $(\boldsymbol{k}, \omega)$, and sublattice indices, and include both normal and anomalous propagators. The explicit evaluation of these diagrams is provided in Appendix A.

Real-time Green's functions

Oftentimes, we are interested in the real-time retarded (advanced) Green's functions $\boldsymbol{G}^{R(A)}(\boldsymbol{k}, \omega)$, defined respectively as

$$G^{R(A),-+}_{ab}(\boldsymbol{k},\omega) = \mp i \int \mathrm{d}t \;\; e^{i\omega t}\theta(\pm t)\left\langle\left[a_{\boldsymbol{k},a}(t), a^{\dagger}_{\boldsymbol{k},b}(0)\right]\right\rangle, \tag{2.69}$$

$$G^{R(A),+-}_{ab}(\boldsymbol{k},\omega) = \mp i \int \mathrm{d}t \;\; e^{i\omega t}\theta(\pm t)\left\langle\left[a^{\dagger}_{-\boldsymbol{k},a}(t), a_{-\boldsymbol{k},b}(0)\right]\right\rangle, \tag{2.70}$$

$$G^{R(A),++}_{ab}(\boldsymbol{k},\omega) = \mp i \int \mathrm{d}t \;\; e^{i\omega t}\theta(\pm t)\left\langle\left[a^{\dagger}_{-\boldsymbol{k},a}(t), a^{\dagger}_{\boldsymbol{k},b}(0)\right]\right\rangle, \tag{2.71}$$

$$G^{R(A),--}_{ab}(\boldsymbol{k},\omega) = \mp i \int \mathrm{d}t \;\; e^{i\omega t}\theta(\pm t)\left\langle\left[a_{\boldsymbol{k},a}(t), a_{-\boldsymbol{k},b}(0)\right]\right\rangle. \tag{2.72}$$

[8] One-particle irreducible diagrams are those that cannot be disconnected into two distinct self-energy diagrams by cutting a single internal propagator line.

The Green's functions in real-time and imaginary time can be related by analytic continuation. This amounts to the replacement $i\omega_n \to \omega \pm i0^+$ for the retarded and advanced Green's functions, respectively. In particular, we have [53]

$$\boldsymbol{G}^{R(A)}(\boldsymbol{k}, \omega) = -\boldsymbol{\mathcal{G}}(\boldsymbol{k}, i\omega_n \to \omega \pm i0^+). \tag{2.73}$$

The details of spin wave theory developed in this chapter are used throughout the remainder of the thesis. In Chapter 3, linear spin wave theory is used to characterize ObD in the system at hand, while non-linear corrections are included perturbatively to characterize the stability of magnetic order. In Chapter 4, the finite-temperature self-energy operator is computed to characterize the fluctuation-induced gap in systems with ObD. In Chapter 5, linear spin wave theory is used to calculate the thermodynamic and anomalous transport properties of $Lu_2V_2O_7$.

Chapter 3

Order-by-disorder without quantum zero-point fluctuations

3.0 Preface

Order-by-disorder (ObD), where competing interactions lead to a collection of "accidentally" degenerate ground-state configurations that are not protected by any symmetries, arises naturally in many frustrated magnetic systems. The absence of symmetry makes the system susceptible to selecting a subset of degenerate configurations due to fluctuations, both thermal or quantum in origin. Although such fluctuations are often viewed as mechanisms that undermine the stability of conventional long-range order [54], ObD can occur when the level of frustration is present but not overwhelmingly strong [55].

Throughout the existing literature on ObD, there is typically a distinction made between ObD arising from either thermal or quantum fluctuations. Although these two mechanisms of ObD often select the same magnetic order [56–59], there are a number of previously studied circumstances where this is not the case [60–63], leading to an additional degree of competition between different magnetic orders. Therefore, to obtain a comprehensive understanding of the ordered phases at finite temperature, it is generally necessary to treat both thermal and quantum fluctuations on the same footing.

The motivating question for this chapter is whether ObD via one mode of fluctuations is even possible without the other present. In the published work contained in this chapter, this question is addressed by studying the ferromagnetic pyrochlore Heisenberg model with Dzyaloshinskii-Moriya (DM) interactions. In particular, we present the completely worked out example of

ObD on the pyrochlore lattice with nearest-neighbour DM interactions. For a wide range of parameters, the ground state of this model is a simple collinear ferromagnetic configuration. It is demonstrated that such a system exhibits thermal ObD in the *absence* of any quantum zero-point fluctuations, as the exact ground state of the model is a product state. In addition, the stability of the magnetic order in the model considered in the quantum limit for an $S = \frac{1}{2}$ system using the non-linear spin wave theory developed in Chapter 2. It is proposed that these results should extend to a more general class of anisotropic Heisenberg ferromagnets.

PHYSICAL REVIEW B **111**, 184434 (2025)

©2025 American Physical Society

Order-by-disorder without quantum zero-point fluctuations in the pyrochlore Heisenberg ferromagnet with Dzyaloshinskii-Moriya interactions

Alexander Hickey,[1,*] Daniel Lozano-Gómez,[1,2,*] and Michel J. P. Gingras[1]

[1]*Department of Physics and Astronomy, University of Waterloo, Waterloo, Ontario N2L 3G1, Canada*
[2]*Institut für Theoretische Physik and Würzburg-Dresden Cluster of Excellence ct.qmat, Technische Universität Dresden, 01062 Dresden, Germany*

Order-by-disorder, whereby fluctuations lift an accidental classical ground state degeneracy to stabilize a subset of ordered states, is a recurrent and prominent theme in the field of frustrated magnetism, where magnetic moments, or spins, are subject to competing spin-spin interactions. Thus far, such a phenomenon has been discussed in systems where the quantum ground state is not a "classical" product state. In such a case, both thermal and quantum fluctuations act to lift the accidental classical degeneracy, begging the question of whether one mechanism of order-by-disorder is possible without the other. In this paper, we present results exposing an uncharted route to order-by-disorder, one without quantum zero-point fluctuations, in the ferromagnetic pyrochlore Heisenberg system with the DM interaction as the leading perturbation. We prove that any collinear ferromagnetic state is an *exact* eigenstate even in the presence of the anisotropic DM interaction, while thermal fluctuations give rise to a preference in the magnetization direction. Using linear spin wave theory, we find that the anisotropy appears at lowest order as a sub-leading term in the low-temperature expansion of the free energy, proportional to $T^{7/2}$. Our results thus show that the phenomenon of thermal order-by-disorder can, in principle, occur even in the absence of quantum zero-point fluctuations driving quantum order-by-disorder – this being so in particular when the accidentally degenerate ground state of the classical model turns out to be an exact eigenstate of the quantum version of the model. However, and in addition, we find that when the DM interaction is large, the fully polarized ferromagnetic ground state becomes unstable for a spin-$\frac{1}{2}$ system within the framework of non-linear spin wave theory, a result that is presumably closely related to the recent report of a quantum spin liquid in this spin-$\frac{1}{2}$ model at $D/J \approx 2$ reported in [Lozano-Gómez *et al.*, Proc. Natl. Acad. Sci. USA **121**, e2403487121 (2024)].

[*] These authors contributed equally to the project.

3.1 Introduction

In correlated many-body systems with competing or frustrated interactions, thermal and quantum fluctuations may suppress the development of a symmetry-breaking transition to long-range order down to extremely low temperatures and, in some cases, completely prevent it [22, 54, 55, 64–69]. This observation, however, does not mean that the presence of such fluctuations only has the effect of undermining the development of long-range ordered phases. Indeed, a contrary and at first sight seemingly paradoxical scenario may arise where the long-range order can be *assisted* by the presence of quantum or thermal fluctuations, when the level of frustration is "not too high" [55], a phenomenon known as *order-by-disorder* [10, 56, 70].[11]

The study of frustrated magnetic systems has proven to be fruitful ground in the study and realization of this phenomenon, where competing exchange interactions result in a set of "accidentally" degenerate ground-state configurations at the classical level that are not protected by symmetries of the Hamiltonian [56, 71, 72]. Thanks to the lack of any symmetry protecting this ground state degeneracy, the system becomes prone to selecting a subset of configurations within the degenerate manifold of classical ground states due to spin fluctuations at temperature T. These fluctuations can be both thermal ($T > 0$) or quantum ($T = 0$) in origin. In the thermal case, first discussed in Ref. [10], a subset of the degenerate states is selected at $T = 0^+$ by maximizing the entropy associated with fluctuations about the ultimately "selected" ordered magnetic moment direction [73]. Conversely, the lifting of degeneracy at the quantum level [71, 74] occurs as a result of perturbative corrections to the ground state energy, relative to the classical model, from an inherently semi-classical description of a quantum many-body system [75] — the true ground state of the quantum model not having any accidental degeneracy to lift in the first place.[12]

Despite the distinction between thermal and quantum fluctuations, both of these routes to fluctuation-induced selection are referred to colloquially as order-by-disorder (ObD). Over the last five decades, there has been a large body of theoretical work focusing on models which exhibit thermal ObD [10, 57, 72, 73, 76–84] or quantum ObD [70, 71, 74, 85–105]. In this context, it has been commonplace in the literature to focus on a single mechanism of fluctuations, either thermal or quantum. While it is often the case that both quantum and thermal fluctuations select the

[11] Since frozen random disorder can also lift the accidental classical degeneracy of the parent disorder-free system [56, 64], the term order-by-disorder may be confusing in this context and should perhaps be referred to as "order-by-fluctuations".

[12] From that perspective, and as the present work illustrates through the specific model considered, quantum order-by-disorder ($T = 0$) is not *per se* a "real" physical phenomenon. Rather, it is a statement reflecting a mathematical procedure that perturbatively corrects the approximation of a classical (direct product) ground state for a quantum spin model. Conversely, thermal order-by-disorder ($T > 0$), being driven by "real" thermal fluctuations, can be viewed as a genuine physical phenomenon.

same configurations [56–59], these two mechanisms of fluctuations may instead favour *distinct* long-range order, resulting in an additional transition between two ordered states at $T < T_c$, where T_c is the paramagnetic critical temperature [60–63]. This implies that, in the most general case, both thermal and quantum fluctuations ought to be accounted for to obtain a comprehensive understanding of the selected ordered phases at finite temperature. We note that the lifting of degeneracy due to quenched random disorder can also be referred to as ObD [64, 106–113]. This is, however, a distinct physical mechanism that is not considered in this paper.

While there is an abundance of theoretical work about ObD in spin models, the prevalence of material realizations of ObD is still not fully appreciated. So far, there is only a handful of real materials in which experimental evidence for ObD exists. Examples of magnetic materials where ObD selection is somewhat compelling include $Er_2Ti_2O_7$ [97, 98, 114–117],[13] $CoTiO_3$ [118], $Sr_2Cu_3O_4Cl_2$ [119], $Fe_2Ca_3\,(GeO_4)_3$ [120], $Yb_2Ge_2O_7$ [121], $RbFe(MoO_4)_2$ [122, 123], $Ba_3CoSb_2O_9$ [124], $NaYbSe_2$ [125] and $BaCoS_2$ [126]. However, it is perhaps fair to say that in no case has ObD being at play in these systems been definitively established. This is because there is no agreed-upon "smoking gun" evidence that ObD is operating in a material without proceeding to quantitatively relate experimental results with theoretical calculations predicting ObD for the spin model argued to faithfully describe the material under consideration [58].

To the best of our knowledge, all known examples of ObD selection in magnetic systems where both quantum ($T = 0$) and thermal ($T > 0$) ObD have been studied, exhibit both of these effects.[14] Naturally, this leads to a fundamental question surrounding our current framework for understanding ObD: does the existence of thermal ObD *necessarily* imply the existence of quantum ObD? Or, can we have one form of ObD without the other? In the present work, we address this question by studying the *ferromagnetic* pyrochlore Heisenberg model with an additional anisotropic Dzyaloshinskii-Moriya (DM) interaction as the leading perturbation. In particular, we present the completely worked out example of ObD on the pyrochlore lattice with nearest-neighbour DM interactions. For a wide range of parameters, the classical ground state of this Hamiltonian is a uniform collinear ferromagnet. As our principal result, we show that this system displays a *purely* thermal ObD selection, while quantum ObD selection is *absent* at zero temperature. This illustrates that thermal ObD can, in principle, exist independently of quantum ObD in a quantum magnetic system. We investigate how the ground state degeneracy is lifted due to thermal fluctuations, using both classical and quantum calculation methods, to provide insight into the order parameter selection at all temperatures within the ordered phase. The results pertaining to this spin model therefore represent a rather rare realization of a system exhibiting ObD in the absence of zero-point fluctuations. Additionally, we analyze the stability of

[13] Although selection, at least in part, due to virtual crystal field fluctuations has not been ruled out [115–117].

[14] It is worth noting that the classical (thermal) and quantum ObD selection in the $T \to 0^+$ limit might be distinct than that produced at higher temperatures and in particular for $T \lesssim T_c$ [62, 63].

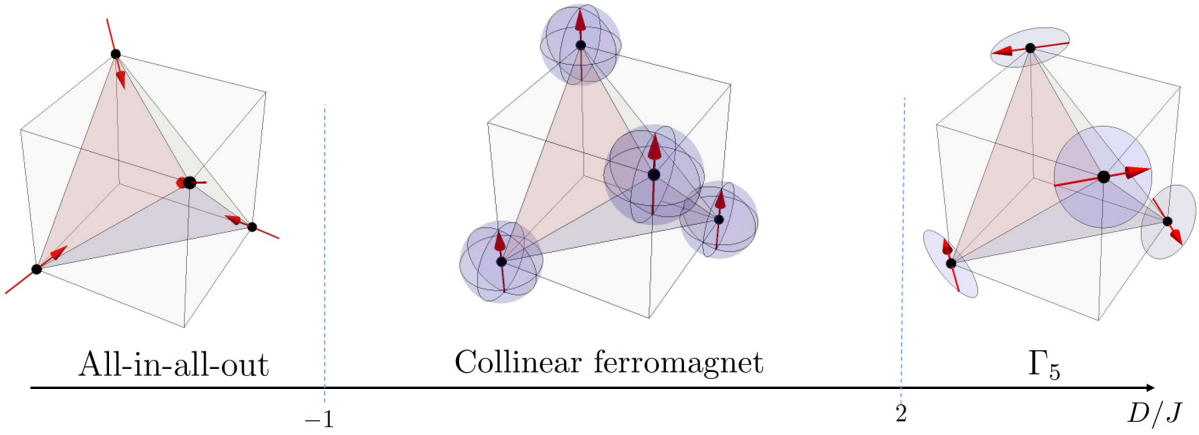


Figure 3.1: Classical ground state configurations of the Hamiltonian in Eq. (3.1) with ferromagnetic $J > 0$, depicted on a single tetrahedron of the pyrochlore lattice. The ground state configuration corresponds to a collinear ferromagnet for $-1 < D/J < 2$, as well as the all-in-all-out and Γ_5 antiferromagnetic configurations for $D/J < -1$ and $D/J > 2$, respectively. The spheres and discs surrounding the spins illustrate manifolds of degenerate spin configurations. The point where $D/J = 0$ corresponds to the Heisenberg ferromagnet.

the ferromagnetic order in the model considered in the quantum limit for an $S = \frac{1}{2}$ system using non-linear spin wave theory. This allows us to identify a region of instability of the ferromagnetic order, which was first alluded to in very recent work [63, 127]. While the results presented here are specifically for the pyrochlore lattice, we propose that the same qualitative effects should arise in any Heisenberg ferromagnet with DM interactions as long as the sum of the DM vectors along the bonds surrounding each site vanishes, such as the kagome lattice with out-of-plane DM vectors.[15]

[15]The kagome Heisenberg ferromagnet with out-of-plane DM vectors has been studied previously in the context of topological effects and interaction-induced damping of magnons [128–133]. The focus of the present paper is ObD at finite temperature $T > 0$, while the cited papers focus mainly on spectral properties at $T = 0$. We note that such a model on the kagome lattice relates to its analogue on the pyrochlore lattice. Indeed, along a cubic (111) direction, the pyrochlore lattice can be seen as a collection of stacked kagome and triangular lattices. Taken on its own, a single kagome layer would then result in a closely related model to the one considered by Ref. [132]. As such, we expect that this model on the pyrochlore lattices exhibits an analogous phenomenon of thermal ObD without quantum zero-point fluctuations.

3.2 Model

We consider the Heisenberg and Dzyaloshinskii-Moriya (DM) Hamiltonian on the pyrochlore lattice, described by the Hamiltonian

$$\mathcal{H} = -J \sum_{\langle i,j \rangle} \boldsymbol{S}_i \cdot \boldsymbol{S}_j - D \sum_{\langle i,j \rangle} \boldsymbol{d}_{ij} \cdot (\boldsymbol{S}_i \times \boldsymbol{S}_j), \tag{3.1}$$

where $\langle i, j \rangle$ refers to the sum over all nearest-neighbour sites, $J > 0$ is the ferromagnetic Heisenberg coupling,[16] and $\{\boldsymbol{d}_{ij}\}$ are the nearest-neighbour DM vectors determined by the Moriya rules [134] and listed in Appendix 3A. This choice of the DM vectors, along with sign convention of the DM interaction in Eq. (3.1), is referred to as being *indirect* (*direct*) when $D > 0$ ($D < 0$) [78].

Classically, the ground states of this model are magnetically ordered phases with $\boldsymbol{q} = \boldsymbol{0}$ ordering wavevector [135], i.e., the magnetic order is fully determined by the spin configuration on a single (basis cell) tetrahedron. The classical ground state configurations are determined by expressing Eq. (3.1) as a sum over all individual tetrahedra, each labelled $\boxtimes$, $\mathcal{H} = \sum_{\boxtimes} \mathcal{H}^{\boxtimes}$, and then minimizing the resulting single-tetrahedron Hamiltonian $\mathcal{H}^{\boxtimes}$. The result of this calculation is pictorially illustrated in Fig. 3.1, where three distinct sets of classical spin configurations are identified: the "all-in-all-out" antiferromagnetic states for $D/J < -1$,[17] collinear ferromagnetic configurations for $-1 < D/J < 2$, and the antiferromagnetic "Γ_5" configurations for $D/J > 2$ [63, 78, 80].

It is well known that the Γ_5 region of the phase diagram exhibits an accidental ground state degeneracy at the classical level, parameterized by the global rotation group U(1) [97, 135]. This continuous symmetry group is reduced by both thermal and quantum fluctuations, resulting in six degenerate ordered configurations that are related by local discrete rotation about a local z axis (the local cubic [111] direction) [63, 78, 80]. In the present work, we point out that the ferromagnetic regime ($-1 < D/J < 2$) of Eq. (3.1) also exhibits an accidental ground state degeneracy at the classical level whenever $D \neq 0$. Inspecting each term in Eq. (3.1), we note that the Heisenberg exchange is completely isotropic, while the cross product appearing in the DM interaction term obviously vanishes for any perfectly collinear configuration. This implies that the different ferromagnetic ground states are related by rotations in three-dimensional space, which can be parametrized by the continuous rotation group O(3). This degeneracy of the classical

[16] In this work we do not consider the possibility of antiferromagnetic $J < 0$ [63].

[17] Although at $D/J = -1$ there is a degeneracy between the internal energy of the all-in-all-out and collinear ferromagnetic phases, we note that, according to our classical Monte Carlo simulation, the collinear ferromagnetic phase is selected at $D/J = -1$ at T_c down to the $T \to 0^+$ limit.

ground state is accidental, as Eq. (3.1) has no continuous symmetry for an arbitrary spin state.[18] Naturally, one may ask whether this accidental degeneracy is lifted by $T = 0$ quantum or $T > 0$ thermal fluctuations, selecting a subset of the ferromagnetic configurations.

Physically, the DM interaction arises as the leading order exchange interaction generated by spin-orbit interactions [134, 136], while, in general, the spin-orbit interaction will give rise to additional anisotropic exchange interactions that are typically weaker than the DM interaction [134, 137]. In particular, for the pyrochlore lattice, there are two additional symmetry-allowed nearest-neighbour exchange couplings in the bilinear spin Hamiltonian [115, 138]. These two couplings correspond to a bond-dependent diagonal "Kitaev" interaction K,[19] and a symmetric off-diagonal "pseudo-dipolar" interaction Γ [115, 139]. When spin-orbit coupling is one of the dominant energy scales, these additional couplings cannot be ignored in general, as is the case of rare-earth pyrochlore magnets [23, 140]. The effect of a small but nonzero Γ/J is to induce a finite canting angle to the spins, splaying away from a perfect collinear ferromagnetic configuration [135].

In this paper, we only consider the Heisenberg and DM interactions, and ignore the remaining two symmetry-allowed K and Γ couplings. This model was shown to display collinear ferromagnetic order in both the classical and quantum scenarios [63], resulting in an accidental O(3) degeneracy in the ground state manifold. From a material perspective, this model is justified in the regime where spin-orbit interactions can be treated perturbatively, in which case the isotropic Heisenberg coupling is expected to be the dominant exchange interaction, and the DM coupling is the leading order anisotropic exchange [63, 134, 136, 137]. This situation is relevant to $3d$ transition metal ions, where spin-orbit interactions are expected to be perturbatively small. This model is of particular relevance for the ferromagnetic materials $Lu_2V_2O_7$ and $Y_2V_2O_7$ which crystallize into a pyrochlore lattice, with a magnetic V^{4+} ion ($S = \frac{1}{2}$) located at each pyrochlore lattice site [141–144]. Indeed, the realization of a collinear ferromagnet in $Lu_2V_2O_7$ is supported by neutron scattering measurements [145], as well as density-functional theory calculations [137]. In passing, we note that this material has garnered significant interest due to the observation of a thermal Hall effect of magnons [15].

The remainder of this paper focuses on ObD in the ferromagnetic regime of Eq. (3.1), which, to the best of our knowledge, has not been explored previously. As discussed just above, the case

[18] There is an exception to this statement when $D = 0$. In this case, Eq. (3.1) is simply the ferromagnetic Heisenberg model, which has an exact O(3) symmetry, and therefore the ground state degeneracy is no longer accidental.

[19] Here, we refer to the Kitaev interaction for the pyrochlore lattice in the same way that it is used in Ref. [139]. The collinear ferromagnet is still the classical ground state configuration when a small but non-zero Kitaev interaction is present. However, the ferromagnetic product state will no longer be an exact eigenstate of the quantum Hamiltonian. This, in turn, will generate zero-point fluctuations proportional to K, and there will be quantum ObD present in addition to thermal ObD, as is expected in a typical quantum ObD scenario.

of "weak DM" ($|D| < J$) is motivated by material realizations of this model in the context of transition metal pyrochlores. However, out of theoretical interest, we extend our analysis to the entirety of the ferromagnetic phase as depicted in Fig. 3.1, which ranges from $D/|J| = -1$ to $D/J = +2$ [63, 127]. While the region where $|D| > J$ may not have any particular relevance to real known regular pyrochlore materials,[20] it is of theoretical interest in the broader context of the mechanism of ObD in the *absence* of quantum fluctuations. In the following section, we discuss the methods used to investigate ObD in the ferromagnetic regime of Eq. (3.1).

3.3 Methods

In the present work, we use a number of methods to determine the direction of the global (bulk) magnetization per spin order parameter, denoted as $\boldsymbol{m}$, in the ferromagnetic regime of Eq.(3.1). This section briefly discusses each of these methods and their implementation.

3.3.1 Classical low-temperature expansion

For the classical version of the Hamiltonian in Eq. (3.1), the low-temperature selection of the magnetization direction as a function of the reduced interaction parameter D/J is studied using a classical low-temperature expansion (CLTE), describing Gaussian spin fluctuations δn_i^α about an ordered ground state configuration, where $\alpha = 1, 2$ labels the two transverse directions. At low temperatures, only small transverse spin deviations away from the local spin direction occur, i.e. $|\delta n_i^\alpha| \ll S$. Under this assumption, the spins take the form

$$\boldsymbol{S}_i \simeq \delta n_i^1 \hat{\boldsymbol{e}}_1 + \delta n_i^2 \hat{\boldsymbol{e}}_2 + S\left(1 - \frac{(\delta n_i^1)^2}{2S^2} - \frac{(\delta n_i^2)^2}{2S^2}\right)\hat{\boldsymbol{m}}, \tag{3.2}$$

where $\hat{\boldsymbol{m}} = \boldsymbol{m}/|\boldsymbol{m}|$ is the unit vector in the direction of the bulk magnetization, and $\hat{\boldsymbol{e}}_1, \hat{\boldsymbol{e}}_2$ are two unit vectors that form an orthonormal triad with the magnetization direction, i.e. $\hat{\boldsymbol{e}}_\alpha \cdot \hat{\boldsymbol{e}}_{\alpha'} = \delta_{\alpha\alpha'}$ and $\hat{\boldsymbol{m}} = \hat{\boldsymbol{e}}_1 \times \hat{\boldsymbol{e}}_2$. Substituting Eq. (3.2) into Eq. (3.1) and keeping only terms quadratic in δn_i^α gives a quadratic form

$$\mathcal{H}_{\text{CLTE}}^{(\hat{\boldsymbol{m}})} = S^2 E_0 + \frac{1}{2}\sum_{\boldsymbol{q}}\sum_{\mu,\nu=0}^{3}\sum_{\alpha,\beta=1}^{2} \delta n_\mu^\alpha(-\boldsymbol{q})\mathsf{H}_{\alpha\beta,\mu\nu}^{(\hat{\boldsymbol{m}})}(\boldsymbol{q})\delta n_\nu^\beta(\boldsymbol{q}), \tag{3.3}$$

[20] Interestingly, the breathing pyrochlore material $Ba_3Yb_2Zn_5O_{11}$ seems well-described by the Hamiltonian of Eq. (3.1) over the "small" tetrahedra of the breathing pyrochlore structure [140].

where $S^2 E_0 = -12JNS^2$ is the classical ground state energy, N is the number of face-centred cubic (FCC) primitive unit cells, each containing four sublattices defining a tetrahedron, where μ, ν label the sublattices, and

$$\begin{aligned}\mathsf{H}^{(\hat{\boldsymbol{m}})}_{\alpha\beta,\mu\nu}(\boldsymbol{q}) \equiv\ & 6J\delta_{\alpha\beta}\delta_{\mu\nu} - 2J\delta_{\alpha\beta}\left(1-\delta_{\mu\nu}\right)\cos\left(\boldsymbol{q}\cdot\boldsymbol{r}_{\mu\nu}\right) \\ & + 2D\boldsymbol{d}_{\mu\nu}\cdot\hat{\boldsymbol{m}}(-1)^{\alpha}\left(1-\delta_{\alpha\beta}\right)\left(1-\delta_{\mu\nu}\right)\cos\left(\boldsymbol{q}\cdot\boldsymbol{r}_{\mu\nu}\right)\end{aligned} \tag{3.4}$$

is the Hessian matrix expressed in momentum ($\boldsymbol{q}$) space. The entropy associated with the fluctuations about a given polarized configuration $\hat{\boldsymbol{m}}$ is then given by the expression [58, 83, 135]

$$\mathcal{S}_{\hat{\boldsymbol{m}}} = \text{constant} - \frac{1}{2}\sum_{\boldsymbol{q}} \ln\left(\det\left\{\mathsf{H}^{(\hat{\boldsymbol{m}})}(\boldsymbol{q})\right\}\right). \tag{3.5}$$

The thermal selection among the fully polarized states can be exposed by maximizing the entropy in Eq. (3.5) with respect to the direction of the magnetization, $\hat{\boldsymbol{m}}$. Note that throughout this paper, calculations are carried out in units where $\hbar = k_{\mathrm{B}} = 1$.

3.3.2 Classical Monte Carlo

The finite temperature properties of the ferromagnetic phase of Eq. (3.1) are explored using classical Monte Carlo (MC) simulations. Simulations were carried out on a finite pyrochlore lattice with $4L^3$ spins with $L = 10$ and periodic boundaries, using both Metropolis importance sampling and over-relaxation updates [146–148], and averaged over 10 independent MC simulations. For each simulation, the system was initialized in a random configuration at high temperature $T > T_{\mathrm{c}}$, and then gradually cooled down to the target temperature, thermalizing with 5×10^4 sweeps between each step in temperature. Each of the thermodynamic observables measured is averaged over 10^5 independent MC sweeps and then averaged over the independent simulations.

For the collinear ferromagnetic phase, the onset of long-range order is tracked by measuring the magnetization per spin, $\boldsymbol{m}$

$$\boldsymbol{m} \equiv \frac{1}{4N}\sum_i \boldsymbol{S}_i, \tag{3.6}$$

where $4N$ is the number of spins in a system consisting of $N = L^3$ FCC unit cells. To investigate the evolution and selection of the orientation of the magnetization, $\boldsymbol{m}$, as a function of temperature, it is not enough to study the thermodynamic average of Eq. (3.6). Indeed, a generic Ginzburg-Landau (GL) expansion of the free energy for a system with cubic symmetry yields [149, 150]

$$\mathcal{F} = \frac{r}{2}|\boldsymbol{m}|^2 + \frac{u}{4}|\boldsymbol{m}|^4 + v\left(m_x^4 + m_y^4 + m_z^4\right) + \frac{w}{6}|\boldsymbol{m}|^6 + \gamma\left(m_x^2 m_y^2 m_z^2\right) + \cdots \tag{3.7}$$

where the coefficients $\{r, u, v, w, \gamma\}$ are temperature dependent. The resulting terms can be broadly separated into isotropic terms, i.e., those involving powers of the magnitude of magnetization, $|\boldsymbol{m}|$, in Eq. (3.7), which do not distinguish between different magnetization orientations, and the anisotropic terms, which do. While the GL free energy in Eq. (3.7) is not necessarily valid away from the critical temperature, it motivates the lowest order symmetry allowed functions of the order parameter, which can distinguish between different orientations of the order parameter. In our MC simulations, we study the temperature evolution of the average magnetization per spin $\langle|\boldsymbol{m}|\rangle$, as well as the anisotropic observables

$$M_4 \equiv \langle m_x^4 + m_y^4 + m_z^4 \rangle, \tag{3.8}$$

$$\delta M_4 \equiv \frac{3}{2}\left(\langle |\boldsymbol{m}|^4 \rangle - M_4\right), \tag{3.9}$$

$$M_6 \equiv 27\langle m_x^2 m_y^2 m_z^2 \rangle, \tag{3.10}$$

where $\langle \cdots \rangle$ denotes thermal averaging, and the factors of $3/2$ and 27 are introduced to normalize the range of expectation values between 0 and 1. We refer to the anisotropic terms defined in Eqs. (3.8)-(3.10) as the *cubic parameters*. The values of the cubic parameters for the magnetization $\boldsymbol{m}$ along various high symmetry directions are listed in Table 3.1 in Appendix 3B. Note that throughout this work, we use the notation $\langle hkl \rangle$ to denote the direct space vector $h\hat{\boldsymbol{x}} + k\hat{\boldsymbol{y}} + l\hat{\boldsymbol{z}}$, along with all other symmetry-related directions.

To further investigate the evolution of the magnetization, we sample the *instantaneous* magnetization direction of the system, $\hat{\boldsymbol{m}} \equiv \sum_i \mathbf{S}_i / |\sum_i \mathbf{S}_i|$, along each Cartesian direction 2×10^4 times for each temperature, using a set of temperatures ranging from $T \leq T_c$ to $T \ll T_c$. The resulting distribution, $p(\hat{\boldsymbol{m}})$, is visualized as a function of the polar and azimuthal angles, θ and ϕ, of the global magnetization $\boldsymbol{m}$ restricted to the first octant where $\phi \in [0, \pi/2]$ and $\cos(\theta) \in [0, 1]$. Clustering of the magnetization distribution about a given magnetization orientation is therefore considered as evidence for a thermal selection of the corresponding magnetization direction.

3.3.3 Quantum spin waves

To investigate the putative thermal ObD selection in the low temperature quantum version of Eq. (3.1), we perform a Holstein-Primakoff spin wave expansion. While the results presented in the remainder of this paper focus on the quantum limit $S = \frac{1}{2}$, we first leave the spin quantum number S as a free parameter in our equations for organizing the $1/S$ Holstein-Primakoff expansion. In

particular, spin operators are recast as Holstein-Primakoff bosons [35, 75]

$$\begin{aligned} S^{(\hat{\boldsymbol{m}})}_{\boldsymbol{R},\mu} &= S - a^{\dagger}_{\boldsymbol{R},\mu} a_{\boldsymbol{R},\mu}, \\ S^{+}_{\boldsymbol{R},\mu} &= (2S - a^{\dagger}_{\boldsymbol{R},\mu} a_{\boldsymbol{R},\mu})^{1/2} a_{\boldsymbol{R},\mu}, \\ S^{-}_{\boldsymbol{R},\mu} &= a^{\dagger}_{\boldsymbol{R},\mu} (2S - a^{\dagger}_{\boldsymbol{R},\mu} a_{\boldsymbol{R},\mu})^{1/2}, \end{aligned} \tag{3.11}$$

where $S^{(\hat{\boldsymbol{m}})}_{\boldsymbol{R},\mu} = \boldsymbol{S}_{\boldsymbol{R},\mu} \cdot \hat{\boldsymbol{m}}$ is the component of the spin operator aligned along the global polarization axis $\hat{\boldsymbol{m}}$ of the ferromagnetic configuration, and $\boldsymbol{R}$ is a FCC lattice vector. In this picture, each boson is interpreted as a quantum of spin fluctuation about the ordered ground state. Plugging this transformation into the spin Hamiltonian in Eq. (3.1) and expanding the square root in powers of $a^{\dagger}_{\boldsymbol{R},\mu} a_{\boldsymbol{R},\mu}/2S$ yields a semi-classical expansion

$$\mathcal{H} = \sum_{n=0}^{\infty} S^{2-n/2} \mathcal{H}^{(\hat{\boldsymbol{m}})}_{n}, \tag{3.12}$$

where each order of the expansion is now dependent on the global polarization axis. Truncating at $O(S)$ gives the non-interacting magnon Hamiltonian

$$\mathcal{H}^{(\hat{\boldsymbol{m}})}_{\mathrm{QSW}} = S^2 \mathcal{H}^{(\hat{\boldsymbol{m}})}_{0} + S^{3/2} \mathcal{H}^{(\hat{\boldsymbol{m}})}_{1} + S \mathcal{H}^{(\hat{\boldsymbol{m}})}_{2}. \tag{3.13}$$

Note that $\mathcal{H}^{(\hat{\boldsymbol{m}})}_{1} = 0$ whenever the spin configuration is classically metastable [75], in which case Eq. (3.13) simplifies to

$$\mathcal{H}^{(\hat{\boldsymbol{m}})}_{\mathrm{QSW}} = S(S+1)E_0 + \frac{S}{2} \sum_{\boldsymbol{q}} \sum_{\mu,\nu=0}^{3} \left[X^{(\hat{\boldsymbol{m}})}_{\mu\nu}(\boldsymbol{q}) a^{\dagger}_{\mu,\boldsymbol{q}} a_{\nu,\boldsymbol{q}} + X^{(\hat{\boldsymbol{m}})}_{\nu\mu}(-\boldsymbol{q}) a_{\mu,-\boldsymbol{q}} a^{\dagger}_{\nu,-\boldsymbol{q}} \right], \tag{3.14}$$

where

$$X^{(\hat{\boldsymbol{m}})}_{\mu\nu}(\boldsymbol{q}) = 6J\delta_{\mu\nu} - 2\left(J - iD\boldsymbol{d}_{\mu\nu} \cdot \hat{\boldsymbol{m}}\right)(1 - \delta_{\mu\nu}) \cos\left(\boldsymbol{q} \cdot \boldsymbol{r}_{\mu\nu}\right). \tag{3.15}$$

An appropriate unitary transformation of the magnon operators $a_{\mu,\boldsymbol{q}} = \sum_{\alpha} U^{(\hat{\boldsymbol{m}})}_{\mu,\alpha}(\boldsymbol{q}) b_{\alpha,\boldsymbol{q}}$ brings Eq. (3.14) to the diagonal form

$$\mathcal{H}^{(\hat{\boldsymbol{m}})}_{\mathrm{QSW}} = S^2 E_0 + S E^{(\hat{\boldsymbol{m}})}_{2} + S \sum_{\boldsymbol{q}} \sum_{\mu=0}^{3} \omega^{(\hat{\boldsymbol{m}})}_{\mu,\boldsymbol{q}} b^{\dagger}_{\mu,\boldsymbol{q}} b_{\mu,\boldsymbol{q}}, \tag{3.16}$$

where $\omega^{(\hat{\boldsymbol{m}})}_{\mu,\boldsymbol{q}}$ is the magnon dispersion and

$$S E^{(\hat{\boldsymbol{m}})}_{2} = S E_0 + \frac{S}{2} \sum_{\boldsymbol{q}} \sum_{\mu=0}^{3} \omega^{(\hat{\boldsymbol{m}})}_{\mu,\boldsymbol{q}} \tag{3.17}$$

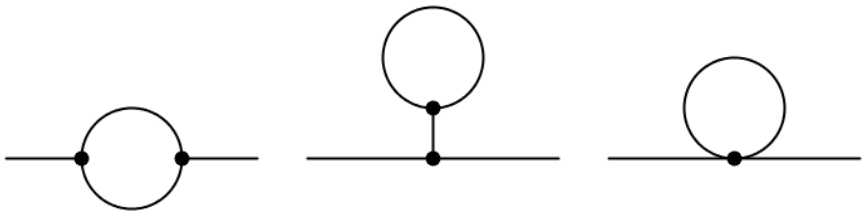


Figure 3.2: Diagrams contributing to the magnon self-energy at $O(S^0)$ in the Holstein-Primakoff expansion. At $T = 0$, only the first diagram, connecting a pair of three-magnon interaction vertices, has a non-zero contribution. The explicit evaluation of these diagrams is discussed in Appendix 3F.

is the $O(S)$ correction to the ground state energy from quantum zero-point fluctuations [75]. The free energy, $\mathcal{F}^{(\hat{\boldsymbol{m}})}$, in linear spin wave theory is then calculated as

$$\mathcal{F}^{(\hat{\boldsymbol{m}})} = S^2 E_0 + S E_2^{(\hat{\boldsymbol{m}})} + T \sum_{\boldsymbol{q}} \sum_{\mu=0}^{3} \ln\left(1 - e^{-S\omega_{\mu,\boldsymbol{q}}^{(\hat{\boldsymbol{m}})}/T}\right). \tag{3.18}$$

The selection of certain configurations over others is understood at this level by minimizing Eq. (3.18) with respect to the various classical ground state configurations characterized by $\hat{\boldsymbol{m}}$. At $T = 0$, this amounts to minimizing the zero-point energy in Eq. (3.17), which is the typical approach taken to expose quantum ObD [63, 97, 114, 121, 135]. At nonzero temperature, the thermal population of quasiparticles leads to an entropic contribution to Eq. (3.18) as well as a nonzero temperature contribution to the total internal energy, which may or may not select the same configurations as the zero-point contribution [62, 63].

3.3.4 Non-linear spin waves

To analyze the stability of the ferromagnetic phase, we extend our spin wave theory to include magnon-magnon interactions. Corrections to the linear spin wave theory can be included perturbatively using the leading order magnon-magnon interactions in the $1/S$ expansion in Eq. (3.12), given by the symmetrized three-magnon and four-magnon interaction terms [151]

$$\mathcal{H}_3^{(\hat{\boldsymbol{m}})} = \frac{1}{2!\sqrt{N}} \sum_{\boldsymbol{k}\boldsymbol{q}} \sum_{\mu\nu\lambda} \left[Y_{\mu\nu\lambda}^{(\hat{\boldsymbol{m}})}(\boldsymbol{k}, \boldsymbol{q}) a_{\boldsymbol{k},\mu}^\dagger a_{\boldsymbol{q},\nu}^\dagger a_{\boldsymbol{k}+\boldsymbol{q},\lambda} + \text{H.c.} \right] \tag{3.19}$$

and

$$\mathcal{H}_4^{(\hat{\boldsymbol{m}})} = \frac{1}{N(2!)^2} \sum_{\boldsymbol{k}\boldsymbol{q}\boldsymbol{q}} \sum_{\mu\nu\lambda\rho} V_{\mu\nu\lambda\rho}^{(\hat{\boldsymbol{m}})}(\boldsymbol{k},\boldsymbol{q},\boldsymbol{q}) a_{\boldsymbol{k}+\boldsymbol{q},\mu}^\dagger a_{\boldsymbol{q}-\boldsymbol{q},\nu}^\dagger a_{\boldsymbol{q},\lambda} a_{\boldsymbol{k},\rho}, \tag{3.20}$$

where the interaction vertices $Y_{\mu\nu\lambda}^{(\hat{\boldsymbol{m}})}(\boldsymbol{k},\boldsymbol{q})$ and $V_{\mu\nu\lambda\rho}^{(\hat{\boldsymbol{m}})}(\boldsymbol{k},\boldsymbol{q},\boldsymbol{q})$, are defined in Appendix 3F.

We note that while the presence of a three-magnon interaction is somewhat atypical for a collinear spin configuration, it will generally appear in the Holstein-Primakoff expansion from terms proportional to $S_i^z S_j^\pm$ in the local basis. For a ferromagnetic system, these same off-diagonal couplings would typically cause a spin canting and lead to a non-collinear spin configuration. In the present model (3.1), however, the geometry of the pyrochlore lattice leads to a set of DM vectors that satisfy the following property: given any site on the pyrochlore lattice, the sum of all DM vectors relative to this site vanishes. This property of the lattice allows the collinear configuration to remain an eigenstate, even in the presence of the anisotropic DM interaction.

To probe the stability of the ferromagnetic phase, we analyze the single-magnon spectrum at $T = 0$ in the presence of three and four-magnon interactions by numerically computing the magnon spectral function, $\mathcal{A}(\boldsymbol{k},\omega)$, which can be understood as the momentum-resolved single-magnon density of states. This quantity is closely related to observables such as the dynamical structure factor [152], which is experimentally accessible from inelastic neutron scattering.

The single-magnon spectral function is given by [52]

$$\mathcal{A}(\boldsymbol{k},\omega) = -\frac{1}{\pi}\mathrm{Im}\left\{\mathrm{Tr}\left[\boldsymbol{G}_{\mathrm{ret}}^{(\hat{\boldsymbol{m}})}(\boldsymbol{k},\omega)\right]\right\}, \tag{3.21}$$

where

$$\boldsymbol{G}_{\mathrm{ret}}^{(\hat{\boldsymbol{m}})}(\mathbf{k},\omega) = \left[\omega - S\boldsymbol{\Omega}_{\boldsymbol{k}}^{(\hat{\boldsymbol{m}})} - \boldsymbol{\Sigma}^{(\hat{\boldsymbol{m}})}(\boldsymbol{k},\omega) + i0^+\right]^{-1}, \tag{3.22}$$

is the retarded magnon Green's function and $\left[\boldsymbol{\Omega}_{\boldsymbol{k}}^{(\hat{\boldsymbol{m}})}\right]_{\mu\nu} = \delta_{\mu\nu}\omega_{\mu,\boldsymbol{k}}^{(\hat{\boldsymbol{m}})}$ is the diagonalized linear-spin wave Hamiltonian. The (retarded) self-energy $\boldsymbol{\Sigma}^{(\hat{\boldsymbol{m}})}(\boldsymbol{k},\omega)$ arises from magnon-magnon interactions and can be included perturbatively in the $1/S$ expansion. At $O(S^0)$, the self-energy is calculated by evaluating the one-loop Feynman diagrams depicted in Fig. 3.2. At $T = 0$, we find that only the leftmost diagram has a non-zero contribution (see Appendix 3F for more details). In this case, the components of the self-energy matrix are evaluated as

$$\Sigma_{\mu\nu}^{(\hat{\boldsymbol{m}})}(\boldsymbol{k},\omega) = \frac{S}{2N}\sum_{\boldsymbol{q}}\sum_{\lambda\rho} \frac{T_{\lambda\rho\mu}^{(\hat{\boldsymbol{m}})}(\boldsymbol{q},\boldsymbol{k}-\boldsymbol{q})\overline{T}_{\lambda\rho\nu}^{(\hat{\boldsymbol{m}})}(\boldsymbol{q},\boldsymbol{k}-\boldsymbol{q})}{\omega + i0^+ - S\omega_{\lambda,\boldsymbol{k}-\boldsymbol{q}}^{(\hat{\boldsymbol{m}})} - S\omega_{\rho,\boldsymbol{q}}^{(\hat{\boldsymbol{m}})}}, \tag{3.23}$$

where the $T^{(\hat{\boldsymbol{m}})}_{\alpha\beta\mu}(\boldsymbol{q}, \boldsymbol{k}-\boldsymbol{q})$ coefficients are the three-magnon vertices in the basis that diagonalizes the linear spin wave theory, and the overbar represents complex conjugation. A more detailed derivation of Eq. (3.23) is given in Appendix 3F.

In the absence of magnon-magnon interactions, the single-magnon excitations have an infinite lifetime and appear as sharp delta function peaks. In general, the self-energy will consist of both real and imaginary parts, which will renormalize and broaden the single-magnon spectrum, respectively, the latter of which is interpreted as the magnons acquiring a finite (quasiparticle) lifetime. In practice, the self-energy real and imaginary components are calculated by numerically computing the sum over wavevectors in Eq. (3.23) with a finite broadening factor $0^+ \approx 10^{-3}J$. This sum is convergent in three dimensions, in contrast with lower-dimensional magnets where, for example, an iterative self-consistent solution of the self-energy must be introduced as fluctuations of the zero-mode are infrared divergent (see Refs. [105, 132] for more discussion). The self-energy is then used to calculate the leading $1/S$ correction to the bare Green's function using Eq. (3.22).

3.4 Results

In this section, we present results regarding ObD in the ferromagnetic regime of Eq. (3.1), for both the classical and quantum versions of the model. We begin our discussion of ObD with a purely classical outlook on the entropic selection of the magnetization order parameter, using the classical low-temperature expansion (CLTE) supplemented with classical Monte Carlo (MC) simulations. Next, we study the ObD selection in the quantum case by using linear spin wave theory. Finally, we extend this analysis to the non-linear spin wave theory to assess the stability of the ferromagnetic ground state in the purely quantum model.

3.4.1 Classical selection

To set the stage, we begin by considering the classical system described by Eq. (3.1) for which the resulting MC phase diagram reveals a collinear ferromagnetic phase stabilized for $-1 \leq D/J < 2$, see Fig. 3.3. Therein, a classical spin liquid, referred to as R_1-R_2 spin liquid, lying on the $D/J = 2$ boundary between the collinear ferromagnetic phase and the antiferromagnetic Γ_5 phase, was recently identified [127]. We note in passing that the Γ_5 phase displays a rich behaviour of thermal order by disorder selection of discrete spin directions, the so-called ψ_2 and ψ_3 states [98]). In this work, we are concerned with the thermal and quantum mechanisms driving a selection of the magnetization direction in the ferromagnetic (FM) phase and do not further

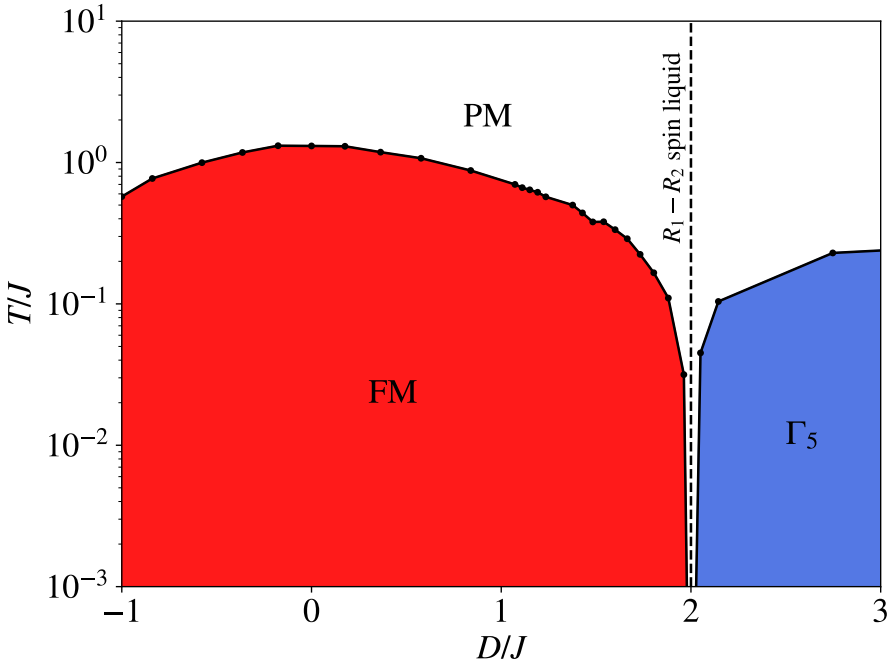


Figure 3.3: Temperature phase diagram obtained via classical Monte Carlo of the ferromagnetic Heisenberg and Dzyaloshinskii-Moriya Hamiltonian of Eq. (3.1). There are two long-range ordered phases: a collinear FM phase for $-1 \leq D/J < 2$ and an antiferromagnetic (Γ_5) phase beyond $D/J = 2$. A classical spin liquid, referred to as R_1-R_2 spin liquid, is realized at $D/J = 2$ [127].

discuss the properties of the antiferromagnetic Γ_5 phase or those of the $R_1 - R_2$ spin liquid. We refer the reader to Refs. [63, 127] for an extended discussion of the spin liquid phase and the nature of the antiferromagnetic Γ_5 phase below the paramagnetic–Γ_5 boundary.

As a first step toward exposing thermal ObD selection in the FM regime of the phase diagram of Fig. 3.3, we use the CLTE to study the preferred orientation of the net magnetization at low temperatures ($0 < T \ll T_c$). We note that in the classical low-temperature limit, the equipartition theorem guarantees that the free energy is minimized by the maximal entropy configurations (further discussion regarding this point can be found in Appendix 3D). We therefore calculate the entropy from Eq. (3.5) about all possible collinear ground-state configurations within the first spherical angle octant (of the magnetization direction $\hat{\boldsymbol{m}}$) for various values of D/J, see Fig. 3.4. In this figure, we illustrate the second term of Eq. (3.5) whereby the configuration with the highest

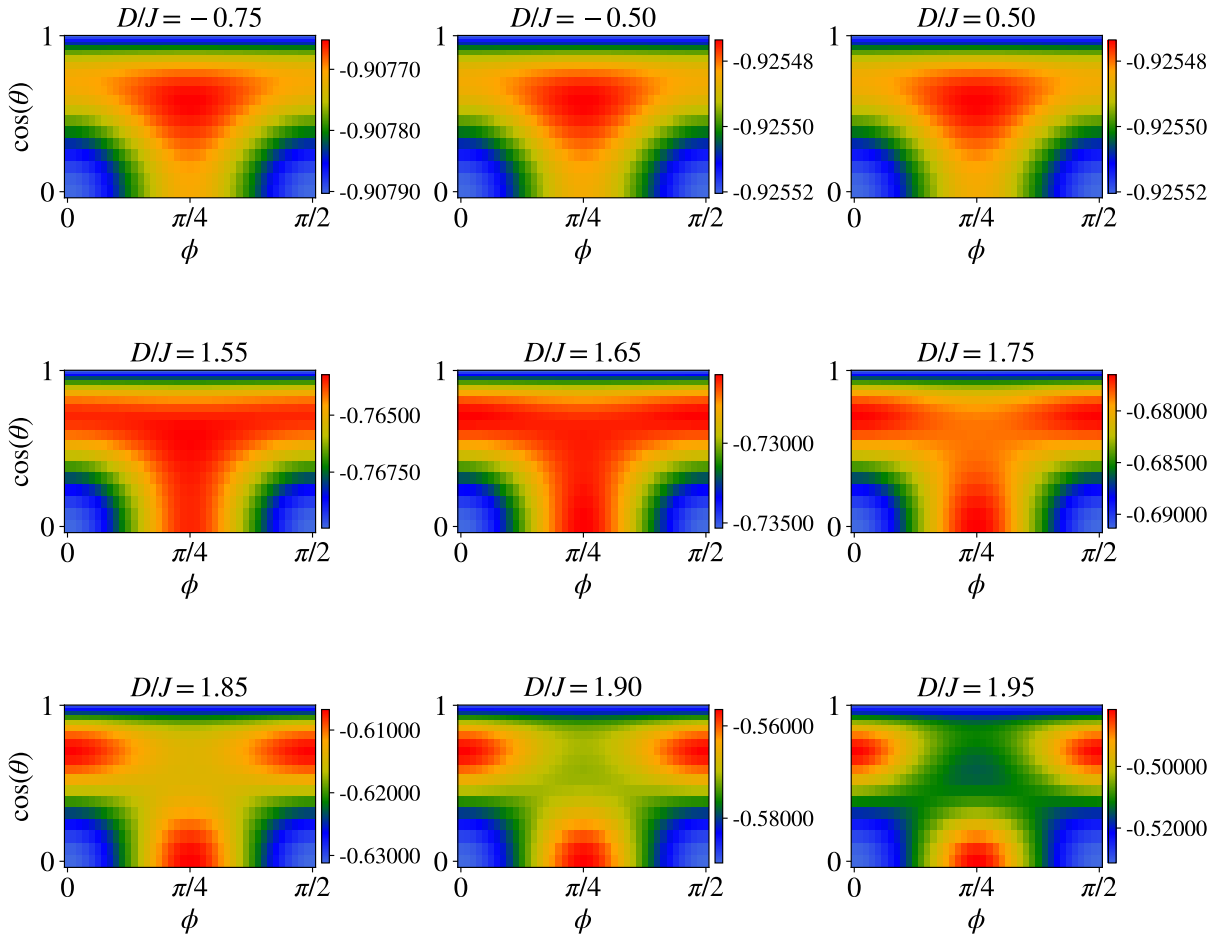


Figure 3.4: Entropy from the CLTE about a ferromagnetic ground state for various values of D/J. Here, the magnetization is expressed in spherical coordinates $\hat{\boldsymbol{m}} = (\sin\theta\cos\phi, \sin\theta\sin\phi, \cos\theta)$.

entropy is expected to be selected at low temperatures.

For $D/J \lesssim 1.66$, the evolution of the entropy displays a high-intensity T-shaped pattern with a maximum near the centre. In spherical coordinates, this location corresponds to an $\hat{\boldsymbol{m}}$ orientation along $[111]$. As the value of D/J is increased towards the $D/J = 2$ FM–Γ_5 boundary, the maxima shift to the sides and bottom of the T-shaped pattern. In spherical coordinates, these new locations correspond to the three symmetry-equivalent $\langle 110\rangle$ orientations. This first calculation illustrates how the entropy becomes maximal for high-symmetry orientations of the collinear magnetization.

Therefore, we henceforth compute the entropy using Eq. (3.5) for magnetization along the $\langle 100\rangle$, $\langle 110\rangle$, and $\langle 111\rangle$ cubic directions. The results of this calculation are shown in Fig. 3.5, where the difference in entropy between distinct magnetization directions is shown. First, we find that the configuration for which the magnetization is polarized along $\langle 100\rangle$ has the lowest entropy, as exemplified by the blue curve in Fig. 3.5 illustrating the entropy difference between the $\langle 110\rangle$ and the $\langle 100\rangle$ magnetization directions, i.e. $\mathcal{S}_{\langle 110\rangle} - \mathcal{S}_{\langle 100\rangle} > 0$.[21] A similar comparison of the entropy associated with the $\langle 111\rangle$ and the $\langle 110\rangle$ directions allows us to identify two distinct regimes, one for $D/J \in (-1, 1.66)$ and another for $D/J \in (1.66, 2)$, where a magnetization along the $\langle 111\rangle$ and $\langle 110\rangle$ directions respectively maximizes the entropy. We recall here the results of Fig. 3.1 showing that the collinear ferromagnet transitions to the all-in-all-out (antiferromagnetic) phase at $D/J = -1$ while the former transitions to the Γ_5 (planar antiferromagnet) at $D/J = 2$. Hence, the entropic selection of the $\langle 111\rangle$ magnetization directions for the collinear ferromagnet persists all the way to its transition point with the all-in-all-out phase at $D/J = -1$. We also note that the entropy difference grows as the ratio D/J approaches either one of the phase boundaries with the other ordered phases (see Fig. 3.1).

Although the CLTE calculation of the entropy already predicts a selection of the magnetization at low temperatures, we cannot assume that the same state selection remains as the temperature increases upon approaching T_c from below. Indeed, taking the example of the Γ_5 phase depicted in Fig. 3.1, it was previously found that different states may be selected near the critical temperature $T \lesssim T_c$ compared to the low-temperature selection at $T \ll T_c$ [63, 80]. We use classical MC simulations to follow the evolution of the magnetization direction [63, 112]. We record the magnetization direction, $\hat{\boldsymbol{m}} = \sum_i \mathbf{S}_i / |\sum_i \mathbf{S}_i|$, to generate a magnetization orientation distribution function, $p(\hat{\boldsymbol{m}})$, as a function of temperature. This distribution function allows one to probe the free energy difference between configurations, given by

$$\frac{p(\hat{\boldsymbol{m}})}{p(\hat{\boldsymbol{n}})} = \exp\left(-\frac{\mathcal{F}^{(\hat{\boldsymbol{m}})} - \mathcal{F}^{(\hat{\boldsymbol{n}})}}{T}\right). \tag{3.24}$$

In other words, the configuration minimizing the free energy occurs when $p(\hat{\boldsymbol{m}})$ is maximized. We therefore refer to a magnetization direction as being "selected" if it is the most probable orientation to occur at the specified temperature. For clarity, and without loss of generality, we display the distribution $p(\hat{\boldsymbol{m}})$ solely in the first octant and use spherical coordinates $\hat{\boldsymbol{m}} = (\cos\phi \sin\theta, \sin\phi \sin\theta, \cos\theta)$ where θ and ϕ are the polar and azimuthal angles, respectively.

To illustrate the evolution of the thermal selection via the evolution of the magnetization distribution, we show the temperature evolution of the distribution $p(\hat{\boldsymbol{m}})$ for two values of the

[21] Similar results where obtained for the entropy difference between the $\langle 111\rangle$ and the $\langle 100\rangle$ magnetization directions, i.e. $\mathcal{S}_{\langle 111\rangle} - \mathcal{S}_{\langle 100\rangle} > 0$ (not shown).

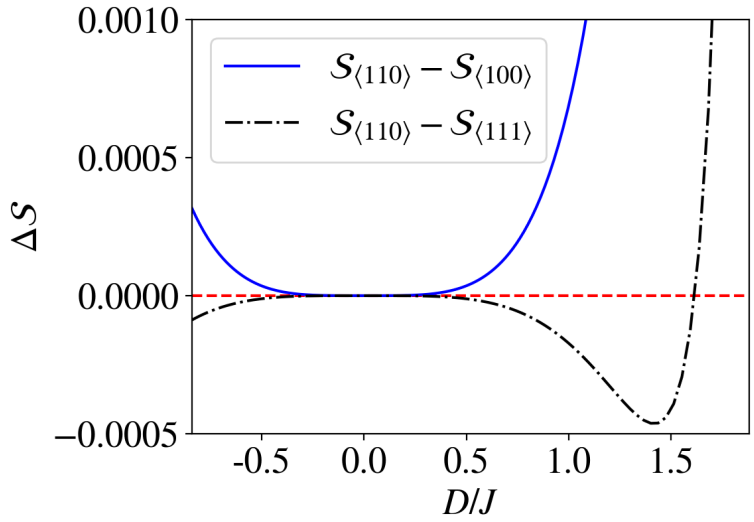


Figure 3.5: Entropy from the CLTE about a ferromagnetic ground state. The entropy difference between the $\langle 110\rangle$ and the $\langle 100\rangle$ (blue line), and the $\langle 110\rangle$ and the $\langle 111\rangle$ (black line) cubic directions is calculated using Eq. (3.5). We note that the entropy is maximized for the magnetization along the $\langle 111\rangle$ directions for $-1 < D/J \lesssim 1.66$ and along the $\langle 110\rangle$ directions for $1.66 \lesssim D/J < 2$, except at $D/J = 0$ when the magnetization is isotropic. We note that the two curves never cross each other, i.e. $\mathcal{S}_{\langle 110\rangle} - \mathcal{S}_{\langle 100\rangle} \geq \mathcal{S}_{\langle 110\rangle} - \mathcal{S}_{\langle 111\rangle}$.

DM interaction: one with $D/J \simeq 1.43$ and another with $D/J \simeq 1.73$. As will be made clear later, these two values of D/J have been chosen as they each illustrate distinct temperature-dependent evolution of the magnetization distribution functions. Figures 3.6 (a)-(d) illustrate the evolution of $p(\hat{\boldsymbol{m}})$ as a function of temperature for the system with $D/J \simeq 1.43$. At temperatures above the critical temperature, $T > T_c$, the magnetization distribution shown in Fig. 3.6(a) is uniformly distributed. Just below the critical temperature, $T \lesssim T_c$, our MC simulations reveal that the distribution $p(\hat{\boldsymbol{m}})$, shown in Fig. 3.6(b), clusters around the points $\cos(\theta) \in \{0, 1\}$ and $\phi \in \{0, \pi/2\}$. These clusters indicate that the magnetization aligns along the $\langle 100\rangle$ directions near and not too far below the critical temperature. As the temperature is decreased, a triangle-shaped pattern develops, where the distribution clusters around $\phi = \pi/4$ and $\cos(\theta) = 1/\sqrt{3}$ (see Fig. 3.6(c) and (d)). The centre of the triangle, with these ϕ and $\cos(\theta)$ values, corresponds to an orientation of the magnetization along $\langle 111\rangle$. We note that the variance of the distribution becomes smaller as the temperature is lowered, implying that the selection of the $\langle 111\rangle$ orientations becomes stronger at lower temperatures.

Figures 3.6 (e)-(h) illustrate the evolution of the magnetization distribution $p(\hat{\boldsymbol{m}})$ as a function

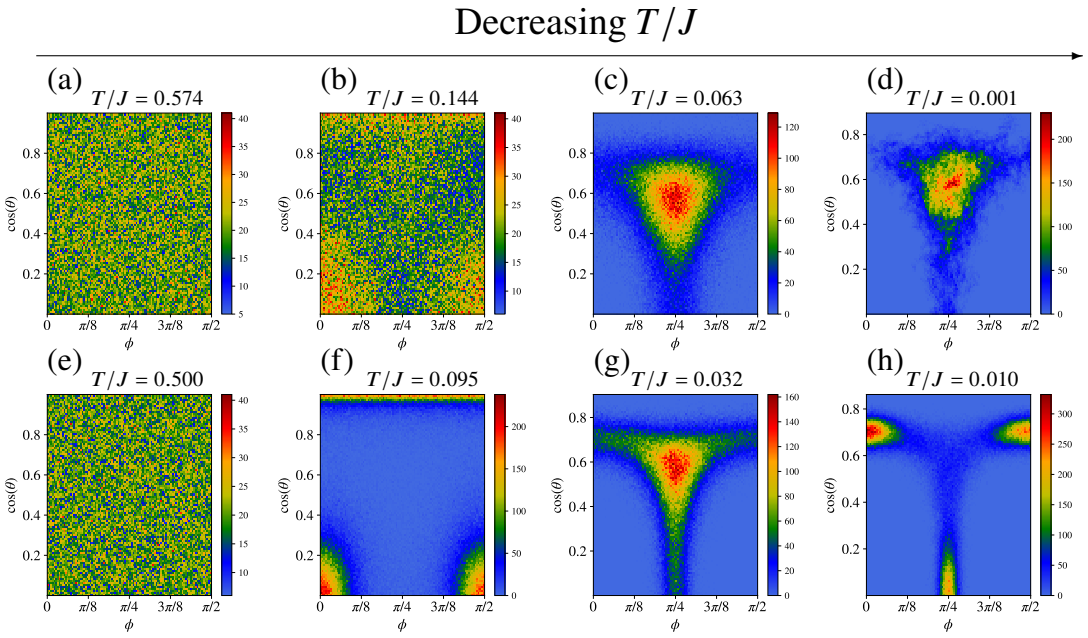


Figure 3.6: Distribution of the global magnetization direction, $p(\hat{\boldsymbol{m}})$, from classical Monte Carlo simulations for the two systems labelled by red triangles and red squares in Fig.3.7(d). Panels (a-d) correspond to the triangular markers in Fig. 3.7(d), that is, to $D/J = 1.42$, while panels (e-h) correspond to the square markers in Fig. 3.7(d), where $D/J = 1.73$, shown for decreasing temperatures when read left to right. Here, the magnetization direction is expressed in spherical coordinates $\hat{\boldsymbol{m}} = (\cos\phi\sin\theta, \sin\phi\sin\theta, \cos\theta)$ and temperature is measured in units of J ($k_{\mathrm{B}} = 1$).

of temperature for the system with $D/J \simeq 1.73$. We note that for this set of parameters, the system develops three distinct patterns in the distribution of the magnetization direction as a function of temperature. For $T \lesssim T_{\mathrm{c}}$, the magnetization is similarly oriented along one of the $\langle 100\rangle$ directions, as found for the case $D/J = 1.43$ above [Fig. 3.6(b)], as shown in Fig. 3.6(f). As the temperature is further decreased, a triangular pattern develops again, indicating a preference to order along the $\langle 111\rangle$ directions (Fig. 3.6(g)), analogous to Fig. 3.6(c). In contrast, however, as the system is cooled down into the low-temperature region, the magnetization distribution shows a distinct clustering at three lobes, centred around the points $(\cos(\theta), \phi) \in \{(1/\sqrt{2}, 0), (0, \pi/4), (1/\sqrt{2}, \pi/2)\}$. These magnetization directions correspond to the $\langle 110\rangle$ directions. No further qualitative changes in the pattern of the distribution occur as the temperature is further decreased and approaches zero.

Altogether, the evolution of the magnetization distributions $p(\hat{\boldsymbol{m}})$ shown in Fig. 3.6 for two representative values of D/J suggests that the collinear ferromagnetic phase of the classical Hamiltonian of Eq. (3.1) presents *at least* two distinct ordered phases for a given set of interaction

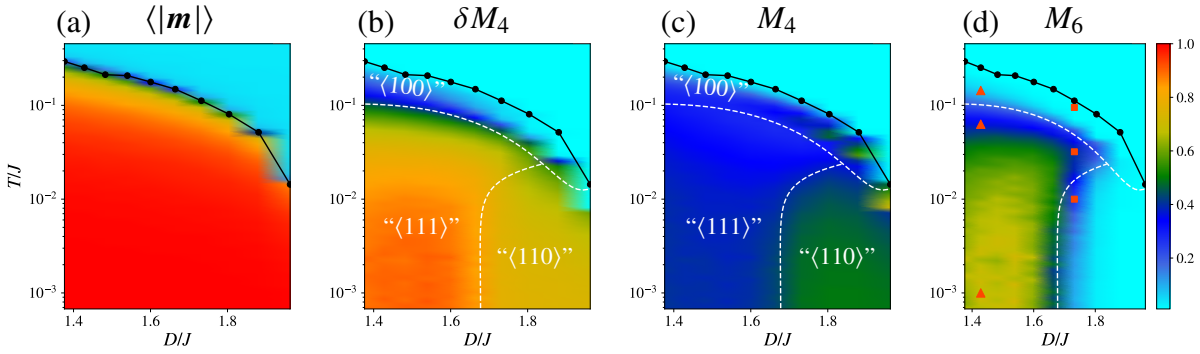


Figure 3.7: Thermal evolution of the (a) magnetization per spin $\langle|\boldsymbol{m}|\rangle$, and the anisotropic cubic parameters (b) δM_4, (c) M_4, and (d) M_6, as defined in Eqs. (3.8)-(3.10). Panels (b) and (c) illustrate the three regions where a distinct easy axis for the magnetization is chosen from ObD. The triangles in panel (d) label the temperatures at which the magnetization distribution was measured as illustrated in Fig. 3.6(b-d), and the squares correspond to Fig. 3.6(f-h). The white dashed lines in panels (b)-(d) are guides to the eye, and the directions are indicated in quotation marks to emphasize the fact that these regions are somewhat loosely identified based on the distinct values of the cubic parameters.

parameters. The range in temperature and ratio D/J where these phases are observed, however, is not trivially identified through the sole measurement of the distribution $p(\hat{\boldsymbol{m}})$. To provide an approximate identification of the boundaries between the different magnetization orientations, we measured the temperature evolution of the thermally averaged cubic parameters δM_4, M_4 and M_6 [as defined in Eqs. (3.8)-(3.10)], to construct a phase diagram as a function of temperature and D/J, which we show in Fig. 3.7(a-d). The critical temperature T_c is marked by black dots, determined by the onset of a nonzero magnetization $\langle|\boldsymbol{m}|\rangle$ in Fig. 3.7(a). We note that the critical temperature collapses to zero in the limit $D/J \to 2^-$, corresponding to the spin liquid phase reported in Refs. [63, 127]. The white dashed lines in Fig. 3.7(b-d) are drawn as guides to the eye to separate regions of distinct values of the cubic parameters. In Fig. 3.7(d), the locations at which the magnetization distributions $p(\hat{\boldsymbol{m}})$ were calculated are marked with red triangles corresponding to Fig. 3.6(b-d) and red squares corresponding to Fig. 3.6(f-h). By comparing the regions separated by the white lines with the distributions in Fig. 3.6, we are able to qualitatively identify that these regions coincide with magnetization along distinct cubic crystalline directions. These ordering directions are labelled in Fig. 3.7(b,c) in quotation marks, to emphasize that our identification of these regions is approximate. We observe that the (extrapolated) zero-temperature boundary separating the $\langle 111\rangle$ and $\langle 110\rangle$ regions is $D/J \sim 1.66$, which is consistent with the CLTE entropy calculation reported in Fig. 3.5. Further details regarding the calculation

of the cubic M_4, δM_4, and M_6 parameters are given in Appendix 3B.

In Fig. 3.5, we found from the CLTE calculations that the entropy difference between the different magnetization direction states selected at low temperature decreases upon approaching the Heisenberg point $D \to 0^{\pm}$. Similarly, we found that our ability to determine what magnetization direction is selected just below T_c becomes very difficult as $D/J \to 0$, as the $p(\hat{\boldsymbol{m}})$ histograms such as those in Fig. 3.6 become extremely noisy. For example, see Fig. 3.11 for the case $D/J = -0.84$, which is close to the ferromagnet to all-in-all-out boundary.

3.4.2 Quantum selection at $0^+ < T \ll T_c$

Within the classical ferromagnetic regime, the manifold of classical ground states possesses full rotational symmetry, despite the Hamiltonian in Eq. (3.1) lacking such a symmetry for an arbitrary spin configuration when the DM interaction is nonzero. In a typical scenario, such as this, one might naively expect that quantizing the Hamiltonian in Eq. (3.1) would partially lift the accidental degeneracy between classical ground states due to the zero-point fluctuations in Eq. (3.17). In the present case, we find a somewhat unusual situation, where zero-point fluctuations are absent, owing to the fact that the classical ferromagnetic (product) state is an exact eigenstate of the Hamiltonian. To see this, consider a fully polarized product state oriented along a global magnetization unit vector $\hat{\boldsymbol{m}}$:

$$|\hat{\boldsymbol{m}}\rangle \equiv \bigotimes_{i=1}^{4N} |{\uparrow_{\hat{\boldsymbol{m}}}}\rangle_i \,, \tag{3.25}$$

where $|{\uparrow_{\hat{\boldsymbol{m}}}}\rangle_i$ is the eigenstate of the spin operator $\boldsymbol{S}_i \cdot \hat{\boldsymbol{m}}$ corresponding to the maximum eigenvalue. We find that

$$\begin{aligned} \mathcal{H}\,|\hat{\boldsymbol{m}}\rangle &= S^2 E_0\,|\hat{\boldsymbol{m}}\rangle + iDS \sum_{\langle i,j\rangle} \boldsymbol{d}_{ij} \cdot (\hat{\boldsymbol{e}}_1 + i\hat{\boldsymbol{e}}_2)\, S_i^-\,|\hat{\boldsymbol{m}}\rangle \\ &= S^2 E_0\,|\hat{\boldsymbol{m}}\rangle\,, \end{aligned} \tag{3.26}$$

where $\hat{\boldsymbol{e}}_1, \hat{\boldsymbol{e}}_2$ are two unit vectors that form an orthonormal triad with the magnetization direction, i.e. $\hat{\boldsymbol{e}}_\alpha \cdot \hat{\boldsymbol{e}}_{\alpha'} = \delta_{\alpha\alpha'}$ and $\hat{\boldsymbol{m}} = \hat{\boldsymbol{e}}_1 \times \hat{\boldsymbol{e}}_2$. It is then straightforward to verify that the sum over nearest-neighbour DM vectors vanishes from Eq. (3.33). That is to say, $|\hat{\boldsymbol{m}}\rangle$ is an *exact* eigenstate of the quantum many-body Hamiltonian in Eq. (3.1). Any fully polarized configuration therefore displays no zero-point fluctuations about $|\hat{\boldsymbol{m}}\rangle$. This peculiar scenario motivates our investigation of *thermal* ObD in the ferromagnetic phase of the *quantum model* in the large S limit.

Since the fully polarized product state is an exact eigenstate of the normal-ordered Hamiltonian, we combine Eq. (3.26) with Eq. (3.16) to find that $E_2^{(\hat{\boldsymbol{m}})} = 0$. More generally, the classical ground state energy is equivalent to the energy of the ferromagnetic product state in the quantum model, implying that there are no quantum zero-point fluctuations in the fully polarized ferromagnetic phase. At nonzero temperature, the ObD selection, now operating in the quantum model, can be exposed by minimizing the free energy difference per unit cell (using Eq. (3.18))

$$\mathcal{F}^{(\hat{\boldsymbol{m}})} - \mathcal{F}^{(\hat{\boldsymbol{n}})} = \frac{T}{N} \sum_{\boldsymbol{q}} \sum_{\mu=0}^{3} \ln \left(\frac{1 - e^{-S\omega_{\mu,\boldsymbol{q}}^{(\hat{\boldsymbol{m}})}/T}}{1 - e^{-S\omega_{\mu,\boldsymbol{q}}^{(\hat{\boldsymbol{n}})}/T}} \right) \tag{3.27}$$

with respect to $\hat{\boldsymbol{m}}$, relative to a fixed reference magnetization axis $\hat{\boldsymbol{n}}$.

Comparing the free energy difference between configurations calculated using Eq. (3.27), we find that, for a given value of $T/J = 0.1$ and depending on the ratio of D/J for $D/J < 2$, there are two distinct scenarios as to whether the magnetization is directed along either the $\langle 111 \rangle$ or $\langle 110 \rangle$ directions (see Fig. 3.8).[22] This is similar to what was found with the CLTE calculation for the classical version of the model. Being limited to a low-temperature description of the magnon excitations well below T_c, the (quantum) linear spin wave theory does not capture a selection of the magnetization along the $\langle 100 \rangle$ directions similar to what was found in the Monte Carlo simulations of the classical model for $T \lesssim T_c$ (c.f. Fig. 3.7(b-d)).

Upon determining which configurations from Eq. (3.25) minimize the free energy in Eq. (3.27), we construct a low-temperature phase diagram depicted in Fig. 3.9 for the case where $S = \frac{1}{2}$. We find that, for D/J corresponding to the classical ferromagnetic regime in Fig. 3.1, the $\langle 111 \rangle$ directions are selected at $T = 0^+$. On the other hand, we observe that the $\langle 110 \rangle$ directions are the ones selected above a $\langle 111 \rangle \to \langle 110 \rangle$ critical temperature that increases as D/J is decreased from $D/J = 2^-$ down to $D/J \sim 1.2$. Over the same $1.2 \lesssim D/J < 2$ range, the phase diagram exhibits a region of $\langle 111 \rangle$ magnetic order re-entrance (i.e. $\langle 110 \rangle \to \langle 111 \rangle$) upon warming with an intermediate region with $\langle 110 \rangle$ order bracketed between a high and low temperature $\langle 111 \rangle$ magnetic order selection.

We note that the thermodynamic mechanism for the low-temperature selection of the magnetization direction (i.e., internal energy versus entropy) in the quantum model is distinct from the classical one. In the classical case, one can explicitly identify the $\boldsymbol{m}$-dependence of the entropy

[22] The two different values of D/J for the plots in Fig. 3.8 are chosen to depict the free energy distribution in each of the two distinct regions of the spin-wave phase diagram in Fig. 3.9. Similarly, in Fig. 3.6, we choose two representative values of D/J that depict the magnetization distribution in each of the distinct regions of the classical phase diagram in Fig. 3.7. The reason different values of D/J were chosen for the classical and quantum plots is that the boundaries are different in each of the two phase diagrams. In addition, we note that Figs. 3.6 and 3.8 are polar maps of different quantities and should only be compared in an overall qualitative sense.

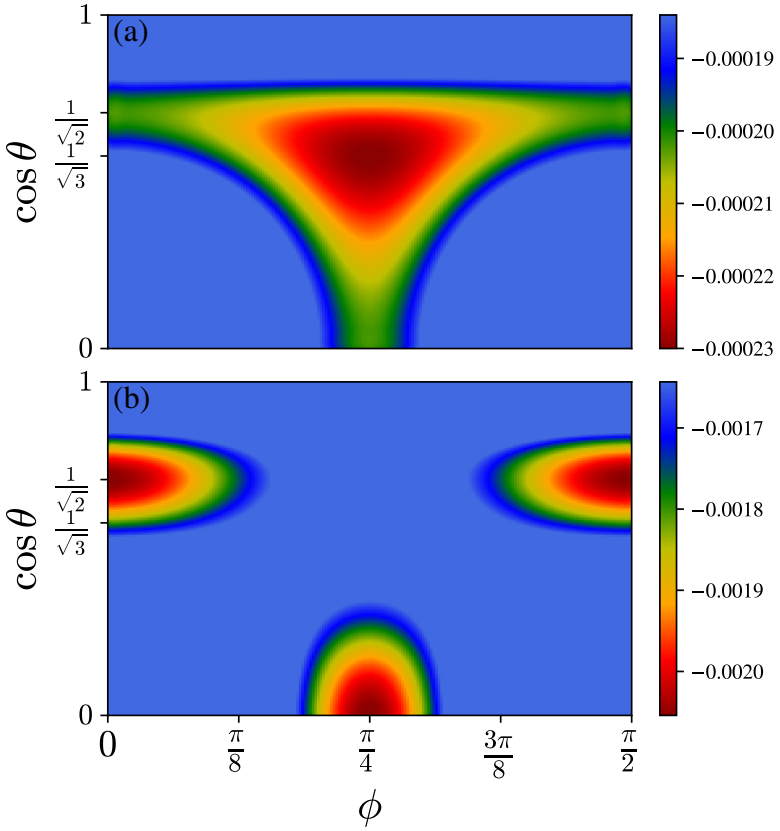


Figure 3.8: Free energy difference between configurations obtained from linear spin wave theory using Eq. (3.27) with $T/J = 0.1$, $\hat{\boldsymbol{n}} = \langle 100 \rangle$ and $S = \frac{1}{2}$. Panel (a) depicts the free energy distribution for $D/J = 1.0$, which is minimized by $\hat{\boldsymbol{m}} = \langle 111 \rangle$. Panel (b) depicts the free energy distribution for $D/J = 1.8$, which is minimized by $\hat{\boldsymbol{m}} = \langle 110 \rangle$.

as the mechanism for the selection at low temperatures. As there is not an extensive number of quadratic zero modes in the present model,[23] the equipartition theorem guarantees that the energy per spin is $k_B T$, independent of the magnetization direction. Conversely, both the energy and entropy in quantum spin wave theory depend on the magnetization direction, contributing to the free energy in Eq. (3.27), with the low-temperature dependence of each of these two (energy and entropy) contributing terms being discussed in the next subsection. More details regarding the thermal selection mechanism in the quantum case can be found in Appendix 3D.

[23] In a system where there are an extensive number of quadratic zero modes, there will be a thermal contribution to the internal energy, see for example Ref. [153].

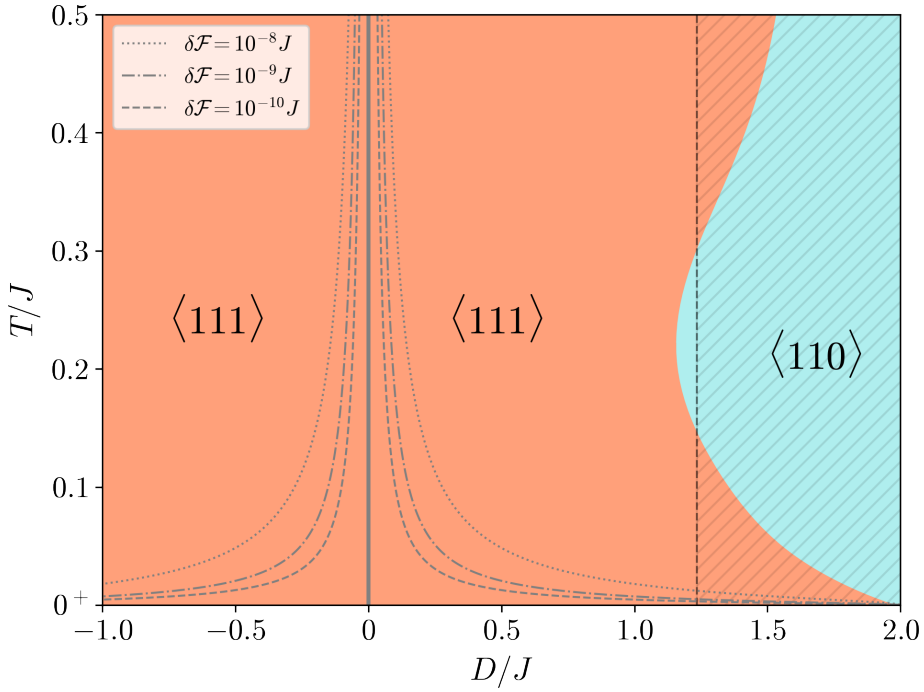


Figure 3.9: Low temperature phase diagram obtained from linear spin wave theory using Eq. (3.27) and $S = \frac{1}{2}$. The solid gray line at $D/J = 0$ is the Heisenberg line, where the model has an exact O(3) symmetry and no ObD selection. Several contours of equal free energy are plotted in the region surrounding the Heisenberg line, where $\delta\mathcal{F} \equiv \mathcal{F}^{\langle 110 \rangle} - \mathcal{F}^{\langle 111 \rangle}$. The hatched region where $D/J > 1.235$ corresponds to the non-linear spin wave instability as described in Sec. 3.4.4. The temperature axis is scaled by the ferromagnetic exchange interaction J.

As expected, we see in Fig. 3.9 (by tracking the contours of equal free energy) that the free energy difference between magnetization orientations vanishes in two distinct limits, when $D \to 0$ (the Heisenberg limit) or as $T \to 0^+$. We note here that since the eigenvalue problem of the linear spin wave theory can be exactly solved for the Heisenberg model ($D = 0$), some analytical inferences about ObD of the quantum model can be made using perturbation theory for $D/J \ll 1$. We use this approach in the following subsection to expose analytically what is the relative contribution of the internal energy and entropy, along with their temperature dependence, in selecting the direction of $\hat{\boldsymbol{m}}$ at $T \ll J$ in the limit $D/J \ll 1$.

3.4.3 Quantum selection at $T = 0^+$

We now proceed to perform a low-temperature expansion of the free energy to obtain the temperature dependence of the leading contribution responsible for thermal ObD in the quantum model. We calculate this contribution perturbatively, expanding about the Heisenberg point ($D = 0$). We first note that the linear spin wave Hamiltonian in Eq. (3.14) can be diagonalized analytically at $\boldsymbol{q} = \mathbf{0}$ when $D = 0$. The matrix

$$X_0 \equiv X^{(\hat{\boldsymbol{m}})}(\boldsymbol{q} = \mathbf{0})\Big|_{D=0}, \tag{3.28}$$

given in Eq. (3.15), and appearing in the right-hand side of Eq. (3.14), has one zero-eigenvalue and three degenerate eigenvalues of $8J$. The remaining part of the spin wave Hamiltonian is treated as a perturbation, namely $\delta X^{(\hat{\boldsymbol{m}})}(\boldsymbol{q}) \equiv X^{(\hat{\boldsymbol{m}})}(\boldsymbol{q}) - X_0$.

Next, in the framework of non-degenerate perturbation theory, we calculate the energy shift of the zero-energy magnon due to the perturbation $\delta X^{(\hat{\boldsymbol{m}})}(\boldsymbol{q})$. To find the low-temperature contribution of ObD to the free energy, we must find the leading order terms in the magnon dispersion that couple to the magnetization direction. This involves calculating the associated energy shift in perturbation theory, and subsequently expanding the dispersion in powers of the wavevector components. We find that such terms appear at both fourth order in D/J, and fourth order in the wavevector components. The resulting dispersion is expressed as $\varepsilon_2(\boldsymbol{q}) + \varepsilon_4^{(\hat{\boldsymbol{m}})}(\boldsymbol{q}) + O(q^6)$, where $\varepsilon_n(\boldsymbol{q})$ contains all terms of $O(q^n)$ in the wavevector components. The low-temperature contribution of the quartic terms to the free energy is calculated to be

$$\mathcal{F}^{(\hat{\boldsymbol{m}})} \approx TV \int \frac{\mathrm{d}^3 q}{(2\pi)^3} \ln\left(1 - e^{S\varepsilon_2(\boldsymbol{q})/T}\right) + VS \int \frac{\mathrm{d}^3 q}{(2\pi)^3} \frac{\varepsilon_4^{(\hat{\boldsymbol{m}})}(\boldsymbol{q})}{e^{S\varepsilon_2(\boldsymbol{q})/T} - 1}. \tag{3.29}$$

The leading order term in $\mathcal{F}^{(\hat{\boldsymbol{m}})}$ that depends on the magnetization direction yields

$$\mathcal{F}^{(\hat{\boldsymbol{m}})} \sim \frac{3S\zeta\left(\frac{7}{2}\right)}{32\pi^{3/2}} \frac{D^4}{J^3} \left(\hat{m}_x^4 + \hat{m}_y^4 + \hat{m}_z^4\right) \left(\frac{T}{2JS}\right)^{7/2}, \tag{3.30}$$

where $\zeta(z) = \sum_{n=1}^{\infty} n^{-z}$ is the Riemann zeta function. This term is minimized when $\hat{\boldsymbol{m}} = \langle 111 \rangle$, which is consistent with the low-temperature selection that was found by direct numerical evaluation of Eq. (3.27), and reported in Fig. 3.9. More details of the perturbative calculation are provided in Appendix 3C. We note that Eq. (3.30) is a sub-leading term in the low-temperature expansion of the free energy, as there is a term proportional to $T^{5/2}$ that is independent of $\hat{\boldsymbol{m}}$ [see Eq. (3.45)]. The free energy contribution in Eq. (3.30) explicitly depends on the magnetization direction, and therefore describes how (in zero magnetic field) the DM interaction lifts the

accidental degeneracy of the ferromagnetic ground state to lowest order in D/J and T/J. Next, we briefly discuss how ObD manifests itself at low temperature in the presence of an external magnetic field.

The ferromagnetic pyrochlore $Lu_2V_2O_7$ is believed to be well-described by Eq. (3.1). Interestingly, measurements of the magnetization of $Lu_2V_2O_7$ in Ref. [15] appear to be anisotropic with respect to the applied field direction, begging the question of whether anisotropic field response may be related to the ObD discussed in the present work and possibly operating in this material. Motivated by this question, we generalize the perturbative calculation above to include a weak external magnetic field $\boldsymbol{B}$, which removes the accidental degeneracy of the ground state. As the model Eq. (3.1) does not benefit from a quantum ObD at zero temperature generating a magnetic anisotropy, in the $T = 0$ limit, the magnetization will immediately align parallel to the external field, as this configuration minimizes the energy. This contrasts with the competition between quantum ObD and the Zeeman energy in the $Er_2Ti_2O_7$ pyrochlore antiferromagnet [154]. Conversely, at small nonzero temperature, the $\hat{\boldsymbol{m}} = \langle 111 \rangle$ configuration is preferred by thermal fluctuations when the field is absent. It follows that there must be a rotation of the magnetization direction as a function of the applied field, whereby $\hat{\boldsymbol{m}} = \langle 111 \rangle$ when $\boldsymbol{B} = \boldsymbol{0}$, and $\hat{\boldsymbol{m}}$ aligns parallel to $\hat{\boldsymbol{B}}$ when the applied external magnetic field is large in magnitude. We generalize the perturbative calculation of the free energy above to include a weak magnetic field in Appendix 3E. However, we find that such a change of the magnetization direction occurs for extremely weak magnetic fields, where the Zeeman coupling is one million times smaller than the ferromagnetic exchange $\left(\mu_B g|\boldsymbol{B}|/J \sim 10^{-6}\right)$ even for a sizeable DM interaction $D/J = 0.5$ and at a temperature $T/J = 0.15$ [see Fig. 3.15(b)]. This large separation of energy scales would likely make it challenging to measure this change in magnetization experimentally for this system. For reference, the DM interaction for $Lu_2V_2O_7$ is much smaller at $D/J \lesssim 0.13$ [137, 145].

Finally, it is important to mention that although the fully polarized product state is an exact eigenstate as shown in Eq. (3.26), it is not necessarily the case that this eigenstate is the true many-body ground state outside of the perturbative regime $|D| \ll J$. To address this possibility, we next extend our calculations to the lowest order in non-linear spin wave theory to analyze the presence (or lack of) magnetic order in the many-body ground state.

3.4.4 Limit of Stability

The classical ground states depicted in Fig. 3.1 have thus far been found to be consistent with the magnetic order observed in both the CLTE and classical MC calculations. Conversely, while Eq. (3.26) shows that the ferromagnetic product state is an exact eigenstate, it is not necessarily the true quantum ground state of Eq. (3.1) for the whole $-1 < D/J < 2$ range. For example, recent

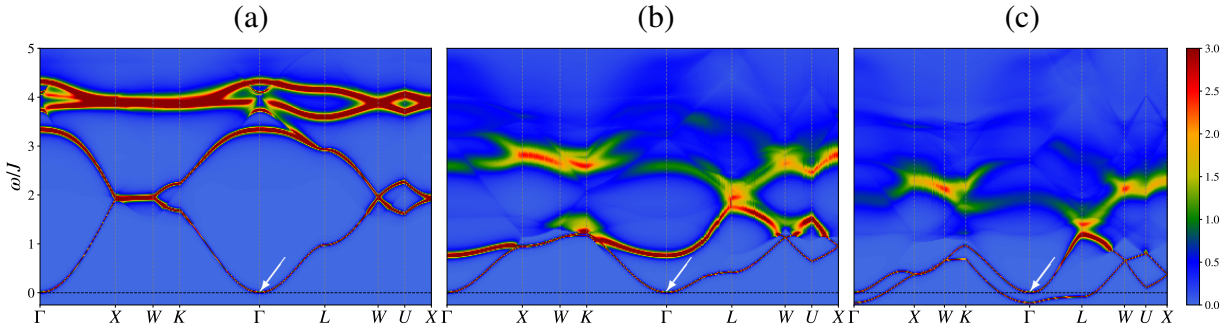


Figure 3.10: Zero-temperature magnon spectral function $\mathcal{A}(\boldsymbol{k}, \omega)$ for $\hat{\boldsymbol{m}} = \langle 111 \rangle$ and $S = \frac{1}{2}$ to $O(S^0)$ in non-linear spin wave theory, calculated using Eq. (3.21) for (a) $D/J = 0.25$, (b) $D/J = 1.00$ and (c) $D/J = 1.3$. The white arrows indicate the gapless pseudo-Goldstone mode in the magnon spectrum.

work investigating the quantum ground states of this model using functional renormalization group methods did identify a ferromagnetic ordered state for $-1 < D/J \lesssim 1.3$, but found a lack of conventional magnetic order for $1.3 \lesssim D/J \leq 2$ [63, 127]. These last results suggest that while Eq. (3.25) may be the ground state when $-1 < D/J \lesssim 1.3$, there exists the possibility that for spin-$\frac{1}{2}$, an exotic quantum spin liquid of lower energy than the ferromagnetic state may be realized in the range $1.3 \lesssim D/J \leq 2$.[24] This raises the question of whether linear spin wave theory provides an accurate description of the low-temperature excitations of this model.

Motivated by these results, and to further address the question of stability of the ferromagnetic ordered phase, we go beyond linear spin wave theory to calculate the $O(S^0)$ correction to the single-magnon spectral function at $T = 0$, using Eq. (3.21). Analogous to linear spin wave theory, where a classical instability is characterized by the appearance of soft modes, we investigate whether there are soft modes in the renormalized spectrum in the $-1 < D/J < 2$ range.

Given that the ferromagnetic configuration is characterized by an O(3) degeneracy, which persists in the quantum model, at least one gapless mode is guaranteed to be observed in the linear spin wave theory at $\boldsymbol{q} = \boldsymbol{0}$ — the pseudo-Goldstone mode [5, 155]. In a larger number of frustrated spin models, the presence of quantum fluctuations drives the pseudo-Goldstone mode to become gapped at $O(S^0)$, as revealed in the self-energy [101]. However, the fact that the ferromagnetic configuration is an exact eigenstate of the Hamiltonian implies that this mode remains gapless

[24] Using a number of numerical and analytical methods, Ref. [127] found evidence that the $D/J = 2$ point for a spin-$\frac{1}{2}$ system may be a quantum spin liquid, described by the combination of a rank-1 and rank-2 emergent gauge field, which corresponds to a triple point in the classical phase diagram where two long-range ordered quadrupolar phases meet with a spin ice state. In the classical $S = \infty$ limit, evidence is compelling that the point $D/J = 2$ is a classical spin liquid [127]

at all orders of the $1/S$ expansion at $T = 0$, a somewhat peculiar property of the current model in Eq. (3.1). Conversely, we expect the accidental degeneracy of the quantum spin-$\frac{1}{2}$ model to be lifted by thermal fluctuations, leading to the dynamical generation of a pseudo-Goldstone gap at nonzero temperature [58]. Since our self-energy calculations are carried out at $T = 0$, the pseudo-Goldstone mode remains gapless. We therefore look for instabilities in the form of additional soft modes in the magnon spectral function, $\mathcal{A}(\boldsymbol{k}, \omega)$ in Eq. (3.21). Details of this calculation are provided in Appendix 3F.

The results of these calculations are depicted in Fig. 3.10, showing the single-magnon spectral function to $O(S^0)$ in non-linear spin wave theory. As D/J becomes large, the optical magnon bands become significantly broadened, displaying a Lorentzian-like form in frequency space. This broadening originates from decay effects; the width of the Lorentzian profile close to the spectral peaks is precisely the decay rate, encoded in the imaginary part of the self-energy, $\Sigma^{(\hat{\boldsymbol{m}})}(\boldsymbol{k}, \omega)$. While the self-energy renormalizes the spectral function peaks, we find that there remains a stable and gapless pseudo-Goldstone mode at $\boldsymbol{q} = \boldsymbol{0}$ for all $-1 < D/J < 2$ as expected. This gapless mode is indicated by the white arrows in Fig. 3.10. We note that a similar result is discussed in Ref. [132], where the optical magnon branches exhibit broadening in the kagome Heisenberg ferromagnet with DM interactions, to leading order in $1/S$.

We find that one of the magnon branches becomes soft and shifts to negative frequencies at $\boldsymbol{q} = \boldsymbol{0}$ (Γ point) for a large indirect DM interaction ($J > 0$, $D > 0$), as depicted in Fig. 3.10(b-c). In particular, this mode goes soft at a critical DM interaction $D/J \approx 1.235$, indicating that the long-range ferromagnetic order becomes unstable at $O(S^0)$ in the non-linear spin wave theory for $1.235 \lesssim D/J < 2$. The D/J value for which this instability occurs was calculated for $\hat{\boldsymbol{m}} = \langle 100 \rangle$, $\langle 110 \rangle$, and $\langle 111 \rangle$ and was found to be independent of the classical magnetization direction $\hat{\boldsymbol{m}}$. For reference, the instability is marked by the vertical dashed line at $D/J \sim 1.235$ on the linear spin wave phase diagram in Fig. 3.9. Importantly, we note that the instability approximately coincides with the value of the DM interaction where $\langle 110 \rangle$ order is found in the linear spin wave theory at $T > 0$ (see Fig. 3.9). The region of instability $1.235 \lesssim D/J < 2$ is consistent with the pseudo-fermion functional renormalization group calculations for the same model in Refs. [63, 127], where no long-range magnetic order was detected in the range $1.3 \lesssim D/J < 2$. Conversely, Noculak *et al.* [63] report conventional long-range magnetic order for $D/J \gtrsim 2$, corresponding to the Γ_5 phase in Fig. 3.1. The breakdown of spin wave theory in the classically ferromagnetic region of this model is likely tied to the spin-liquid phase discussed in Ref. [127]. Our results suggest that the ferromagnetic product state in Eq. (3.25) is the exact ground state of Eq. (3.1) for $-1 \lesssim D/J \lesssim 1.235$, and that the phase diagram in Fig. (3.9), along with the establishment of ObD without zero-point fluctuations, is reasonably accurate in this region.

3.5 Discussion and Conclusion

In this work, we studied the classical and quantum order-by-disorder selection of a collinear ferromagnetic phase of the Heisenberg and Dzyaloshinskii-Moriya Hamiltonian on the pyrochlore lattice. In the classical model, we found three distinct regions in parameter space *and* as a function of temperature where three distinct magnetization orientations are thermally selected. For large and indirect DM interaction $D \lesssim 2J$ with $J > 0$, classical Monte Carlo simulations find a cascade of reorientations of the magnetization direction as a function of temperature, as depicted in Fig. 3.6, and summarized in the phase diagram of Fig. 3.7. Considering our classical MC results for $T \lesssim T_c$, the behaviour of the observed ferromagnetic transition is consistent with that of an O(3) vector model with cubic anisotropy, governed by the Ginzburg-Landau-Wilson (GLW) free energy functional [156]

$$\mathcal{F}[\boldsymbol{m}] \approx \int \mathrm{d}^3x \left[\frac{1}{2} \sum_{\mu=1}^{3} \left(\boldsymbol{\nabla} m_\mu\right)^2 + \frac{r}{2}|\boldsymbol{m}|^2 + \frac{u}{4}|\boldsymbol{m}|^4 + v \sum_{\mu=1}^{3} m_\mu^4 \right]. \tag{3.31}$$

When $v > 0$, the cubic anisotropy favours the magnetization to be aligned with the $\langle 111 \rangle$ directions. When $v < 0$, the anisotropy favours the magnetization to be aligned along the $\langle 001 \rangle$ directions. From a renormalization group perspective, the O(n) vector model with cubic anisotropy in three dimensions has a critical order parameter dimension $n = n_c$, below which the Heisenberg fixed point is stable and above which the cubic fixed point is stable [150]. Incidentally, $n_c \approx 3$ [157–160], and it remains an open debate as to which of the fixed points of Eq. (3.31) is the one that is stable. In addition, the transition is first order if $u < 0$, and may be fluctuation-induced first order if $u > 0$ and $v < 0$, depending on the ratio of the couplings v/u [161–163]. In our work, we have not explored the nature of the paramagnetic to ferromagnetic transition (i.e., first or second order and universality class of the latter). We leave this topic for future studies.

In contrast, Eq. (3.31) does not predict the $\langle 110 \rangle$ configurations which are observed in our classical MC simulations in the region where $D/J \to 2^-$.[25] This would require, for example, the addition of a (irrelevant, in the renormalization group sense) 6$^{\text{th}}$ order term to the GLW free energy, similar to the terms appearing in Eq. (3.7). Additionally, the critical temperature completely vanishes at the boundary between the collinear ferromagnet and the Γ_5 phase ($D/J = 2$), where a classical spin liquid has recently been reported and characterized by fluctuating rank-1 vector and rank-2 tensor gauge fields [127]. A more in-depth characterization of the predicted configurations and the transitions between these phases across the full collinear ferromagnetic phase would require a large-scale simulation and careful finite-size scaling analysis. We leave this study for future work.

[25] For the classical model, the instability discussed for the spin-$\frac{1}{2}$ does not occur for any $|D|/J < 2$.

In the quantum model, we find that the fully polarized product state in Eq. (3.25) is an exact eigenstate of the Hamiltonian regardless of the magnetization direction. As a result, the accidental degeneracy of the ferromagnetic phase is not lifted by zero-point fluctuations at $T = 0$. This accidental degeneracy is, however, lifted by the low-energy spin wave excitations at nonzero temperature ($T > 0$), leading to a selection of a discrete set of magnetization directions as depicted in Fig. 3.9. This is the first realization of such an ObD mechanism that we are aware of, where the selection of an ordered phase in a quantum system is purely thermal — thus answering the question we set in the Introduction whether one form of ObD can occur without the other.

Again, for the quantum model, we find that when $|D| \ll J$, the selection of the magnetization direction enters as a sub-leading term in the low-temperature expansion of the free energy. Using non-linear spin wave theory, we found that the ferromagnetic order does not seem to persist for $D/J \gtrsim 1.235$. We note that the instability in non-linear spin wave theory coincides reasonably well with the region of the linear spin wave phase diagram (Fig. 3.9) where the magnetization orders in the $\langle 110 \rangle$ directions above a certain temperature. The possible relationship between these two observations is unclear at this point and is left for future work. That being said, this result may suggest that the narrow window of $\langle 110 \rangle$ order for $T \gtrsim 0.15$ for $1.1 \lesssim D/J \lesssim 1.235$ observed in Fig. 3.9 may actually not occur in the $S = \frac{1}{2}$ system, but would presumably be present as S is increased above a critical value.

The results from the present work may have implications for real ferromagnetic materials where the DM interaction is the leading perturbation. In particular, the magnetism of the ferromagnetic Mott insulators $Lu_2V_2O_7$ and $Y_2V_2O_7$ is rather well described by Eq. (3.1) [143–145]. Recently, it was proposed in Ref. [58] that the thermal contribution to ObD can be diagnosed by a temperature-dependent energy gap measured via inelastic neutron scattering. We expect this would be the strongest experimental signature of ObD in these materials. However, since $D/J \sim 0.1$ in these materials [137, 145], the T-dependent ObD gap may be very small and could possibly be overwhelmed by a quantum ($T = 0$) ObD gap induced by a small nonzero Kitaev K interaction[19] with, in addition, an energetically-induced gap caused by a small pseudo-dipolar interaction Γ. In addition, the tendency of the magnetization to cant away from the direction selected by ObD in a small external field would result in further challenges to identifying ObD experimentally.

Finally, we note that a more general class of spin models may be expected to exhibit ObD without zero-point fluctuations. Specifically, any ferromagnetic Heisenberg model with DM interactions will satisfy Eq. (3.26) as long as the sum over DM vectors along the bonds surrounding each site vanishes, such as the kagome Heisenberg ferromagnet with out-of-plane DM vectors.[15] We then expect that the ferromagnetic product state will remain the exact ground state of such a Hamiltonian as long as the DM interactions are sufficiently small with respect to the Heisenberg exchange J. Our calculations may then serve as a template to study thermal ObD in these

analogous models.

Acknowledgements

The authors acknowledge useful discussions with Itamar Aharony, Kristian Chung, Yasir Iqbal, Subhankar Khatua, Paul McClarty, Vincent Noculak, Jeffrey Rau, Johannes Reuther, Addison Richards, Rajiv Singh, and Mike Zhitomirsky. We also thank Vincent Noculak for comments on an early version of the manuscript, and Alexander Chernyshev for bringing to our attention previous work on the related kagome Heisenberg ferromagnets. AH acknowledges support from the NSERC of Canada CGS-D Scholarship. DLG acknowledges financial support from the DFG through the Hallwachs-Röntgen Postdoc Program of the Würzburg-Dresden Cluster of Excellence on Complexity and Topology in Quantum Matter – *ct.qmat* (EXC 2147, project-id 390858490) and through SFB 1143 (project-id 247310070). The work at the University of Waterloo was supported by the NSERC of Canada and the Canada Research Chair (Tier 1, M.J.P.G.) program. This research was enabled in part by computing resources provided by the Digital Research Alliance of Canada.

Data Availibility

The data that support the findings of this article are openly available [164].

Appendices

3A Pyrochlore lattice convention

The pyrochlore lattice is a face-centred cubic (FCC) lattice with four sites, defining a regular tetrahedron, per primitive unit cell. The primitive FCC lattice vectors are given by

$$\boldsymbol{a}_1 = \frac{a}{2}\left(\hat{\boldsymbol{y}} + \hat{\boldsymbol{z}}\right) \qquad \boldsymbol{a}_2 = \frac{a}{2}\left(\hat{\boldsymbol{x}} + \hat{\boldsymbol{z}}\right) \qquad \boldsymbol{a}_3 = \frac{a}{2}\left(\hat{\boldsymbol{x}} + \hat{\boldsymbol{y}}\right). \tag{3.32}$$

At each FCC lattice site, there is a spin of type 0. The remaining three spins within a unit cell are separated by the sublattice vectors $\boldsymbol{r}_{0\mu} = \boldsymbol{a}_\mu/2$. The sublattice vectors between a spin of type μ to a spin of type ν can then be constructed as $\boldsymbol{r}_{\mu\nu} \equiv \boldsymbol{r}_{0\nu} - \boldsymbol{r}_{0\mu}$.

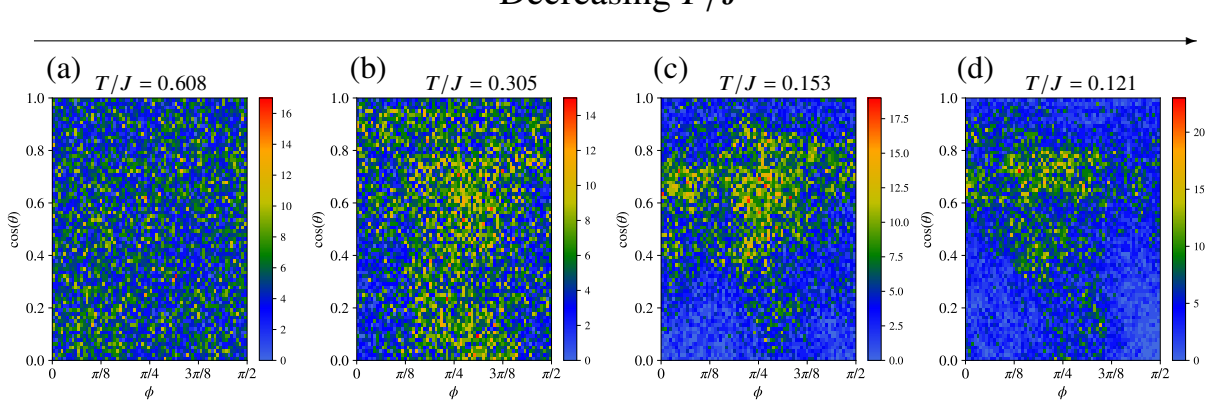


Figure 3.11: Distribution of the global magnetization direction, $p(\hat{\boldsymbol{m}})$, from classical Monte Carlo simulations for a system with $D/J = -0.84$ for which $T_c/J \sim 0.64$. Here, the magnetization direction is expressed in spherical coordinates $\hat{\boldsymbol{m}} = (\cos\phi\sin\theta, \sin\phi\sin\theta, \cos\theta)$ and temperature is measured in units of J ($k_B = 1$). In panels (b)-(d), which are below $T_c/2$, the highest intensity is found near $\cos(\theta) = 1/\sqrt{3}, \phi = \pi/4$, suggesting the $\langle 111\rangle$ configurations are selected.

The (indirect) DM vectors in this representation are given by

$$\begin{aligned} \boldsymbol{d}_{01} &= \hat{\boldsymbol{z}} - \hat{\boldsymbol{y}} \qquad \boldsymbol{d}_{02} = \hat{\boldsymbol{x}} - \hat{\boldsymbol{z}} \qquad \boldsymbol{d}_{03} = \hat{\boldsymbol{y}} - \hat{\boldsymbol{z}} \\ \boldsymbol{d}_{21} &= \hat{\boldsymbol{x}} + \hat{\boldsymbol{y}} \qquad \boldsymbol{d}_{13} = \hat{\boldsymbol{x}} + \hat{\boldsymbol{z}} \qquad \boldsymbol{d}_{32} = \hat{\boldsymbol{y}} + \hat{\boldsymbol{z}}, \end{aligned} \tag{3.33}$$

where the remaining DM vectors can be determined using the antisymmetry property $\boldsymbol{d}_{ji} = -\boldsymbol{d}_{ij}$. Note that in this representation, the DM vectors used in the present work are *unnormalized*, with $|\boldsymbol{d}_{ij}| = \sqrt{2}$.

3B Monte Carlo calculation of M_4, δM_4 and M_6

In the main text, we illustrated in Fig. 3.6 the thermal evolution of the distribution $p(\boldsymbol{m})$ of the global magnetization direction, $\hat{\boldsymbol{m}}$, for two sets of parameters of the Hamiltonian in Eq. (3.1). The evolution of these distributions displayed an intricate and rich phase diagram attributed to a thermal ObD selection of the magnetization direction $\hat{\boldsymbol{m}}$ in the classical Hamiltonian in Eq. (3.1). To further characterize these phases, we introduced the cubic parameters M_4, δM_4, and M_6 in Eqs. (3.8)-(3.10) and calculated their averaged value using classical Monte Carlo, as depicted in Fig. 3.7. In this figure, we mainly focused on the region for which $D/J > 1.3$ where the ObD selection is stronger, agreeing with the CLTE analysis in Fig 3.5. In this appendix, we further discuss the thermal evolution of these parameters and the expected values these would have for different magnetization orientations. Importantly, one should note that for an isotropically

	M_4	δM_4	M_6
Isotropic	3/5	3/5	9/35
$\langle 100 \rangle$	1	0	0
$\langle 110 \rangle$	1/2	3/4	0
$\langle 111 \rangle$	1/3	1	1

Table 3.1: Expected values of the cubic parameters in Eqs. (3.8)-(3.10) for a magnetization along different directions.

distributed magnetization direction, the values of the cubic parameters will be distinct from the case where there is a selected $\hat{\boldsymbol{m}}$ direction, as shown in Table 3.1.

In Fig. 3.7(d), we mark with triangles [squares] the locations at which the distributions $p(\hat{\boldsymbol{m}})$ shown in Fig. 3.6(b-d) [Fig. 3.6(f-h)] were measured below the critical temperature. As discussed in the main text, the temperature evolution of the cubic parameters depicted in Fig. 3.7(b-d) identifies three distinct regions in both temperature T and DM interaction D/J where the white dashed lines are guides to the eye, separating the labelled phases. The first, highest, temperature region, which we label "$\langle 100 \rangle$", is observed just below the critical temperature T_c as shown in Fig. 3.7. This phase is most clearly exposed in the regime $1 \lesssim D/J < 2$, and likely extends to lower values of D/J for $D/J > 0$.[26] In this region, the δM_4 and the M_6 cubic parameters acquire small values well below the isotropic limit, which are consistent with the $\langle 100 \rangle$ magnetization orientations. As expected, the deviation of the cubic parameters from the isotropic values increases as D/J increases. The second region, which we labelled region "$\langle 111 \rangle$", is observed at low temperatures in the range $-1 < D/J \lesssim 1.66$ excluding the isotropic point $D/J = 0$. We note that this phase appears to be the only possible orientation of the magnetization for $D/J < 0$ where no sign of a $\langle 100 \rangle$ or a $\langle 110 \rangle$ region is detected, as illustrated by the magnetization distribution in Fig. 3.11 for $D/J = -0.84$ where $T_c/J \sim 0.64$.[27] In the "$\langle 111 \rangle$" region, the cubic parameters δM_4, M_4, and M_6 evolve smoothly, plateauing to the approximate values 9/10, 1/3, and 7/10, respectively, see Fig. 3.7(b-d). We note that the cubic parameters in this region suggest a $\langle 111 \rangle$ selection where all cubic parameters are non-vanishing. The third region, which we label "$\langle 110 \rangle$", is delimited at low temperatures by a range of interaction parameters $1.66 \lesssim D/J < 2$, and delimited at higher temperatures by regions "$\langle 100 \rangle$" and "$\langle 111 \rangle$". In the "$\langle 110 \rangle$" region,

[26] The precise determination of the extension of the $\langle 100 \rangle$ phase as the temperature drops below T_c is challenged by the strong thermal fluctuations near criticality as well as the weak thermal selection associated to this phase, as well as the $\langle 111 \rangle$ (see Fig. 3.5) as $|D|/J \to 0^+$. As such, the identification of a clearer $\langle 100 \rangle$ /$\langle 111 \rangle$ phase boundary in this region of the phase diagram would require a significantly more extensive numerical study while also considering larger system sizes.

[27] In these distributions of the magnetization direction, the highest intensity appears near the point $\cos(\theta) = 1/\sqrt{3}, \phi = \pi/4$, suggesting the $\langle 111 \rangle$ orientations.

the M_6 cubic parameter appears to nearly vanish while the δM_4 and M_4 parameters plateau to the approximate intermediate values $7/10$ and $1/2$, respectively. The values of the cubic parameters for this region are consistent with the $\langle 110 \rangle$ magnetization directions. We note that, as the value of D/J is tuned towards the Γ_5 phase, the low-temperature transition to the [110] orientation becomes stronger as exposed by the evolution of the specific heat and the cubic parameters, see Fig. 3.12. Indeed, for $D/J \to 2$, the specific heat develops a secondary peak at a temperature where the cubic parameters suddenly change, signalling an abrupt reorientation of the magnetization direction and thus identifying the transition to the [110] orientation. In contrast, we do not observe this secondary peak in the specific heat for slightly smaller values of D/J where the cubic parameters evolve smoothly down to the lowest temperature. The absence of a secondary feature in the specific heat signalling the transition between the different magnetic orientations is likely associated with finite-size effects. We note that a similar scenario exists for the Γ_5 phase: for $D/J \in (11.43, \infty)$, there is a transition between a paramagnetic phase to the ψ_2 state of Γ_5 at $T = T_c$, followed by a further transition between the ψ_2 and ψ_3 states at a finite temperature $T_{\Gamma_5} < T_c$ [63]. The authors of Ref. [63] claim that they are unable to detect a peak in the Monte Carlo specific heat due to finite-size effects. This is analogous to the specific heat presented in Fig. 3.12(a), where we do not see a peak in the specific heat for $D/J < 1.88$, despite observing a transition between different magnetization directions in Fig. 3.7. Obtaining significantly more precise phase boundaries would require quite large-scale simulation studies involving careful finite-size scaling analysis, an investigation that is outside the scope of the present work.

3C Perturbative calculation of the free energy

Using the matrix elements of the linear spin wave Hamiltonian in Eq. (3.15), we estimate the dispersion of the lowest magnon branch by first diagonalizing the Hamiltonian for the case when $D = 0$ and $\boldsymbol{q} = \mathbf{0}$, finding

$$X_0 \equiv X^{(\hat{\boldsymbol{m}})}(\boldsymbol{q} = \mathbf{0})\Big|_{D=0} = 0\,|E_0\rangle\langle E_0| + 8J\,(1 - |E_0\rangle\langle E_0|)\,, \tag{3.34}$$

where $|E_0\rangle = \left(\frac{1}{2} \quad \frac{1}{2} \quad \frac{1}{2} \quad \frac{1}{2}\right)^{\mathsf{T}}$. We then treat the remaining part of the spin wave Hamiltonian as a perturbation, namely $\delta X^{(\hat{\boldsymbol{m}})}(\boldsymbol{q}) \equiv X^{(\hat{\boldsymbol{m}})}(\boldsymbol{q}) - X_0$. It is convenient to define dimensionless expectation values $G_n(\boldsymbol{q}, \hat{\boldsymbol{m}}) \equiv \langle E_0 | \left(J^{-1}\delta X^{(\hat{\boldsymbol{m}})}(\boldsymbol{q})\right)^n | E_0 \rangle$. The shift of the lowest energy branch

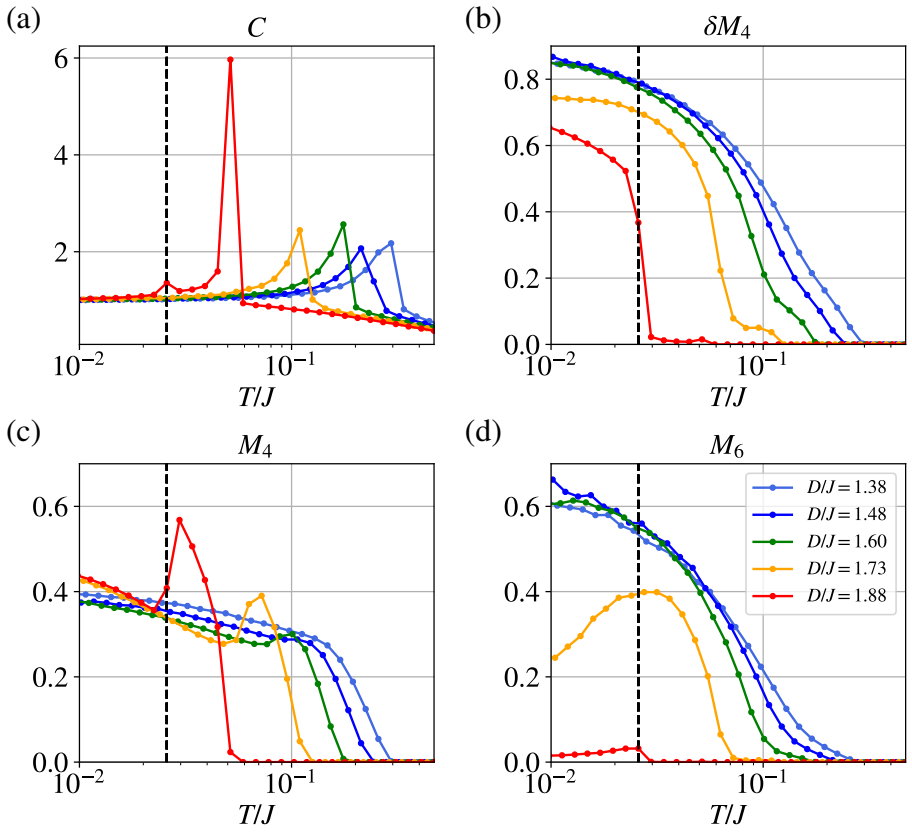


Figure 3.12: Temperature dependence of the specific heat (a), and the δM_4 (b), M_4 (c) and M_6 (d) cubic parameters for values of D/J in the vicinity of the Γ_5 boundary obtained from classical Monte Carlo calculations. The values of D/J considered are indicated in panel (d). In this figure, the vertical dashed line marks the position of the secondary peak in the specific heat for $D/J = 1.88$. The absence of a secondary peak in the specific heat for $D/J < 1.88$ is likely due to finite-size effects.

to 4^{th} order in perturbation theory is then given by the expression

$$E_{\boldsymbol{q}}^{(\hat{\boldsymbol{m}})}/J = G_1 + \frac{1}{8}\left(G_1^2 - G_2\right) + \frac{1}{64}\left(2G_1^3 - 3G_2G_1 + G_3\right) + \frac{1}{512}\left(5G_1^4 - 10G_2G_1^2 + 2G_2^2 + 4G_3G_1 - G_4\right). \tag{3.35}$$

The resulting dispersion is then expanded to 4^{th} order in the components of the wavevector about $\boldsymbol{q} = \mathbf{0}$, where the coefficient of the term $q_x^{n_x} q_y^{n_y} q_z^{n_z}$ is calculated as

$$\frac{1}{n_x! n_y! n_z!} \frac{\partial^{n_x+n_y+n_z} E_{\boldsymbol{q}}^{(\hat{\boldsymbol{m}})}}{\partial q_x^{n_x} \partial q_y^{n_y} \partial q_z^{n_z}}\bigg|_{\boldsymbol{q}=\mathbf{0}}. \tag{3.36}$$

This expansion can be written compactly as

$$E_{\boldsymbol{q}}^{(\hat{\boldsymbol{m}})} \approx \varepsilon_2(\boldsymbol{q}) + \varepsilon_4^{(\hat{\boldsymbol{m}})}(\boldsymbol{q}), \tag{3.37}$$

where

$$\varepsilon_2(\boldsymbol{q}) \equiv \frac{Ja^2}{8} |\boldsymbol{q}|^2 \tag{3.38}$$

is the part of the dispersion which is quadratic in the wave vector components, while $\varepsilon_4^{(\hat{\boldsymbol{m}})}(\boldsymbol{q})$ contains all of the quartic terms. There are no linear or cubic terms due to the inversion symmetry of the pyrochlore lattice, and there is no constant term (corresponding to a spin wave gap) because of the accidental degeneracy of the ground state. To write the expression for $\varepsilon_4^{(\hat{\boldsymbol{m}})}$ more compactly, we define $\eta_{\mu\nu} \equiv 1 - \delta_{\mu\nu}$, finding

$$\begin{aligned}\varepsilon_4^{(\hat{\boldsymbol{m}})}(\boldsymbol{q}) \equiv &- \frac{a^4}{2048} \sum_{\mu} A_{\mu}^{(\hat{\boldsymbol{m}})} q_{\mu}^4 - \frac{a^4}{4096} \sum_{\mu\nu} \eta_{\mu\nu} B_{\mu\nu}^{(\hat{\boldsymbol{m}})} q_{\mu}^2 q_{\nu}^2 \\ &+ \frac{3a^4 D^2}{1024J} \left(\hat{m}_x \hat{m}_y q_z + \hat{m}_z \hat{m}_x q_y + \hat{m}_y \hat{m}_z q_x\right) q_x q_y q_z \\ &+ \frac{a^4}{2048} \sum_{\mu\nu} \eta_{\mu\nu} C_{\mu\nu}^{(\hat{\boldsymbol{m}})} q_{\mu}^3 q_{\nu},\end{aligned} \tag{3.39}$$

with coefficients

$$A_{\mu}^{(\hat{\boldsymbol{m}})} \equiv \frac{D^4}{2J^3} \sum_{\nu} \eta_{\mu\nu} \hat{m}_{\nu}^2 \left[\frac{1}{2} \hat{m}_{\mu}^2 + \sum_{\lambda} \eta_{\mu\lambda} \eta_{\nu\lambda} \hat{m}_{\lambda}^2\right] + \frac{D^2}{J} \left(1 - \hat{m}_{\mu}^2\right) - \frac{4J}{3}, \tag{3.40}$$

$$B_{\mu\nu}^{(\hat{\boldsymbol{m}})} \equiv \frac{D^4}{J^3} \left(\hat{m}_{\mu}^4 + \hat{m}_{\nu}^4 + \frac{5}{2} \hat{m}_{\mu}^2 \hat{m}_{\nu}^2\right) + \frac{11D^2}{J} \left(\hat{m}_{\mu}^2 + \hat{m}_{\nu}^2 - \frac{2}{11}\right) + 8J, \tag{3.41}$$

$$C_{\mu\nu}^{(\hat{\boldsymbol{m}})} \equiv \left(\frac{D^4}{J^3} + \frac{6D^2}{J}\right) \hat{m}_{\mu} \hat{m}_{\nu}. \tag{3.42}$$

We now proceed to find the contribution of these quartic terms to the free energy, to lowest order in temperature. Assuming $T \ll J$, the dominant contribution to the free energy will come from

the spin wave modes in the vicinity of $\boldsymbol{q} = \boldsymbol{0}$. We therefore approximate the free energy as a functional of the quartic part of the dispersion

$$\mathcal{F}\left[g_4^{(\hat{\boldsymbol{m}})}(\boldsymbol{q})\right] = TV \int_{\mathbb{R}^3} \frac{\mathrm{d}^3 q}{(2\pi)^3} \ln\left(1 - e^{-\frac{JSa^2}{8T}|\boldsymbol{q}|^2} e^{-g_4^{(\hat{\boldsymbol{m}})}(\boldsymbol{q})}\right), \tag{3.43}$$

where $g_4^{(\hat{\boldsymbol{m}})}(\boldsymbol{q}) \equiv S\varepsilon_4^{(\hat{\boldsymbol{m}})}(\boldsymbol{q})/T$, and we assume that the integration bounds extend over all $\boldsymbol{q}$ space. At low temperature, the contribution of the quartic terms to the free energy becomes sub-dominant, and we can expand the functional to lowest order in $g_4^{(\hat{\boldsymbol{m}})}(\boldsymbol{q})$ about $g_4^{(\hat{\boldsymbol{m}})}(\boldsymbol{0}) = 0$ as [165]

$$\begin{aligned}\mathcal{F}\left[g_4^{(\hat{\boldsymbol{m}})}(\boldsymbol{q})\right] &\approx \mathcal{F}\left[g_4^{(\hat{\boldsymbol{m}})}(\boldsymbol{0})\right] + \int \mathrm{d}^3 q \left.\frac{\delta \mathcal{F}}{\delta g_4(\boldsymbol{q})}\right|_{g_4^{(\hat{\boldsymbol{m}})}(\boldsymbol{q}) = g_4^{(\hat{\boldsymbol{m}})}(\boldsymbol{0})} g_4^{(\hat{\boldsymbol{m}})}(\boldsymbol{q}) \\ &= TV \int \frac{\mathrm{d}^3 q}{(2\pi)^3} \ln\left(1 - e^{-\frac{JSa^2}{8T}|\boldsymbol{q}|^2}\right) + VS \int \frac{\mathrm{d}^3 q}{(2\pi)^3} \frac{\varepsilon_4^{(\hat{\boldsymbol{m}})}(\boldsymbol{q})}{e^{\frac{JSa^2}{8T}|\boldsymbol{q}|^2} - 1}.\end{aligned} \tag{3.44}$$

The first term in Eq. (3.44) simply corresponds to the free energy of an ideal Bose gas with a quadratic dispersion. This evaluates to

$$TV \int \frac{\mathrm{d}^3 q}{(2\pi)^3} \ln\left(1 - e^{-\frac{JSa^2}{8T}|\boldsymbol{q}|^2}\right) = -\frac{4JS\zeta\left(\frac{5}{2}\right)}{\pi^{3/2}} \left(\frac{T}{2JS}\right)^{5/2}, \tag{3.45}$$

giving the expected contribution proportional to $T^{5/2}$. Note that since the DM interaction does not enter the quadratic part of the dispersion at this order of perturbation theory, this contribution to the free energy does not couple to the magnetization direction $\hat{\boldsymbol{m}}$. The second integral in Eq. (3.44) evaluates to

$$\frac{3S\zeta\left(\frac{7}{2}\right)}{32\pi^{3/2}} \left[\left(\hat{m}_x^4 + \hat{m}_y^4 + \hat{m}_z^4 - \frac{7}{3}\right)\frac{D^4}{J^3} - \frac{44D^2}{3J} - 24J\right] \left(\frac{T}{2JS}\right)^{7/2}, \tag{3.46}$$

leading to the free energy contribution in Eq. (3.30), which is minimized for $\hat{\boldsymbol{m}} = \langle 111 \rangle$. A comparison of this perturbative calculation to the numerically integrated free energy in Eqs. (3.27) and (3.30) are shown in Fig. 3.13, where we see that the two calculations agree in the limit $T \to 0^+$ when $|D| \ll J$. Note that the next term in the free energy expansion is given by

$$\frac{1}{2!} \int \mathrm{d}^3 k \, \mathrm{d}^3 q \left.\frac{\delta^2 \mathcal{F}}{\delta g_4(\boldsymbol{k}) \delta g_4(\boldsymbol{q})}\right|_{g_4(\boldsymbol{k}) = g_4(\boldsymbol{q}) = g_4(\boldsymbol{0})} g_4(\boldsymbol{k}) g_4(\boldsymbol{q}), \tag{3.47}$$

and leads to a contribution proportional to $T^{9/2}$.

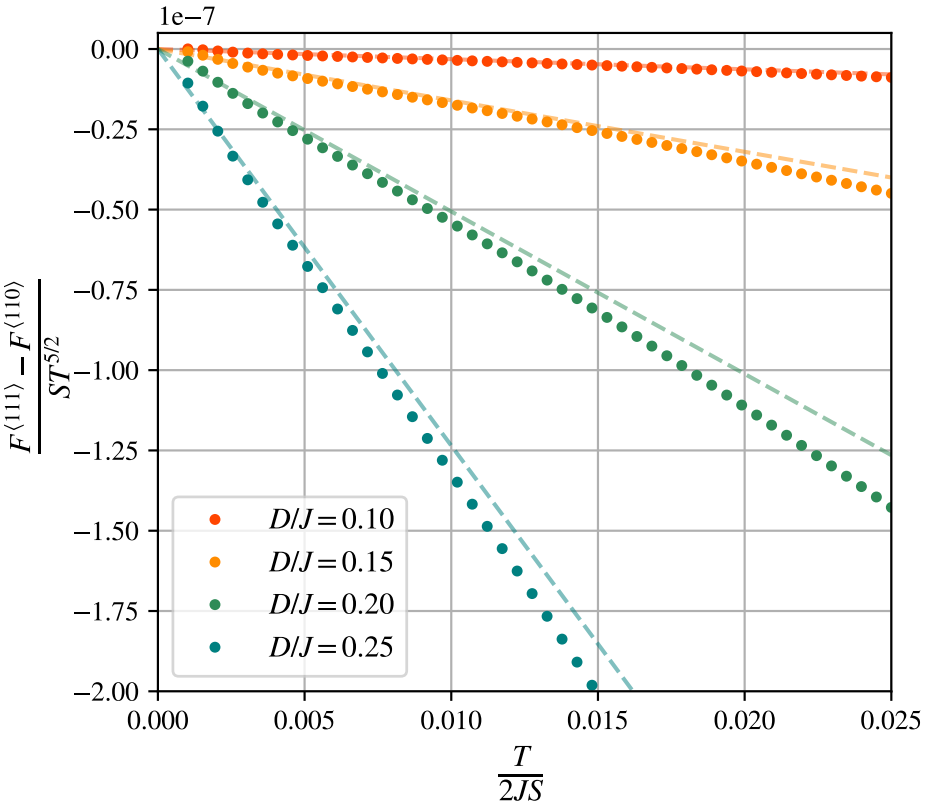


Figure 3.13: Free energy difference in linear spin wave theory between the $\hat{\boldsymbol{m}} = \langle 111\rangle$ and $\hat{\boldsymbol{m}} = \langle 110\rangle$ configurations. The negative slope $\left(\mathcal{F}^{\langle 111\rangle} - \mathcal{F}^{\langle 110\rangle}\right)/(ST^{5/2})$ indicates that the $\hat{\boldsymbol{m}} = \langle 111\rangle$ directions are selected. The points are obtained by numerically calculating Eq. (3.27), while the dashed lines are obtained from the perturbative calculation in Eq. (3.30) [or equivalently, Eq. (3.46)]. We see that both calculations agree in the limit $T \to 0^+$ when $|D| \ll J$.

3D Energy versus entropy as the mechanism for selection

Consider two distinct ferromagnetic configurations with ordering directions $\hat{\boldsymbol{m}}$ and $\hat{\boldsymbol{n}}$, the free energy difference between configurations can, in the absence of zero-point corrections, be decomposed as

$$\mathcal{F}^{(\hat{\boldsymbol{m}})} - \mathcal{F}^{(\hat{\boldsymbol{n}})} = \mathcal{E}^{(\hat{\boldsymbol{m}})} - \mathcal{E}^{(\hat{\boldsymbol{n}})} - T\left(\mathcal{S}^{(\hat{\boldsymbol{m}})} - \mathcal{S}^{(\hat{\boldsymbol{n}})}\right), \tag{3.48}$$

where $\mathcal{E}$ and $\mathcal{S}$ are the internal energy and entropy, respectively. In the classical case, the low-energy excitations are spin waves, arising from the two quadratic modes of fluctuation about each ordered magnetic moment. From the equipartition theorem, the energy is simply $\mathcal{E}^{(\hat{\boldsymbol{m}})} = 4NT$,

where N is the number of FCC unit cells, independent of the ordering direction. The low-temperature classical selection is thus dictated solely by the entropy, as depicted in Fig. 3.5.

In the quantum case, the low-energy excitations are magnons and their contribution to the energy in the linear spin-wave approximation is given by

$$\mathcal{E}^{(\hat{\boldsymbol{m}})} = \sum_{\mu,\boldsymbol{q}} \frac{S\omega_{\mu,\boldsymbol{q}}^{(\hat{\boldsymbol{m}})}}{\exp\left(\frac{S\omega_{\mu,\boldsymbol{q}}^{(\hat{\boldsymbol{m}})}}{T}\right) - 1}. \tag{3.49}$$

By computing Eq. (3.49) in conjunction with Eq. (3.27), we are able to separate the energy and entropy contributions to the free energy. These are depicted in Fig. 3.14, comparing the thermodynamic quantities for $\hat{\boldsymbol{m}}$ along $\langle 111\rangle$ and $\hat{\boldsymbol{n}}$ along $\langle 110\rangle$. We see from Fig. 3.14 that the free energy changes sign when $D/J > 1$, indicating a change in the ordering direction. Furthermore, we find the entropy difference changes sign at a *different* value of D/J, when compared to the free energy calculation. Therefore, in the quantum case, the low-temperature selection is no longer determined solely from the entropy contribution when $D > J$, in contrast to the classical calculation. That being said, it is worthwhile to note that this $D \gtrsim J$ region, where both the energy and entropy compete to select the magnetic order in linear spin wave theory, approximately coincides with the region in Fig. 3.9 where we find that the ferromagnetic order is unstable in non-linear spin wave theory. At this point, however, it is not clear to us if these two observations are related.

To gain some analytical insight into the relative contribution of the energy, $\mathcal{E}(T)$ and entropy, $\mathcal{S}(T)$, to the selection of the $\hat{\boldsymbol{m}}$ direction at low temperature, we may calculate the low-temperature contributions of both the energy and entropy in the framework of perturbation theory discussed in Appendix 3C when $|D| \ll J$, by following the same steps used to derive Eq. (3.44). The energy and entropy, to the lowest order that couple to the magnetization direction are

$$\begin{aligned}\mathcal{E}^{(\hat{\boldsymbol{m}})} \approx{}& \frac{6JS\zeta\left(\frac{5}{2}\right)}{\pi^{3/2}}\left(\frac{T}{2JS}\right)^{5/2} + \frac{15S\zeta\left(\frac{7}{2}\right)}{64\pi^{3/2}}\left(\frac{44D^2}{3J} + 8J\right)\left(\frac{T}{2JS}\right)^{7/2} \\ &+ \frac{15S\zeta\left(\frac{7}{2}\right)}{64\pi^{3/2}}\left[\frac{D^4}{J^3}\left(\frac{7}{3} - \hat{m}_x^4 - \hat{m}_y^4 - \hat{m}_z^4\right)\right]\left(\frac{T}{2JS}\right)^{7/2},\end{aligned} \tag{3.50}$$

$$\begin{aligned}T\mathcal{S}^{(\hat{\boldsymbol{m}})} \approx{}& \frac{10JS\zeta\left(\frac{5}{2}\right)}{\pi^{3/2}}\left(\frac{T}{2JS}\right)^{5/2} + \frac{21S\zeta\left(\frac{7}{2}\right)}{64\pi^{3/2}}\left(\frac{44D^2}{3J} + 8J\right)\left(\frac{T}{2JS}\right)^{7/2} \\ &+ \frac{21S\zeta\left(\frac{7}{2}\right)}{64\pi^{3/2}}\left[\frac{D^4}{J^3}\left(\frac{7}{3} - \hat{m}_x^4 - \hat{m}_y^4 - \hat{m}_z^4\right)\right]\left(\frac{T}{2JS}\right)^{7/2}.\end{aligned} \tag{3.51}$$

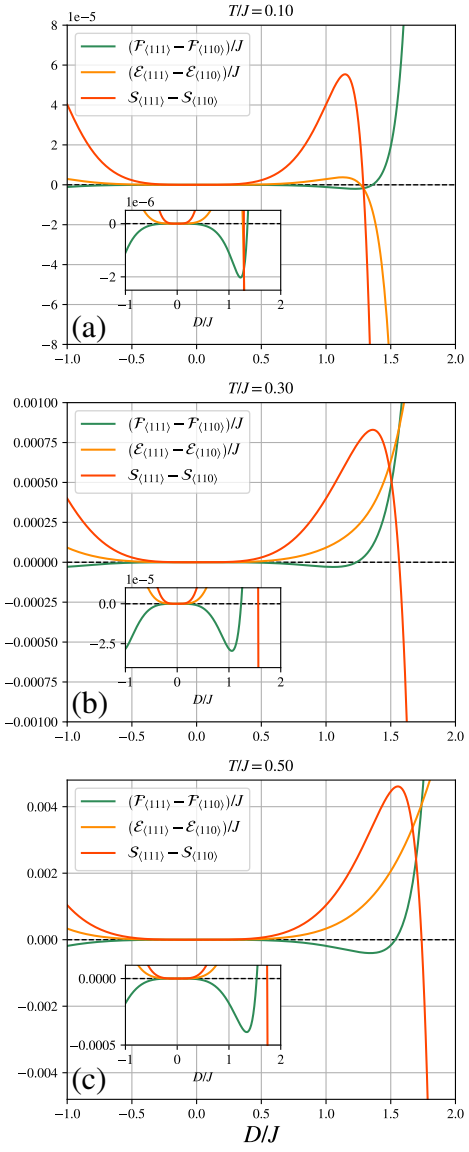


Figure 3.14: Quantum (linear) spin wave comparison of the thermodynamic free energy, energy, and entropy between the $\langle 111\rangle$ and $\langle 110\rangle$ configurations for (a) $T/J = 0.10$, (b) $T/J = 0.30$, and (c) $T/J = 0.50$. We find that the entropy difference (red curve) changes sign at a different value of D/J when compared with the free energy calculation (green curve), indicating that both energy and entropy play a role in the selection mechanism when $D > J$. The insets depict the same plots with a re-scaled vertical axis to clearly show the profile of the free energy curves.

In this limit, the energy term is *minimized* for $\hat{\boldsymbol{m}} = \langle 100 \rangle$, while the entropy term is *maximized* for $\hat{\boldsymbol{m}} = \langle 111 \rangle$ (note that all of the terms in Eqs. (3.50)-(3.51) are positive as the magnetization direction is normalized $|\hat{\boldsymbol{m}}| = 1$). The net contribution of these terms to the free energy $\mathcal{F}^{(\hat{\boldsymbol{m}})} = \mathcal{E}^{(\hat{\boldsymbol{m}})} - T\mathcal{S}^{(\hat{\boldsymbol{m}})}$ leads to Eq. (3.30). We see that the coefficient of the entropy term in (third line of Eq. (3.51)) is always larger in magnitude than the coefficient of the energy term (third line of Eq. (3.50)), implying that *entropy maximization* is the mechanism for the selection of the magnetization direction in the limit $T \to 0^+$ and $|D| \ll J$.

3E Magnetization direction in a field

Here, we generalize the perturbative calculation of the free energy to include an external magnetic field, while still expanding about an arbitrary polarized configuration $\hat{\boldsymbol{m}}$. One must take caution when carrying out this expansion as such a configuration is not necessarily metastable, and there will be terms that are linear in the bosonic operators appearing in the Holstein-Primakoff expansion. Assuming an external magnetic field $\boldsymbol{B}$, we include an additional Zeeman coupling to the Hamiltonian of the form

$$-\mu_{\mathrm{B}} g \sum_i \boldsymbol{B} \cdot \boldsymbol{S}_i, \tag{3.52}$$

where μ_{B} is the Bohr magneton and g is the g-factor of the magnetic ion, which we assume to be isotropic, which would be a reasonable approximation for a 3d transition metal such as V^{4+} in $Lu_2V_2O_7$ [15, 137, 142–145], for example. For convenience, we define the projection of the field onto the magnetization direction as $h_0^{(\hat{\boldsymbol{m}})} \equiv \mu_{\mathrm{B}} g \boldsymbol{B} \cdot \hat{\boldsymbol{m}}/S$ and the two orthogonal components $h_\pm^{(\hat{\boldsymbol{m}})} \equiv \mu_{\mathrm{B}} g \boldsymbol{B} \cdot \hat{\boldsymbol{e}}_\pm / S$, where $\boldsymbol{e}^\pm \equiv \hat{\boldsymbol{e}}_1 \pm i\hat{\boldsymbol{e}}_2$. The linear spin wave Hamiltonian is then found to be

$$\begin{aligned} H &= S^2 E_0 - \sqrt{N} S^{3/2} \sum_\mu \left[h_+^{(\hat{\boldsymbol{m}})} a_{\mu,\boldsymbol{0}}^\dagger + h_-^{(\hat{\boldsymbol{m}})} a_{\mu,\boldsymbol{0}} \right] \\ &\quad + S \sum_{\boldsymbol{q},\mu,\nu} \left(X_{\mu\nu}^{(\hat{\boldsymbol{m}})}(\boldsymbol{q}) + h_0^{(\hat{\boldsymbol{m}})} \delta_{\mu\nu} \right) a_{\mu,\boldsymbol{q}}^\dagger a_{\nu,\boldsymbol{q}} \qquad (3.53) \\ &= S^2 E_0 - 4NS^2 h_+^{(\hat{\boldsymbol{m}})} h_-^{(\hat{\boldsymbol{m}})} \langle E_0 | \left(X^{(\hat{\boldsymbol{m}})}(\boldsymbol{0}) + h_0^{(\hat{\boldsymbol{m}})} \mathbb{I} \right)^{-1} | E_0 \rangle \\ &\quad + S \sum_{\boldsymbol{q},\mu} \left(\omega_{\mu,\boldsymbol{q}}^{(\hat{\boldsymbol{m}})} + h_0^{(\hat{\boldsymbol{m}})} \right) b_{\mu,\boldsymbol{q}}^\dagger b_{\mu,\boldsymbol{q}}. \qquad (3.54) \end{aligned}$$

where the second equality comes from completing the square (involving the $a^\dagger$ and a operators), $X_{\mu\nu}^{(\hat{\boldsymbol{m}})}(\boldsymbol{q})$ is the linear spin wave Hamiltonian from Eq. (3.15) and $|E_0\rangle = \left(\frac{1}{2} \quad \frac{1}{2} \quad \frac{1}{2} \quad \frac{1}{2}\right)^{\mathsf{T}}$. We must now re-evaluate the free energy using the Hamiltonian in Eq. (3.54). Firstly, to evaluate the

expectation value, we decompose the matrices into the sum of Heisenberg and DM couplings, i.e. $X^{(\hat{\boldsymbol{m}})}(\mathbf{0}) + h_0^{(\hat{\boldsymbol{m}})}\mathbb{I} = \mathcal{M}_0^{(\hat{\boldsymbol{m}})} + \mathcal{M}_{\mathrm{DM}}^{(\hat{\boldsymbol{m}})}$, where

$$\left[\mathcal{M}_{\mathrm{DM}}^{(\hat{\boldsymbol{m}})}\right]_{\mu\nu} \equiv 2iD(1-\delta_{\mu\nu})\boldsymbol{d}_{\mu\nu}\cdot\hat{\boldsymbol{m}}, \tag{3.55}$$

and

$$\mathcal{M}_0^{(\hat{\boldsymbol{m}})} \equiv X^{(\hat{\boldsymbol{m}})}(\mathbf{0}) + h_0^{(\hat{\boldsymbol{m}})}\mathbb{I} - \mathcal{M}_{\mathrm{DM}}^{(\hat{\boldsymbol{m}})}. \tag{3.56}$$

We can then expand the matrix inverse that enters in Eq. (3.54) as

$$\left(X^{(\hat{\boldsymbol{m}})}(\mathbf{0}) + h_0^{(\hat{\boldsymbol{m}})}\mathbb{I}\right)^{-1} = \left[\mathcal{M}_0^{(\hat{\boldsymbol{m}})}\right]^{-1}\sum_{n=0}^{\infty}\left(-\mathcal{M}_{\mathrm{DM}}^{(\hat{\boldsymbol{m}})}\left[\mathcal{M}_0^{(\hat{\boldsymbol{m}})}\right]^{-1}\right)^n. \tag{3.57}$$

The spectral decomposition of the Heisenberg and field contributions is

$$\left[\mathcal{M}_0^{(\hat{\boldsymbol{m}})}\right]^{-1} = \frac{1}{h_0^{(\hat{\boldsymbol{m}})}}|E_0\rangle\langle E_0| + \frac{1}{8J + h_0^{(\hat{\boldsymbol{m}})}}\left(1 - |E_0\rangle\langle E_0|\right). \tag{3.58}$$

It is straightforward to check that $\mathcal{M}_{\mathrm{DM}}^{(\hat{\boldsymbol{m}})}\left[\mathcal{M}_0^{(\hat{\boldsymbol{m}})}\right]^{-1}|E_0\rangle = 0$, therefore

$$\langle E_0|\left(X^{(\hat{\boldsymbol{m}})}(\mathbf{0}) + h_0^{(\hat{\boldsymbol{m}})}\mathbb{I}\right)^{-1}|E_0\rangle = \frac{1}{h_0^{(\hat{\boldsymbol{m}})}}. \tag{3.59}$$

The low-temperature contribution to the free energy per unit cell is then calculated in the same way as described in Appendix 3C, thus obtaining

$$\begin{aligned}\mathcal{F}^{(\hat{\boldsymbol{m}})} \approx S^2\frac{E_0}{N} - 4S^2\frac{h_+^{(\hat{\boldsymbol{m}})}h_-^{(\hat{\boldsymbol{m}})}}{h_0^{(\hat{\boldsymbol{m}})}} + \frac{TV}{(2\pi)^3}\int \mathrm{d}^3k\ \ln\left(1 - e^{-\frac{JSa^2}{8T}|\boldsymbol{k}|^2 - \frac{S}{T}h_0^{(\hat{\boldsymbol{m}})}}\right)\\ + \frac{VS}{(2\pi)^3}\int \mathrm{d}^3k\ \frac{\varepsilon_4(\boldsymbol{k})}{e^{\frac{JSa^2}{8T}|\boldsymbol{k}|^2 + \frac{S}{T}h_0^{(\hat{\boldsymbol{m}})}} - 1}.\end{aligned} \tag{3.60}$$

Evaluating the integrals in Eq. (3.60), we obtain an expression for the free energy to order $\left(\frac{D}{J}\right)^4\left(\frac{T}{J}\right)^{7/2}$

$$\begin{aligned}\mathcal{F}^{(\hat{\boldsymbol{m}})} \approx -2\mu_{\mathrm{B}}gS\left(\frac{|\boldsymbol{B}|^2 + (\boldsymbol{B}\cdot\hat{\boldsymbol{m}})^2}{\boldsymbol{B}\cdot\hat{\boldsymbol{m}}}\right) - \frac{4JS}{\pi^{3/2}}\left(\frac{T}{2JS}\right)^{5/2}\mathrm{Li}_{\frac{5}{2}}\left(e^{-\frac{\mu_{\mathrm{B}}g}{T}\boldsymbol{B}\cdot\hat{\boldsymbol{m}}}\right)\\ + \frac{3S}{32\pi^{3/2}}\left[\frac{D^4}{J^3}\left(\hat{m}_x^4 + \hat{m}_y^4 + \hat{m}_z^4 - \frac{7}{3}\right) - \frac{44D^2}{3J} - 24J\right]\left(\frac{T}{2JS}\right)^{7/2}\mathrm{Li}_{\frac{7}{2}}\left(e^{-\frac{\mu_{\mathrm{B}}g}{T}\boldsymbol{B}\cdot\hat{\boldsymbol{m}}}\right).\end{aligned} \tag{3.61}$$

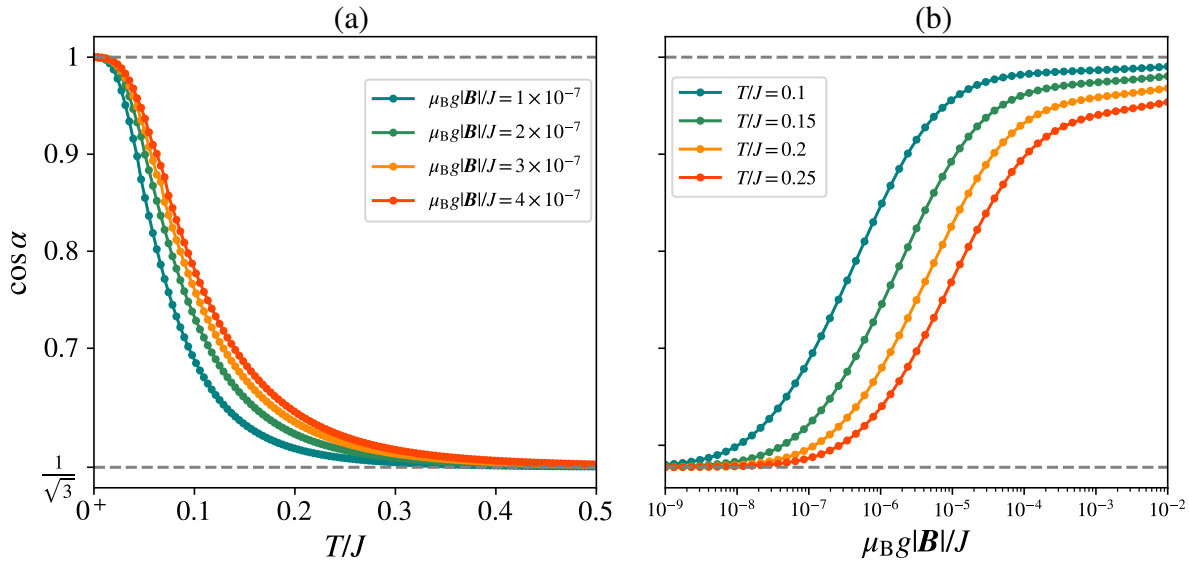


Figure 3.15: Magnetization direction as a function of (a) temperature and (b) magnetic field magnitude obtained by minimizing Eq. (3.61) for $D/J = 0.5$ and $\boldsymbol{B}$ oriented along the $\langle 100\rangle$ directions. Here, α is the angle between the external field and the magnetization direction $\boldsymbol{B}\cdot\hat{\boldsymbol{m}} = |\boldsymbol{B}|\cos\alpha$, such that $\cos\alpha = 1$ corresponds to $\hat{\boldsymbol{m}} = \langle 100\rangle$ and $\cos\alpha = 1/\sqrt{3}$ corresponds to $\hat{\boldsymbol{m}} = \langle 111\rangle$.

where $\mathrm{Li}_\alpha(z) \equiv \sum_{n=1}^{\infty} n^{-\alpha} z^n$ is the polylogarithm. We may then minimize Eq. (3.61) with respect to the $\hat{\boldsymbol{m}}$ to find the magnetization direction at finite temperature. The results of this minimization procedure are depicted in Fig. 3.15 for an external magnetic field oriented along the [100] direction. At finite temperature, we observe a crossover between magnetization oriented along the $\langle 111\rangle$ directions, favoured by thermal fluctuations, to the $\langle 100\rangle$ directions as the magnetic field is increased (see Fig. 3.15(b)). This change in the magnetization direction is induced by a very weak magnetic field. For illustration purposes, taking for example $D/J = 0.5$ and $T/J = 0.15$, the magnetization changes direction for a magnitude $\left(\mu_B g|\boldsymbol{B}|/J \sim 10^{-6}\right)$. Using a ferromagnetic exchange $J \sim 8$ meV and g-factor $g \sim 2$ (as in $Lu_2V_2O_7$ [137, 145]), this would correspond to a magnetic field of magnitude $|\boldsymbol{B}| \sim 70\,\mu$T at a temperature $T \sim 14$ K. This reflects the weakness of thermal order by disorder of the quantum model against the energetic perturbation (here the magnetic Zeeman energy), at least for this $D/J = 0.5$ value, which is already quite large considering a system such as $Lu_2V_2O_7$ [15, 137, 142–145].

3F Calculation of the magnon self-energy

In this appendix, we explicitly derive the expression for the magnon self-energy to $O(S^0)$ using the imaginary-time Green's function formalism. The three and four-magnon interaction vertices in Eqs. (3.19)-(3.20) are given by

$$Y^{(\hat{\boldsymbol{m}})}_{\mu\nu\lambda}(\boldsymbol{k},\boldsymbol{q}) = i\sqrt{2}D\boldsymbol{d}_{\mu\nu}\cdot\boldsymbol{e}^{-}\left(\delta_{\nu\lambda}\cos\big(\boldsymbol{k}\cdot\boldsymbol{r}_{\mu\nu}\big)-\delta_{\mu\lambda}\cos\big(\boldsymbol{q}\cdot\boldsymbol{r}_{\mu\nu}\big)\right), \tag{3.62}$$

$$\begin{aligned} V^{(\hat{\boldsymbol{m}})}_{\mu\nu\lambda\rho}(\boldsymbol{k},\boldsymbol{q},\boldsymbol{q}) = {} & -2J(1-\delta_{\mu\nu})\Big[\delta_{\mu\rho}\delta_{\nu\lambda}\cos\big(\boldsymbol{q}\cdot\boldsymbol{r}_{\mu\nu}\big) \\ & \quad +\delta_{\mu\lambda}\delta_{\nu\rho}\cos\big((\boldsymbol{k}-\boldsymbol{q}+\boldsymbol{q})\cdot\boldsymbol{r}_{\mu\nu}\big)\Big] \\ & +(J-iD\boldsymbol{d}_{\mu\nu}\cdot\hat{\boldsymbol{m}})(1-\delta_{\mu\rho})\Big[\delta_{\mu\nu}\delta_{\mu\lambda}\cos\big(\boldsymbol{k}\cdot\boldsymbol{r}_{\mu\rho}\big) \\ & \quad +\delta_{\lambda\rho}\delta_{\lambda\nu}\cos\big((\boldsymbol{k}+\boldsymbol{q})\cdot\boldsymbol{r}_{\mu\rho}\big)\Big] \\ & +(J-iD\boldsymbol{d}_{\nu\lambda}\cdot\hat{\boldsymbol{m}})(1-\delta_{\nu\lambda})\Big[\delta_{\mu\nu}\delta_{\mu\rho}\cos(\boldsymbol{q}\cdot\boldsymbol{r}_{\nu\lambda}) \\ & \quad +\delta_{\mu\lambda}\delta_{\mu\rho}\cos((\boldsymbol{q}-\boldsymbol{q})\cdot\boldsymbol{r}_{\nu\lambda})\Big], \end{aligned} \tag{3.63}$$

where $\boldsymbol{e}^{-}\equiv\hat{\boldsymbol{e}}_1-i\hat{\boldsymbol{e}}_2$.

We calculate the self-energy to $O(S^0)$ by evaluating the diagrams depicted in Fig. 3.2 in the imaginary time formalism at finite temperature $T=1/\beta$, and subsequently extrapolate to zero temperature ($\beta\to\infty$). First, we express the interactions in terms of the operators $a_{\boldsymbol{q},\mu}=\sum_\nu U^{(\hat{\boldsymbol{m}})}_{\mu,\nu}(\boldsymbol{q})b_{\boldsymbol{q},\nu}$ that diagonalize the linear spin wave theory. Equations (3.19)-(3.20) then become

$$\mathcal{H}^{(\hat{\boldsymbol{m}})}_3=\frac{1}{2!\sqrt{N}}\sum_{\boldsymbol{k}\boldsymbol{q}}\sum_{\mu\nu\lambda}\left[T^{(\hat{\boldsymbol{m}})}_{\mu\nu\lambda}(\boldsymbol{k},\boldsymbol{q})b^\dagger_{\boldsymbol{k},\mu}b^\dagger_{\boldsymbol{q},\nu}b_{\boldsymbol{k}+\boldsymbol{q},\lambda}+\text{H.c.}\right] \tag{3.64}$$

and

$$\mathcal{H}^{(\hat{\boldsymbol{m}})}_4=\frac{1}{N(2!)^2}\sum_{\boldsymbol{k}\boldsymbol{q}\boldsymbol{q}}\sum_{\mu\nu\lambda\rho}W^{(\hat{\boldsymbol{m}})}_{\mu\nu\lambda\rho}(\boldsymbol{k},\boldsymbol{q},\boldsymbol{q})b^\dagger_{\boldsymbol{k}+\boldsymbol{q},\mu}b^\dagger_{\boldsymbol{q}-\boldsymbol{q},\nu}b_{\boldsymbol{q},\lambda}b_{\boldsymbol{k},\rho}, \tag{3.65}$$

with the interaction vertices expressed in the energy basis (i.e. involving the b and $b^\dagger$ operators) defined as

$$T^{(\hat{\boldsymbol{m}})}_{\mu\nu\lambda}(\boldsymbol{k},\boldsymbol{q})=\sum_{\alpha\beta\gamma}\overline{U}^{(\hat{\boldsymbol{m}})}_{\alpha\mu}(\boldsymbol{k})\overline{U}^{(\hat{\boldsymbol{m}})}_{\beta\nu}(\boldsymbol{q})U^{(\hat{\boldsymbol{m}})}_{\gamma\lambda}(\boldsymbol{k}+\boldsymbol{q})Y^{(\hat{\boldsymbol{m}})}_{\alpha\beta\gamma}(\boldsymbol{k},\boldsymbol{q}), \tag{3.66}$$

and

$$W^{(\hat{\boldsymbol{m}})}_{\mu\nu\lambda\rho}(\boldsymbol{k},\boldsymbol{q},\boldsymbol{q}) = \sum_{\alpha\beta\gamma\sigma}\Bigg[\overline{U}^{(\hat{\boldsymbol{m}})}_{\alpha\mu}(\boldsymbol{k}+\boldsymbol{q})\overline{U}^{(\hat{\boldsymbol{m}})}_{\beta\nu}(\boldsymbol{q}-\boldsymbol{q}) \times U^{(\hat{\boldsymbol{m}})}_{\gamma\lambda}(\boldsymbol{q})U^{(\hat{\boldsymbol{m}})}_{\sigma\rho}(\boldsymbol{k})V^{(\hat{\boldsymbol{m}})}_{\alpha\beta\gamma\sigma}(\boldsymbol{k},\boldsymbol{q},\boldsymbol{q})\Bigg]. \tag{3.67}$$

The bare imaginary-time Green's function in the energy basis is given by

$$\mathcal{G}^{(\hat{\boldsymbol{m}})}_{\lambda\rho}(\boldsymbol{k},i\omega) = \frac{\delta_{\lambda\rho}}{-i\omega + S\omega^{(\hat{\boldsymbol{m}})}_{\lambda,\boldsymbol{k}}}. \tag{3.68}$$

We decompose the imaginary-time self-energy into the sum of each of the diagram contributions in Fig. 3.2 as $\Sigma^{(\hat{\boldsymbol{m}})} = \Sigma^a + \Sigma^b + \Sigma^c$. In order of appearance in Fig. 3.2, the diagrams are evaluated as

$$\begin{aligned}
\Sigma^a_{\mu\nu}(\boldsymbol{k},i\omega) = &-\frac{S}{2N\beta}\sum_{\boldsymbol{q},n}\sum_{\lambda\rho}\Bigg[T^{(\hat{\boldsymbol{m}})}_{\lambda\rho\mu}(\boldsymbol{q},\boldsymbol{k}-\boldsymbol{q})\overline{T}^{(\hat{\boldsymbol{m}})}_{\lambda\rho\nu}(\boldsymbol{q},\boldsymbol{k}-\boldsymbol{q}) \\
&\times \mathcal{G}^{(\hat{\boldsymbol{m}})}_{\lambda\lambda}(\boldsymbol{q},i\Omega_n)\mathcal{G}^{(\hat{\boldsymbol{m}})}_{\rho\rho}(\boldsymbol{k}-\boldsymbol{q},i\omega-i\Omega_n)\Bigg] \\
&-\frac{S}{N\beta}\sum_{\boldsymbol{q},n}\sum_{\lambda\rho}\Bigg[T^{(\hat{\boldsymbol{m}})}_{\nu\rho\lambda}(\boldsymbol{k},\boldsymbol{q}-\boldsymbol{k})\overline{T}^{(\hat{\boldsymbol{m}})}_{\mu\rho\lambda}(\boldsymbol{k},\boldsymbol{q}-\boldsymbol{k}) \\
&\times \mathcal{G}^{(\hat{\boldsymbol{m}})}_{\lambda\lambda}(\boldsymbol{q},i\Omega_n)\mathcal{G}^{(\hat{\boldsymbol{m}})}_{\rho\rho}(\boldsymbol{q}-\boldsymbol{k},i\Omega_n-i\omega)\Bigg],
\end{aligned} \tag{3.69}$$

$$\begin{aligned}
\Sigma^b_{\mu\nu}(\boldsymbol{k},i\omega) = &-\frac{S}{N\beta}\sum_{\boldsymbol{q},n}\sum_{\lambda\rho}\mathcal{G}^{(\hat{\boldsymbol{m}})}_{\lambda\lambda}(\boldsymbol{0},i0)\mathcal{G}^{(\hat{\boldsymbol{m}})}_{\rho\rho}(\boldsymbol{q},i\Omega_n) \\
&\times\left[T^{(\hat{\boldsymbol{m}})}_{\nu\lambda\mu}(\boldsymbol{k},\boldsymbol{0})\overline{T}^{(\hat{\boldsymbol{m}})}_{\rho\lambda\rho}(\boldsymbol{q},\boldsymbol{0}) + \overline{T}^{(\hat{\boldsymbol{m}})}_{\mu\lambda\nu}(\boldsymbol{k},\boldsymbol{0})T^{(\hat{\boldsymbol{m}})}_{\rho\lambda\rho}(\boldsymbol{q},\boldsymbol{0})\right],
\end{aligned} \tag{3.70}$$

$$\Sigma^c_{\mu\nu}(\boldsymbol{k},i\omega) = \frac{S}{N\beta}\sum_{\boldsymbol{q},n}\sum_{\lambda}W^{(\hat{\boldsymbol{m}})}_{\nu\lambda\lambda\mu}(\boldsymbol{k},\boldsymbol{q},\boldsymbol{0})\mathcal{G}^{(\hat{\boldsymbol{m}})}_{\lambda\lambda}(\boldsymbol{q},i\Omega_n), \tag{3.71}$$

where $\Omega_n = 2\pi n/\beta$ are the bosonic Matsubara frequencies. We can then evaluate each of the frequency summations and subsequently take the $\beta\to\infty$ limit as

$$\frac{1}{\beta}\sum_n \mathcal{G}^{(\hat{\boldsymbol{m}})}_{\lambda\lambda}(\boldsymbol{q},i\Omega_n) = n_{\mathrm{B}}\left(S\omega^{(\hat{\boldsymbol{m}})}_{\lambda,\boldsymbol{q}}\right)\xrightarrow{\beta\to\infty}0, \tag{3.72}$$

which enters in Eqs. (3.70) and (3.71). We also have

$$\frac{1}{\beta}\sum_n \mathcal{G}^{(\hat{\boldsymbol{m}})}_{\lambda\lambda}(\boldsymbol{q}, i\Omega_n)\mathcal{G}^{(\hat{\boldsymbol{m}})}_{\rho\rho}(\boldsymbol{q}-\boldsymbol{k}, i\Omega_n - i\omega) = \frac{n_{\mathrm{B}}\left(S\omega^{(\hat{\boldsymbol{m}})}_{\lambda,\boldsymbol{q}}\right) - n_{\mathrm{B}}\left(S\omega^{(\hat{\boldsymbol{m}})}_{\rho,\boldsymbol{q}-\boldsymbol{k}}\right)}{i\omega - S\omega^{(\hat{\boldsymbol{m}})}_{\rho,\boldsymbol{q}} + S\omega^{(\hat{\boldsymbol{m}})}_{\lambda,\boldsymbol{q}-\boldsymbol{k}}} \xrightarrow{\beta\to\infty} 0, \tag{3.73}$$

which enters in Eq. (3.69), along with

$$\begin{aligned}\frac{1}{\beta}\sum_n \mathcal{G}^{(\hat{\boldsymbol{m}})}_{\lambda\lambda}(\boldsymbol{q}, i\Omega_n)\mathcal{G}^{(\hat{\boldsymbol{m}})}_{\rho\rho}(\boldsymbol{k}-\boldsymbol{q}, i\omega - i\Omega_n) &= \frac{n_{\mathrm{B}}\left(S\omega^{(\hat{\boldsymbol{m}})}_{\lambda,\boldsymbol{q}}\right) - n_{\mathrm{B}}\left(-S\omega^{(\hat{\boldsymbol{m}})}_{\rho,\boldsymbol{k}-\boldsymbol{q}}\right)}{-i\omega + S\omega^{(\hat{\boldsymbol{m}})}_{\rho,\boldsymbol{q}} + S\omega^{(\hat{\boldsymbol{m}})}_{\lambda,\boldsymbol{k}-\boldsymbol{q}}} \\ &\xrightarrow{\beta\to\infty} \frac{1}{-i\omega + S\omega^{(\hat{\boldsymbol{m}})}_{\rho,\boldsymbol{q}} + S\omega^{(\hat{\boldsymbol{m}})}_{\lambda,\boldsymbol{k}-\boldsymbol{q}}},\end{aligned} \tag{3.74}$$

where $n_{\mathrm{B}}(z) \equiv \left(e^{\beta z}-1\right)^{-1}$ is the Bose distribution function. It thus finally follows that $\Sigma^b = \Sigma^c = 0$, and

$$\Sigma^a_{\mu\nu}(\boldsymbol{k}, i\omega) = \frac{S}{2N}\sum_{\boldsymbol{q}}\sum_{\lambda\rho}\frac{T^{(\hat{\boldsymbol{m}})}_{\lambda\rho\mu}(\boldsymbol{q}, \boldsymbol{k}-\boldsymbol{q})\overline{T}^{(\hat{\boldsymbol{m}})}_{\lambda\rho\nu}(\boldsymbol{q}, \boldsymbol{k}-\boldsymbol{q})}{i\omega - S\omega^{(\hat{\boldsymbol{m}})}_{\lambda,\boldsymbol{k}-\boldsymbol{q}} - S\omega^{(\hat{\boldsymbol{m}})}_{\rho,\boldsymbol{q}}}. \tag{3.75}$$

The retarded self-energy is then obtained by analytic continuation, which, making the substitution $i\omega \to \omega + i0^+$, leads to Eq. (3.23). The instability discussed in Sec. 3.4.4 then corresponds to a pole at $\omega < 0$ of the single-magnon Green's function (Eq. (3.22), with $S = \frac{1}{2}$) to $O(S^0)$.

Chapter 4

Fluctuation-induced gaps in quantum magnets

4.0 Preface

Identifying order-by-disorder (ObD) in real materials has been a long-standing open problem in the field of frustrated magnetism. Indeed, there is no universally accepted experimental signature of order-by-disorder that does not rely on quantitatively fitting experimental data to extract model exchange interactions, and subsequently checking theoretically that said model exhibits ObD [58].

The most direct experimental probe comes from inelastic neutron scattering (INS) experiments, which effectively provide an observation of the spin-wave excitation spectrum. In this case, ObD manifests as a very small gap in the spectrum, known as a pseudo-Goldstone (PG) mode. The PG is nearly gapless due to the underlying classical degeneracy, but acquires a small gap when the degeneracy is lifted by fluctuations. Two recent papers have characterized the formation of the fluctuation-induced PG gap in both the zero-temperature quantum [101] and finite-temperature classical [58] limits. Notably in Ref. [58], it was proposed that thermal ObD manifests as a PG gap that increases with temperature. This begs the question of whether an analogous statement holds in the low-temperature quantum regime.

So far, there is a small number of real materials for which there is evidence for ObD operating [118–126]. Perhaps the most compelling candidate material for ObD is the pyrochlore antiferromagnet $Er_2Ti_2O_7$ [97, 98, 114–117] because (a) theoretical calculations using the exchange parameters of "best-fit" predict that ObD is operating [97, 98] and (b) there is a small gap observed

in the INS spectrum [114, 116]. A small spectral gap certainly does not imply that ObD must be at play, as such a gap could in principle arise as a "trivial" energetic gap due to interactions not accounted for in the model at hand. It is therefore of great interest to characterize the finite temperature properties of the PG gap, which serves as the motivating principle for this chapter.

In the manuscript contained in this chapter, it is argued that the PG gap obeys a universal characteristic temperature-dependence, which increases with temperature, and can be used as an unambiguous experimental signature of ObD in quantum magnets. This temperature dependence opposes what one would expect for a typical energetic gap, where the effect of thermal fluctuations is to decrease the gap (the interested reader is referred to Appendix B for an example of this statement). In addition, it is shown that said gap can be computed within the framework of linear spin wave theory alone, greatly simplifying the otherwise tedious finite-temperature quantum many-body calculation.

arXiv:2505.18253 [cond-mat.str-el]

Universal temperature-dependent power law excitation gaps in frustrated quantum spin systems harbouring order-by-disorder

Alexander Hickey,[1] Jeffrey G. Rau,[2] Subhankar Khatua,[1, 2, 3] and Michel J. P. Gingras[1, 4]

[1]*Department of Physics and Astronomy, University of Waterloo, Waterloo, Ontario N2L 3G1, Canada*
[2]*Department of Physics, University of Windsor, 401 Sunset Avenue, Windsor, Ontario, N9B 3P4, Canada*
[3]*Institute for Theoretical Solid State Physics, IFW Dresden and Würzburg-Dresden Cluster of Excellence ct.qmat, Helmholtzstr. 20, 01069 Dresden, Germany*
[4]*Waterloo Institute for Nanotechnology, Department of Physics and Astronomy, University of Waterloo, Waterloo, Ontario, N2L 3G1, Canada*

In frustrated magnetic systems with competing interactions, classical ground states often exhibit continuous degeneracies that are not protected by any symmetry of the spin Hamiltonian. These accidental degeneracies are typically lifted by thermal and quantum fluctuations through a mechanism known as order-by-disorder (ObD). A leading proposal for detecting and characterizing ObD in real materials – distinguishing it from standard energetic selection – is to measure the small fluctuation-induced pseudo-Goldstone (PG) gap Δ in the excitation spectrum. While the properties of Δ have been understood to leading order in magnon-magnon interactions at zero temperature and in the classical limit at nonzero temperature, the temperature dependence $\Delta(T)$ in quantum magnets remains largely unexplored. In this work, we compute $\Delta(T)$ at low temperatures to leading order in a $1/S$ expansion, using non-linear spin-wave theory for a variety of frustrated quantum spin systems. To support and generalize these results, we develop a complementary formalism that allows one to compute $\Delta(T)$ using only linear spin-wave theory, thus circumventing the need for cumbersome many-body calculations. We find that, at leading order in $1/S$, $\Delta(T)$ exhibits a distinct power-law temperature dependence, scaling as either T^{d+1} or $T^{d/2+1}$ depending on whether the PG mode is linearly or quadratically gapless at the harmonic level, respectively. Finally, we discuss the implications of our results for the pyrochlore compound $Er_2Ti_2O_7$ where experimental evidence strongly supports an ObD scenario.

4.1 Introduction

In systems of interacting degrees of freedom, both thermal and quantum fluctuations *generally* act to destabilize long-range order. In certain condensed matter systems, these fluctuations can be so pronounced that they completely suppress order even at absolute zero temperature. A striking

example is liquid helium, which avoids freezing into a crystalline solid at atmospheric pressure due to strong quantum zero-point fluctuations [166]. Within the field of magnetism, the quest for spin liquids—phases that lack long-range magnetic order down to the lowest temperatures—has long been a central pursuit. One prominent setting for this search considers highly frustrated magnetic systems in which competing spin-spin interactions produce an exponentially large number of classically degenerate ground states [55, 64]. This large degeneracy can then prevent magnetic ordering down to absolute zero temperature, even in three-dimensional systems, thereby realizing a classical spin liquid [55, 127, 167]. Such a classical perspective has inspired extensive theoretical and experimental efforts to uncover their quantum counterparts – quantum spin liquids [22, 54, 67–69].

An intriguing intermediate situation between energetically stabilized long-range magnetic order and fluctuation-driven spin-liquid behaviour occurs in certain frustrated spin models whose manifold of classical ground states grows only sub-exponentially with system size. In these systems, the degeneracies are accidental and not protected by any global symmetry of the spin Hamiltonian, but instead arise from the specific form of the spin-spin interactions.[28] Although no unique ground state (modulo global symmetries) is energetically preferred at the classical level, thermal or quantum fluctuations can lift this degeneracy, selecting a subset of configurations from the manifold and thereby stabilizing long-range magnetic order. This celebrated phenomenon, known as order-by-disorder (ObD) [10, 56, 71], is a conceptual cornerstone of frustrated magnetism.

While order-by-disorder driven by thermal or quantum fluctuations has been firmly established in numerous theoretical models of frustrated spin systems [1, 10, 56, 59, 62, 63, 70–74, 76, 79–81, 83–102, 104, 105, 168–170], a long-standing question is whether ObD is actually realized in real magnetic materials and, if so, what experimental signatures could unambiguously reveal its role in stabilizing the observed long-range order. The conventional route to identifying ObD experimentally is largely indirect: one first constructs a theoretical model of the material, demonstrates ObD within that framework, and then verifies as many of the model's predictions as possible against measured material properties [97, 114, 118–121]. This strategy faces two important limitations. First, it poses substantial methodological challenges: establishing quantitative agreement between theory and experiment in an ObD regime often demands intricate, high-order quantum many-body perturbation theory calculations. Second, even when successful, such an approach offers only an indirect confirmation. It leaves open the question of whether there exists more direct, and perhaps fundamental, experimental signatures of ObD – ones that do not depend on a lengthy "back-and-forth dialogue" between theory and the fitting of extensive experimental datasets.

[28] Note that the existence of an accidental degeneracy by no means implies this intermediate scenario.

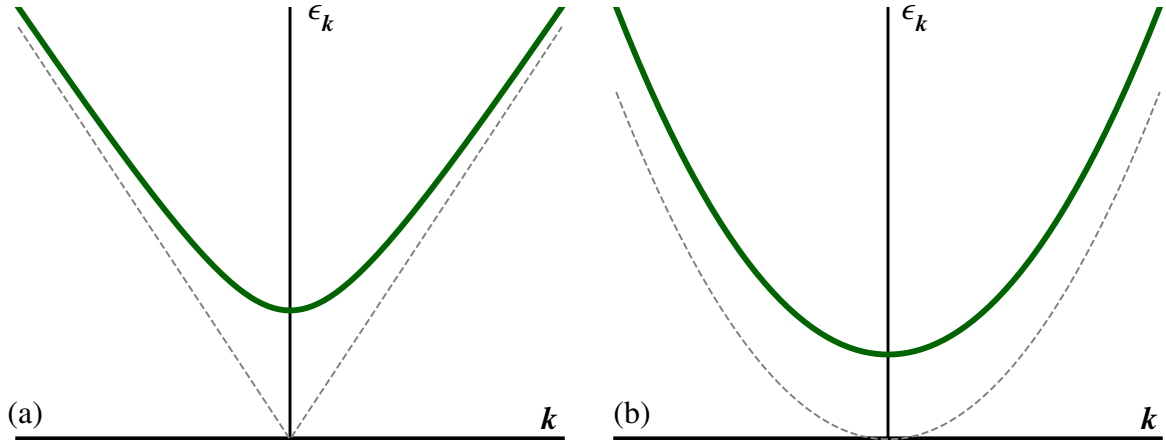


Figure 4.1: Schematic picture depicting the spectrum of a pseudo-Goldstone mode for (a) type I with a linearly dispersing mode, $\epsilon = v|\boldsymbol{k}|$, and (b) type II with a quadratically dispersing mode, $\epsilon = v|\boldsymbol{k}|^2$. In both cases, the mode acquires a gap Δ via the order-by-disorder (ObD) mechanism, modifying the dispersion. Quantum fluctuations at zero temperature ($T = 0$) generates a gap Δ_0 (quantum ObD), which then *increases* with T as a power-law, T^{d+1} and $T^{d/2+1}$, for type I and type II modes, respectively.

Two recent developments [58, 101] have begun addressing the challenges outlined above by considering the formation of an ObD-induced energy gap Δ in the otherwise gapless pseudo-Goldstone (PG) modes (i.e., spin-wave excitations) predicted at the harmonic level (see Fig. 4.1). The first development is the realization that, given the Hamiltonian of a quantum spin-S system, the curvatures of the classical plus quantum zero-point energies, expressed in terms of deviations of the spin operators and computed at $O(S)$, are sufficient to determine the PG zero-temperature gap, Δ_0, *exactly* to $O(S^0)$, without resorting to involved self-energy calculations from magnon-magnon interactions [101]. The second development is the observation that frustrated *classical* spin systems, which exhibit thermal but not quantum ObD, acquire a temperature-dependent PG gap from magnon interactions that scales as $\Delta(T) \propto T^{\mu}$ with $\mu = \frac{1}{2}$ ($\mu = 1$) for linearly dispersing (quadratically dispersing) PG modes [58]. These results naturally raise two important follow-up questions:

1. What is the expected temperature dependence of the PG gap in a *quantum treatment* of spin models with linearly or quadratically dispersing PG modes? – an issue of critical relevance for real materials where a classical description breaks down at low-temperature [58].

2. Can a temperature dependence of the PG gap for a quantum model be computed by extending the "curvature framework" of Ref. [101] – replacing the zero-temperature energy curvatures with those of the free-energy density and using only linear spin-wave theory?

In this work, we answer the second question in the affirmative and, in regard to the first question, find that the above exponent μ becomes $d+1$ (for a linearly dispersing PG mode, $\epsilon_{\boldsymbol{k}} \propto |\boldsymbol{k}|$) and $\frac{d}{2}+1$ (for a quadratically dispersing PG mode, $\epsilon_{\boldsymbol{k}} \propto |\boldsymbol{k}|^2$), respectively (see Fig. 4.1). In short, we identify a strongly compelling experimental signature of ObD in the form of two universal types of temperature-dependent ObD-generated PG gaps $\Delta(T)$, and which can be computed in a way that avoids the complexities of finite-temperature quantum many-body calculations.

4.2 Spin-wave theory

We begin by first using the standard spin-wave theory formalism to investigate the temperature dependence of the fluctuation-induced gap. Spin operators are mapped to Holstein-Primakoff bosons [35, 171] and subsequently expanded in powers of $1/S$, where S is the spin quantum number.[29] Substituting this expansion into the Hamiltonian and keeping only the bilinear terms gives the linear spin-wave Hamiltonian

$$H_2 = S \sum_{\boldsymbol{k}} \sum_{\alpha\alpha'} \left[A_{\boldsymbol{k}}^{\alpha\alpha'} a_{\boldsymbol{k},\alpha}^\dagger a_{\boldsymbol{k},\alpha'} + \frac{1}{2} \left(B_{\boldsymbol{k}}^{\alpha\alpha'} a_{\boldsymbol{k},\alpha}^\dagger a_{-\boldsymbol{k},\alpha'}^\dagger + \text{H.c.} \right) \right]. \tag{4.1}$$

Here, $a_{\boldsymbol{k},\alpha}$ is a Holstein-Primakoff boson with wavevector $\boldsymbol{k}$ on sublattice α of the magnetic unit cell, and the coefficients $A_{\boldsymbol{k}}^{\alpha\alpha'}$ and $B_{\boldsymbol{k}}^{\alpha\alpha'}$ depend on both the magnetic exchange interactions and the specific classical ground state configuration(s) considered [171].[29] The quasiparticle dispersion is then determined by the eigenvalues of the (non-Hermitian) Bogoliubov-de Gennes matrix [49, 171]

$$\boldsymbol{\sigma}_3 \boldsymbol{M}_{\boldsymbol{k}} = \boldsymbol{\sigma}_3 \begin{pmatrix} \boldsymbol{A}_{\boldsymbol{k}} & \boldsymbol{B}_{\boldsymbol{k}} \\ \boldsymbol{B}_{\boldsymbol{k}}^\dagger & \boldsymbol{A}_{-\boldsymbol{k}}^\intercal \end{pmatrix}, \tag{4.2}$$

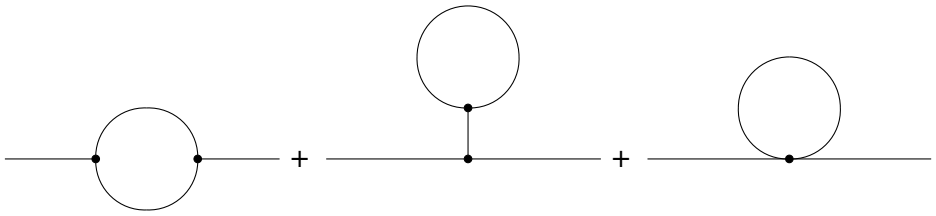
where $\boldsymbol{\sigma}_3 = \text{diag}(\mathbb{I}, -\mathbb{I})$ is a Pauli matrix acting on the particle-hole degree of freedom.

[29] Refer to the Supplemental Material for details of spin-wave theory and the proof of the curvature formula. The Supplemental Material includes Refs. [38, 48–52, 101].

Beyond linear spin-wave theory, the quasiparticle energies correspond to poles of the (retarded) single-magnon propagator

$$\boldsymbol{G}^{\mathrm{R}}(\boldsymbol{k},\omega) = \left[\omega + i0^{+} - \boldsymbol{\sigma}_3 \left(S\boldsymbol{M}_{\boldsymbol{k}} + \boldsymbol{\Sigma}^{\mathrm{R}}(\boldsymbol{k},\omega)\right)\right]^{-1} \boldsymbol{\sigma}_3, \tag{4.3}$$

where $\boldsymbol{\Sigma}^{\mathrm{R}}(\boldsymbol{k},\omega)$ is the retarded (thermal) self-energy matrix. We note that the matrix in Eq. (4.3) has both sublattice indices and indices that track the normal and anomalous boson terms [49, 101].[30] We then proceed to include the leading order effects of spin-wave interactions perturbatively by computing the self-energy to $O(S^0)$ in the $1/S$ expansion [38]. This contribution to the self-energy can be represented as the sum of three one-particle irreducible diagrams [53]

$\boldsymbol{\Sigma}^{\mathrm{R}} =$  , (4.4)

constructed from both three- and four-magnon interaction vertices. In general, these diagrams carry a conserved wavevector and frequency $(\boldsymbol{k},\omega)$ at each interaction vertex marked as black dots, sublattice indices, and include both normal and anomalous propagators.[29,30] Note that in order to incorporate thermal effects into the self-energy, we must take the limit $1/S \to 0$ while keeping T/S fixed.[29]

Next, we consider a gapless PG mode, which falls into one of the two categories depending on its spectral properties, referred to as "type I" and "type II" [101, 172]. Throughout this paper, we assume that this mode is located at the first Brillouin zone (BZ) centre ($\boldsymbol{k} = \boldsymbol{0}$), although this assumption can be relaxed in general. Under this assumption, the poles of Eq. (4.3) at $\boldsymbol{k} = \boldsymbol{0}$ correspond to an effective Hamiltonian for the PG mode H_{PG} arising from magnon-magnon interactions, with the temperature dependence encoded in the self-energy. At the level of linear spin-wave theory, a type I PG mode has linear dispersion, $\epsilon_{\boldsymbol{k}} \propto |\boldsymbol{k}|$, while a type II mode disperses quadratically, $\epsilon_{\boldsymbol{k}} \propto |\boldsymbol{k}|^2$, as depicted in Fig. 4.1.

For a type I mode, $\boldsymbol{\sigma}_3\boldsymbol{M}_{\boldsymbol{0}}$ has a single linearly independent eigenvector $\boldsymbol{V}_0$ corresponding to a zero eigenvalue. In this case, the PG gap appears at $O(S^{1/2})$ as

$$\Delta(T) = S^{1/2}\sqrt{\boldsymbol{V}_0^{\dagger}\left[\boldsymbol{\Sigma}^{\mathrm{R}}(\boldsymbol{0},0)\boldsymbol{\sigma}_3\boldsymbol{M}_{\boldsymbol{0}} + \boldsymbol{M}_{\boldsymbol{0}}\boldsymbol{\sigma}_3\boldsymbol{\Sigma}^{\mathrm{R}}(\boldsymbol{0},0)\right]\boldsymbol{V}_0}. \tag{4.5}$$

[30] Here, "normal" refers to the number-conserving blocks of Eq. (4.1) (i.e. terms proportional to $a^{\dagger}a$ and $aa^{\dagger}$) and "anomalous" refers to the number-non-conserving blocks (i.e. terms proportional to $a^{\dagger}a^{\dagger}$ and aa).

For a type II mode, there are two linearly independent eigenvectors, $\boldsymbol{V}_0$ and $\boldsymbol{W}_0$, corresponding to a zero eigenvalue. In this case, the PG gap appears at $O(S^0)$ as

$$\Delta(T) = S^0\sqrt{\left(\boldsymbol{V}_0^\dagger \boldsymbol{\Sigma}^{\mathrm{R}}(\boldsymbol{0},0)\boldsymbol{V}_0\right)^2 - \left|\boldsymbol{V}_0^\dagger \boldsymbol{\Sigma}^{\mathrm{R}}(\boldsymbol{0},0)\boldsymbol{W}_0\right|^2}. \tag{4.6}$$

We refer the interested reader to the Supplemental Material for a more detailed derivation of Eqs. (4.5) and (4.6).[29] With the PG gap generated by quantum *and* thermal fluctuations now determined, the low-energy dispersion takes the form $\sqrt{v^2|\boldsymbol{k}|^2+\Delta^2}$ for a type I mode and $v|\boldsymbol{k}|^2+\Delta$ for a type II mode, as depicted in Fig. 4.1.

4.3 Curvature formula

In previous works characterizing the PG gap in both the quantum zero-temperature [101] and classical finite-temperature [58] scenarios, it was argued that the gap at leading order can be calculated exactly by computing the curvature of the linear spin-wave free energy. Here, we develop a similar formalism analogous to Refs. [58, 101] that allows us to compute the PG gap at $O(S^0)$ using only the linear spin-wave energy eigenvalues at $O(S)$. First, consider a *local* reference frame $(\hat{\boldsymbol{e}}_{x,\alpha}, \hat{\boldsymbol{e}}_{y,\alpha}, \hat{\boldsymbol{e}}_{0,\alpha})$ where $\hat{\boldsymbol{e}}_{0,\alpha}$ is the classical ordering direction, rotations about $\hat{\boldsymbol{e}}_{y,\alpha}$ correspond to a soft mode, and $\hat{\boldsymbol{e}}_{x,\alpha} = \hat{\boldsymbol{e}}_{y,\alpha} \times \hat{\boldsymbol{e}}_{0,\alpha}$. We may parametrize the soft mode by an angle ϕ (along with its canonically conjugate pair θ) and define the rotated Hamiltonian $\mathcal{H}(\phi,\theta) = U(\phi,\theta)^\dagger H U(\phi,\theta)$ where $U(\phi,\theta)$ is a unitary transformation that generates the soft modes of the spin configurations. Formally, this modifies the local frame as

$$\begin{pmatrix} \hat{\boldsymbol{e}}_{x,\alpha}(\phi,\theta) \\ \hat{\boldsymbol{e}}_{y,\alpha}(\phi,\theta) \\ \hat{\boldsymbol{e}}_{0,\alpha}(\phi,\theta) \end{pmatrix} = \begin{pmatrix} \cos\phi & -\sin\phi\sin\theta & \sin\phi\cos\theta \\ 0 & \cos\theta & \sin\theta \\ -\sin\phi & -\cos\phi\sin\theta & \cos\phi\cos\theta \end{pmatrix} \begin{pmatrix} \hat{\boldsymbol{e}}_{x,\alpha} \\ \hat{\boldsymbol{e}}_{y,\alpha} \\ \hat{\boldsymbol{e}}_{0,\alpha} \end{pmatrix}. \tag{4.7}$$

We subsequently expand the rotated Hamiltonian to $O(S)$ to obtain

$$\mathcal{H}(\phi,\theta) = S(S+1)N\epsilon_{\mathrm{cl}}(\theta) + SN\epsilon_{\mathrm{qu}}(\phi,\theta) + S\sum_{\boldsymbol{k},\alpha} \epsilon_{\boldsymbol{k},\alpha}(\phi,\theta) b^\dagger_{\boldsymbol{k},\alpha} b_{\boldsymbol{k},\alpha}, \tag{4.8}$$

where $S^2\epsilon_{\mathrm{cl}}$ is the classical energy (per spin) and $S(\epsilon_{\mathrm{cl}}+\epsilon_{\mathrm{qu}})$ is the quantum zero-point energy (per spin), and $S\epsilon_{\boldsymbol{k},\alpha}$ is the linear spin-wave dispersion [171].[29] Eq. (4.8) effectively parametrizes the magnons with respect to the zero-mode subspace. For a type I mode, only ϕ corresponds to a soft mode at the classical level, with the classical configuration energy depending on θ. When $\theta \neq 0$, the spin configuration is classically unstable, implying that the zero-point and spin-wave energies

are not well-defined. For a type II mode, both angles are classically soft, so $\epsilon_{\rm cl}(\theta) = \epsilon_{\rm cl}(0)$. In general, the free energy per spin at $O(S)$ is

$$f(\phi,\theta) = S(S+1)\epsilon_{\rm cl}(\theta) + S\epsilon_{\rm qu}(\phi,\theta) + \frac{k_{\rm B}T}{N}\sum_{\boldsymbol{k},\alpha}\ln\left(1 - e^{-S\epsilon_{\boldsymbol{k},\alpha}(\phi,\theta)/k_{\rm B}T}\right). \tag{4.9}$$

We may now establish a relation between the effective Hamiltonian to $O(S^1)$ in Eq. (4.8) and the PG gap at $O(S^0)$ using a sum rule for the magnon spectral function (see Supplemental Material[29])

$$\begin{aligned}\int_{-\infty}^{\infty} {\rm d}\omega\omega\mathcal{A}_0(\omega)\boldsymbol{\sigma}_3 = \frac{1}{2SN}\Bigg[&(\boldsymbol{\sigma}_3 - i\boldsymbol{\sigma}_2)\left\langle\left(\frac{\partial^2\mathcal{H}}{\partial\phi^2}\right)_0\right\rangle \\ &+ (\boldsymbol{\sigma}_3 + i\boldsymbol{\sigma}_2)\left\langle\left(\frac{\partial^2\mathcal{H}}{\partial\theta^2}\right)_0\right\rangle - 2i\boldsymbol{\sigma}_1\left\langle\left(\frac{\partial^2\mathcal{H}}{\partial\phi\partial\theta}\right)_0\right\rangle\Bigg],\end{aligned} \tag{4.10}$$

where $(\cdots)_0$ is used to denote an evaluation at $\phi = \theta = 0$ (the ObD selected state), $\mathcal{A}_0(\omega)$ is the single-magnon spectral function projected into the zero-mode subspace, and $\boldsymbol{\sigma}_1, \boldsymbol{\sigma}_2$ are the remaining two Pauli matrices (i.e. $[\boldsymbol{\sigma}_1, \boldsymbol{\sigma}_2] = 2i\boldsymbol{\sigma}_3$). Indeed, Eq. (4.10) is readily shown to be *precisely* the effective Hamiltonian $H_{\rm PG}$ for the PG mode obtained earlier on the basis of the self-energy calculations to leading order in $1/S$.[29] By diagonalizing Eq. (4.10), we find the thermal gap at leading order in $1/S$ is given by

$$\Delta(T) = \begin{cases} S^{1/2}\sqrt{\left(\frac{\partial^2\epsilon_{\rm cl}}{\partial\theta^2}\right)_0 g_{\phi\phi}} & \text{(type I)} \\ S^0\sqrt{g_{\phi\phi}g_{\theta\theta} - g_{\phi\theta}^2} & \text{(type II)}, \end{cases} \tag{4.11}$$

where

$$g_{\lambda_1\lambda_2}(T) \equiv \frac{1}{S}\left[\left(\frac{\partial^2 f}{\partial\lambda_1\partial\lambda_2}\right)_0 + K_{\lambda_1\lambda_2}\right], \tag{4.12}$$

and

$$K_{\lambda_1\lambda_2} \equiv \frac{S^2}{4k_{\rm B}TN}\sum_{\boldsymbol{k},\alpha}\left(\frac{\partial\epsilon_{\boldsymbol{k},\alpha}}{\partial\lambda_1}\right)_0\left(\frac{\partial\epsilon_{\boldsymbol{k},\alpha}}{\partial\lambda_2}\right)_0 {\rm csch}^2\left(\frac{S\epsilon_{\boldsymbol{k},\alpha}}{2k_{\rm B}T}\right), \tag{4.13}$$

with $\lambda_i = \phi, \theta$. As $T \to 0$, $\frac{S^2}{k_{\rm B}T}{\rm csch}^2\left(\frac{S\epsilon_{\boldsymbol{k},\alpha}}{2k_{\rm B}T}\right) \to \frac{4k_{\rm B}T}{\epsilon_{\boldsymbol{k},\alpha}^2}$ for small $\epsilon_{\boldsymbol{k},\alpha}$, while ${\rm csch}^2\left(\frac{S\epsilon_{\boldsymbol{k},\alpha}}{2k_{\rm B}T}\right) \to 0$ exponentially otherwise. Therefore, $K_{\lambda_1\lambda_2}$ vanishes in the zero temperature limit, recovering the curvature formula for the zero-temperature PG gap in Ref. [101]. At high temperature, $K_{\lambda_1\lambda_2} \propto T$, consistent with the scaling proposed in Ref. [58] for the PG gap in the classical limit. Note that

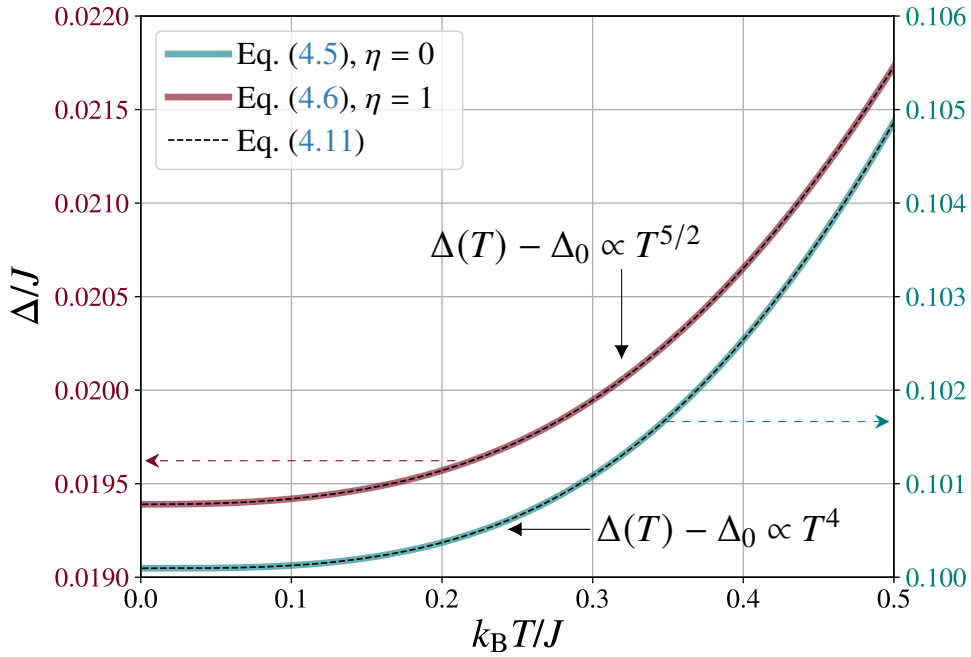


Figure 4.2: PG gap for the Heisenberg-compass model Eq. (4.14) on a simple cubic lattice with $\eta = 0$ (type I mode) and $\eta = 1$ (type II mode). In both cases, we use $K/J = 0.5$ and $S = 1/2$.

since T/S is kept fixed in the perturbation theory, $g_{\lambda_1\lambda_2}$ is formally of $O(S^0)$ whenever both λ_1 and λ_2 correspond to soft modes. The derivatives in Eq. (4.13) can be readily calculated using the Hellmann-Feynman theorem [173]. More details regarding the proof of Eq. (4.11) and the calculation of Eq. (4.13) are provided in the Supplemental Material.[29]

4.4 Models

As a first example, we consider a ferromagnetic Heisenberg-compass model on the simple cubic lattice, defined by the Hamiltonian

$$H = -\sum_{\boldsymbol{r}} \left[J \sum_{\boldsymbol{\delta}=\boldsymbol{x},\boldsymbol{y},\boldsymbol{z}} \boldsymbol{S}_{\boldsymbol{r}} \cdot \boldsymbol{S}_{\boldsymbol{r}+\boldsymbol{\delta}} + K \left(S^x_{\boldsymbol{r}} S^x_{\boldsymbol{r}+\boldsymbol{x}} + S^y_{\boldsymbol{r}} S^y_{\boldsymbol{r}+\boldsymbol{y}} + \eta\, S^z_{\boldsymbol{r}} S^z_{\boldsymbol{r}+\boldsymbol{z}} \right) \right], \tag{4.14}$$

where $\boldsymbol{S}_{\boldsymbol{r}}$ is a spin-S operator at site $\boldsymbol{r}$ and $\boldsymbol{\delta} = \boldsymbol{x}, \boldsymbol{y}, \boldsymbol{z}$ are the nearest-neighbour bonds, and $J, K > 0$. For $K = 0$, Eq. (4.14) is simply the Heisenberg ferromagnet, with collinear ground

states related by a global SU(2) symmetry. When $K > 0$, there is no longer an exact continuous symmetry. In the following, we consider the cases of $\eta = 0$ and $\eta = 1$.

When $\eta = 0$, the classical ground state corresponds to a collinear ferromagnet with magnetization along any direction in the $\hat{\boldsymbol{x}} - \hat{\boldsymbol{y}}$ plane. In contrast to the ($K = 0$) Heisenberg model, this degeneracy is *accidental*. This accidental U(1) degeneracy is lifted by quantum and thermal fluctuations that select one of four magnetization directions along the $\pm\hat{\boldsymbol{x}}, \pm\hat{\boldsymbol{y}}$ directions. In this case, the associated PG mode is of type I.

When $\eta = 1$, the classical ground state is a collinear ferromagnet with arbitrary magnetization direction, signalling an accidental O(3) degeneracy. The degeneracy is lifted by fluctuations that select one of six magnetization directions along the cubic axes $\pm\hat{\boldsymbol{x}}, \pm\hat{\boldsymbol{y}}, \pm\hat{\boldsymbol{z}}$. In this latter case, the associated PG mode is of type II.[29]

The PG gap at $O(S^0)$ for Eq. (4.14) is depicted in Fig. 4.2 over a range of temperature in the case of both a type I ($\eta = 0$) and type II ($\eta = 1$) mode. We find an excellent quantitative agreement between the gap calculated using the curvature formula of Eq. (4.11) and the one from the self-energy calculation of Eqs. (4.5) and (4.6). We emphasize that these two calculations are carried out independently of one another, and there are no free parameters introduced to make them agree. We note that the gap calculation is relatively simple for this model, as the lack of three-magnon interactions implies that $K_{\lambda_1\lambda_2} = 0$ in Eq. (4.12).[29] In both cases, there is a zero-temperature contribution due to the gap, Δ_0, induced by quantum ObD (i.e. zero-point fluctuations) [101]. At low temperatures, the leading thermal contribution to the gap is proportional to T^4 for a type I mode and $T^{5/2}$ for a type II mode.

4.5 Discussion

The curvature formula in Eq. (4.11) directly implies that at low temperatures the PG gap satisfies a universal scaling relation as a function of temperature. By noting that at the harmonic level the spin-wave dispersion is linear ($\epsilon_{\boldsymbol{k}} \sim |\boldsymbol{k}|$) for a type I mode and quadratic ($\epsilon_{\boldsymbol{k}} \sim |\boldsymbol{k}|^2$) for a type II mode, a straightforward dimensional analysis of Eq. (4.12) implies that the leading thermal correction generically satisfies

$$\Delta(T) - \Delta_0 \propto \begin{cases} S^{1/2} \left(\frac{T}{S}\right)^{d+1} & \text{(type I)} \\ S^0 \left(\frac{T}{S}\right)^{d/2+1} & \text{(type II)}, \end{cases} \tag{4.15}$$

where d is the spatial dimension, and is consistent with the results in Fig. 4.2. We propose that this universal temperature-dependence of the gap *increasing* with temperature at $0 < T \ll T_c$,

where T_c is the critical temperature, can serve as direct experimental evidence for ObD in a spin system that does not rely on fitting exchange couplings to a microscopic model.

The ability to calculate the PG gap using only linear spin-wave theory [Eq. (4.11)] provides a substantial simplification when compared to the tedious calculation of the magnon self-energy, particularly in cases with non-collinear order. In addition, the presence of a gapless mode in the linear spin-wave spectrum renders a direct calculation of the self-energy infrared divergent when $d < 3$ [174], drawing an analogy to the Hohenberg-Mermin-Wagner theorem [175–178]. To circumvent this divergence, one could employ a more involved, self-consistent approach to calculate the self-energy, such as those described in Refs. [58, 179–182]. Alternatively, the curvature formula for the gap in Eq. (4.11) is well-defined for $d < 3$, avoiding the need to regularize an infrared divergence in the first place.

Our observation that the PG gap obeys a universal, temperature-dependent scaling relation can serve as a framework to diagnose ObD in real materials in a way that is independent of the microscopic spin Hamiltonian describing the material. Leading candidates where ObD may be present include the compounds $Er_2Ti_2O_7$ [114, 116, 183], $CoTiO_3$ [118], $Sr_2Cu_3O_4Cl_2$ [119], and $Fe_2Ca_3(GeO_4)_3$ [120]. It remains unclear, however, whether the small gap measured in these materials is truly a PG gap, as it is possible that such a gap can arise from further neighbour exchange, anisotropic spin interactions or higher-order spin interactions such as a biquadratic interaction. The experimental observation of a temperature-dependent gap, such as in Eq. (4.15), would aid in resolving these questions.

We are then left with the question of whether the results presented here are relevant to real materials. In the End Matter, we calculate the PG gap for several pyrochlore material candidates using Eqs. (4.5), (4.6), and (4.11). For the pyrochlore material $Er_2Ti_2O_7$, the thermal correction to the gap up to $T = 700$ mK is predicted to be within $\Delta(700\text{ mK}) - \Delta_0 = 2.9\ \mu$eV, approximately 10% of the zero-temperature gap (see Fig. 4.3(a)). This will likely be challenging to measure experimentally with high resolution in temperature, as this energy scale is at the lower end of what is currently accessible using high-resolution inelastic neutron backscattering measurements [184]. The experimental details of how to resolve and characterize small thermal corrections to the PG gap remain an open and challenging problem. In addition, there will be a crossover temperature, T^*, where thermal fluctuations and the progressive restoration of symmetry as T_c is approached from below, will take over and make $\Delta(T)$ begin decreasing. The treatment of corrections to $\Delta(T)$ arising from pre-critical fluctuations is beyond the scope of this work, as we focus only on $\Delta(T)$ in the limit $T \ll T_c$. Nonetheless, our work provides a robust theoretical framework to guide future experimental efforts in this exciting field of research.

Note—In the process of finalizing this manuscript, we became aware of a very recent preprint [185] that reports calculations of the PG gap at nonzero temperature similar to those

presented here.

Acknowledgements

We thank Michael Burke, Anton Burkov and Griffin Howson for useful technical discussions, and Jason Gardner, Bruce Gaulin and Romain Sibille for discussions about inelastic neutron backscattering measurements. A. H. acknowledges support from the NSERC of Canada CGS-D Scholarship. S. K. acknowledges financial support from the Deutsche Forschungsgemeinschaft (DFG, German Research Foundation) under Germany's Excellence Strategy through the Hallwachs-Röntgen Postdoc Program of the Würzburg-Dresden Cluster of Excellence on Complexity and Topology in Quantum Matter – ct.qmat (EXC 2147, project-id 390858490). The work at the U. of Waterloo and the U. of Windsor was supported by the NSERC of Canada (M. J. P. G. and J. G. R.) and the Canada Research Chair program (M. J. P. G., Tier 1). This research was enabled in part by computing resources provided by the Digital Research Alliance of Canada.

End Matter

4.EI Material candidate, $Er_2Ti_2O_7$

First, we discuss an application to the XY pyrochlore antiferromagnet $Er_2Ti_2O_7$, which is arguably one of the best material candidates for ObD [97, 114, 116]. The spin-orbit entangled electronic states of Er^{3+} are subject to a highly anisotropic crystal-field producing a ground doublet described using an effective (pseudo) spin-$\frac{1}{2}$ with the Er^{3+}–Er^{3+} interactions described by an anisotropic exchange-like model [23, 97, 138]

$$\begin{aligned} H = \sum_{\langle i,j \rangle} \Big[& J_{zz} S_i^z S_j^z - J_{\pm} \left(S_i^+ S_j^- + S_i^- S_j^+ \right) \\ & + J_{\pm\pm} \left(\gamma_{ij} S_i^+ S_j^+ + \text{H.c.} \right) \\ & + J_{z\pm} \left(\zeta_{ij} \left[S_i^z S_j^+ + S_i^+ S_j^z \right] + \text{H.c.} \right) \Big]. \end{aligned} \tag{4.16}$$

Here $\langle i, j \rangle$ denotes the sum over nearest-neighbour bonds, and γ_{ij}, ζ_{ij} are bond-dependent phase factors uniquely determined by the lattice geometry and symmetries of the single-ion crystal-field

wavefunctions [23]. The four nearest-neighbour couplings J_{uv} in Eq. (4.16) have been fitted to reproduce INS data on $Er_2Ti_2O_7$, with the best fit given by [97]

$$\begin{aligned} J_{zz} &= -25\ \mu\text{eV}, \quad J_{\pm} = +65\ \mu\text{eV}, \\ J_{\pm\pm} &= +42\ \mu\text{eV}, \quad J_{z\pm} = -8.8\ \mu\text{eV}. \end{aligned} \tag{4.17}$$

The classical ground states are non-collinear antiferromagnetic configurations of spins lying in the local XY planes perpendicular to the local $\langle 111 \rangle$ cubic axes of the pyrochlore lattice [23], parametrized by an accidental U(1) degeneracy [83, 186]. Below $T_c \approx 1.17$ K [93], ObD selects one of the six "ψ_2" states, leading to a type I PG mode [23, 97].

The PG gap for $Er_2Ti_2O_7$ is depicted in Fig. 4.3(a) over a range of temperatures up to $T = 700$mK. We find a zero-temperature contribution to the gap of $\Delta_0 = 31.1\ \mu$eV, consistent with the gap calculated in Ref. [101], and somewhat smaller than the experimentally determined values of 43 μeV [183] and 53 μeV [114]. At low temperatures, the gap scales proportional to T^4, similar to the type I mode in Fig. 4.2.

4.EII Material candidate, $Yb_2Ge_2O_7$

This compound is another XY pyrochlore antiferromagnet [121] whose Hamiltonian is the same as for $Er_2Ti_2O_7$ given in Eq. (4.16). The four nearest-neighbour couplings have been fitted to INS data, with the best fit given by [121]

$$\begin{aligned} J_{zz} &= 0.128\ \text{meV}, \quad J_{\pm} = 0.138\ \text{meV}, \\ J_{\pm\pm} &= 0.044\ \text{meV}, \quad J_{z\pm} = -0.188\ \text{meV}. \end{aligned} \tag{4.18}$$

The classical ground states are the same as in the case of $Er_2Ti_2O_7$, i.e., non-collinear antiferromagnetic configurations of spins lying in the local XY planes perpendicular to the local $\langle 111 \rangle$ cubic axes of the pyrochlore lattice [23], parametrized by the same accidental U(1) degeneracy [186]. Below $T_c \approx 0.572$ K [121], ObD selects one of the six "ψ_3" states, leading to a type I PG mode.

The temperature dependence of PG gap for $Yb_2Ge_2O_7$ is depicted in Fig. 4.3(b) over a range of temperatures up to $T_c/2$. We find a zero-temperature contribution to the gap of $\Delta_0 = 13.028$ μeV, and a very small thermal correction within $\Delta(T_c/2) - \Delta_0 \approx 6$ neV. At low temperatures, the gap scales proportional to T^4, as predicted for a type I mode.

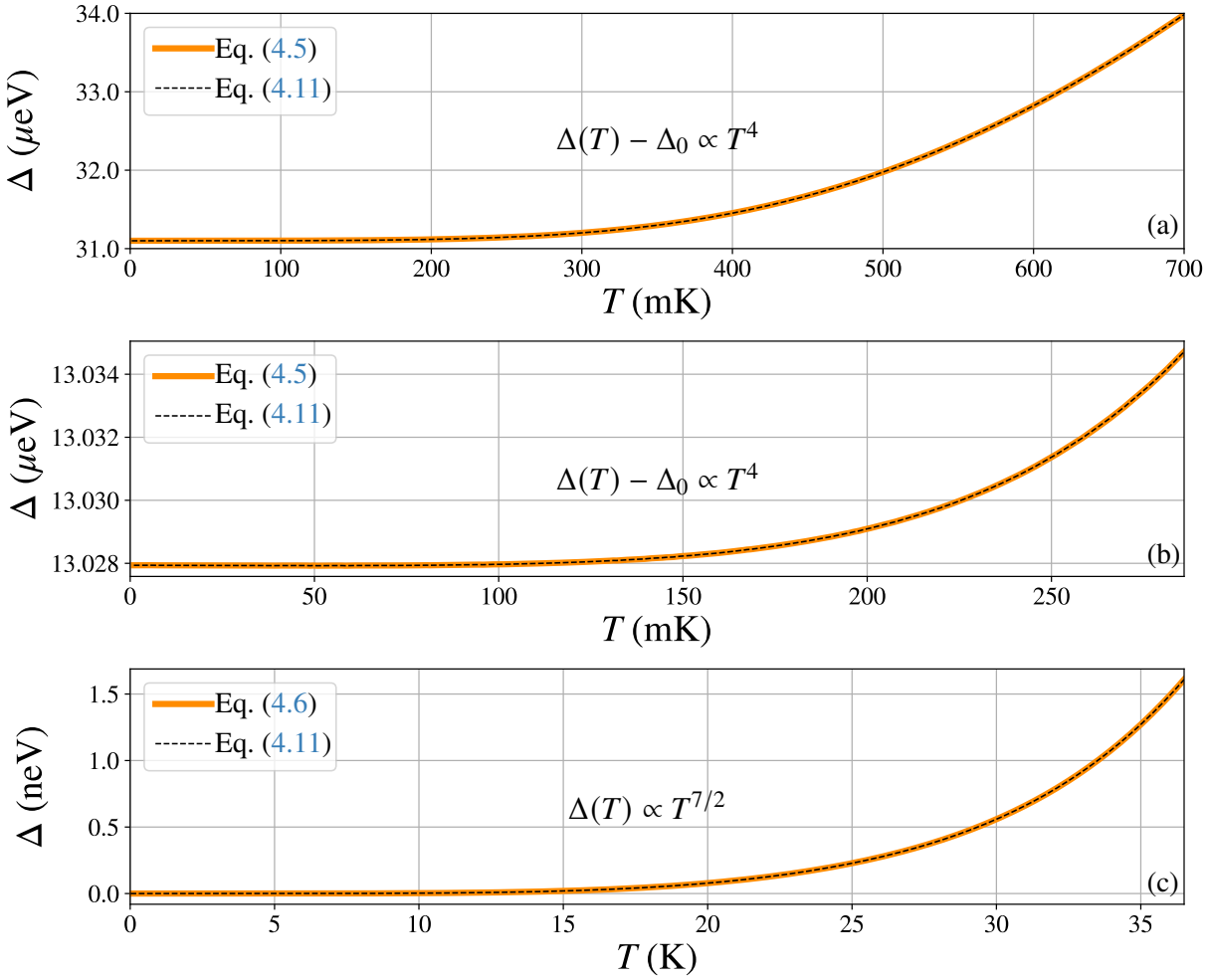


Figure 4.3: (a) PG gap for the pyrochlore antiferromagnet $Er_2Ti_2O_7$, calculated using the exchange couplings from Ref. [97]. The classical ground states are parametrized by an accidental U(1) degeneracy, corresponding to a type I mode. The gap is plotted up to $T = 700$ mK. (b) PG gap for the pyrochlore antiferromagnet $Yb_2Ge_2O_7$, calculated using the exchange couplings from Ref. [121]. The classical ground states are parametrized by an accidental U(1) degeneracy, corresponding to a type I mode. The gap is plotted up to $T_c/2 = 286$ mK. (c) PG gap for the pyrochlore ferromagnet $Lu_2V_2O_7$, calculated using the exchange couplings from Ref. [145]. The ground states are parametrized by an accidental O(3) degeneracy, corresponding to a type II mode. The gap is plotted up to $T_c/2 = 36.5$ K.

4.EIII Material candidate, $Lu_2V_2O_7$

Finally, we discuss the somewhat unique scenario of the pyrochlore ferromagnet $Lu_2V_2O_7$. In this material, the V^{4+} transition metal $3d^1$ ions are magnetic, leading to the effective spin-$\frac{1}{2}$ model

$$H = -J \sum_{\langle i,j \rangle} \boldsymbol{S}_i \cdot \boldsymbol{S}_j - \sum_{\langle i,j \rangle} \boldsymbol{D}_{ij} \cdot (\boldsymbol{S}_i \times \boldsymbol{S}_j), \tag{4.19}$$

where the Dzyaloshinskii-Moriya (DM) vectors are of the "indirect" type [78]. The two nearest-neighbour couplings have been fitted to INS data, with the best fit given by [145]

$$J = 8.22 \text{ meV}, \qquad |\boldsymbol{D}_{ij}| = 1.5 \text{ meV}. \tag{4.20}$$

The ground states are *collinear ferromagnetic* configurations parametrized by an accidental O(3) degeneracy [1]. Below $T_c \approx 73$ K [145], ObD (within the model of Eq. (4.19)) selects one of the $\langle 111 \rangle$ directions for the bulk magnetization [1], leading to a type II PG mode.

The temperature dependence of the PG gap for $Lu_2V_2O_7$ is depicted in Fig. 4.3(c) over a range of temperatures up to $T_c/2$. In this case, there is no zero-temperature contribution to the gap, consistent with the recent work of Ref. [1] arguing that this material exhibits ObD at finite temperatures *without* quantum zero-point fluctuations. However, we find at low temperatures a thermally-generated pseudogap that scales proportional to $T^{7/2}$, distinct from the expected $T^{5/2}$ scaling for a type II mode. This exception arises due to the observation pointed out in Ref. [1], that the anisotropy [originating from the DM interactions – the second term in Eq. (4.19)] enters the spin-wave dispersion at $O(k^4)$ in the wavevector $k \equiv |\boldsymbol{k}|$, when $|\boldsymbol{D}_{ij}| \ll J$. This implies the linear spin-wave free energy, at low temperatures, takes the form

$$f(\phi, \theta) = aT^{5/2} + b(\phi, \theta)T^{7/2} + O(T^{9/2}), \tag{4.21}$$

with the coefficient a being independent of the orientation of the magnetization. The $K_{\lambda_1 \lambda_2}$ terms entering the curvature formula will have a similar low-temperature expansion, and Eq. (4.11) is consistent with this power-law scaling.

Supplemental Material

4.SI Details of spin wave theory

Holstein-Primakoff expansion

We consider a general bilinear spin model

$$H = \frac{1}{2}\sum_{\boldsymbol{r}\boldsymbol{r}'}\sum_{\alpha\alpha'} \boldsymbol{S}^{\intercal}_{\boldsymbol{r},\alpha}\, \boldsymbol{J}_{\boldsymbol{r}-\boldsymbol{r}',\alpha\alpha'}\boldsymbol{S}_{\boldsymbol{r}',\alpha'}, \tag{4.22}$$

where $\boldsymbol{r}$ represents the position of a unit cell and α is a sublattice index. The associated spin wave theory can be obtained by expressing the spin-operators as Holstein-Primakoff bosons [35],

$$\boldsymbol{S}_{\boldsymbol{r},\alpha} = \left(S - n_{\boldsymbol{r},\alpha}\right)\hat{\boldsymbol{e}}_{\alpha,0} + \sqrt{S}\left[\left(1-\frac{n_{\boldsymbol{r},\alpha}}{2S}\right)^{1/2} a_{\boldsymbol{r},\alpha}\hat{\boldsymbol{e}}_{\alpha,-} + a^{\dagger}_{\boldsymbol{r}\alpha}\left(1-\frac{n_{\boldsymbol{r},\alpha}}{2S}\right)^{1/2}\hat{\boldsymbol{e}}_{\alpha,+}\right], \tag{4.23}$$

where $n_{\boldsymbol{r},\alpha} = a^{\dagger}_{\boldsymbol{r},\alpha}a_{\boldsymbol{r},\alpha}$ and the vectors $\hat{\boldsymbol{e}}_{\alpha,\pm} \equiv (\hat{\boldsymbol{e}}_{\alpha,x} \pm i\hat{\boldsymbol{e}}_{\alpha,y})/\sqrt{2}$, $\hat{\boldsymbol{e}}_{\alpha,0}$ define a local reference frame with respect to the classical ordering direction $\hat{\boldsymbol{e}}_{\alpha,0}$ (i.e. $\hat{\boldsymbol{e}}_{\alpha,x}\times\hat{\boldsymbol{e}}_{\alpha,y} = \hat{\boldsymbol{e}}_{\alpha,0}$). We define the Fourier transform of the exchange interactions in this local frame as

$$\mathcal{J}^{\mu\nu}_{\boldsymbol{k},\alpha\beta} \equiv \sum_{\boldsymbol{\delta}} e^{i\boldsymbol{k}\cdot\boldsymbol{\delta}}\hat{\boldsymbol{e}}^{\intercal}_{\alpha,\mu}\boldsymbol{J}_{\boldsymbol{\delta},\alpha\beta}\hat{\boldsymbol{e}}_{\beta,\nu}, \tag{4.24}$$

where the sum is taken over all bonds $\boldsymbol{\delta}$ between a site on sublattice α to a site on sublattice β. Expanding Eq. (4.23) in powers of $1/S$ about an ordered state (typically a classical ground state), leads to the series representation $H = S^2\sum_{n=0}^{\infty} S^{-n/2}H_n$. The magnon interactions to $O(S^0)$ are given by

$$H_0 = N\left(1+\frac{1}{S}\right)\epsilon_{\mathrm{cl}}, \tag{4.25}$$

$$H_1 = \sqrt{N_c}\sum_{\alpha}\left[L^{\alpha}a^{\dagger}_{\boldsymbol{0},\alpha} + \overline{L}^{\alpha}a_{\boldsymbol{0},\alpha}\right], \tag{4.26}$$

$$H_2 = \frac{1}{2}\sum_{\boldsymbol{k}}\sum_{\alpha\beta}\left[A^{\alpha\beta}_{\boldsymbol{k}}a^{\dagger}_{\boldsymbol{k},\alpha}a_{\boldsymbol{k},\beta} + A^{\beta\alpha}_{-\boldsymbol{k}}a_{-\boldsymbol{k},\alpha}a^{\dagger}_{-\boldsymbol{k},\beta} + B^{\alpha\beta}_{\boldsymbol{k}}a^{\dagger}_{\boldsymbol{k},\alpha}a^{\dagger}_{-\boldsymbol{k},\beta} + \overline{B}^{\alpha\beta}_{\boldsymbol{k}}a_{-\boldsymbol{k},\beta}a_{\boldsymbol{k},\alpha}\right], \tag{4.27}$$

$$H_3 = \frac{1}{2!\sqrt{N_c}}\sum_{\boldsymbol{k}\boldsymbol{q}}\sum_{\alpha\beta\mu}\left[T^{\alpha\beta\mu}_{\boldsymbol{k},\boldsymbol{q}}a^{\dagger}_{\boldsymbol{k},\alpha}a^{\dagger}_{\boldsymbol{q},\beta}a_{\boldsymbol{k}+\boldsymbol{q},\mu} + \overline{T}^{\alpha\beta\mu}_{\boldsymbol{k},\boldsymbol{q}}a^{\dagger}_{\boldsymbol{k}+\boldsymbol{q},\mu}a_{\boldsymbol{q},\beta}a_{\boldsymbol{k},\alpha}\right], \tag{4.28}$$

$$H_4 = \frac{1}{N_c}\sum_{\boldsymbol{k}\boldsymbol{q}\boldsymbol{Q}}\sum_{\alpha\beta\mu\nu}\left[\frac{1}{(2!)^2}V^{\alpha\beta\mu\nu}_{\boldsymbol{k},\boldsymbol{q},\boldsymbol{Q}}a^{\dagger}_{\boldsymbol{k}+\boldsymbol{Q},\alpha}a^{\dagger}_{\boldsymbol{q}-\boldsymbol{Q},\beta}a_{\boldsymbol{q},\mu}a_{\boldsymbol{k},\nu} + \frac{1}{3!}\left(D^{\alpha\beta\mu\nu}_{\boldsymbol{k},\boldsymbol{q},\boldsymbol{Q}}a^{\dagger}_{\boldsymbol{k},\alpha}a^{\dagger}_{\boldsymbol{q},\beta}a^{\dagger}_{\boldsymbol{Q},\mu}a_{\boldsymbol{k}+\boldsymbol{q}+\boldsymbol{Q},\nu} + \mathrm{H.c.}\right)\right], \tag{4.29}$$

where $N = N_c N_s$ is the number of spins in a system with N_c primitive unit cells and N_s sublattices per unit cell. $NS^2\epsilon_{\text{cl}}$ is the energy of the classical configuration, and the symmetrized interaction vertices are

$$\epsilon_{\text{cl}} = \frac{1}{2N_s}\sum_{\alpha\beta}\mathcal{J}^{00}_{\mathbf{0},\alpha\beta}, \tag{4.30}$$

$$L^{\alpha} = \sum_{\beta}\mathcal{J}^{+0}_{\mathbf{0},\alpha\beta}, \tag{4.31}$$

$$A^{\alpha\beta}_{\boldsymbol{k}} = \mathcal{J}^{+-}_{\boldsymbol{k},\alpha\beta} - \delta_{\alpha\beta}\sum_{\mu}\mathcal{J}^{00}_{\mathbf{0},\alpha\mu}, \tag{4.32}$$

$$B^{\alpha\beta}_{\boldsymbol{k}} = \mathcal{J}^{++}_{\boldsymbol{k},\alpha\beta}, \tag{4.33}$$

$$T^{\alpha\beta\mu}_{\boldsymbol{k}\boldsymbol{q}} = -\delta_{\beta\mu}\mathcal{J}^{+0}_{\boldsymbol{k},\alpha\beta} - \delta_{\alpha\mu}\mathcal{J}^{+0}_{\boldsymbol{q},\beta\alpha}, \tag{4.34}$$

$$\begin{aligned} V^{\alpha\beta\mu\nu}_{\boldsymbol{k},\boldsymbol{q},\boldsymbol{Q}} = {} & \frac{1}{2}\delta_{\alpha\mu}\delta_{\beta\nu}\left(\mathcal{J}^{00}_{\boldsymbol{k}-\boldsymbol{q}+\boldsymbol{Q},\alpha\beta} + \mathcal{J}^{00}_{-\boldsymbol{k}+\boldsymbol{q}-\boldsymbol{Q},\beta\alpha}\right) + \frac{1}{2}\delta_{\alpha\nu}\delta_{\beta\mu}\left(+\mathcal{J}^{00}_{\boldsymbol{Q},\alpha\beta} + \mathcal{J}^{00}_{-\boldsymbol{Q},\beta\alpha}\right) \\ & - \frac{1}{2}\left(\delta_{\beta\mu}\delta_{\beta\nu}\mathcal{J}^{+-}_{\boldsymbol{k}+\boldsymbol{Q},\alpha\beta} + \delta_{\alpha\mu}\delta_{\alpha\nu}\mathcal{J}^{+-}_{\boldsymbol{q}-\boldsymbol{Q},\beta\alpha} + \delta_{\alpha\beta}\delta_{\alpha\nu}\mathcal{J}^{+-}_{\boldsymbol{q},\alpha\mu} + \delta_{\alpha\beta}\delta_{\alpha\mu}\mathcal{J}^{+-}_{\boldsymbol{k},\alpha\nu}\right), \end{aligned} \tag{4.35}$$

$$D^{\alpha\beta\mu\nu}_{\boldsymbol{k},\boldsymbol{q},\boldsymbol{Q}} = -\frac{1}{2}\left(\delta_{\mu\beta}\delta_{\nu\beta}\mathcal{J}^{++}_{\boldsymbol{k},\alpha\beta} + \delta_{\alpha\mu}\delta_{\alpha\nu}\mathcal{J}^{++}_{\boldsymbol{q},\beta\alpha} + \delta_{\alpha\beta}\delta_{\alpha\nu}\mathcal{J}^{++}_{\boldsymbol{Q},\mu\alpha}\right). \tag{4.36}$$

The one-magnon vertex, L^{α}, vanishes so long as the classical configuration energy is at a local minimum.

Linear spin wave theory

The linear spin wave Hamiltonian results from truncating the Holstein-Primakoff expansion at $O(S)$ about a configuration corresponding to a classical ground state

$$H = NS^2\epsilon_{\text{cl}} + S\sum_{\boldsymbol{k}}\sum_{\alpha\alpha'}\left[A^{\alpha\alpha'}_{\boldsymbol{k}}a^{\dagger}_{\boldsymbol{k},\alpha}a_{\boldsymbol{k},\alpha'} + \frac{1}{2}\left(B^{\alpha\alpha'}_{\boldsymbol{k}}a^{\dagger}_{\boldsymbol{k},\alpha}a^{\dagger}_{-\boldsymbol{k},\alpha'} + \text{H.c.}\right)\right] + O(S^{1/2}). \tag{4.37}$$

The linear spin wave energies and corresponding wavefunctions are determined by diagonalizing the $2N_s \times 2N_s$ boson Bogoliubov-de Gennes matrix [49]

$$\boldsymbol{\sigma}_3\boldsymbol{M}_{\boldsymbol{k}} \equiv \begin{pmatrix} \boldsymbol{A}_{\boldsymbol{k}} & \boldsymbol{B}_{\boldsymbol{k}} \\ -\boldsymbol{B}^{\dagger}_{\boldsymbol{k}} & -\boldsymbol{A}^{\intercal}_{-\boldsymbol{k}} \end{pmatrix}, \tag{4.38}$$

where $\boldsymbol{\sigma}_3 = \mathrm{diag}(\mathbb{I}, -\mathbb{I})$ is a block Pauli matrix. We may diagonalize Eq. (4.38) by defining a new set of bosons $b_{\boldsymbol{k},\alpha}$ such that

$$\begin{pmatrix} \boldsymbol{a}_{\boldsymbol{k}} \\ \boldsymbol{a}^{\dagger}_{-\boldsymbol{k}} \end{pmatrix} = \boldsymbol{\mathcal{T}}_{\boldsymbol{k}} \begin{pmatrix} \boldsymbol{b}_{\boldsymbol{k}} \\ \boldsymbol{b}^{\dagger}_{-\boldsymbol{k}} \end{pmatrix}. \tag{4.39}$$

By requiring $\left[b_{\boldsymbol{k},\alpha}, b_{\boldsymbol{k},\beta}\right] = 0$ and $\left[b_{\boldsymbol{k},\alpha}, b^{\dagger}_{\boldsymbol{k},\beta}\right] = \delta_{\alpha\beta}$, we obtain the para-unitary condition [48]

$$\boldsymbol{\mathcal{T}}_{\boldsymbol{k}}^{-1} = \boldsymbol{\sigma}_3 \boldsymbol{\mathcal{T}}_{\boldsymbol{k}}^{\dagger} \boldsymbol{\sigma}_3. \tag{4.40}$$

The eigenvectors of Eq. (4.38) come in pairs $\boldsymbol{V}_{\boldsymbol{k},\alpha}$ and $\boldsymbol{W}_{\boldsymbol{k},\alpha} = \boldsymbol{\sigma}_1 \overline{\boldsymbol{V}}_{-\boldsymbol{k},\alpha}$ [50], with eigenvalues $\pm\epsilon_{\pm\boldsymbol{k},\alpha}$, and make up the columns of the transformation matrix, i.e.

$$\boldsymbol{\mathcal{T}}_{\boldsymbol{k}} = \begin{pmatrix} | & & | & | & & | \\ \boldsymbol{V}_{\boldsymbol{k},1} & \cdots & \boldsymbol{V}_{\boldsymbol{k},N_s} & \boldsymbol{W}_{\boldsymbol{k},1} & \cdots & \boldsymbol{W}_{\boldsymbol{k},N_s} \\ | & & | & | & & | \end{pmatrix}. \tag{4.41}$$

Using Eq. (4.40), the eigenvectors can be normalized to satisfy the para-orthogonality conditions

$$\boldsymbol{V}^{\dagger}_{\boldsymbol{k},\alpha} \boldsymbol{\sigma_3} \boldsymbol{V}_{\boldsymbol{k},\beta} = +\delta_{\alpha\beta}, \tag{4.42}$$

$$\boldsymbol{W}^{\dagger}_{\boldsymbol{k},\alpha} \boldsymbol{\sigma_3} \boldsymbol{W}_{\boldsymbol{k},\beta} = -\delta_{\alpha\beta}, \tag{4.43}$$

$$\boldsymbol{V}^{\dagger}_{\boldsymbol{k},\alpha} \boldsymbol{\sigma_3} \boldsymbol{W}_{\boldsymbol{k},\beta} = 0. \tag{4.44}$$

The linear spin wave Hamiltonian then takes the diagonal form

$$H = NS(S+1)\epsilon_{\mathrm{cl}} + NS\epsilon_{\mathrm{qu}} + \frac{S}{2} \sum_{\boldsymbol{k}} \sum_{\alpha} \epsilon_{\boldsymbol{k},\alpha} b^{\dagger}_{\boldsymbol{k},\alpha} b_{\boldsymbol{k},\alpha} + O(S^{1/2}), \tag{4.45}$$

where the quantum zero-point energy (per spin) is

$$S\epsilon_{\mathrm{qu}} \equiv \frac{S}{2N} \sum_{\boldsymbol{k}} \sum_{\alpha} \epsilon_{\boldsymbol{k},\alpha}. \tag{4.46}$$

We may subsequently calculate the free energy (per spin) to $O(S)$ at temperature T as

$$f(T) = S(S+1)\epsilon_{\mathrm{cl}} + S\epsilon_{\mathrm{qu}} + \frac{k_{\mathrm{B}}T}{N} \sum_{\boldsymbol{k}} \sum_{\alpha} \ln\left(1 - e^{-S\epsilon_{\boldsymbol{k},\alpha}/k_{\mathrm{B}}T}\right) + O(S^{1/2}). \tag{4.47}$$

Next, we discuss the circumstance of interest, where the linear spin wave spectrum contains zero modes. This implies that the matrix $\boldsymbol{\sigma}_3 \boldsymbol{M}_{\boldsymbol{k}}$ is positive *semi-definite*. We assume, without

loss of generality, that there is a single zero mode at the BZ centre ($\boldsymbol{k} = \boldsymbol{0}$). This mode can be classified, whether it is type I or type II, based on the spectral properties of $\boldsymbol{M_0}$. In particular, $\boldsymbol{M_0}$ has either one or two linearly independent eigenvectors corresponding to the zero mode, which we refer to as *type I* and *type II* respectively. We define $\boldsymbol{V}_0$ and $\boldsymbol{W}_0$ to be the vectors that span the zero mode subspace, while simultaneously satisfying the normalization conditions Eqs. (4.42)-(4.44). The projection of $\boldsymbol{M_0}$ into the zero mode subspace is then given by [101]

$$\begin{pmatrix} \boldsymbol{V}_0^\dagger \boldsymbol{M_0} \boldsymbol{V}_0 & \boldsymbol{V}_0^\dagger \boldsymbol{M_0} \boldsymbol{W}_0 \\ \boldsymbol{W}_0^\dagger \boldsymbol{M_0} \boldsymbol{V}_0 & \boldsymbol{W}_0^\dagger \boldsymbol{M_0} \boldsymbol{W}_0 \end{pmatrix} = \begin{cases} \boldsymbol{V}_0^\dagger \boldsymbol{M_0} \boldsymbol{V}_0 \begin{pmatrix} 1 & 1 \\ 1 & 1 \end{pmatrix} & \text{(type I)} \\ \begin{pmatrix} 0 & 0 \\ 0 & 0 \end{pmatrix} & \text{(type II)} \end{cases} . \tag{4.48}$$

A more detailed treatment of non-interacting bosons with zero modes can be found in Refs. [49, 101].

Non-linear spin wave theory at finite temperature

To incorporate effects of spin wave interactions at leading order in $1/S$ and at finite temperature, we use the imaginary time formalism. To this effect, we assume the $O(S)$ Hamiltonian in Eq. (4.37) is solvable, and treat the three- and four-body interactions perturbatively to $O(S^0)$ [38]. We are interested in the single-magnon spectrum, encoded in the thermal Green's functions

$$\mathcal{G}^{-+}_{\alpha\beta}(\boldsymbol{k}, i\omega_n) = \int_0^{(k_\mathrm{B}T)^{-1}} \mathrm{d}\tau \, e^{i\omega_n \tau} \left\langle \mathbb{T} a_{\boldsymbol{k},\alpha}(\tau) a^\dagger_{\boldsymbol{k},\beta}(0) \right\rangle , \tag{4.49}$$

$$\mathcal{G}^{+-}_{\alpha\beta}(\boldsymbol{k}, i\omega_n) = \int_0^{(k_\mathrm{B}T)^{-1}} \mathrm{d}\tau \, e^{i\omega_n \tau} \left\langle \mathbb{T} a^\dagger_{-\boldsymbol{k},\alpha}(\tau) a_{-\boldsymbol{k},\beta}(0) \right\rangle , \tag{4.50}$$

$$\mathcal{G}^{++}_{\alpha\beta}(\boldsymbol{k}, i\omega_n) = \int_0^{(k_\mathrm{B}T)^{-1}} \mathrm{d}\tau \, e^{i\omega_n \tau} \left\langle \mathbb{T} a^\dagger_{-\boldsymbol{k},\alpha}(\tau) a^\dagger_{\boldsymbol{k},\beta}(0) \right\rangle , \tag{4.51}$$

$$\mathcal{G}^{--}_{\alpha\beta}(\boldsymbol{k}, i\omega_n) = \int_0^{(k_\mathrm{B}T)^{-1}} \mathrm{d}\tau \, e^{i\omega_n \tau} \left\langle \mathbb{T} a_{\boldsymbol{k},\alpha}(\tau) a_{-\boldsymbol{k},\beta}(0) \right\rangle , \tag{4.52}$$

where α, β label the sublattice structure, $\omega_n = 2\pi n k_\mathrm{B} T$ is a bosonic Matsubara frequency, $\mathbb{T}$ is the (imaginary) time-ordering operator [52], $\langle \cdots \rangle$ denotes the thermal average with respect to the equilibrium density matrix $\rho = Z^{-1} e^{-H/k_\mathrm{B}T}$ [51]. This can be organized more compactly into

a Bogoliubov-de Gennes block matrix, analogous to Eq. (4.38)

$$\mathcal{G}(\boldsymbol{k}, i\omega_n) \equiv \begin{pmatrix} \mathcal{G}^{-+}(\boldsymbol{k}, i\omega_n) & \mathcal{G}^{--}(\boldsymbol{k}, i\omega_n) \\ \mathcal{G}^{++}(\boldsymbol{k}, i\omega_n) & \mathcal{G}^{+-}(\boldsymbol{k}, i\omega_n) \end{pmatrix} = \Big[-i\omega_n + \boldsymbol{\sigma}_3 \left(S\boldsymbol{M}_{\boldsymbol{k}} + \boldsymbol{\Sigma}(\boldsymbol{k}, i\omega_n) \right) \Big]^{-1} \boldsymbol{\sigma}_3, \quad (4.53)$$

where $\boldsymbol{\Sigma}(\boldsymbol{k}, i\omega_n)$ is the imaginary time self-energy that encodes magnon-magnon interactions. The self-energy to $O(S^0)$ is computed by evaluating the diagrams depicted in Eq. (4) of the main text. The single-magnon dispersion then corresponds to poles of the (real-time) retarded Green's function, related to the thermal Green's function via analytic continuation

$$\boldsymbol{G}^{\mathrm{R}}(\boldsymbol{k}, \omega) = -\boldsymbol{\mathcal{G}}(\boldsymbol{k}, i\omega_n \to \omega + i0^+) = \Big[\omega + i0^+ - \boldsymbol{\sigma}_3 \Big(S\boldsymbol{M}_{\boldsymbol{k}} + \boldsymbol{\Sigma}^{\mathrm{R}}(\boldsymbol{k}, \omega) \Big) \Big]^{-1} \boldsymbol{\sigma}_3, \quad (4.54)$$

with the retarded self-energy defined similarly as $\boldsymbol{\Sigma}^{\mathrm{R}}(\boldsymbol{k}, \omega) = \boldsymbol{\Sigma}(\boldsymbol{k}, i\omega_n \to \omega + i0^+)$. In the limit $1/S \to 0$, the self-energy can be treated as a perturbation to the linear spin wave matrix $\boldsymbol{M}_{\boldsymbol{k}}$. Expanding about the linear spin wave energies $S\epsilon_{\boldsymbol{k},\alpha}$, the magnon dispersion at $O(S^0)$ can be determined by the simultaneous eigenvalue problems for each linear spin wave mode

$$\boldsymbol{\sigma}_3 \Big(S\boldsymbol{M}_{\boldsymbol{k}} + \boldsymbol{\Sigma}^{\mathrm{R}}(\boldsymbol{k}, S\epsilon_{\boldsymbol{k},\alpha}) \Big) \mathcal{V}_{\boldsymbol{k},\alpha} = \left(\mathcal{E}_{\boldsymbol{k},\alpha} - i\Gamma_{\boldsymbol{k},\alpha} \right) \boldsymbol{\mathcal{V}}_{\boldsymbol{k},\alpha}, \quad (4.55)$$

$$\boldsymbol{\sigma}_3 \Big(S\boldsymbol{M}_{\boldsymbol{k}} + \boldsymbol{\Sigma}^{\mathrm{R}}(\boldsymbol{k}, S\epsilon_{\boldsymbol{k},\alpha}) \Big) \mathcal{W}_{\boldsymbol{k},\alpha} = -\left(\mathcal{E}_{-\boldsymbol{k},\alpha} - i\Gamma_{-\boldsymbol{k},\alpha} \right) \boldsymbol{\mathcal{W}}_{\boldsymbol{k},\alpha}, \quad (4.56)$$

where $\boldsymbol{\mathcal{W}}_{\boldsymbol{k},\alpha} \equiv \boldsymbol{\sigma}_1 \overline{\boldsymbol{\mathcal{V}}}_{-\boldsymbol{k},\alpha}$. Note that since $\boldsymbol{\Sigma}^{\mathrm{R}}$ is non-Hermitian in general, the magnon energies will generically include both a real and imaginary part.

Calculation of the pseudo-Goldstone gap

For the remainder of this Sec. 4.SI, the calculation of the pseudo-Goldstone (PG) gap proceeds similarly to Ref. [101], with the retarded self-energy $\boldsymbol{\Sigma}^{\mathrm{R}}(\boldsymbol{k}, \omega)$ now generalized to be evaluated at finite temperature T. Since the PG mode appears at zero energy in linear spin-wave theory, we may expand the self-energy to leading order

$$\boldsymbol{\Sigma}^{\mathrm{R}}(\boldsymbol{0}, \omega) = \boldsymbol{\Sigma}^{\mathrm{R}}(\boldsymbol{0}, 0) + O(S^{-1}), \quad (4.57)$$

which is exact to $O(S^0)$. In addition, we can ignore the broadening effects of the pseudo-Goldstone mode to leading order in $1/S$, and take $\boldsymbol{\Sigma}^{\mathrm{R}}(\boldsymbol{0}, 0) = \boldsymbol{\Sigma}^{\mathrm{R}}(\boldsymbol{0}, 0)^\dagger$. The subspace associated with the PG mode is two-dimensional, therefore we must calculate the solution to Eqs (4.55) and (4.56) in

the context of *degenerate* perturbation theory. At $O(S^0)$, this comes down to diagonalizing the perturbed Hamiltonian $S\boldsymbol{M_0} + \boldsymbol{\Sigma}^{\mathrm{R}}(\mathbf{0}, 0)$ projected into the zero-mode subspace [101]

$$H_{\mathrm{PG}} \equiv \boldsymbol{\sigma}_3 \begin{pmatrix} \boldsymbol{V}_0^\dagger \Big[S\boldsymbol{M_0} + \boldsymbol{\Sigma}^{\mathrm{R}}(\mathbf{0}, 0) \Big] \boldsymbol{V}_0 & \boldsymbol{V}_0^\dagger \Big[S\boldsymbol{M_0} + \boldsymbol{\Sigma}^{\mathrm{R}}(\mathbf{0}, 0) \Big] \boldsymbol{W}_0 \\ \boldsymbol{W}_0^\dagger \Big[S\boldsymbol{M_0} + \boldsymbol{\Sigma}^{\mathrm{R}}(\mathbf{0}, 0) \Big] \boldsymbol{V}_0 & \boldsymbol{W}_0^\dagger \Big[S\boldsymbol{M_0} + \boldsymbol{\Sigma}^{\mathrm{R}}(\mathbf{0}, 0) \Big] \boldsymbol{W}_0 \end{pmatrix}, \tag{4.58}$$

where the temperature dependence enters implicitly from the self-energy matrix. Eq. (4.58) is the effective Hamiltonian for the PG mode, arising from the self-energy, to leading order in $1/S$ alluded to in the main text. In the case of a type I mode, we may use Eq. (4.48) to compute the effective Hamiltonian

$$H_{\mathrm{PG}} = \begin{pmatrix} S\boldsymbol{V}_0^\dagger \boldsymbol{M_0} \boldsymbol{V}_0 + \boldsymbol{V}_0^\dagger \boldsymbol{\Sigma}^{\mathrm{R}}(\mathbf{0}, 0) \boldsymbol{V}_0 & S\boldsymbol{V}_0^\dagger \boldsymbol{M_0} \boldsymbol{V}_0 + \boldsymbol{V}_0^\dagger \boldsymbol{\Sigma}^{\mathrm{R}}(\mathbf{0}, 0) \boldsymbol{W}_0 \\ -S\boldsymbol{V}_0^\dagger \boldsymbol{M_0} \boldsymbol{V}_0 - \boldsymbol{W}_0^\dagger \boldsymbol{\Sigma}^{\mathrm{R}}(\mathbf{0}, 0) \boldsymbol{V}_0 & -S\boldsymbol{V}_0^\dagger \boldsymbol{M_0} \boldsymbol{V}_0 - \boldsymbol{V}_0^\dagger \boldsymbol{\Sigma}^{\mathrm{R}}(\mathbf{0}, 0) \boldsymbol{V}_0 \end{pmatrix}. \tag{4.59}$$

Computing the eigenvalues of H_{PG}, we obtain a PG gap of $O(S^{1/2})$,

$$\Delta(T) = S^{1/2} \sqrt{\boldsymbol{V}_0^\dagger \left[\boldsymbol{\Sigma}^{\mathrm{R}}(\mathbf{0}, 0) \boldsymbol{\sigma}_3 \boldsymbol{M_0} + \boldsymbol{M_0} \boldsymbol{\sigma}_3 \boldsymbol{\Sigma}^{\mathrm{R}}(\mathbf{0}, 0) \right] \boldsymbol{V}_0}. \tag{4.60}$$

Similarly, for a type II mode, we use Eq. (4.48) to obtain

$$H_{\mathrm{PG}} = \begin{pmatrix} \boldsymbol{V}_0^\dagger \boldsymbol{\Sigma}^{\mathrm{R}}(\mathbf{0}, 0) \boldsymbol{V}_0 & \boldsymbol{V}_0^\dagger \boldsymbol{\Sigma}^{\mathrm{R}}(\mathbf{0}, 0) \boldsymbol{W}_0 \\ -\boldsymbol{W}_0^\dagger \boldsymbol{\Sigma}^{\mathrm{R}}(\mathbf{0}, 0) \boldsymbol{V}_0 & -\boldsymbol{W}_0^\dagger \boldsymbol{\Sigma}^{\mathrm{R}}(\mathbf{0}, 0) \boldsymbol{W}_0 \end{pmatrix}. \tag{4.61}$$

In this case, the PG gap appears at $O(S^0)$ as

$$\Delta(T) = S^0 \sqrt{\left(\boldsymbol{V}_0^\dagger \boldsymbol{\Sigma}^{\mathrm{R}}(\mathbf{0}, 0) \boldsymbol{V}_0 \right)^2 - \left| \boldsymbol{V}_0^\dagger \boldsymbol{\Sigma}^{\mathrm{R}}(\mathbf{0}, 0) \boldsymbol{W}_0 \right|^2}. \tag{4.62}$$

In general, the magnon self-energy $\boldsymbol{\Sigma}^{\mathrm{R}}(\mathbf{0}, 0)$ must be computed numerically, which requires two important considerations. First, the analytic continuation in Eq. (4.54) requires the use of a finite broadening factor $0^+ \approx 10^{-4}$ in the self-energy evaluation. Second, one must evaluate sums that involve the bare magnon Green's function of the form $[(\omega + i0^+)\boldsymbol{\sigma}_3 - S\boldsymbol{M_k}]^{-1}$. These sums are rendered infrared divergent in the presence of PG modes. To regularize this unphysical divergence, we include a small positive chemical potential term of the form $\mu \sum_{\boldsymbol{k},\alpha} a^\dagger_{\boldsymbol{k},\alpha} a_{\boldsymbol{k},\alpha}$ and extrapolate numerically to the limit $\mu \to 0^+$ until convergence is achieved [101].

4.SII Curvature formula

Next, we show how the PG gap computed to $O(S^0)$, at finite temperature, can be related to the curvatures of the linear spin-wave dispersion by computing the first moment of the relevant magnon spectral functions. This is, in essence, a nonzero temperature generalization of the curvature formula derived in Ref. [101], where it was shown that the relationship between these two quantities can be established through the first moment of the magnon spectral function, projected into the zero-mode subspace. We consider the Holstein-Primakoff expansion about a configuration that is related to the classical ground state by small rotations about the local $\hat{\boldsymbol{e}}_{\alpha,x}$ and $\hat{\boldsymbol{e}}_{\alpha,y}$ axes, labelled by the angles θ and ϕ respectively. Relative to the classical ground state, this transforms the local frame as

$$\hat{\boldsymbol{e}}_{\alpha,0}(\zeta) = \left(1 - |\zeta|^2\right)\hat{\boldsymbol{e}}_{\alpha,0} + \bar{\zeta}\hat{\boldsymbol{e}}_{\alpha,+} + \zeta\hat{\boldsymbol{e}}_{\alpha,-} + O(\zeta^3), \tag{4.63}$$

$$\hat{\boldsymbol{e}}_{\alpha,+}(\zeta) = \left(1 - \frac{1}{2}|\zeta|^2 + \frac{1}{4}\bar{\zeta}^2 - \frac{1}{4}\zeta^2\right)\hat{\boldsymbol{e}}_{\alpha,+} - \zeta\hat{\boldsymbol{e}}_{\alpha,0} - \frac{1}{4}\zeta^2\hat{\boldsymbol{e}}_{\alpha,-} + O(\zeta^3), \tag{4.64}$$

$$\hat{\boldsymbol{e}}_{\alpha,-}(\zeta) = \left(1 - \frac{1}{2}|\zeta|^2 + \frac{1}{4}\zeta^2 - \frac{1}{4}\bar{\zeta}^2\right)\hat{\boldsymbol{e}}_{\alpha,-} - \bar{\zeta}\hat{\boldsymbol{e}}_{\alpha,0} - \frac{1}{4}\bar{\zeta}^2\hat{\boldsymbol{e}}_{\alpha,+} + O(\zeta^3), \tag{4.65}$$

where $\zeta \equiv (\phi + i\theta)/\sqrt{2}$. One can subsequently calculate the appropriate spin-wave theory using Eqs. (4.25)-(4.29). Alternatively, these small rotations can be related to the magnon zero-modes

$$b_0 \equiv \boldsymbol{V}_0^\dagger \boldsymbol{\sigma}_3 \begin{pmatrix} \boldsymbol{a_0} \\ \boldsymbol{a_0}^\dagger \end{pmatrix}, \qquad b_0^\dagger \equiv -\boldsymbol{W}_0^\dagger \boldsymbol{\sigma}_3 \begin{pmatrix} \boldsymbol{a_0} \\ \boldsymbol{a_0}^\dagger \end{pmatrix}, \tag{4.66}$$

using the Hermitian operators

$$\Phi \equiv \sqrt{\frac{SN}{2}}\left[b_0^\dagger + b_0\right] + O(S^{-1/2}) \tag{4.67}$$

$$\Theta \equiv i\sqrt{\frac{SN}{2}}\left[b_0^\dagger - b_0\right] + O(S^{-1/2}). \tag{4.68}$$

These operators generate rotations about the soft directions [101], given by the unitary operator

$$U(\phi, \theta) \equiv e^{-i\phi\Phi}e^{-i\theta\Theta}. \tag{4.69}$$

This can be used to define a transformed Hamiltonian that encodes these rotations $\mathcal{H}(\phi, \theta) \equiv U(\phi, \theta)^\dagger H U(\phi, \theta)$. Expanding to second order in ϕ and θ using the Baker-Campbell-Hausdorff formula, we obtain

$$\begin{aligned}\mathcal{H}(\phi, \theta) = H &+ i\theta[\Theta, H] + i\phi[\Phi, H] \\ &- \frac{1}{2}\theta^2[\Theta, [\Theta, H]] - \frac{1}{2}\phi^2[\Phi, [\Phi, H]] - \phi\theta[\Phi, [\Theta, H]] + O(\zeta^3).\end{aligned} \tag{4.70}$$

Proceeding to compute the curvatures of $\mathcal{H}(\phi,\theta)$, we find they are related to the nested commutators

$$\left(\frac{\partial^2\mathcal{H}}{\partial\phi^2}\right)_0 = -\,[\Phi,[\Phi,H]], \qquad \left(\frac{\partial^2\mathcal{H}}{\partial\theta^2}\right)_0 = -[\Theta,[\Theta,H]],$$
$$\left(\frac{\partial^2\mathcal{H}}{\partial\phi\partial\theta}\right)_0 = \left(\frac{\partial^2\mathcal{H}}{\partial\theta\partial\phi}\right)_0 = -[\Phi,[\Theta,H]], \tag{4.71}$$

where $(\cdots)_0$ is used as a shorthand for the evaluation at $\phi=\theta=0$ corresponding to the ObD selected state.

First moment of the spectral function

To relate the curvatures in Eqs. (4.71) to the PG gap, we first establish a sum rule for the first moment of the magnon spectral function. More generally, the real-time retarded and advanced Green's functions for a pair of operators X and Y are respectively [52]

$$G^{\mathrm{R}}_{XY}(t) \equiv -i\theta(t)\,\langle[X(t),Y(0)]\rangle\,, \tag{4.72}$$
$$G^{\mathrm{A}}_{XY}(t) \equiv i\theta(-t)\,\langle[X(t),Y(0)]\rangle\,, \tag{4.73}$$

with $\theta(t)$ the Heaviside step function and the time evolution is assumed to be in the Heisenberg picture, i.e. $\frac{\mathrm{d}X}{\mathrm{d}t} = i[H,X]$. The corresponding spectral function is defined as

$$\mathcal{A}_{XY}(\omega) \equiv \frac{1}{2i}\int_{-\infty}^{\infty}\mathrm{d}t\, e^{i\omega t}\left[G^{\mathrm{R}}_{XY}(t) - G^{\mathrm{A}}_{XY}(t)\right]. \tag{4.74}$$

The first moment of this spectral function is then

$$\int_{-\infty}^{\infty}\mathrm{d}\omega\,\omega\mathcal{A}_{XY}(\omega) = \frac{1}{2}\int_{-\infty}^{\infty}\mathrm{d}\omega\int_{-\infty}^{\infty}\mathrm{d}t\, e^{i\omega t}\frac{\mathrm{d}}{\mathrm{d}t}\left[G^{\mathrm{R}}_{XY}(t) - G^{\mathrm{A}}_{XY}(t)\right] = -\,\langle[Y,[X,H]]\rangle\,. \tag{4.75}$$

The following sum rules then directly follow from Eqs. (4.71)

$$\int_{-\infty}^{\infty}\mathrm{d}\omega\,\omega\mathcal{A}_{\Phi\Phi}(\omega) = \left\langle\left(\frac{\partial^2\mathcal{H}}{\partial\phi^2}\right)_0\right\rangle, \qquad \int_{-\infty}^{\infty}\mathrm{d}\omega\,\omega\mathcal{A}_{\Theta\Theta}(\omega) = \left\langle\left(\frac{\partial^2\mathcal{H}}{\partial\theta^2}\right)_0\right\rangle, \tag{4.76}$$
$$\int_{-\infty}^{\infty}\mathrm{d}\omega\,\omega\mathcal{A}_{\Phi\Theta}(\omega) = \left\langle\left(\frac{\partial^2\mathcal{H}}{\partial\phi\partial\theta}\right)_0\right\rangle, \qquad \int_{-\infty}^{\infty}\mathrm{d}\omega\,\omega\mathcal{A}_{\Theta\Phi}(\omega) = \left\langle\left(\frac{\partial^2\mathcal{H}}{\partial\theta\partial\phi}\right)_0\right\rangle. \tag{4.77}$$

Next, we relate these spectral functions to the single magnon spectral function at $O(S^0)$, defined using Eq. (4.54) as

$$\boldsymbol{\mathcal{A}}(\boldsymbol{k},\omega) = \frac{1}{2i}\left[\boldsymbol{G}^{\mathrm{R}}(\boldsymbol{k},\omega) - \boldsymbol{G}^{\mathrm{R}}(\boldsymbol{k},\omega)^{\dagger}\right], \tag{4.78}$$

Projecting into the zero mode subspace, using Eq. (4.66), we find

$$\boldsymbol{\mathcal{A}}_0(\omega) \equiv \begin{pmatrix} \mathcal{A}_{b_0 b_0^{\dagger}}(\omega) & \mathcal{A}_{b_0 b_0}(\omega) \\ \mathcal{A}_{b_0^{\dagger} b_0^{\dagger}}(\omega) & \mathcal{A}_{b_0^{\dagger} b_0}(\omega) \end{pmatrix} = \begin{pmatrix} \boldsymbol{V}_0^{\dagger}\boldsymbol{\sigma}_3\boldsymbol{\mathcal{A}}(\boldsymbol{0},\omega)\boldsymbol{\sigma}_3\boldsymbol{V}_0 & -\boldsymbol{V}_0^{\dagger}\boldsymbol{\sigma}_3\boldsymbol{\mathcal{A}}(\boldsymbol{0},\omega)\boldsymbol{\sigma}_3\boldsymbol{W}_0 \\ -\boldsymbol{W}_0^{\dagger}\boldsymbol{\sigma}_3\boldsymbol{\mathcal{A}}(\boldsymbol{0},\omega)\boldsymbol{\sigma}_3\boldsymbol{V}_0 & \boldsymbol{W}_0^{\dagger}\boldsymbol{\sigma}_3\boldsymbol{\mathcal{A}}(\boldsymbol{0},\omega)\boldsymbol{\sigma}_3\boldsymbol{W}_0 \end{pmatrix}. \tag{4.79}$$

It follows from Eqs. (4.67)-(4.68) that

$$\begin{aligned} \boldsymbol{\mathcal{A}}_0(\omega) = \frac{1}{2SN}\Big[&(1+\boldsymbol{\sigma}_1)\mathcal{A}_{\Phi\Phi}(\omega) + (1-\boldsymbol{\sigma}_1)\mathcal{A}_{\Theta\Theta}(\omega) \\ &- (\boldsymbol{\sigma}_2 + i\boldsymbol{\sigma}_3)\mathcal{A}_{\Phi\Theta}(\omega) - (\boldsymbol{\sigma}_2 - i\boldsymbol{\sigma}_3)\mathcal{A}_{\Theta\Phi}(\omega)\Big]. \end{aligned} \tag{4.80}$$

This implies that the first moment can be written as

$$\begin{aligned} \int_{-\infty}^{\infty} \mathrm{d}\omega\, \omega \boldsymbol{\mathcal{A}}_0(\omega) = \frac{1}{2SN}\Bigg[&(1+\boldsymbol{\sigma}_1)\left\langle\left(\frac{\partial^2\mathcal{H}}{\partial\phi^2}\right)_0\right\rangle \\ &+ (1-\boldsymbol{\sigma}_1)\left\langle\left(\frac{\partial^2\mathcal{H}}{\partial\theta^2}\right)_0\right\rangle - 2\boldsymbol{\sigma}_2\left\langle\left(\frac{\partial^2\mathcal{H}}{\partial\phi\partial\theta}\right)_0\right\rangle\Bigg]. \end{aligned} \tag{4.81}$$

Multiplying Eq. (4.81) on the right by $\boldsymbol{\sigma}_3$, we obtain Eq. (4.10) in the main text, which we now show is equal to the effective Hamiltonian for the pseudo-Goldstone mode H_{PG}.

In particular, we denote $\boldsymbol{\mathcal{V}}_0$ and $\boldsymbol{\mathcal{W}}_0$ to be the eigenvectors of $S\boldsymbol{M_0} + \boldsymbol{\Sigma}^{\mathrm{R}}(\boldsymbol{0},0)$ to first order in perturbation theory, related to the zero mode subspace. To first order in perturbation theory, these are simply linear combinations of the unperturbed eigenvectors $\boldsymbol{V}_0$ and $\boldsymbol{W}_0$ of $S\boldsymbol{M_0}$. This implies that, in the projection to the zero-mode subspace, only the terms involving $\boldsymbol{\mathcal{V}}_0$ and $\boldsymbol{\mathcal{W}}_0$ in the spectral decomposition will survive. Explicitly, the zero-mode spectral functions take the form

$$\mathcal{A}_{b_0 b_0^{\dagger}}(\omega) = +\boldsymbol{V}_0^{\dagger}\boldsymbol{\sigma}_3\left[\delta(\omega-\Delta)\boldsymbol{\mathcal{V}}_0\boldsymbol{\mathcal{V}}_0^{\dagger} - \delta(\omega+\Delta)\boldsymbol{\mathcal{W}}_0\boldsymbol{\mathcal{W}}_0^{\dagger}\right]\boldsymbol{\sigma}_3\boldsymbol{V}_0 \tag{4.82}$$

$$\mathcal{A}_{b_0 b_0}(\omega) = -\boldsymbol{V}_0^{\dagger}\boldsymbol{\sigma}_3\left[\delta(\omega-\Delta)\boldsymbol{\mathcal{V}}_0\boldsymbol{\mathcal{V}}_0^{\dagger} - \delta(\omega+\Delta)\boldsymbol{\mathcal{W}}_0\boldsymbol{\mathcal{W}}_0^{\dagger}\right]\boldsymbol{\sigma}_3\boldsymbol{W}_0 \tag{4.83}$$

$$\mathcal{A}_{b_0^{\dagger} b_0^{\dagger}}(\omega) = -\boldsymbol{W}_0^{\dagger}\boldsymbol{\sigma}_3\left[\delta(\omega-\Delta)\boldsymbol{\mathcal{V}}_0\boldsymbol{\mathcal{V}}_0^{\dagger} - \delta(\omega+\Delta)\boldsymbol{\mathcal{W}}_0\boldsymbol{\mathcal{W}}_0^{\dagger}\right]\boldsymbol{\sigma}_3\boldsymbol{V}_0 \tag{4.84}$$

$$\mathcal{A}_{b_0^{\dagger} b_0}(\omega) = +\boldsymbol{W}_0^{\dagger}\boldsymbol{\sigma}_3\left[\delta(\omega-\Delta)\boldsymbol{\mathcal{V}}_0\boldsymbol{\mathcal{V}}_0^{\dagger} - \delta(\omega+\Delta)\boldsymbol{\mathcal{W}}_0\boldsymbol{\mathcal{W}}_0^{\dagger}\right]\boldsymbol{\sigma}_3\boldsymbol{W}_0 \tag{4.85}$$

The first moment of the spectral function is therefore

$$\int_{-\infty}^{\infty} \mathrm{d}\omega\, \omega \boldsymbol{\mathcal{A}}_0(\omega) = \Delta \begin{pmatrix} \boldsymbol{V}_0^\dagger \\ -\boldsymbol{W}_0^\dagger \end{pmatrix} \boldsymbol{\sigma}_3 \left[\boldsymbol{\mathcal{V}}_0 \boldsymbol{\mathcal{V}}_0^\dagger + \boldsymbol{\mathcal{W}}_0 \boldsymbol{\mathcal{W}}_0^\dagger \right] \boldsymbol{\sigma}_3 \begin{pmatrix} \boldsymbol{V}_0 & -\boldsymbol{W}_0 \end{pmatrix}. \tag{4.86}$$

Conversely, the spectral decomposition of $S\boldsymbol{M_0} + \boldsymbol{\Sigma}^{\mathrm{R}}(\boldsymbol{0}, 0)$ implies that

$$H_{\mathrm{PG}} = \Delta \begin{pmatrix} \boldsymbol{V}_0^\dagger \\ -\boldsymbol{W}_0^\dagger \end{pmatrix} \boldsymbol{\sigma}_3 \left[\boldsymbol{\mathcal{V}}_0 \boldsymbol{\mathcal{V}}_0^\dagger + \boldsymbol{\mathcal{W}}_0 \boldsymbol{\mathcal{W}}_0^\dagger \right] \boldsymbol{\sigma}_3 \begin{pmatrix} \boldsymbol{V}_0 & \boldsymbol{W}_0 \end{pmatrix}. \tag{4.87}$$

Comparing Eqs. (4.86) and (4.87), we find that the effective Hamiltonian for the PG gap is related to the first moment of the spectral function as

$$H_{\mathrm{PG}} = \int_{-\infty}^{\infty} \mathrm{d}\omega\, \omega \boldsymbol{\mathcal{A}}_0(\omega) \boldsymbol{\sigma}_3. \tag{4.88}$$

Calculation of the gap

Next, we discuss how to, in practice, use Eq. (4.81) to calculate the PG gap for both type I and type II modes. Using Eqs. (4.63)-(4.65), we carry out a Holstein-Primakoff expansion about a rotated spin configuration to obtain $\mathcal{H}(\phi, \theta)$. First, we discuss the case of a type II PG mode, where both angles ϕ and θ correspond to soft fluctuations. In this case, the Holstein-Primakoff expansion is

$$\mathcal{H}(\phi, \theta) = S(S+1)N\epsilon_{\mathrm{cl}} + SN\epsilon_{\mathrm{qu}}(\phi, \theta) + S \sum_{\boldsymbol{k},\alpha} \epsilon_{\boldsymbol{k},\alpha}(\phi, \theta) b_{\boldsymbol{k},\alpha}^\dagger b_{\boldsymbol{k},\alpha} + O(S^{1/2}),$$

as the classical configuration energy ϵ_{cl} is independent of ϕ and θ. The second derivative is then [101]

$$\frac{1}{SN} \left\langle \left(\frac{\partial^2 \mathcal{H}}{\partial \lambda_1 \partial \lambda_2} \right)_0 \right\rangle = \left(\frac{\partial^2 \epsilon_{\mathrm{qu}}}{\partial \lambda_1 \partial \lambda_2} \right)_0 + \frac{1}{N} \sum_{\boldsymbol{k}} \sum_{\alpha} \left(\frac{\partial^2 \epsilon_{\boldsymbol{k}\alpha}}{\partial \lambda_1 \partial \lambda_2} \right)_0 n_{\mathrm{B}}(\epsilon_{\boldsymbol{k},\alpha}) + O(S^{-1}), \tag{4.89}$$

where $\lambda_i = \phi$ or θ and $n_{\mathrm{B}}(\epsilon_{\boldsymbol{k},\alpha}) \equiv \left(\exp\left(\frac{S\epsilon_{\boldsymbol{k},\alpha}}{k_{\mathrm{B}}T} \right) - 1 \right)^{-1}$ is the Bose distribution function. Eq. (4.89) can be written in a more tractable form involving the free energy per spin, defined as

$$f(\phi, \theta) = S(S+1)\epsilon_{\mathrm{cl}} + S\epsilon_{\mathrm{qu}}(\phi, \theta) + \frac{k_{\mathrm{B}}T}{N} \sum_{\boldsymbol{k}} \sum_{\alpha} \ln\left(1 - e^{-S\epsilon_{\boldsymbol{k},\alpha}(\phi,\theta)/k_{\mathrm{B}}T} \right). \tag{4.90}$$

It follows that

$$g_{\lambda_1\lambda_2} \equiv \frac{1}{SN}\left\langle\left(\frac{\partial^2\mathcal{H}}{\partial\lambda_1\partial\lambda_2}\right)_0\right\rangle = \frac{1}{S}\left[\left(\frac{\partial^2 f}{\partial\lambda_1\partial\lambda_2}\right)_0 + K_{\lambda_1\lambda_2}\right], \tag{4.91}$$

where

$$K_{\lambda_1\lambda_2} \equiv \frac{S^2}{4k_{\mathrm{B}}TN}\sum_{\boldsymbol{k},\alpha}\left(\frac{\partial\epsilon_{\boldsymbol{k},\alpha}}{\partial\lambda_1}\right)_0\left(\frac{\partial\epsilon_{\boldsymbol{k},\alpha}}{\partial\lambda_2}\right)_0 \operatorname{csch}^2\left(\frac{S\epsilon_{\boldsymbol{k},\alpha}}{2k_{\mathrm{B}}T}\right). \tag{4.92}$$

To calculate the PG gap, we use the fact that the first moment of the spectral function is related to the effective Hamiltonian. Combining Eqs. (4.81) and (4.88), we find

$$H_{\mathrm{PG}} = \int_{-\infty}^{\infty}\mathrm{d}\omega\,\omega\mathcal{A}_0(\omega)\boldsymbol{\sigma}_3 = \frac{1}{2}\begin{pmatrix} g_{\theta\theta}+g_{\phi\phi} & g_{\theta\theta}-g_{\phi\phi}-2ig_{\phi\theta} \\ g_{\phi\phi}-g_{\theta\theta}-2ig_{\phi\theta} & -g_{\theta\theta}-g_{\phi\phi}\end{pmatrix}. \tag{4.93}$$

Diagonalizing H_{PG}, we find for the PG gap

$$\Delta(T) = S^0\sqrt{g_{\theta\theta}g_{\phi\phi}-g_{\phi\theta}^2} \qquad \text{(type II)}. \tag{4.94}$$

Next, we consider the case of a type I PG mode, where only the angle ϕ corresponds to a soft fluctuation. In this case, the Holstein-Primakoff expansion is only stable when $\theta = 0$. Following the same line of reasoning as Ref. [101], we find

$$H_{\mathrm{PG}} = \int_{-\infty}^{\infty}\mathrm{d}\omega\,\omega\mathcal{A}_0(\omega)\boldsymbol{\sigma}_3 = \frac{1}{2}\begin{pmatrix} S\left(\frac{\partial^2\epsilon_{\mathrm{cl}}}{\partial\theta^2}\right)_0+g_{\phi\phi} & S\left(\frac{\partial^2\epsilon_{\mathrm{cl}}}{\partial\theta^2}\right)_0-g_{\phi\phi} \\ g_{\phi\phi}-S\left(\frac{\partial^2\epsilon_{\mathrm{cl}}}{\partial\theta^2}\right)_0 & -S\left(\frac{\partial^2\epsilon_{\mathrm{cl}}}{\partial\theta^2}\right)_0-g_{\phi\phi}\end{pmatrix}. \tag{4.95}$$

Diagonalizing H_{PG}, we find for the PG gap

$$\Delta(T) = S^{1/2}\sqrt{\left(\frac{\partial^2\epsilon_{\mathrm{cl}}}{\partial\theta^2}\right)_0 g_{\phi\phi}} \qquad \text{(type I)}. \tag{4.96}$$

Evaluation of Eq. (4.92)

In this subsection, we discuss the evaluation of Eq. (4.92) and the circumstances when this term vanishes. One can work out an explicit form of these derivatives in terms of the spin exchange matrices in a local reference frame, avoiding the need to approximate them numerically. For this, we make use of the Hellmann-Feynmann theorem [173], generalized to bosonic Bogoliubov-de Gennes systems.

To begin, suppose the spin-wave theory depends on some continuous parameter λ. The linear spin-wave energies satisfy the eigenvalue equation $\boldsymbol{\sigma}_3 \boldsymbol{M}_{\boldsymbol{k}}(\lambda)\boldsymbol{V}_{\boldsymbol{k},\alpha}(\lambda) = \epsilon_{\boldsymbol{k},\alpha}(\lambda)\boldsymbol{V}_{\boldsymbol{k},\alpha}(\lambda)$. So long as the normalization conditions Eqs. (4.42)-(4.44) are satisfied, the derivatives of the spin-wave energies satisfy

$$\frac{\partial \epsilon_{\boldsymbol{k},\alpha}}{\partial \lambda} = \boldsymbol{V}^{\dagger}_{\boldsymbol{k},\alpha} \frac{\partial \boldsymbol{M}_{\boldsymbol{k}}}{\partial \lambda} \boldsymbol{V}_{\boldsymbol{k},\alpha}. \tag{4.97}$$

Making use of the local rotated frame in Eqs. (4.63)-(4.65), the first derivatives are evaluated to

$$\begin{aligned}
\left(\frac{\partial \hat{\boldsymbol{e}}_{a,0}}{\partial \theta}\right)_0 &= -\frac{i}{\sqrt{2}}\left(\hat{\boldsymbol{e}}_{a,+} - \hat{\boldsymbol{e}}_{a,-}\right), \quad \left(\frac{\partial \hat{\boldsymbol{e}}_{a,+}}{\partial \theta}\right)_0 = -\frac{i}{\sqrt{2}}\hat{\boldsymbol{e}}_{a,0}, \quad \left(\frac{\partial \hat{\boldsymbol{e}}_{a,-}}{\partial \theta}\right)_0 = +\frac{i}{\sqrt{2}}\hat{\boldsymbol{e}}_{a,0}, \\
\left(\frac{\partial \hat{\boldsymbol{e}}_{a,0}}{\partial \phi}\right)_0 &= +\frac{1}{\sqrt{2}}\left(\hat{\boldsymbol{e}}_{a,+} + \hat{\boldsymbol{e}}_{a,-}\right), \quad \left(\frac{\partial \hat{\boldsymbol{e}}_{a,+}}{\partial \phi}\right)_0 = -\frac{1}{\sqrt{2}}\hat{\boldsymbol{e}}_{a,0}, \quad \left(\frac{\partial \hat{\boldsymbol{e}}_{a,-}}{\partial \phi}\right)_0 = -\frac{1}{\sqrt{2}}\hat{\boldsymbol{e}}_{a,0}.
\end{aligned} \tag{4.98}$$

It follows that the derivatives of the local exchange couplings are given by

$$\begin{aligned}
\left(\frac{\partial \mathcal{J}^{+-}_{\boldsymbol{k},\alpha\beta}}{\partial \theta}\right)_0 &= +\frac{i}{\sqrt{2}}\left(\mathcal{J}^{+0}_{\boldsymbol{k},\alpha\beta} - \bar{\mathcal{J}}^{+0}_{\boldsymbol{k},\beta\alpha}\right), \quad \left(\frac{\partial \mathcal{J}^{++}_{\boldsymbol{k},\alpha\beta}}{\partial \theta}\right)_0 = -\frac{i}{\sqrt{2}}\left(\mathcal{J}^{+0}_{\boldsymbol{k},\alpha\beta} + \mathcal{J}^{+0}_{-\boldsymbol{k},\beta\alpha}\right), \\
\left(\frac{\partial \mathcal{J}^{+-}_{\boldsymbol{k},\alpha\beta}}{\partial \phi}\right)_0 &= -\frac{1}{\sqrt{2}}\left(\mathcal{J}^{+0}_{\boldsymbol{k},\alpha\beta} + \bar{\mathcal{J}}^{+0}_{\boldsymbol{k},\beta\alpha}\right), \quad \left(\frac{\partial \mathcal{J}^{++}_{\boldsymbol{k},\alpha\beta}}{\partial \phi}\right)_0 = -\frac{1}{\sqrt{2}}\left(\mathcal{J}^{+0}_{\boldsymbol{k},\alpha\beta} + \mathcal{J}^{+0}_{-\boldsymbol{k},\beta\alpha}\right),
\end{aligned} \tag{4.99}$$

where we have used the properties $\mathcal{J}^{0-}_{\boldsymbol{k},\alpha\beta} = \bar{\mathcal{J}}^{+0}_{\boldsymbol{k},\beta\alpha}$ and $\mathcal{J}^{0+}_{\boldsymbol{k},\alpha\beta} = \mathcal{J}^{+0}_{-\boldsymbol{k},\beta\alpha}$. We may then evaluate the derivatives of the spin-wave energies using Eqs. (4.97) and (4.99) as

$$\left(\frac{\partial \epsilon_{\boldsymbol{k},\alpha}}{\partial \lambda}\right)_0 = \boldsymbol{V}^{\dagger}_{\boldsymbol{k},\alpha} \begin{pmatrix} \boldsymbol{C}_{\boldsymbol{k},\lambda} & \boldsymbol{D}_{\boldsymbol{k},\lambda} \\ \boldsymbol{D}^{\dagger}_{\boldsymbol{k},\lambda} & \boldsymbol{C}^{\intercal}_{-\boldsymbol{k},\lambda} \end{pmatrix} \boldsymbol{V}_{\boldsymbol{k},\alpha}, \tag{4.100}$$

where

$$\left[\boldsymbol{C}_{\boldsymbol{k},\lambda}\right]_{\alpha\beta} \equiv \left(\frac{\partial \mathcal{J}^{+-}_{\boldsymbol{k},\alpha\beta}}{\partial \lambda}\right)_0, \quad \left[\boldsymbol{D}_{\boldsymbol{k},\lambda}\right]_{\alpha\beta} \equiv \left(\frac{\partial \mathcal{J}^{++}_{\boldsymbol{k},\alpha\beta}}{\partial \lambda}\right)_0. \tag{4.101}$$

The $K_{\lambda_1\lambda_2}$ term may then be evaluated as

$$K_{\lambda_1\lambda_2}(T) = \frac{S^2}{4k_{\mathrm{B}}TN} \sum_{\boldsymbol{k},\alpha} \boldsymbol{V}^{\dagger}_{\boldsymbol{k},\alpha} \begin{pmatrix} \boldsymbol{C}_{\boldsymbol{k},\lambda_1} & \boldsymbol{D}_{\boldsymbol{k},\lambda_1} \\ \boldsymbol{D}^{\dagger}_{\boldsymbol{k},\lambda_1} & \boldsymbol{C}^{\intercal}_{-\boldsymbol{k},\lambda_1} \end{pmatrix} \boldsymbol{V}_{\boldsymbol{k},\alpha} \boldsymbol{V}^{\dagger}_{\boldsymbol{k},\alpha} \begin{pmatrix} \boldsymbol{C}_{\boldsymbol{k},\lambda_2} & \boldsymbol{D}_{\boldsymbol{k},\lambda_2} \\ \boldsymbol{D}^{\dagger}_{\boldsymbol{k},\lambda_2} & \boldsymbol{C}^{\intercal}_{-\boldsymbol{k},\lambda_2} \end{pmatrix} \boldsymbol{V}_{\boldsymbol{k},\alpha} \operatorname{csch}^2\left(\frac{S\epsilon_{\boldsymbol{k},\alpha}}{2k_{\mathrm{B}}T}\right). \tag{4.102}$$

This expression vanishes in the zero-temperature limit, that is $K_{\lambda_1\lambda_2} \to 0$ as $T \to 0^+$. The expression in Eq. (4.102) is enormously useful as it involves only the linear spin-wave eigenvectors

and exchange matrices, and therefore circumvents the need to calculate derivatives of the spin-wave energies numerically (e.g. using a finite difference method).

We note the $\mathcal{J}^{+0}_{\boldsymbol{k},\alpha\beta}$ exchange couplings appearing in Eq. (4.99) are directly related to the three-magnon interaction vertices in Eq. (4.28), given by

$$T^{\alpha\beta\mu}_{\boldsymbol{k}\boldsymbol{k}'} = -\delta_{\alpha\mu}\mathcal{J}^{+0}_{\boldsymbol{k}',\beta\alpha} - \delta_{\beta\mu}\mathcal{J}^{+0}_{\boldsymbol{k},\alpha\beta}. \tag{4.103}$$

We may therefore conclude that if the spin-wave theory does not have any three-magnon interactions, i.e., $\mathcal{T}^{\alpha\beta\mu}_{\boldsymbol{k}\boldsymbol{k}'} = 0$, then $K_{\lambda_1\lambda_2}(T) = 0$ and the PG gap can be calculated to $O(S^0)$ from the curvature of the linear spin-wave free energy [see Eq. (4.91)]. In the general case where three-body interactions are present, this additional term $K_{\lambda_1\lambda_2}(T)$ will be nonzero; however, we emphasize that it still allows one to compute the PG gap within the framework of linear spin-wave theory.

Scaling of the PG gap

Finally, we discuss how the curvature formulas in Eqs. (4.94), (4.96) imply a *universal* scaling relation for the PG gap. Without loss of generality, the dispersion of the zero mode in linear spin wave theory takes the low-energy form $\epsilon_{\boldsymbol{k}} \sim v(\phi,\theta)|\boldsymbol{k}|^m$ where $m = 1$ ($m = 2$) for a type I (type II) PG mode. The free energy per spin takes the form

$$f(\phi,\theta) \sim S(S+1)\epsilon_{\mathrm{cl}}(\theta) + S\epsilon_{\mathrm{qu}}(\phi,\theta) + k_{\mathrm{B}}T\int_{\mathrm{BZ}}\frac{\mathrm{d}^d k}{V_{\mathrm{BZ}}}\ln\left(1 - e^{-Sv(\phi,\theta)|\boldsymbol{k}|^m/k_{\mathrm{B}}T}\right), \tag{4.104}$$

where the integral is taken over the first Brillouin zone (BZ) and V_{BZ} is its volume. To lowest order in temperature, the free energy is

$$\begin{aligned} f(\phi,\theta) &\sim S(S+1)\epsilon_{\mathrm{cl}}(\theta) + S\epsilon_{\mathrm{qu}}(\phi,\theta) - \frac{2S\pi^{d/2}}{m\Gamma(\frac{d}{2})V_{\mathrm{BZ}}}\zeta\left(\frac{1}{m}+1\right)\Gamma\left(\frac{1}{m}\right)(v(\phi,\theta))^{-d/m}\left(\frac{k_{\mathrm{B}}T}{S}\right)^{d/m+1} \\ &\equiv A(\phi,\theta) + B(\phi,\theta)\left(\frac{T}{S}\right)^{d/m+1}, \end{aligned} \tag{4.105}$$

where $A(\phi,\theta)$ and $B(\phi,\theta)$ are independent of temperature. Similarly, dimensional analysis of Eq. (4.92) implies

$$K_{\lambda_1\lambda_2} \sim C_{\lambda_1\lambda_2}\left(\frac{T}{S}\right)^{d/m+1} \tag{4.106}$$

as $T \to 0^+$, where $C_{\lambda_1\lambda_2}$ is independent of temperature and the angles ϕ, θ. Eq. (4.91) therefore takes the low-temperature form

$$g_{\lambda_1\lambda_2} \sim \frac{1}{S}\left(\frac{\partial^2 A}{\partial\lambda_1\partial\lambda_2}\right)_0 + \frac{1}{S}\left[\left(\frac{\partial^2 B}{\partial\lambda_1\partial\lambda_2}\right)_0 + C_{\lambda_1\lambda_2}\right]\left(\frac{T}{S}\right)^{d/m+1}. \tag{4.107}$$

Plugging Eq. (4.107) into Eqs. (4.94) and (4.96), and subsequently expanding for small temperature, we find the following functional form of the PG gap

$$\Delta(T) \sim \begin{cases} \Delta_0 + c\ \left(\frac{T}{S}\right)^{d+1} & \text{(type I)}, \\ \Delta_0 + c\ \left(\frac{T}{S}\right)^{d/2+1} & \text{(type II)}, \end{cases} \tag{4.108}$$

where c is a constant independent of temperature. This is the low-temperature form of the PG gap presented in the main text.

Chapter 5

Excess thermal conductivity and specific heat in $Lu_2V_2O_7$

5.0 Preface

Topological materials have emerged as a central theme in contemporary condensed matter physics, offering deep insights into the role of symmetry, geometry, and topology in governing the behaviour of quantum systems. As discussed in Chapter 1, topology is agnostic to whether (quasi)particles are fermions or bosons, so magnons can also be responsible for intrinsic anomalous transport. One of the most striking manifestations of this is the magnon Hall effect, in which a temperature gradient applied to certain magnetic insulators induces a transverse flow of spin and heat carried by magnons. This phenomenon arises from the *Berry phase* [187, 188] in momentum space, generated by the combination of lattice geometry, broken time-reversal symmetry, and spin-orbit interactions. In this sense, thermal transport measurements offer insight into a material's quantum many-body wavefunction.

The pyrochlore ferromagnet $Lu_2V_2O_7$ has attracted considerable attention as the first realization of the magnon Hall effect. In this material, the Lu^{3+} and V^{4+} ions each crystallize to a pyrochlore lattice. The rare-earth ion Lu^{3+} has a filled electronic subshell, and therefore no magnetic moment. Alternatively, the transition metal ion V^{4+} is magnetic, with electronic configuration $[Ar]3d^1$. In 3d transition metals, spin-orbit interactions are sub-leading to crystal field splitting within the hierarchy of energy scales [189]. The crystal field splits the five d-orbital

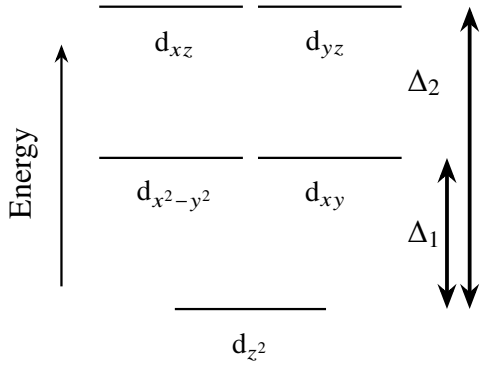


Figure 5.1: Crystal field splitting of the V^{4+} orbitals in $Lu_2V_2O_7$, where $\Delta_1 \approx 4\,600$ K and $\Delta_2 \approx 23\,000$ K [192, 193].

states,[31] leading to a single orbital ground state configuration as depicted in Fig. 5.1. Owing to the single ground state orbital, the angular momentum of V^{4+} is quenched, as the crystal field breaks full rotational symmetry. This is because the corresponding ground state wavefunction can be chosen to be purely real, and the orbital angular momentum averages to zero [189]. It follows that the magnetism of this material is dictated solely by the single valence electron of the V^{4+} ions, with pseudo-spin $S = 1/2$. This material has been determined to order as a collinear ferromagnet [141, 191], due to the dominant ferromagnetic Heisenberg exchange [192].

Despite the significant interest in $Lu_2V_2O_7$ and its interesting transport properties, it is argued in the manuscript making up this chapter that the microscopic interactions of this material are still unclear. By examining existing thermal conductivity, inelastic neutron scattering (INS) intensity data, and density functional theory (DFT) calculations, we propose that further neighbour interactions likely play an important role in the topological properties of this material. Conversely, we find that existing specific heat measurements are inconsistent with other experimental probes that cannot be reconciled by local exchange interactions.

[31] Many of the essential features of how the crystal field splits the orbitals can be determined by the point-group symmetries [189]. In particular, the pyrochlore oxides have the space group $Fd\bar{3}m$, which leads to a crystal field splitting of the d-orbitals with trigonal symmetry [190].

Excess thermal conductivity and specific heat in the pyrochlore ferromagnet $Lu_2V_2O_7$

Alexander Hickey and Michel J. P. Gingras

Department of Physics and Astronomy, University of Waterloo, Waterloo, Ontario N2L 3G1, Canada

Over the last decade, there has been immense interest in magnetic materials which host topologically non-trivial excitations. In ordered magnetic insulators, features analogous to those of topological insulators and semimetals can arise in the magnon band structure, and the associated Berry phases can manifest themselves into observable heat and spin transport phenomena. This was unambiguously observed in $Lu_2V_2O_7$ in the form of a magnon thermal Hall signal, and proposed to arise from the antisymmetric Dzyaloshinskii-Moriya (DM) interaction of spin-orbit origin. A precise value of the nearest-neighbour DM interaction is not known, as the values obtained from fitting both thermal transport and inelastic neutron scattering (INS) data, as well as from density functional theory (DFT), are all mutually inconsistent. Motivated by this, we investigate the effect of additional symmetry allowed perturbations to the spin Hamiltonian of $Lu_2V_2O_7$ in an attempt to reconcile the different experimental probes of this material, which has generally become viewed as the paradigmatic insulating material harbouring topological magnons. We find that the thermal transport and neutron scattering measurements are consistent with the addition of a small second nearest-neighbour DM interaction to the spin Hamiltonian. Conversely, we argue that existing specific heat measurements are inconsistent with neutron scattering experiments and cannot be reconciled with any additional exchange couplings to the bilinear spin-model in the perturbative regime. Our results motivate future thermal transport and specific heat measurements of this material.

5.1 Introduction

Since the groundbreaking prediction of the quantized Hall effect in the absence of Landau levels [194], the intrinsic topological structure of electronic systems has become a pillar of modern condensed matter physics. A key insight from this framework is that the geometry of Bloch wavefunctions can be described by a gauge field known as the *Berry connection*, and its associated field strength, the *Berry curvature* [195, 196]. This gauge structure can encode nontrivial topological features that have wide-ranging physical consequences, such as anomalous transport properties [197–214] and the existence of surface states that are robust to perturbations [215–224].

Although initially developed in the context of electronic (or more generally, fermionic) systems, interest has grown towards understanding how topology affects the transport of (bosonic) collective excitations in a broader class of materials. Magnetic insulators are of particular relevance to the field of spintronics, as they offer a potential platform for spin and thermal transport without Joule heating [225–230]. Recent theoretical and experimental studies have shown that topological band structures can emerge for photons [231–236], lattice vibrations (phonons) [237–248], triplons [249–254], and spin waves (magnons) [12–16, 19, 50, 128, 130, 131, 133, 255–283]. These findings have opened new directions for the research of topological transport in insulating materials, with implications for both fundamental physics and energy-efficient technologies [20]. Among these, magnons have attracted special attention due to their intrinsic connection to spin transport and their sensitivity to external magnetic fields.

One particular manifestation of magnon anomalous transport is the thermal Hall effect – a transverse thermal conductivity κ_{xy} in the presence of a temperature gradient, analogous to the electrical Hall effect. The first experimental observation of the magnon thermal Hall effect was reported in the insulating pyrochlore ferromagnet $Lu_2V_2O_7$ [15], attributed to the Berry curvature arising from the anisotropic Dzyaloshinskii-Moriya (DM) spin-spin interaction of spin-orbit origin. This experiment provided a clear link between magnon band topology and thermal transport, motivating extensive efforts to identify and understand analogous behaviour in other magnetic insulators. The magnon thermal Hall effect (MTHE) has since been observed in several pyrochlore, perovskite [16], kagome [17], and honeycomb [18] structured ferromagnets, and theoretically proposed in many other magnetic systems [129, 284–295]. Nonetheless, as $Lu_2V_2O_7$ was the first system in which the magnon thermal Hall effect was measured, it has served as a prototype for modelling topological magnon transport in insulating magnets.

$Lu_2V_2O_7$ is a ferromagnetic insulator, where the magnetic V^{4+} ions reside on the sites of a pyrochlore lattice of corner-sharing tetrahedra with effective spin-$\frac{1}{2}$ magnetic moments and cubic lattice parameter $a = 9.94$ Å [141, 144]. The moments order in a collinear ferromagnetic configuration below the Curie temperature, $T_c \approx 70$ K [15, 16, 141, 296, 297]. The ferromagnetic Heisenberg exchange is the dominant magnetic interaction [193], while the antisymmetric DM interaction appears as the leading perturbation, with the latter giving rise to the thermal Hall effect of magnons [13, 14, 256]. Thus, the *prima facie* magnetic model for $Lu_2V_2O_7$ is given by

$$\mathcal{H} = -J \sum_{\langle i,j \rangle} \boldsymbol{S}_i \cdot \boldsymbol{S}_j + D \sum_{\langle i,j \rangle} \hat{\boldsymbol{d}}_{ij} \cdot (\boldsymbol{S}_i \times \boldsymbol{S}_j), \tag{5.1}$$

where $\langle i, j \rangle$ denotes the sum over nearest-neighbour bonds, $J, D > 0$ are the nearest-neighbour Heisenberg and DM exchange couplings respectively, and $\hat{\boldsymbol{d}}_{ij}$ are the normalized *indirect* nearest-

neighbour DM vectors for the pyrochlore lattice [78],[32] determined by the Moriya rules [134]. The Heisenberg exchange favours collinear order, while the DM interaction introduces a chiral component that generates a nonzero Berry curvature in the magnon bands, an essential ingredient for producing the magnon thermal Hall effect.[33]

Despite the central role that the DM interaction plays in the thermal transport of $Lu_2V_2O_7$, its precise value at the nearest-neighbour level remains rather uncertain, raising questions as to what extent a quantitative understanding of the thermal Hall conductivity in this material – emerging as a paradigmatic example of MTHE – is currently at hand. By fitting thermal Hall conductivity measurements, Ideue *et al.* estimated the ratio $D/J = 0.38$ [16],[34] whereas subsequent inelastic neutron scattering (INS) experiments and density functional theory (DFT) calculations reported significantly lower values of $D/J \approx 0.18$ [145] and $D/J \approx 0.07$ [137], respectively. Although qualitatively, the intrinsic thermal Hall conductivity of magnons arises from broken time-reversal symmetry in addition to some degree of magnetic anisotropy [256], there does not appear to be a clear and intuitive picture of how individual anisotropic couplings in a spin Hamiltonian affect the thermal Hall response quantitatively. In addition, Onose *et al.*, by fitting the low-temperature specific heat, obtained a Heisenberg exchange of $J = 3.4$ meV. This value is significantly smaller than the commonly accepted estimates of $J = 8.2$ and 7.99 meV obtained from INS measurements [145][35] and DFT [137], respectively. This lack of consensus of the two key energy scales describing $Lu_2V_2O_7$ significantly muddles our understanding of the microscopic mechanisms driving the thermal Hall effect in $Lu_2V_2O_7$. This motivates a closer examination of how additional spin-spin couplings impact the thermal transport in this material.

Motivated by the discrepancies among various experimental probes of $Lu_2V_2O_7$, we investigate whether the inclusion of additional symmetry-allowed perturbations to Eq. (5.1) can reconcile these conflicting observations. In particular, we consider extensions to the bilinear spin model that preserve the underlying lattice symmetries, focusing on the role of first and second nearest-neighbour interactions. We find that the thermal Hall conductivity, INS spectra and existing DFT calculations are consistent with the presence of a small second nearest-neighbour DM interaction, which *preserves both* the collinear ferromagnetic ground state *and* the low-energy magnon dispersion. In contrast, we find that the excess specific heat data reported in Ref. [15] can in no obvious way be accounted for within any perturbative extension of the bilinear spin

[32] Refer to the Supplemental Material for details of the lattice conventions, spin-wave theory, and the calculation of the Berry curvature. It includes Refs. [1, 13, 15, 35, 48–50, 134, 145, 196, 257, 284, 294, 298–300].

[33] Note that the collinear order remains stable even in the presence of the DM interaction [1, 63].

[34] The thermal Hall conductivity was first fit by Onose *et al.* [15] to be $D/J = 0.32$, however, this calculation used an incorrect formula for the magnon Hall conductivity [13, 14]. This was later corrected in Ref. [16] to obtain $D/J = 0.38$, while retaining the value of $J = 3.4$ meV obtained in Ref. [15].

[35] In Ref. [145], it is noted that the average energy of the two weakly dispersing magnon optical bands is $\hbar\omega \approx 4J$, which unambiguously pins the Heisenberg exchange to $J \approx 8$ meV.

Hamiltonian. These findings highlight the sensitivity of the intrinsic magnon thermal Hall conductivity to longer-range interactions and, given its prominent place in the field of topological transport, call for further experiments on $Lu_2V_2O_7$.

5.2 Magnon Hall effect

To investigate the thermal Hall effect, we use linear spin-wave theory to model the low-temperature magnon transport. In this approach, spin operators are mapped to Holstein-Primakoff bosons [35] and subsequently expanded in powers of $1/S$, where S is the spin quantum number.[32] At leading order, the resulting quadratic Hamiltonian captures the essential features of the magnon band structure, including the influence of anisotropies such as the DM interaction, which leads to a finite Berry curvature in momentum space. This Berry curvature is the key quantity responsible for the transverse thermal transport of magnons and serves as the foundation for computing the magnon thermal Hall conductivity. In the following, we outline the spin-wave formalism and computation of thermal Hall transport coefficients.

More generally, the magnon spectrum is encoded in the Bogoliubov-de Gennes matrix $\boldsymbol{M}_{\boldsymbol{k}}$ [49, 171],[32] where the diagonalizing transformation $\boldsymbol{\mathcal{T}}_{\boldsymbol{k}}$ must simultaneously satisfy

$$\boldsymbol{\sigma}_3 \boldsymbol{\mathcal{T}}_{\boldsymbol{k}}^{\dagger} \boldsymbol{M}_{\boldsymbol{k}} \boldsymbol{\mathcal{T}}_{\boldsymbol{k}} = \boldsymbol{\Lambda}_{\boldsymbol{k}}, \tag{5.2}$$

$$\boldsymbol{\mathcal{T}}_{\boldsymbol{k}}^{\dagger} \boldsymbol{\sigma}_3 \boldsymbol{\mathcal{T}}_{\boldsymbol{k}} = \boldsymbol{\sigma}_3, \tag{5.3}$$

where $\boldsymbol{\sigma}_3 = \mathrm{diag}(\mathbb{I}, -\mathbb{I})$ is a block Pauli matrix acting on the particle-hole degree of freedom and

$$\boldsymbol{\Lambda}_{\boldsymbol{k}} = \mathrm{diag}(\epsilon_{\boldsymbol{k},1}, ..., \epsilon_{\boldsymbol{k},N_s}, \epsilon_{-\boldsymbol{k},1}, ..., \epsilon_{-\boldsymbol{k},N_s}), \tag{5.4}$$

is a diagonal matrix consisting of the magnon dispersions $\epsilon_{\boldsymbol{k},\alpha}$ where N_s is the number of sites in the magnetic unit cell, with $N_s = 4$ in the present case. The U(1) Berry connection can be conveniently expressed in matrix form [257]

$$\mathcal{A}_{\mu}^{(\alpha)}(\boldsymbol{k}) = i \ \mathrm{Tr}\left[\boldsymbol{\Gamma}_{\alpha} \boldsymbol{\sigma}_3 \boldsymbol{\mathcal{T}}_{\boldsymbol{k}}^{\dagger} \boldsymbol{\sigma}_3 \partial_{k_\mu} \boldsymbol{\mathcal{T}}_{\boldsymbol{k}}\right], \tag{5.5}$$

along with the corresponding Berry curvature

$$\mathcal{F}_{\mu\nu}^{(\alpha)}(\boldsymbol{k}) = \partial_{k_\mu} \mathcal{A}_{\nu}^{(\alpha)}(\boldsymbol{k}) - \partial_{k_\nu} \mathcal{A}_{\mu}^{(\alpha)}(\boldsymbol{k}), \tag{5.6}$$

where $[\boldsymbol{\Gamma}_{\alpha}]_{ij} \equiv \delta_{ij}\delta_{i\alpha}$ and μ, ν are Cartesian space components. The components of the thermal Hall conductivity are then given by [13, 14, 256]

$$\kappa_{\mu\nu} = -\frac{k_{\mathrm{B}}^2 T}{\hbar N_c} \sum_{\boldsymbol{k},\alpha} c_2[n_{\mathrm{B}}(\epsilon_{\boldsymbol{k},\alpha})] \mathcal{F}_{\mu\nu}^{(\alpha)}(\boldsymbol{k}), \tag{5.7}$$

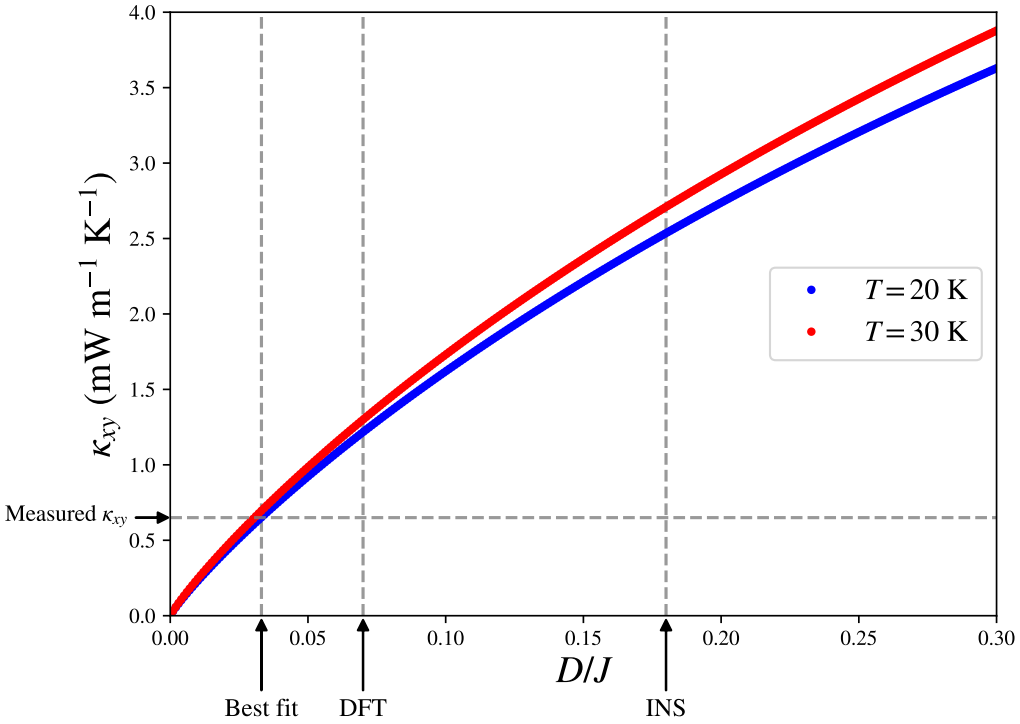


Figure 5.2: Calculated zero-field intrinsic thermal Hall conductivity at $T = 20$ K and $T = 30$ K due to magnons, using a ferromagnetic Heisenberg exchange of $J = 8$ meV. The measured value in Ref. [15] is $\kappa_{xy} \approx 0.65$ mW m^{-1} K^{-1} for both temperatures, corresponding to a DM interaction of $D/J = 0.03$. Using the exchange couplings from inelastic neutron scattering (INS) [145] or density functional theory (DFT) [137] results in an *excess* of thermal Hall conductivity.

where N_c is the number of magnetic unit cells, $n_{\mathrm{B}}(z) = \left(e^{Sz/k_{\mathrm{B}}T} - 1\right)^{-1}$ is the Bose distribution function and $c_2(z) \equiv \int_0^z \mathrm{d}\xi \ln^2(1 + \xi^{-1})$. Additional details regarding spin-wave theory and the numerical evaluation of Eq. (5.7) are provided in the Supplemental Material.[32]

We begin by computing the magnon thermal Hall conductivity for the minimal spin model of $Lu_2V_2O_2$ using Eq. (5.7), which incorporates the full magnon band structure obtained from linear spin-wave theory. Our benchmark is to obtain a thermal Hall conductivity of approximately $\kappa_{xy} \approx 0.65$ mW m^{-1} K^{-1} measured both at temperatures $T = 20$ K and $T = 30$ K at zero magnetic field, for a bulk magnetization aligned along the [001] cubic direction [15]. As shown in Fig. 5.2, we find that the DM interactions reported from INS and DFT result in a significantly overestimated thermal Hall conductivity relative to what was measured [15]. Our best fit to the experimental

data corresponds to a substantially smaller ratio of $D/J = 0.03$, well below all of the previous estimates. A key distinction in our approach is that we compute the thermal Hall conductivity using the full set of magnon bands across the whole BZ, rather than restricting to the lowest quadratically dispersing mode as in Refs. [15, 16]. Notably, we find that the higher-energy optical magnon bands contribute significantly to the total Berry curvature, particularly due to the presence of Weyl nodes [259], which act as sources of topological charge [222]. This raises an important question: how do we reconcile the apparent excess of thermal Hall conductivity predicted by Eq. (5.1) when using exchange parameters from INS or DFT? To address this, we ask whether small (perturbative) symmetry-allowed spin-spin interactions on the pyrochlore, neglected in the fits of INS data or in DFT calculations, could allow us to resolve the paradox articulated via the results in Fig. 5.2. To this end, we re-calculate the thermal Hall conductivity while including additional symmetry-allowed exchange interactions.

The simplest extension of Eq. (5.1) is to include all symmetry-allowed nearest-neighbour couplings beyond the isotropic Heisenberg and DM terms. For a spin-$\frac{1}{2}$ on the pyrochlore lattice, the most general nearest-neighbour Hamiltonian is [23, 135]

$$\mathcal{H} = \sum_{\langle i,j \rangle} \boldsymbol{S}_i \cdot \boldsymbol{J}_{ij} \cdot \boldsymbol{S}_j, \tag{5.8}$$

where $\boldsymbol{J}_{ij}$ are a set of bond-dependent exchange matrices, consisting of four independent exchange couplings. For example, the "0−1" bond[32] has exchange matrix (expressed in the global Cartesian frame) [139]

$$\boldsymbol{J}_{01} \equiv \begin{pmatrix} -J+K & -\frac{D}{\sqrt{2}} & -\frac{D}{\sqrt{2}} \\ \frac{D}{\sqrt{2}} & -J & \Gamma \\ \frac{D}{\sqrt{2}} & \Gamma & -J \end{pmatrix}, \tag{5.9}$$

where $J, D > 0$ are the same parameters that appear in Eq. (5.1). In addition, two more interactions, K and Γ, are included to incorporate subdominant anisotropic contributions. We show in Fig. 5.3 the calculated thermal Hall conductivity for this extended model, assuming a fixed nearest-neighbour Heisenberg exchange $J = 8$ meV and DM interaction $D/J = 0.07$ as given by the DFT calculations of Ref. [137]. We estimate that reproducing the experimentally measured thermal Hall response would then require a very large value of $|\Gamma|/J \gtrsim 0.3$. However, including both K and Γ results in a canted ferromagnetic ground state, which would lead to a sizeable anisotropy gap in the magnon spectrum, a value that is constrained by the energy resolution of the INS measurements [145]. We also note that these nearest-neighbour couplings were estimated using DFT, giving $K/J \approx -0.009$ and $\Gamma/J \approx 0.003$ [137]. We see from Fig. 5.3 that these small couplings result in a negligible change in the computed thermal Hall conductivity.

Given that the most general nearest-neighbour model fails to reconcile the discrepancy between DFT and the measured thermal Hall conductivity, we extend Eq. (5.8) to include small second

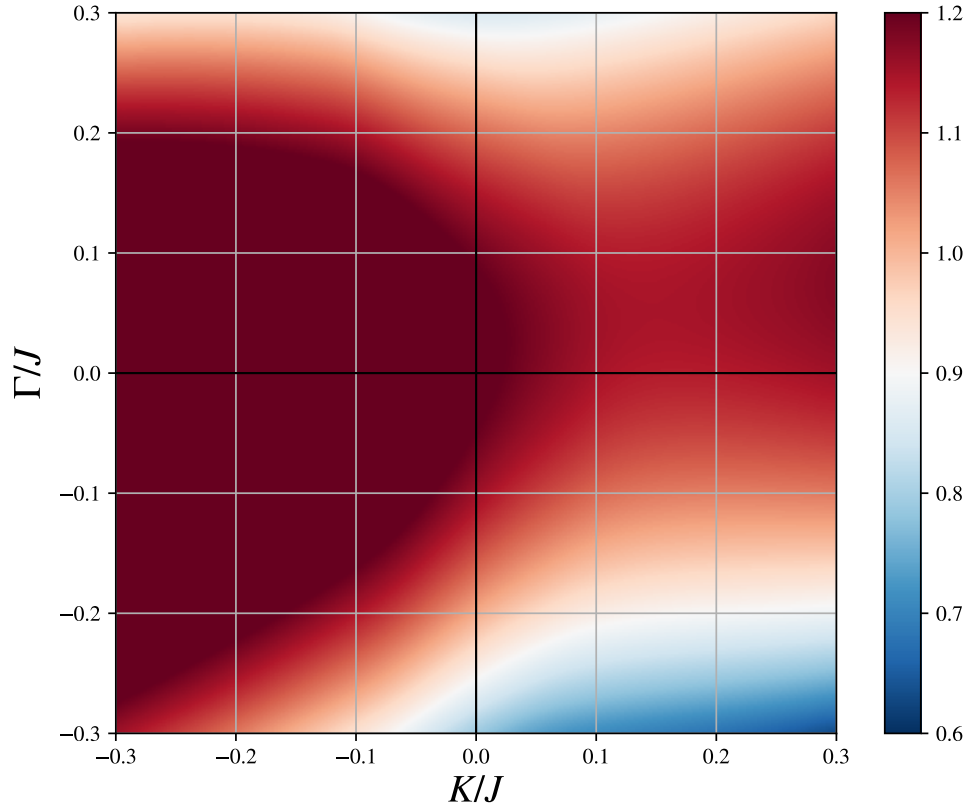


Figure 5.3: Zero-field thermal Hall conductivity at $T = 20$ K arising from additional nearest-neighbour anisotropic couplings to Eq. (5.1), with $J = 8$ meV and $D/J = 0.07$, in units of mW K^{-1} m^{-1}. The measured value of 0.65 mW K^{-1} m^{-1} [15] is obtained only for a large value of the symmetric off-diagonal exchange $|\Gamma|/J \gtrsim 0.3$.

nearest-neighbour interactions that both preserve the collinear ferromagnetic ground state and do not open a gap in the magnon spectrum. This condition allows for both a second-neighbour Heisenberg exchange and a second-neighbour DM interaction of the form

$$H' = \sum_{\langle\langle i,j \rangle\rangle} \left[-J_2 \boldsymbol{S}_i \cdot \boldsymbol{S}_j + \boldsymbol{D}_2(\boldsymbol{r}_j - \boldsymbol{r}_i) \cdot (\boldsymbol{S}_i \times \boldsymbol{S}_j) \right]. \tag{5.10}$$

The most general second-neighbour DM interaction on the pyrochlore lattice is described by two independent exchange couplings, which we label as $D_2^{(a)}$ and $D_2^{(b)}$.[32] As shown in Fig. 5.4, we find that a rather small second nearest-neighbour DM interaction of $D_2^{(b)}/J \approx -0.02$ brings the

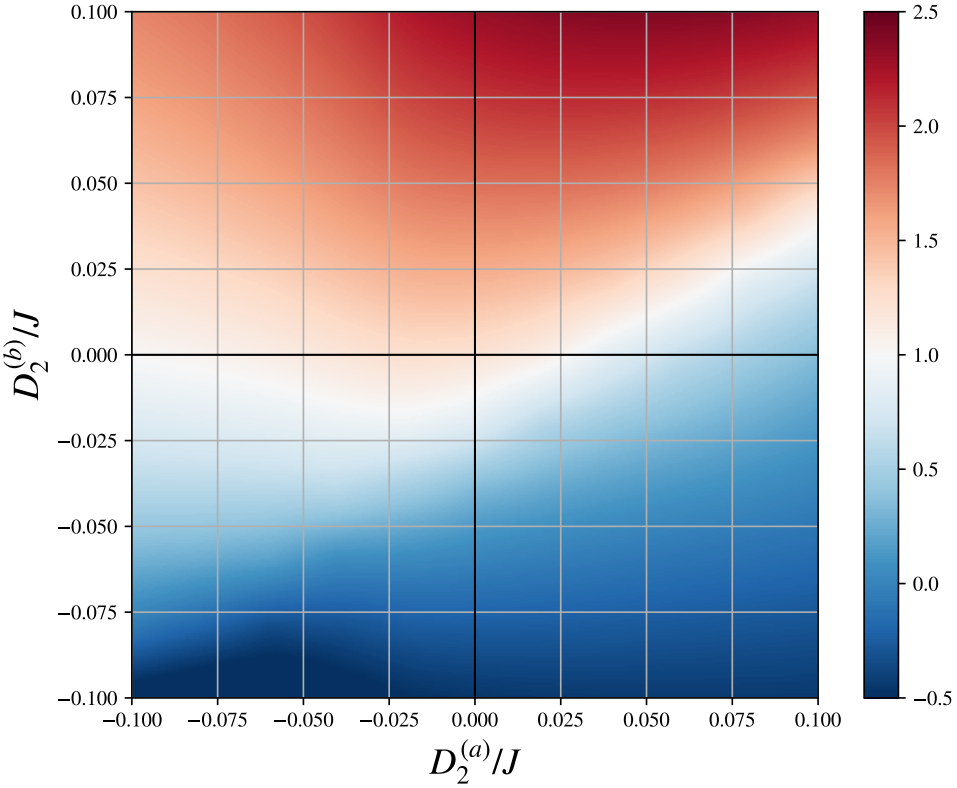


Figure 5.4: Zero-field thermal Hall conductivity at $T = 20$ K arising from the addition of the two second nearest-neighbour DM interactions to Eq. (5.1), with $J = 8$ meV and $D/J = 0.07$, in units of mW K^{-1} m^{-1}. The measured value of 0.65 mW K^{-1} m^{-1} [15] can be recovered for relatively small values of $D_2^{(a)}/J$ and $D_2^{(b)}/J$.

calculated thermal Hall conductivity into agreement with the measured value. Importantly, this correction remains within the perturbative regime and does not qualitatively alter the magnon spectrum, remaining consistent with the INS results reported in Ref. [145], as small modifications to the dispersion due to weak anisotropy would not be resolved. We also find that the second nearest-neighbour Heisenberg exchange leads to a negligible change in the thermal Hall conductivity; we refer the interested reader to the Supplemental Material for more details.[32] These results suggest that a modest second-neighbour DM interaction can significantly alter the Berry curvature and potentially resolve the discrepancy between previous thermal Hall and estimates of D within the range defined by the INS-determined value [145] and that from the DFT calculations [137].

5.3 Specific heat

The specific heat of $Lu_2V_2O_7$ in zero magnetic field was measured by Onose *et al.* [15] as a way to determine the exchange constant J. Doing so, Ref. [15] reported a ferromagnetic exchange coupling of $J = 3.4$ meV by fitting their low-temperature data,[36] in contrast to the significantly larger estimates of $J = 8.20, 7.99$ meV obtained from INS [145] and DFT [137] respectively. The discrepancy between these independently determined values of the ferromagnetic exchange motivates our re-examination of the existing low-temperature specific heat data.

Assuming $T \ll T_c$, the specific heat can be decomposed into contributions from magnons and phonons, respectively $C_V = C_{\text{mag}} + C_{\text{phonon}}$ where

$$C_{\text{mag}} = \frac{S^2}{k_B T^2} \sum_{\boldsymbol{k},\alpha} \epsilon_{\boldsymbol{k},\alpha}^2 n_B^2(\epsilon_{\boldsymbol{k},\alpha}) \exp\left(\frac{S\epsilon_{\boldsymbol{k},\alpha}}{k_B T}\right) \tag{5.11}$$

is the total contribution of the specific heat from the magnons. At low temperature, the magnon specific heat is controlled by gapless (pseudo-)Goldstone mode, with dispersion $\epsilon_{\boldsymbol{k}} = \frac{Ja^2}{16}|\boldsymbol{k}|^2$ [1, 15].[37] The specific heat per mole of $Lu_2V_2O_7$ is then

$$C_{\text{mag}} = \frac{15\zeta\left(\frac{5}{2}\right) N_A k_B}{4\pi^{3/2}} \left(\frac{k_B T}{J}\right)^{3/2}, \tag{5.12}$$

where N_A is the Avogadro number and $\zeta(z) \equiv \sum_{n=1}^{\infty} n^{-z}$ is the Riemann zeta function. Similarly, for the Debye contribution, we find

$$C_{\text{phonon}} = \frac{12\pi^4 N_A k_B}{5} \left(\frac{T}{\theta_D}\right)^3, \tag{5.13}$$

where θ_D is the characteristic Debye temperature. The phonon contribution to the specific heat is therefore sub-leading in temperature, relative to the magnon contribution.

The specific heat computed from Eq. (5.11) is shown in Fig. 5.5 along with the low-temperature measurements from Ref. [15]. We find that the best fit to the $T^{3/2}$ contribution corresponds to a Heisenberg exchange $J = 4.44$ meV,[38] notably higher than what was reported in Ref. [15], while

[36] The low-temperature specific heat in Ref. [15] fit by expanding the magnon dispersion to lowest order in wavevector $\epsilon_{\boldsymbol{k}} = \frac{Ja^2}{16}|\boldsymbol{k}|^2$.

[37] Notably, the dispersion of the gapless magnon mode is independent of the DM interaction to leading order in wavevector [1, 15].

[38] The specific heat is reported per mol of $Lu_2V_2O_7$.

still considerably smaller than the other reported values of $J \approx 8$ meV [137, 145]. We emphasize here that the INS measurements quite clearly pin the ferromagnetic exchange to $J \approx 8$ meV with reasonably high resolution [145].[32] Conversely, we see in Fig. 5.5 that a Heisenberg exchange of $J = 8$ meV significantly underestimates the specific heat, i.e. there appears to be an *excess* of specific heat in this material relative to what is naively expected from the magnons and phonons of a ferromagnetic insulator. While the addition of a second-neighbour DM interaction resolves the discrepancy between DFT, INS, and thermal Hall measurements, such an interaction does not simultaneously account for the missing specific heat in Fig. 5.5, as the curvature of the lowest magnon dispersion remains *unmodified* by the DM interaction. Furthermore, if one were to include other anisotropic couplings, these would generically open a gap in the magnon spectrum [1], leading to a thermally activated specific heat of the form $C_V \sim e^{-\Delta/k_B T}$ which would make the discrepancy with experiment even worse. In fact, we argue that there are no bilinear spin-exchange interactions that simultaneously (a) preserve the colinear ferromagnetic ground state, (b) are consistent with a Heisenberg exchange of $J \approx 8$ meV, and (c) fit the low-temperature specific heat measurements in Ref. [15]. This implies that either there are additional gapless quadratically dispersing quasiparticles that are currently unaccounted for in the existing theoretical framework, or there are significant issues with the existing low-temperature specific heat data available for this material. In either case, further experimental work to understand the specific heat of $Lu_2V_2O_7$ is warranted.

5.4 Discussion

In this work, we have re-examined the microscopic spin model of $Lu_2V_2O_7$ in an attempt to reconcile several persisting discrepancies in the magnetic exchange interactions across various independent experiments. Our analysis reveals that the thermal Hall conductivity, INS measurements and existing DFT calculations can be reconciled with the inclusion of a second nearest-neighbour DM interaction, as small as 2% of the nearest-neighbour Heisenberg exchange. Such a coupling, however, cannot account for the apparent excess in specific heat observed in [15].

An open question remains as to the precise origin of the lack of internal consistency in the Heisenberg exchange inferred from thermodynamic and spectroscopic experiments. Future experimental investigations should aim to independently measure and verify whether there is an excess of low-temperature specific heat as shown in Fig. 5.5. This would imply that there are quadratically dispersing excitations that are unaccounted for by both magnons and phonons, opening the door for potentially interesting new physics in $Lu_2V_2O_7$. Another topic not considered here is spin-phonon coupling [243, 246, 301–304], as there is increasing body of work suggesting that magneto-elastic effects play a crucial role in the thermal transport of magnetic insulators

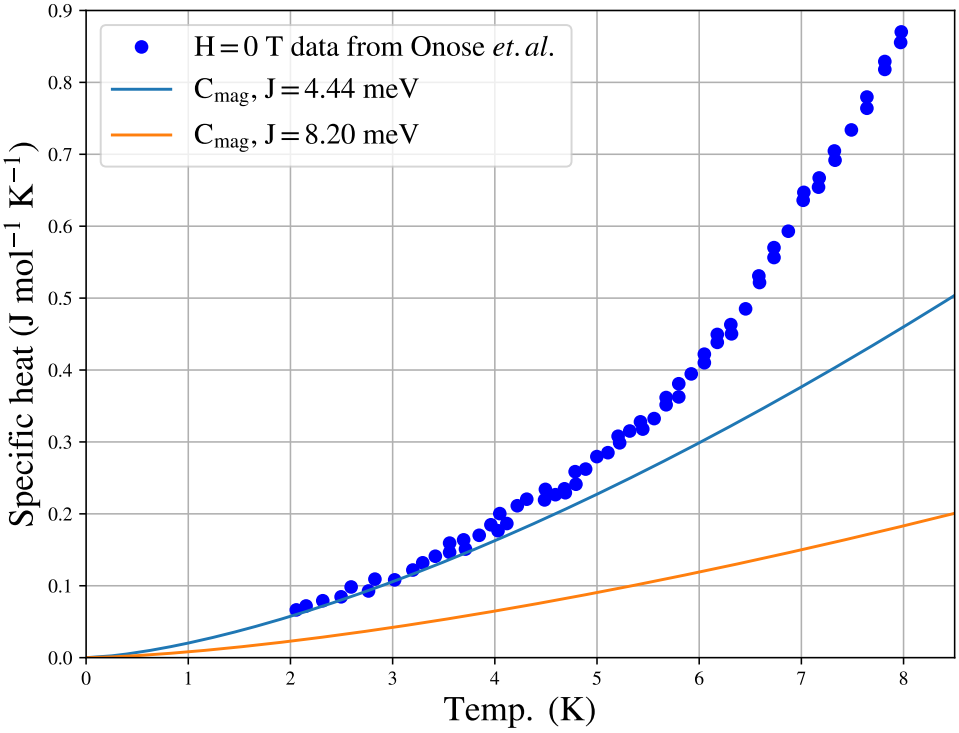


Figure 5.5: Low-temperature specific heat per mol of $Lu_2V_2O_7$ reported in Ref. [15], along with the leading magnon contribution to the specific heat for our best fit of $J = 4.44$ meV and the accepted value of $J = 8.2$ meV. We find that there is an excess of specific heat in these measurements that is not accounted for by magnons and phonons alone.

that is potentially relevant for $Lu_2V_2O_7$, although such a coupling is not likely to account for the additional specific heat. Nonetheless, our work provides a comprehensive analysis to guide future experimental efforts in understanding this most interesting material.

Acknowledgements

We thank Ramesh Dhakal, Griffin Howson, Subhankar Khatua, Yoshinori Onose, Jeffrey Rau, and Stephen Winter for useful discussions, and Yoshinori Onose for sharing with us the experimental data of Ref. [15]. AH acknowledges support from the NSERC of Canada CGS-D Scholarship. The work at the University of Waterloo was supported by the NSERC of Canada and the Canada

Research Chair (Tier 1, M.J.P.G.) program. This research was enabled in part by computing resources provided by the Digital Research Alliance of Canada.

Supplemental Material

Pyrochlore lattice convention

The pyrochlore lattice is a face-centred cubic (FCC) lattice with four sites, defining a regular tetrahedron, per primitive unit cell. The primitive FCC lattice vectors are given by

$$\boldsymbol{a}_1 = \frac{a}{2}(\hat{\boldsymbol{y}} + \hat{\boldsymbol{z}}) \qquad \boldsymbol{a}_2 = \frac{a}{2}(\hat{\boldsymbol{x}} + \hat{\boldsymbol{z}}) \qquad \boldsymbol{a}_3 = \frac{a}{2}(\hat{\boldsymbol{x}} + \hat{\boldsymbol{y}})\,. \tag{5.14}$$

At each FCC lattice site, there is a spin of type 0. The remaining three spins within a unit cell are separated by the sublattice vectors $\boldsymbol{r}_{0\mu} = \boldsymbol{a}_\mu/2$. The sublattice vectors between a spin of type μ to a spin of type ν can then be constructed as $\boldsymbol{r}_{\mu\nu} \equiv \boldsymbol{r}_{0\nu} - \boldsymbol{r}_{0\mu}$.

The nearest-neighbour (indirect) DM vectors in this representation are given by

$$\begin{aligned} \hat{\boldsymbol{d}}_{01} &= \frac{\hat{\boldsymbol{y}} - \hat{\boldsymbol{z}}}{\sqrt{2}}, & \hat{\boldsymbol{d}}_{02} &= \frac{\hat{\boldsymbol{z}} - \hat{\boldsymbol{x}}}{\sqrt{2}}, & \hat{\boldsymbol{d}}_{03} &= \frac{\hat{\boldsymbol{x}} - \hat{\boldsymbol{y}}}{\sqrt{2}}, \\ \hat{\boldsymbol{d}}_{12} &= \frac{\hat{\boldsymbol{x}} - \hat{\boldsymbol{y}}}{\sqrt{2}}, & \hat{\boldsymbol{d}}_{31} &= \frac{\hat{\boldsymbol{x}} + \hat{\boldsymbol{z}}}{\sqrt{2}}, & \hat{\boldsymbol{d}}_{23} &= \frac{\hat{\boldsymbol{y}} + \hat{\boldsymbol{z}}}{\sqrt{2}}, \end{aligned} \tag{5.15}$$

where the remaining DM vectors can be determined using the antisymmetry property $\hat{\boldsymbol{d}}_{ji} = -\hat{\boldsymbol{d}}_{ij}$. The second neighbour DM vectors are listed in Table 5.1, determined using the Sunny package in Julia [298].

Sublattice (α, α')	Unit cell displacement (m, n, ℓ)	$\boldsymbol{D}^{\intercal}(\mathbf{R}_{mn\ell} + \boldsymbol{r}_{\alpha\alpha'})$
$(0,1)$	$(-1,0,1)$	$\begin{pmatrix} D_2^{(a)} & \frac{D_2^{(b)}}{\sqrt{2}} & -\frac{D_2^{(b)}}{\sqrt{2}} \end{pmatrix}$
$(0,1)$	$(-1,1,0)$	$\begin{pmatrix} -D_2^{(a)} & \frac{D_2^{(b)}}{\sqrt{2}} & -\frac{D_2^{(b)}}{\sqrt{2}} \end{pmatrix}$
$(0,1)$	$(0,-1,0)$	$\begin{pmatrix} -D_2^{(a)} & \frac{D_2^{(b)}}{\sqrt{2}} & -\frac{D_2^{(b)}}{\sqrt{2}} \end{pmatrix}$
$(0,1)$	$(0,0,-1)$	$\begin{pmatrix} D_2^{(a)} & \frac{D_2^{(b)}}{\sqrt{2}} & -\frac{D_2^{(b)}}{\sqrt{2}} \end{pmatrix}$
$(0,2)$	$(-1,0,0)$	$\begin{pmatrix} -\frac{D_2^{(b)}}{\sqrt{2}} & D_2^{(a)} & \frac{D_2^{(b)}}{\sqrt{2}} \end{pmatrix}$
$(0,2)$	$(0,-1,1)$	$\begin{pmatrix} -\frac{D_2^{(b)}}{\sqrt{2}} & -D_2^{(a)} & \frac{D_2^{(b)}}{\sqrt{2}} \end{pmatrix}$
$(0,2)$	$(0,0,-1)$	$\begin{pmatrix} -\frac{D_2^{(b)}}{\sqrt{2}} & -D_2^{(a)} & \frac{D_2^{(b)}}{\sqrt{2}} \end{pmatrix}$
$(0,2)$	$(1,-1,0)$	$\begin{pmatrix} -\frac{D_2^{(b)}}{\sqrt{2}} & D_2^{(a)} & \frac{D_2^{(b)}}{\sqrt{2}} \end{pmatrix}$
$(0,3)$	$(-1,0,0)$	$\begin{pmatrix} \frac{D_2^{(b)}}{\sqrt{2}} & -\frac{D_2^{(b)}}{\sqrt{2}} & -D_2^{(a)} \end{pmatrix}$
$(0,3)$	$(0,-1,0)$	$\begin{pmatrix} \frac{D_2^{(b)}}{\sqrt{2}} & -\frac{D_2^{(b)}}{\sqrt{2}} & D_2^{(a)} \end{pmatrix}$
$(0,3)$	$(0,1,-1)$	$\begin{pmatrix} \frac{D_2^{(b)}}{\sqrt{2}} & -\frac{D_2^{(b)}}{\sqrt{2}} & D_2^{(a)} \end{pmatrix}$
$(0,3)$	$(1,0,-1)$	$\begin{pmatrix} \frac{D_2^{(b)}}{\sqrt{2}} & -\frac{D_2^{(b)}}{\sqrt{2}} & -D_2^{(a)} \end{pmatrix}$
$(1,2)$	$(0,-1,0)$	$\begin{pmatrix} \frac{D_2^{(b)}}{\sqrt{2}} & \frac{D_2^{(b)}}{\sqrt{2}} & D_2^{(a)} \end{pmatrix}$
$(1,2)$	$(0,-1,1)$	$\begin{pmatrix} \frac{D_2^{(b)}}{\sqrt{2}} & \frac{D_2^{(b)}}{\sqrt{2}} & -D_2^{(a)} \end{pmatrix}$
$(1,2)$	$(1,0,-1)$	$\begin{pmatrix} \frac{D_2^{(b)}}{\sqrt{2}} & \frac{D_2^{(b)}}{\sqrt{2}} & -D_2^{(a)} \end{pmatrix}$
$(1,2)$	$(1,0,0)$	$\begin{pmatrix} \frac{D_2^{(b)}}{\sqrt{2}} & \frac{D_2^{(b)}}{\sqrt{2}} & D_2^{(a)} \end{pmatrix}$
$(1,3)$	$(0,0,-1)$	$\begin{pmatrix} -\frac{D_2^{(b)}}{\sqrt{2}} & -D_2^{(a)} & -\frac{D_2^{(b)}}{\sqrt{2}} \end{pmatrix}$
$(1,3)$	$(0,1,-1)$	$\begin{pmatrix} -\frac{D_2^{(b)}}{\sqrt{2}} & D_2^{(a)} & -\frac{D_2^{(b)}}{\sqrt{2}} \end{pmatrix}$
$(1,3)$	$(1,-1,0)$	$\begin{pmatrix} -\frac{D_2^{(b)}}{\sqrt{2}} & D_2^{(a)} & -\frac{D_2^{(b)}}{\sqrt{2}} \end{pmatrix}$
$(1,3)$	$(1,0,0)$	$\begin{pmatrix} -\frac{D_2^{(b)}}{\sqrt{2}} & -D_2^{(a)} & -\frac{D_2^{(b)}}{\sqrt{2}} \end{pmatrix}$
$(2,3)$	$(-1,1,0)$	$\begin{pmatrix} -D_2^{(a)} & \frac{D_2^{(b)}}{\sqrt{2}} & \frac{D_2^{(b)}}{\sqrt{2}} \end{pmatrix}$
$(2,3)$	$(0,0,-1)$	$\begin{pmatrix} D_2^{(a)} & \frac{D_2^{(b)}}{\sqrt{2}} & \frac{D_2^{(b)}}{\sqrt{2}} \end{pmatrix}$

Sublattice (α, α')	Unit cell displacement (m, n, ℓ)	$\boldsymbol{D}^{\intercal}(\mathbf{R}_{mn\ell} + \boldsymbol{r}_{\alpha\alpha'})$
$(2, 3)$	$(0, 1, 0)$	$\begin{pmatrix} D_2^{(a)} & \frac{D_2^{(b)}}{\sqrt{2}} & \frac{D_2^{(b)}}{\sqrt{2}} \end{pmatrix}$
$(2, 3)$	$(1, 0, -1)$	$\begin{pmatrix} -D_2^{(a)} & \frac{D_2^{(b)}}{\sqrt{2}} & \frac{D_2^{(b)}}{\sqrt{2}} \end{pmatrix}$

Table 5.1: Second nearest-neighbour DM vectors for the pyrochlore lattice. The remaining DM vectors can be determined using the antisymmetry property $\boldsymbol{D}(-\boldsymbol{R}) = -\boldsymbol{D}(\boldsymbol{R})$.

Details of spin wave theory

We begin with a generic bilinear spin model

$$H = \frac{1}{2} \sum_{\boldsymbol{r}\boldsymbol{r}'} \sum_{\alpha\alpha'} \boldsymbol{S}_{\boldsymbol{r},\alpha}^{\intercal} \, \boldsymbol{J}_{\boldsymbol{r}-\boldsymbol{r}',\alpha\alpha'} \boldsymbol{S}_{\boldsymbol{r}',\alpha'}, \tag{5.16}$$

where r represents the position of a unit cell and α is a sublattice index. The associated spin wave theory can be obtained by expressing the spin-operators as Holstein-Primakoff bosons [35],

$$\boldsymbol{S}_{\boldsymbol{r},\alpha} = \left(S - n_{\boldsymbol{r},\alpha}\right) \hat{\boldsymbol{e}}_{\alpha,0} + \sqrt{S} \left[\left(1 - \frac{n_{\boldsymbol{r},\alpha}}{2S}\right)^{1/2} a_{\boldsymbol{r},\alpha} \hat{\boldsymbol{e}}_{\alpha,-} + a_{\boldsymbol{r}\alpha}^{\dagger} \left(1 - \frac{n_{\boldsymbol{r},\alpha}}{2S}\right)^{1/2} \hat{\boldsymbol{e}}_{\alpha,+} \right], \tag{5.17}$$

where $n_{\boldsymbol{r},\alpha} = a_{\boldsymbol{r},\alpha}^{\dagger} a_{\boldsymbol{r},\alpha}$ and the vectors $\hat{\boldsymbol{e}}_{\alpha,\pm} \equiv (\hat{\boldsymbol{e}}_{\alpha,x} \pm i\hat{\boldsymbol{e}}_{\alpha,y})/\sqrt{2}, \hat{\boldsymbol{e}}_{\alpha,0}$ define a local reference frame with respect to the classical ordering direction $\hat{\boldsymbol{e}}_{\alpha,0}$ (i.e. $\hat{\boldsymbol{e}}_{\alpha,x} \times \hat{\boldsymbol{e}}_{\alpha,y} = \hat{\boldsymbol{e}}_{\alpha,0}$). We define the Fourier transform of the exchange interactions in this local frame as

$$\mathcal{J}_{\boldsymbol{k},\alpha\beta}^{\mu\nu} \equiv \sum_{\boldsymbol{\delta}} e^{i\boldsymbol{k}\cdot\boldsymbol{\delta}} \hat{\boldsymbol{e}}_{\alpha,\mu}^{\intercal} \boldsymbol{J}_{\boldsymbol{\delta},\alpha\beta} \hat{\boldsymbol{e}}_{\beta,\nu}, \tag{5.18}$$

where the sum is taken over all bonds $\boldsymbol{\delta}$ between a site on sublattice α to a site on sublattice β. Expanding Eq. (5.17) in powers of $1/S$ about a classical ground state leads to the series representation $H = S^2 \sum_{n=0}^{\infty} S^{-n/2} H_n$. The linear spin wave Hamiltonian results from truncating the Holstein-Primakoff expansion at $O(S)$ about a configuration corresponding to a classical ground state

$$H = NS^2 \epsilon_{\text{cl}} + S \sum_{\boldsymbol{k}} \sum_{\alpha\alpha'} \left[A_{\boldsymbol{k}}^{\alpha\alpha'} a_{\boldsymbol{k},\alpha}^{\dagger} a_{\boldsymbol{k},\alpha'} + \frac{1}{2} \left(B_{\boldsymbol{k}}^{\alpha\alpha'} a_{\boldsymbol{k},\alpha}^{\dagger} a_{-\boldsymbol{k},\alpha'}^{\dagger} + \text{H.c.} \right) \right] + O(S^{1/2}). \tag{5.19}$$

where $N = N_c N_s$ is the number of spins in a system with N_c primitive unit cells, N_s is the number of spins per magnetic unit cell, here $N_s = 4$ for the $\boldsymbol{k} = \boldsymbol{0}$ ordering wave vector collinear ferromagnet, $NS^2\epsilon_{\text{cl}}$ is the energy of the classical configuration, and the interaction coefficients are

$$\epsilon_{\text{cl}} = \frac{1}{2N_s} \sum_{\alpha\beta} \mathcal{J}^{00}_{\boldsymbol{0},\alpha\beta}, \tag{5.20}$$

$$A^{\alpha\beta}_{\boldsymbol{k}} = \mathcal{J}^{+-}_{\boldsymbol{k},\alpha\beta} - \delta_{\alpha\beta} \sum_{\mu} \mathcal{J}^{00}_{\boldsymbol{0},\alpha\mu}, \tag{5.21}$$

$$B^{\alpha\beta}_{\boldsymbol{k}} = \mathcal{J}^{++}_{\boldsymbol{k},\alpha\beta}. \tag{5.22}$$

The linear spin wave energies and corresponding wavefunctions are determined by diagonalizing the $2N_s \times 2N_s$ boson Bogoliubov-de Gennes matrix [49]

$$\boldsymbol{\sigma}_3 \boldsymbol{M}_{\boldsymbol{k}} \equiv \begin{pmatrix} \boldsymbol{A}_{\boldsymbol{k}} & \boldsymbol{B}_{\boldsymbol{k}} \\ -\boldsymbol{B}^{\dagger}_{\boldsymbol{k}} & -\boldsymbol{A}^{\intercal}_{-\boldsymbol{k}} \end{pmatrix}, \tag{5.23}$$

where $\boldsymbol{\sigma}_3 = \text{diag}(\mathbb{I}, -\mathbb{I})$ is a block Pauli matrix. We may diagonalize Eq. (5.23) by defining a new set of bosons $b_{\boldsymbol{k},\alpha}$, such that

$$\begin{pmatrix} \boldsymbol{a}_{\boldsymbol{k}} \\ \boldsymbol{a}^{\dagger}_{-\boldsymbol{k}} \end{pmatrix} = \boldsymbol{\mathcal{T}}_{\boldsymbol{k}} \begin{pmatrix} \boldsymbol{b}_{\boldsymbol{k}} \\ \boldsymbol{b}^{\dagger}_{-\boldsymbol{k}} \end{pmatrix}. \tag{5.24}$$

By requiring $\left[b_{\boldsymbol{k},\alpha}, b_{\boldsymbol{k},\beta}\right] = 0$ and $\left[b_{\boldsymbol{k},\alpha}, b^{\dagger}_{\boldsymbol{k},\beta}\right] = \delta_{\alpha\beta}$, we obtain the para-unitary condition [48]

$$\boldsymbol{\mathcal{T}}^{\dagger}_{\boldsymbol{k}} \boldsymbol{\sigma}_3 \boldsymbol{\mathcal{T}}_{\boldsymbol{k}} = \boldsymbol{\sigma}_3. \tag{5.25}$$

The eigenvectors of Eq. (5.23) come in pairs $\boldsymbol{V}_{\boldsymbol{k},\alpha}$ and $\boldsymbol{W}_{\boldsymbol{k},\alpha} = \boldsymbol{\sigma}_1 \overline{\boldsymbol{V}}_{-\boldsymbol{k},\alpha}$ [50], with eigenvalues $\pm\epsilon_{\pm\boldsymbol{k},\alpha}$, and make up the columns of the transformation matrix, i.e.

$$\boldsymbol{\mathcal{T}}_{\boldsymbol{k}} = \begin{pmatrix} | & & | & | & & | \\ \boldsymbol{V}_{\boldsymbol{k},1} & \cdots & \boldsymbol{V}_{\boldsymbol{k},N_s} & \boldsymbol{W}_{\boldsymbol{k},1} & \cdots & \boldsymbol{W}_{\boldsymbol{k},N_s} \\ | & & | & | & & | \end{pmatrix}. \tag{5.26}$$

It follows from Eq. (5.25)

$$\boldsymbol{\mathcal{T}}^{-1}_{\boldsymbol{k}} \boldsymbol{\sigma}_3 \boldsymbol{M}_{\boldsymbol{k}} \boldsymbol{\mathcal{T}}_{\boldsymbol{k}} = \boldsymbol{\sigma}_3 \boldsymbol{\mathcal{T}}^{\dagger}_{\boldsymbol{k}} \boldsymbol{M}_{\boldsymbol{k}} \boldsymbol{\mathcal{T}}_{\boldsymbol{k}} = \text{diag}(\epsilon_{\boldsymbol{k},1}, \ldots, \epsilon_{\boldsymbol{k},N_s}, \epsilon_{-\boldsymbol{k},1}, \ldots, \epsilon_{-\boldsymbol{k},N_s}) \equiv \boldsymbol{\Lambda}_{\boldsymbol{k}}. \tag{5.27}$$

Here, we refer to $\boldsymbol{V}_{\boldsymbol{k},\alpha}$ and $\boldsymbol{W}_{\boldsymbol{k},\alpha}$ as the "particle" and "hole" states, respectively, due to their association with positive and negative eigenvalues. This analogy with fermionic systems extends

further, as it follows from Eqs. (5.21)-(5.22) that the spin wave theory has an effective "particle-hole symmetry"

$$\boldsymbol{\sigma}_1 \boldsymbol{M}_{\boldsymbol{k}} \boldsymbol{\sigma}_1 = \boldsymbol{M}_{-\boldsymbol{k}}^{\mathsf{T}}. \tag{5.28}$$

The linear spin wave Hamiltonian then takes the diagonal form

$$H = NS(S+1)\epsilon_{\mathrm{cl}} + NS\epsilon_{\mathrm{qu}} + S\sum_{\boldsymbol{k}}\sum_{\alpha=1}^{N_s} \epsilon_{\boldsymbol{k},\alpha} b^{\dagger}_{\boldsymbol{k},\alpha} b_{\boldsymbol{k},\alpha} + O(S^{1/2}), \tag{5.29}$$

where the quantum zero-point energy (per spin) is

$$\epsilon_{\mathrm{qu}} \equiv \frac{1}{2N}\sum_{\boldsymbol{k}}\sum_{\alpha=1}^{N_s} \epsilon_{\boldsymbol{k},\alpha}. \tag{5.30}$$

Next, to compute the intrinsic thermal Hall conductivity, the quantity of interest is the Berry curvature, arising from the geometric phase of the magnon eigenstates. The Berry connection is defined as [257]

$$\mathcal{A}^{(\alpha)}_{\mu}(\boldsymbol{k}) = i\,\mathrm{Tr}\left[\boldsymbol{\Gamma}_{\alpha}\boldsymbol{\sigma}_3 \boldsymbol{\mathcal{T}}^{\dagger}_{\boldsymbol{k}} \boldsymbol{\sigma}_3 \partial_{k_\mu} \boldsymbol{\mathcal{T}}_{\boldsymbol{k}}\right], \tag{5.31}$$

along with the corresponding Berry curvature

$$\mathcal{F}^{(\alpha)}_{\mu\nu}(\boldsymbol{k}) = \partial_{k_\mu}\mathcal{A}^{(\alpha)}_{\nu}(\boldsymbol{k}) - \partial_{k_\nu}\mathcal{A}^{(\alpha)}_{\mu}(\boldsymbol{k}) = i\,\mathrm{Tr}\left[\boldsymbol{\Gamma}_{\alpha}\boldsymbol{\sigma}_3\left(\frac{\partial \boldsymbol{\mathcal{T}}^{\dagger}_{\boldsymbol{k}}}{\partial k_\mu}\boldsymbol{\sigma}_3\frac{\partial \boldsymbol{\mathcal{T}}_{\boldsymbol{k}}}{\partial k_\nu} - \frac{\partial \boldsymbol{\mathcal{T}}^{\dagger}_{\boldsymbol{k}}}{\partial k_\nu}\boldsymbol{\sigma}_3\frac{\partial \boldsymbol{\mathcal{T}}_{\boldsymbol{k}}}{\partial k_\mu}\right)\right], \tag{5.32}$$

where we have defined $[\boldsymbol{\Gamma}_{\alpha}]_{ij} \equiv \delta_{ij}\delta_{i\alpha}$. Because the Bogoliubov transformation introduces a redundancy (i.e. it double counts the magnon states), we may restrict our attention only to the "particle" sector of the Hilbert space ($\alpha \leq N_s$).[39] Indeed, following from Eq. (5.28), the Berry curvature of the particle and hole sectors of the Hilbert space are related as

$$\mathcal{F}^{(\alpha+N_s)}_{\mu\nu}(\boldsymbol{k}) = -\mathcal{F}^{(\alpha)}_{\mu\nu}(-\boldsymbol{k}), \qquad \alpha \leq N_s. \tag{5.33}$$

The intrinsic components of the thermal Hall conductivity can be computed using the linear response theory, resulting in [13, 284]

$$\kappa_{\mu\nu} = -\frac{k_{\mathrm{B}}^2 T}{\hbar N_c}\sum_{\boldsymbol{k}}\sum_{\alpha=1}^{N_s} c_2[n_{\mathrm{B}}(\epsilon_{\boldsymbol{k},\alpha})]\mathcal{F}^{(\alpha)}_{\mu\nu}(\boldsymbol{k}), \tag{5.34}$$

where $n_{\mathrm{B}}(z) = \left(e^{Sz/k_{\mathrm{B}}T} - 1\right)^{-1}$ is the Bose distribution function and $c_2(z) \equiv \int_0^z \mathrm{d}\xi\, \ln^2(1+\xi^{-1})$.

[39] The term Hilbert space is a misnomer here, the lack of a positive-definite inner product makes this a *Krein space* [299, 300].

Gauge-invariant calculation of the Berry Curvature

Consider a U(1) gauge transformation (change of phase) of the magnon eigenstates $\mathcal{T}(\boldsymbol{k}) \rightarrow \mathcal{T}(\boldsymbol{k}) \exp\left(i\boldsymbol{\sigma}_3\boldsymbol{\Theta}(\boldsymbol{k})\right)$ where the matrix

$$\boldsymbol{\Theta}(\boldsymbol{k}) \equiv \mathrm{diag}(\theta_1(\boldsymbol{k}), ..., \theta_{N_s}(\boldsymbol{k}), \theta_1(-\boldsymbol{k}), ..., \theta_{N_s}(-\boldsymbol{k})), \tag{5.35}$$

is a smooth function of the wavevector $\boldsymbol{k}$. In this case, the Berry connection transforms as $\mathcal{A}_\mu^{(\alpha)}(\boldsymbol{k}) \rightarrow \mathcal{A}_\mu^{(\alpha)}(\boldsymbol{k}) - \mathrm{Tr}\left[\boldsymbol{\Gamma}_\alpha\boldsymbol{\sigma}_3\partial_{k_\mu}\boldsymbol{\Theta}(\boldsymbol{k})\right]$, while the Berry curvature $\mathcal{F}_{\mu\nu}^{(\alpha)}(\boldsymbol{k})$ is invariant, bearing resemblance to a gauge transformation of the electromagnetic vector potential.

As it stands, the computation of the Berry curvature is non-trivial, as Eq. (5.32) contains derivatives of the magnon eigenstates. In practice, the matrix $\boldsymbol{\mathcal{T}}_{\boldsymbol{k}}$ generally needs to be computed by numerically diagonalizing Eq. (5.23) at each wavevector $\boldsymbol{k}$. This procedure yields eigenstates with wildly different phase factors, thereby preventing a calculation of the derivative $\partial_{k_\mu}\boldsymbol{\mathcal{T}}_{\boldsymbol{k}}$. A well-defined derivative requires a locally smooth choice of gauge (i.e. continuous and differentiable).[40] To circumvent the need for a numerical gauge-smoothing procedure, which is highly nontrivial, we derive here a formula for the bosonic Berry curvature that does not involve derivatives of the magnon eigenstates.

To begin, we note that since $\boldsymbol{\Gamma}_\alpha = \boldsymbol{\Gamma}_\alpha^2$ is a projection operator, we can use the cyclic property of the trace to write Eq. (5.32) as

$$\mathcal{F}_{\mu\nu}^{(\alpha)}(\boldsymbol{k}) = i\ \mathrm{Tr}\left[\boldsymbol{\Gamma}_\alpha\boldsymbol{\sigma}_3\frac{\partial\boldsymbol{\mathcal{T}}_{\boldsymbol{k}}^\dagger}{\partial k_\mu}\boldsymbol{\sigma}_3\frac{\partial\boldsymbol{\mathcal{T}}_{\boldsymbol{k}}}{\partial k_\nu}\boldsymbol{\Gamma}_\alpha - (\mu \leftrightarrow \nu)\right]. \tag{5.36}$$

The eigenvalue equation [Eq. (5.27)] is rearranged as

$$\boldsymbol{\sigma}_3\boldsymbol{M}_{\boldsymbol{k}}\boldsymbol{\mathcal{T}}_{\boldsymbol{k}}\boldsymbol{\Gamma}_\alpha = \Lambda_{\boldsymbol{k}}^{\alpha\alpha}\boldsymbol{\mathcal{T}}_{\boldsymbol{k}}\boldsymbol{\Gamma}_\alpha. \tag{5.37}$$

Next, note that

$$\begin{aligned}
\Lambda_{\boldsymbol{k}}^{\alpha\alpha}\partial_{k_\mu}\boldsymbol{\mathcal{T}}_{\boldsymbol{k}}\boldsymbol{\Gamma}_\alpha &= \partial_{k_\mu}\left(\Lambda_{\boldsymbol{k}}^{\alpha\alpha}\boldsymbol{\mathcal{T}}_{\boldsymbol{k}}\boldsymbol{\Gamma}_\alpha\right) - \boldsymbol{\mathcal{T}}_{\boldsymbol{k}}\partial_{k_\mu}\Lambda_{\boldsymbol{k}}^{\alpha\alpha}\boldsymbol{\Gamma}_\alpha \\
&= \partial_{k_\mu}\left(\boldsymbol{\sigma}_3\boldsymbol{M}_{\boldsymbol{k}}\boldsymbol{\mathcal{T}}_{\boldsymbol{k}}\boldsymbol{\Gamma}_\alpha\right) - \boldsymbol{\mathcal{T}}_{\boldsymbol{k}}\partial_{k_\mu}\Lambda_{\boldsymbol{k}}^{\alpha\alpha}\boldsymbol{\Gamma}_\alpha \\
&= \boldsymbol{\sigma}_3\left(\partial_{k_\mu}\boldsymbol{M}_{\boldsymbol{k}}\right)\boldsymbol{\mathcal{T}}_{\boldsymbol{k}}\boldsymbol{\Gamma}_\alpha + \boldsymbol{\sigma}_3\boldsymbol{M}_{\boldsymbol{k}}\left(\partial_{k_\mu}\boldsymbol{\mathcal{T}}_{\boldsymbol{k}}\boldsymbol{\Gamma}_\alpha\right) - \boldsymbol{\mathcal{T}}_{\boldsymbol{k}}\partial_{k_\mu}\Lambda_{\boldsymbol{k}}^{\alpha\alpha}\boldsymbol{\Gamma}_\alpha.
\end{aligned} \tag{5.38}$$

[40] A globally smooth choice of gauge is not possible in the most general case [196], however, we assume that any topological obstruction has measure zero in the BZ volume.

Rearranging Eq. (5.38), we find

$$\partial_{k_\mu} \mathcal{T}_{\boldsymbol{k}} \mathbf{\Gamma}_\alpha = \left(\Lambda_{\boldsymbol{k}}^{\alpha\alpha} - \boldsymbol{\sigma}_3 \boldsymbol{M}_{\boldsymbol{k}}\right)^{-1} \left[\boldsymbol{\sigma}_3 \left(\partial_{k_\mu} \boldsymbol{M}_{\boldsymbol{k}}\right) - \partial_{k_\mu} \Lambda_{\boldsymbol{k}}^{\alpha\alpha}\right] \mathcal{T}_{\boldsymbol{k}} \mathbf{\Gamma}_\alpha, \tag{5.39}$$

and similarly

$$\mathbf{\Gamma}_\alpha \partial_{k_\mu} \mathcal{T}_{\boldsymbol{k}}^\dagger = \mathbf{\Gamma}_\alpha \mathcal{T}_{\boldsymbol{k}}^\dagger \left[\left(\partial_{k_\mu} \boldsymbol{M}_{\boldsymbol{k}}\right) \boldsymbol{\sigma}_3 - \partial_{k_\mu} \Lambda_{\boldsymbol{k}}^{\alpha\alpha}\right] \left(\Lambda_{\boldsymbol{k}}^{\alpha\alpha} - \boldsymbol{M}_{\boldsymbol{k}} \boldsymbol{\sigma}_3\right)^{-1}, \tag{5.40}$$

Combining Eqs. (5.36) and (5.39)-(5.40), the Berry curvature becomes

$$\begin{aligned}
\mathcal{F}_{\mu\nu}^{(\alpha)}(\boldsymbol{k}) = \quad & i \operatorname{Tr}\Big[\boldsymbol{\sigma}_3 \mathbf{\Gamma}_\alpha \mathcal{T}_{\boldsymbol{k}}^\dagger \left[\left(\partial_{k_\mu} \boldsymbol{M}_{\boldsymbol{k}}\right) \boldsymbol{\sigma}_3 - \partial_{k_\mu} \Lambda_{\boldsymbol{k}}^{\alpha\alpha}\right] \boldsymbol{\sigma}_3 \left(\Lambda_{\boldsymbol{k}}^{\alpha\alpha} - \boldsymbol{\sigma}_3 \boldsymbol{M}_{\boldsymbol{k}}\right)^{-2} \\
& \qquad \times \left[\boldsymbol{\sigma}_3 \left(\partial_{k_\nu} \boldsymbol{M}_{\boldsymbol{k}}\right) - \partial_{k_\nu} \Lambda_{\boldsymbol{k}}^{\alpha\alpha}\right] \mathcal{T}_{\boldsymbol{k}} \mathbf{\Gamma}_\alpha - (\mu \leftrightarrow \nu)\Big] \\
= \quad & i \operatorname{Tr}\Big[\boldsymbol{\sigma}_3 \mathbf{\Gamma}_\alpha \mathcal{T}_{\boldsymbol{k}}^\dagger \left(\partial_{k_\mu} \boldsymbol{M}_{\boldsymbol{k}}\right) \left(\Lambda_{\boldsymbol{k}}^{\alpha\alpha} - \boldsymbol{\sigma}_3 \boldsymbol{M}_{\boldsymbol{k}}\right)^{-2} \boldsymbol{\sigma}_3 \left(\partial_{k_\nu} \boldsymbol{M}_{\boldsymbol{k}}\right) \mathcal{T}_{\boldsymbol{k}} \mathbf{\Gamma}_\alpha - (\mu \leftrightarrow \nu)\Big] \\
& - i \operatorname{Tr}\Big[\boldsymbol{\sigma}_3 \mathbf{\Gamma}_\alpha \mathcal{T}_{\boldsymbol{k}}^\dagger \left(\partial_{k_\mu} \Lambda_{\boldsymbol{k}}^{\alpha\alpha}\right) \boldsymbol{\sigma}_3 \left(\Lambda_{\boldsymbol{k}}^{\alpha\alpha} - \boldsymbol{\sigma}_3 \boldsymbol{M}_{\boldsymbol{k}}\right)^{-2} \boldsymbol{\sigma}_3 \left(\partial_{k_\nu} \boldsymbol{M}_{\boldsymbol{k}}\right) \mathcal{T}_{\boldsymbol{k}} \mathbf{\Gamma}_\alpha - (\mu \leftrightarrow \nu)\Big] \\
& - i \operatorname{Tr}\Big[\boldsymbol{\sigma}_3 \mathbf{\Gamma}_\alpha \mathcal{T}_{\boldsymbol{k}}^\dagger \left(\partial_{k_\mu} \boldsymbol{M}_{\boldsymbol{k}}\right) \left(\Lambda_{\boldsymbol{k}}^{\alpha\alpha} - \boldsymbol{\sigma}_3 \boldsymbol{M}_{\boldsymbol{k}}\right)^{-2} \left(\partial_{k_\nu} \Lambda_{\boldsymbol{k}}^{\alpha\alpha}\right) \mathcal{T}_{\boldsymbol{k}} \mathbf{\Gamma}_\alpha - (\mu \leftrightarrow \nu)\Big] \\
& + i \operatorname{Tr}\Big[\boldsymbol{\sigma}_3 \mathbf{\Gamma}_\alpha \mathcal{T}_{\boldsymbol{k}}^\dagger \left(\partial_{k_\mu} \Lambda_{\boldsymbol{k}}^{\alpha\alpha}\right) \boldsymbol{\sigma}_3 \left(\Lambda_{\boldsymbol{k}}^{\alpha\alpha} - \boldsymbol{\sigma}_3 \boldsymbol{M}_{\boldsymbol{k}}\right)^{-2} \left(\partial_{k_\nu} \Lambda_{\boldsymbol{k}}^{\alpha\alpha}\right) \mathcal{T}_{\boldsymbol{k}} \mathbf{\Gamma}_\alpha - (\mu \leftrightarrow \nu)\Big].
\end{aligned} \tag{5.41}$$

Expanding the additional terms with $(\mu \leftrightarrow \nu)$ and utilizing the cyclic property of the trace, we find that the last three lines of Eq. (5.41) will vanish. The Berry curvature is then:

$$\mathcal{F}_{\mu\nu}^{(\alpha)}(\boldsymbol{k}) = -2 \operatorname{Im} \operatorname{Tr}\Big[\boldsymbol{\sigma}_3 \mathbf{\Gamma}_\alpha \mathcal{T}_{\boldsymbol{k}}^\dagger \left(\partial_{k_\mu} \boldsymbol{M}_{\boldsymbol{k}}\right) \left(\Lambda_{\boldsymbol{k}}^{\alpha\alpha} - \boldsymbol{\sigma}_3 \boldsymbol{M}_{\boldsymbol{k}}\right)^{-2} \boldsymbol{\sigma}_3 \left(\partial_{k_\nu} \boldsymbol{M}_{\boldsymbol{k}}\right) \mathcal{T}_{\boldsymbol{k}}\Big]. \tag{5.42}$$

This is equivalent to the expression for the Berry curvature presented in Ref. [294]. The formula in Eq. (5.42) does not explicitly depend on the phases of the magnon eigenstates, so it can be evaluated under any choice of gauge. In other words, it is no longer necessary to pick $\mathcal{T}_{\boldsymbol{k}}$ to be a smooth function of $\boldsymbol{k}$, as the derivatives have been moved from the wavefunction to the magnon Hamiltonian. Furthermore, these derivatives can be calculated analytically, circumventing the need to calculate any derivatives numerically (e.g. using a finite-difference method). In particular, using Eq. (5.23), we find

$$\partial_{k_\mu} \boldsymbol{M}_{\boldsymbol{k}} = \begin{pmatrix} \partial_{k_\mu} \boldsymbol{A}_{\boldsymbol{k}} & \partial_{k_\mu} \boldsymbol{B}_{\boldsymbol{k}} \\ \partial_{k_\mu} \boldsymbol{B}_{\boldsymbol{k}}^\dagger & \partial_{k_\mu} \boldsymbol{A}_{-\boldsymbol{k}}^\intercal \end{pmatrix}, \tag{5.43}$$

where the components are

$$\partial_{k_\mu} A^{\alpha\alpha'}_{\boldsymbol{k}} = i \sum_{\boldsymbol{\delta}} \delta_\mu e^{i\boldsymbol{k}\cdot\boldsymbol{\delta}} \mathcal{J}^{+-}_{\boldsymbol{\delta},\alpha\alpha'}, \tag{5.44}$$

$$\partial_{k_\mu} B^{\alpha\alpha'}_{\boldsymbol{k}} = i \sum_{\boldsymbol{\delta}} \delta_\mu e^{i\boldsymbol{k}\cdot\boldsymbol{\delta}} \mathcal{J}^{++}_{\boldsymbol{\delta},\alpha\alpha'}. \tag{5.45}$$

To calculate the thermal Hall conductivity, we use the Eqs. (5.42)-(5.45) to compute the sum over wavevectors in Eq. (5.34) numerically.

Second nearest-neighbour Heisenberg model

In this section, we discuss the effect of a second nearest-neighbour Heisenberg interaction on the thermal conductivity of $Lu_2V_2O_7$. In this case, we consider the Hamiltonian

$$\mathcal{H} = -J_1 \sum_{\langle i,j\rangle} \boldsymbol{S}_i \cdot \boldsymbol{S}_j - J_2 \sum_{\langle\langle i,j\rangle\rangle} \boldsymbol{S}_i \cdot \boldsymbol{S}_j + D \sum_{\langle i,j\rangle} \hat{\boldsymbol{d}}_{ij} \cdot (\boldsymbol{S}_i \times \boldsymbol{S}_j), \tag{5.46}$$

where $J_1 > 0$ is the dominant ferromagnetic exchange and we allow for J_2 to be positive or negative, while assuming $|J_2|, D \ll |J_1|$. The classical (and quantum [1]) ground state of this model is a collinear ferromagnetic configuration, which we assume is oriented along the [001] cubic direction to be consistent with the thermal Hall measurements in Ref. [15].

Consider first the case when $D = 0$. The linear spin wave theory for Eq. (5.46) is exactly solvable, with two dispersive magnon bands and two degenerate flat bands at energy

$$S\epsilon_{\boldsymbol{k},3} = S\epsilon_{\boldsymbol{k},4} = 8S(J_1 + 2J_2). \tag{5.47}$$

Including now a small DM interaction, the anisotropy leads to the two optical flat bands becoming very weakly dispersive, centred around the energy $8S(J_1 + 2J_2)$. The INS measurements in Ref. [145] show a nearly flat line of intensity at an energy transfer of $\hbar\omega \approx 32$ meV, leading us to conclude that any second nearest-neighbour Heisenberg exchange must be constrained to satisfy the equation $8S(J_1 + 2J_2) \approx 32$ meV.

The intrinsic thermal Hall conductivity, subject to the appropriate constraint, is shown in Fig. 5.6. In the case where $J_1 = 8$ meV, this calculation is equivalent to the nearest-neighbour model from the main text, where $J_2 = 0$. We find that by varying the second nearest-neighbour coupling within a window of 1 meV, there is a negligible change to the thermal Hall conductivity, which does not adequately address the inconsistencies discussed in the main text.

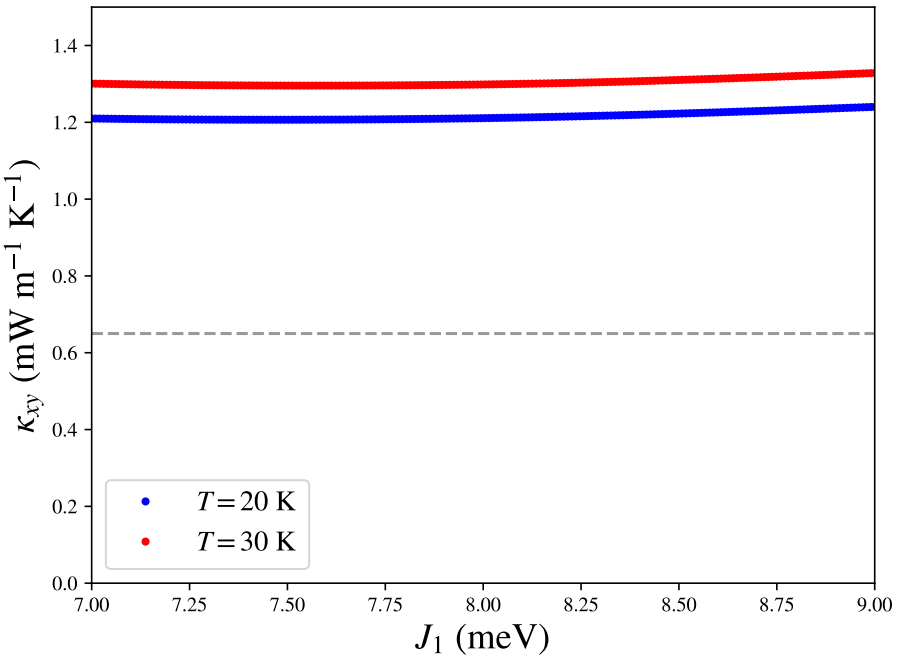


Figure 5.6: Zero-field thermal Hall conductivity at $T = 20$ K and $T = 30$ K, obtained by varying the first nearest-neighbour Heisenberg exchange J_1 in the presence of a second nearest-neighbour Heisenberg interaction J_2, subject to the constraint $J_1 + 2J_2 \approx 8$ meV. This constraint comes from the INS measurements in Ref. [145].

Chapter 6

Conclusion and outlook

In this thesis, we explored various examples of non-conventional order in frustrated quantum magnets. Notably, there is one material that ties together all of the projects presented in this thesis: $Lu_2V_2O_7$. Based on the results from Chapters 3-5, this material is expected to exhibit ObD without quantum zero-point fluctuations, a PG gap proportional to $T^{7/2}$, and a magnon Hall effect. In Chapters 3 and 4, the focus was on ObD, a type of magnetic order that is induced by the presence of fluctuations. Alternatively, in Chapter 5, we explored the consequences of topological order to the collective excitations of the pyrochlore oxide $Lu_2V_2O_7$.

Chapter 3 presented a novel route to ObD in the absence of quantum zero-point fluctuations, in the context of a pyrochlore Heisenberg ferromagnet with DM interactions. It was argued that geometric constraints on the DM vectors of the pyrochlore lattice lead to stable collinear ferromagnetism that is accidentally degenerate at the classical level, while thermal fluctuations lift this degeneracy to select the $\langle 111 \rangle$ direction at low temperatures. The results from Chapter 3 may have implications for real ferromagnetic materials where the DM interaction is the leading perturbation. In particular, the magnetism of the ferromagnetic Mott insulators $Lu_2V_2O_7$ and $Y_2V_2O_7$ is rather well described by Eq. (3.1) [143–145]. We expect the strongest evidence would be the measurement of a temperature-dependent PG gap scaling proportional to $T^{7/2}$ that vanishes in the zero-temperature limit, as depicted in Fig. 4.3(c), although this would pose significant challenges due to the small (neV) energy scales involved. Another open problem is the precise identification of a more general class of spin models that exhibit ObD without zero-point fluctuations. For example, any ferromagnetic Heisenberg model with DM interactions will satisfy Eq. (3.26) as long as the sum over DM vectors along the bonds surrounding each site vanishes. It is then a question of which specific crystalline symmetries (or lack thereof) lead to this sum rule being satisfied. Another example of such a model is the kagome Heisenberg ferromagnet

with out-of-plane DM vectors [132]. Another open problem from Chapter 3 is to understand the nature of the paramagnetic to ferromagnetic transition for this model.

Chapter 4 focused on the characterization of ObD in real materials, and how to distinguish it from conventional energetic ordering. We propose that a universal temperature-dependent gap in the magnon spectrum can serve as a model-independent signature that ObD is operating in a material, distinct from a typical anisotropy gap arising from energetic considerations. In addition, we derived a simplified formula for the PG gap in non-linear spin wave theory that uses only quantities accessible in the (non-interacting) linear spin wave theory. While the experimental observation of a temperature-dependent gap would serve as compelling evidence that ObD is at play in any of the existing candidate materials, the experimental details of how to resolve and characterize small thermal corrections to the PG gap remain an open problem. In the materials considered in Chapter 4, the PG is at least several orders of magnitude smaller than the largest exchange interaction, and the thermal correction to the gap is even smaller than that. Because of this, it will likely be challenging to measure the temperature dependence of the gap to high resolution. An important future direction is the identification of additional ObD candidate materials with larger thermal corrections to the PG that can be measured with current INS resolution. The results of Chapter 4 provide the theoretical tools to guide future experimental efforts in detecting ObD unambiguously.

Chapter 5 exposed a discrepancy with various experimental and numerical datasets of the pyrochlore $Lu_2V_2O_7$, which motivated a re-investigation of the magnon Hall effect of this material. We explored the effect of additional symmetry-allowed couplings to the microscopic spin model and concluded that *most* of these discrepancies can be resolved with the addition of a second nearest-neighbour DM interaction, as small as 2% of the nearest-neighbour Heisenberg exchange. Such a coupling, however, cannot account for the apparent excess in specific heat observed in [15]. These results open the door to several directions of future research on $Lu_2V_2O_7$ to better understand how to reconcile the thermal transport, INS and specific heat measurements. Future experimental investigations should aim to independently measure and verify whether there is an excess of low-temperature specific heat as shown in Fig. 5.5. This would imply that there are quadratically dispersing excitations that are unaccounted for by both magnons and phonons, potentially leading to interesting new physics in $Lu_2V_2O_7$. Another avenue for research is the role of spin-phonon coupling [243, 246, 301–304] in this material, as there is an increasing body of work suggesting that magneto-elastic effects play a crucial role in the thermal transport of magnetic insulators that is potentially relevant for $Lu_2V_2O_7$. Note, however, that such a coupling is not likely to account for the excess of specific heat. Nonetheless, the work presented in Chapter 5 provides a comprehensive analysis to guide future experimental and theoretical efforts in understanding this fascinating material.

References

[1] A. Hickey, D. Lozano-Gómez, and M. J. P. Gingras, Order-by-disorder without quantum zero-point fluctuations in the pyrochlore Heisenberg ferromagnet with Dzyaloshinskii-Moriya interactions, Physical Review B **111**, 184434 (2025).

[2] A. Hickey, J. G. Rau, S. Khatua, and M. J. P. Gingras, Universal temperature-dependent power law excitation gaps in frustrated quantum spin systems harboring order-by-disorder, arXiv:2505.18253 [cond-mat.str-el] (2025).

[3] L. Landau and E. Lifshitz, *Statistical Physics: Volume 5* (Butterworth-Heinemann, 1980).

[4] J. Goldstone, A. Salam, and S. Weinberg, Broken Symmetries, Physical Review **127**, 965 (1962).

[5] S. Weinberg, Approximate Symmetries and Pseudo-Goldstone Bosons, Physical Review Letters **29**, 1698 (1972).

[6] X. Wen, *Quantum Field Theory of Many-Body Systems: From the Origin of Sound to an Origin of Light and Electrons* (Oxford University Press, 2004).

[7] J. E. Moore, The birth of topological insulators, Nature **464**, 194 (2010).

[8] M. Z. Hasan and J. E. Moore, Three-Dimensional Topological Insulators, Annual Review of Condensed Matter Physics **2**, 55 (2011).

[9] S.-Q. Shen, The family of topological phases in condensed matter, National Science Review **1**, 49 (2014).

[10] J. Villain, R. Bidaux, J.-P. Carton, and R. Conte, Order as an effect of disorder, Journal de Physique **41**, 1263 (1980).

[11] J. Dorier, F. Becca, and F. Mila, Quantum compass model on the square lattice, Physical Review B **72**, 024448 (2005).

[12] H. Katsura, N. Nagaosa, and P. A. Lee, Theory of the Thermal Hall Effect in Quantum Magnets, Physical Review Letters **104**, 066403 (2010).

[13] R. Matsumoto and S. Murakami, Rotational motion of magnons and the thermal Hall effect, Physical Review B **84**, 184406 (2011).

[14] R. Matsumoto and S. Murakami, Theoretical Prediction of a Rotating Magnon Wave Packet in Ferromagnets, Physical Review Letters **106**, 197202 (2011).

[15] Y. Onose, T. Ideue, H. Katsura, Y. Shiomi, N. Nagaosa, and Y. Tokura, Observation of the Magnon Hall Effect, Science **329**, 297 (2010).

[16] T. Ideue, Y. Onose, H. Katsura, Y. Shiomi, S. Ishiwata, N. Nagaosa, and Y. Tokura, Effect of lattice geometry on magnon Hall effect in ferromagnetic insulators, Physical Review B - Condensed Matter and Materials Physics **85**, 134411 (2012).

[17] M. Hirschberger, R. Chisnell, Y. S. Lee, and N. P. Ong, Thermal Hall Effect of Spin Excitations in a Kagome Magnet, Physical Review Letters **115**, 106603 (2015).

[18] C. Xu, H. Zhang, C. Carnahan, P. Zhang, D. Xiao, and X. Ke, Thermal Hall effect in the van der Waals ferromagnet CrI_3, Physical Review B **109**, 094415 (2024).

[19] P. A. McClarty, Topological Magnons: A Review, Annual Review of Condensed Matter Physics **13**, 171 (2022).

[20] J. Puebla, J. Kim, K. Kondou, and Y. Otani, Spintronic devices for energy-efficient data storage and energy harvesting, Communications Materials **1**, 24 (2020).

[21] J. S. Gardner, M. J. P. Gingras, and J. E. Greedan, Magnetic pyrochlore oxides, Reviews of Modern Physics **82**, 53 (2010).

[22] L. Savary and L. Balents, Quantum spin liquids: a review, Reports on Progress in Physics **80**, 016502 (2017).

[23] J. G. Rau and M. J. Gingras, Frustrated Quantum Rare-Earth Pyrochlores, Annual Review of Condensed Matter Physics **10**, 357 (2019).

[24] M. J. Harris, S. T. Bramwell, D. F. McMorrow, T. Zeiske, and K. W. Godfrey, Geometrical Frustration in the Ferromagnetic Pyrochlore $Ho_2Ti_2O_7$, Physical Review Letters **79**, 2554 (1997).

[25] M. J. Harris, S. T. Bramwell, T. Zeiske, D. F. McMorrow, and P. J. C. King, Magnetic structures of highly frustrated pyrochlores, Journal of Magnetism and Magnetic Materials **177–181**, 757 (1998).

[26] S. T. Bramwell and M. J. P. Gingras, Spin Ice State in Frustrated Magnetic Pyrochlore Materials, Science **294**, 1495 (2001).

[27] R. G. Melko, B. C. den Hertog, and M. J. P. Gingras, Long-Range Order at Low Temperatures in Dipolar Spin Ice, Physical Review Letters **87**, 067203 (2001).

[28] A. L. Cornelius and J. S. Gardner, Short-range magnetic interactions in the spin-ice compound $Ho_2Ti_2O_7$, Physical Review B **64**, 060406 (2001).

[29] S. T. Bramwell, M. J. Harris, B. C. den Hertog, M. J. P. Gingras, J. S. Gardner, D. F. McMorrow, A. R. Wildes, A. L. Cornelius, J. D. M. Champion, R. G. Melko, and T. Fennell, Spin Correlations in $Ho_2Ti_2O_7$: A Dipolar Spin Ice System, Physical Review Letters **87**, 047205 (2001).

[30] H. Fukazawa, R. G. Melko, R. Higashinaka, Y. Maeno, and M. J. P. Gingras, Magnetic anisotropy of the spin-ice compound $Dy_2Ti_2O_7$, Physical Review B **65**, 054410 (2002).

[31] K. Matsuhira, Z. Hiroi, T. Tayama, S. Takagi, and T. Sakakibara, A new macroscopically degenerate ground state in the spin ice compound $Dy_2Ti_2O_7$ under a magnetic field, Journal of Physics: Condensed Matter **14**, L559 (2002).

[32] T. Fennell, O. A. Petrenko, B. Fåk, J. S. Gardner, S. T. Bramwell, and B. Ouladdiaf, Neutron scattering studies of the spin ices $Ho_2Ti_2O_7$ and $Dy_2Ti_2O_7$ in applied magnetic field, Physical Review B **72**, 224411 (2005).

[33] T. Yavors'kii, T. Fennell, M. J. P. Gingras, and S. T. Bramwell, $Dy_2Ti_2O_7$ Spin Ice: A Test Case for Emergent Clusters in a Frustrated Magnet, Physical Review Letters **101**, 037204 (2008).

[34] F. Bloch, Zur Theorie des Ferromagnetismus, Zeitschrift für Physik **61**, 206 (1930).

[35] T. Holstein and H. Primakoff, Field Dependence of the Intrinsic Domain Magnetization of a Ferromagnet, Physical Review **58**, 1098 (1940).

[36] F. J. Dyson, General Theory of Spin-Wave Interactions, Physical Review **102**, 1217 (1956).

[37] S. V. Maleev, Scattering of Slow Neutrons in Ferromagnets, Zhurnal Éksperimental'noĭ i Teoreticheskoĭ Fiziki **33**, 1010 (1957), [Journal of Experimental and Theoretical Physics **6**, 776 (1958)].

[38] E. Rastelli, *Statistical Mechanics of Magnetic Excitations: from Spin Waves to Stripes to Checkerboards* (World Scientific, London, 2013).

[39] F. J. Dyson, Thermodynamic Behavior of an Ideal Ferromagnet, Physical Review **102**, 1230 (1956).

[40] T. Tonegawa, Two-Magnon Bound States in the Heisenberg Ferromagnet with Anisotropic Exchange and Uniaxial Anisotropy Energies, Progress of Theoretical Physics Supplement **46**, 61 (1970).

[41] M. F. Thorpe, Two-Magnon Bound State in fcc Ferromagnets, Physical Review B **4**, 1608 (1971).

[42] D. A. Pink and P. Tremblay, Effect of Biquadratic Exchange upon Ferromagnetic Two-Magnon Bound States, Canadian Journal of Physics **50**, 1728 (1972).

[43] T. Oguchi and T. Ishikawa, Theory of Two-Magnon Bound States in a Two-Dimensional Antiferromagnet, Journal of the Physical Society of Japan **34**, 1486 (1973).

[44] K. Wada, T. Ishikawa, and T. Oguchi, Two-Magnon Bound States in the Triangular and Honeycomb Heisenberg Ferromagnets, Progress of Theoretical Physics **54**, 1589 (1975).

[45] A. A. Bahurmuz and P. D. Loly, Two-magnon states in the NN FCC Heisenberg-Ising ferromagnet, Journal of Physics C: Solid State Physics **20**, 6277 (1987).

[46] A. V. Chubukov and D. V. Khveschenko, The two-magnon bound states spectrum in generalised ferromagnetic chains, Journal of Physics C: Solid State Physics **20**, L505 (1987).

[47] E. Rastelli, S. Sedazzari, and A. Tassi, Two-magnon bound states in the triangular ferromagnet, Journal of Physics: Condensed Matter **4**, 6283 (1992).

[48] J. Colpa, Diagonalization of the quadratic boson hamiltonian, Physica A: Statistical Mechanics and its Applications **93**, 327 (1978).

[49] J.-P. Blaizot and G. Ripka, *Quantum Theory of Finite Systems* (MIT Press, 1986).

[50] H. Kondo, Y. Akagi, and H. Katsura, Non-Hermiticity and topological invariants of magnon Bogoliubov-de Gennes systems, Progress of Theoretical and Experimental Physics **2020**, 12A104 (2020).

[51] A. Altland and B. Simons, *Condensed Matter Field Theory*, 2nd ed. (Cambridge University Press, 2010).

[52] G. D. Mahan, *Many-Particle Physics*, 3rd ed. (Springer, New York, NY, 2000).

[53] J. W. Negele and H. Orland, *Quantum Many-particle Systems* (Westview Press, 1988).

[54] L. Balents, Spin liquids in frustrated magnets, Nature **464**, 199 (2010).

[55] R. Moessner and J. T. Chalker, Low-temperature properties of classical geometrically frustrated antiferromagnets, Physical Review B **58**, 12049 (1998).

[56] C. L. Henley, Ordering due to disorder in a frustrated vector antiferromagnet, Physical Review Letters **62**, 2056 (1989).

[57] J. Oitmaa, R. R. P. Singh, B. Javanparast, A. G. R. Day, B. V. Bagheri, and M. J. P. Gingras, Phase transition and thermal order-by-disorder in the pyrochlore antiferromagnet $Er_2Ti_2O_7$: A high-temperature series expansion study, Physical Review B **88**, 220404 (2013).

[58] S. Khatua, M. J. P. Gingras, and J. G. Rau, Pseudo-Goldstone Modes and Dynamical Gap Generation from Order by Thermal Disorder, Physical Review Letters **130**, 266702 (2023).

[59] S. Khatua, G. C. Howson, M. J. P. Gingras, and J. G. Rau, Ground state properties of the Heisenberg-compass model on the square lattice, Physical Review B **110**, 104426 (2024).

[60] S. Lee, E. K.-H. Lee, A. Paramekanti, and Y. B. Kim, Order-by-disorder and magnetic field response in the Heisenberg-Kitaev model on a hyperhoneycomb lattice, Physical Review B **89**, 014424 (2014).

[61] B. Danu, G. Nambiar, and R. Ganesh, Extended degeneracy and order by disorder in the square lattice $J_1 - J_2 - J_3$ model, Physical Review B **94**, 094438 (2016).

[62] R. Schick, T. Ziman, and M. E. Zhitomirsky, Quantum versus thermal fluctuations in the fcc antiferromagnet: Alternative routes to order by disorder, Physical Review B **102**, 220405 (2020).

[63] V. Noculak, D. Lozano-Gómez, J. Oitmaa, R. R. P. Singh, Y. Iqbal, M. J. P. Gingras, and J. Reuther, Classical and quantum phases of the pyrochlore $S = \frac{1}{2}$ magnet with Heisenberg and Dzyaloshinskii-Moriya interactions, Physical Review B **107**, 214414 (2023).

[64] J. Villain, Insulating spin glasses, Zeitschrift für Physik B Condensed Matter **33**, 31 (1979).

[65] B. Canals and C. Lacroix, Pyrochlore Antiferromagnet: A Three-Dimensional Quantum Spin Liquid, Physical Review Letters **80**, 2933 (1998).

[66] A. Kitaev, Anyons in an exactly solved model and beyond, Annals of Physics **321**, 2 (2006).

[67] M. J. P. Gingras and P. A. McClarty, Quantum spin ice: A search for gapless quantum spin liquids in pyrochlore magnets, Reports on Progress in Physics **77**, 056501 (2014).

[68] T. Imai and Y. S. Lee, Do quantum spin liquids exist?, Physics Today **69**, 30 (2016).

[69] J. Knolle and R. Moessner, A field guide to spin liquids, Annual Review of Condensed Matter Physics **10**, 451 (2019).

[70] E. Belorizky, R. Casalegno, and J. J. Niez, Calculation of the Spin Wave Energy Gap at $\boldsymbol{k} = 0$ for a Simple Cubic Ferromagnet with Anisotropic Exchange Interactions, Physica Status Solidi B **102**, 365 (1980).

[71] E. F. Shender, Antiferromagnetic garnets with fluctuationally interacting sublattices, Zhurnal Éksperimental'noĭ i Teoreticheskoĭ Fiziki **83**, 326 (1982), [Journal of Experimental and Theoretical Physics **56**, 178 (1982)].

[72] S. Prakash and C. L. Henley, Ordering due to disorder in dipolar magnets on two-dimensional lattices, Physical Review B **42**, 6574 (1990).

[73] C. L. Henley, Ordering by disorder: Ground-state selection in fcc vector antiferromagnets, Journal of Applied Physics **61**, 3962 (1987).

[74] J. R. Tessman, Magnetic Anisotropy at 0°K, Physical Review **96**, 1192 (1954).

[75] C. Kittel, *Quantum Theory of Solids*, 2nd ed. (Wiley, New York, NY, 1991).

[76] J. N. Reimers and A. J. Berlinsky, Order by disorder in the classical Heisenberg kagomé Antiferromagnet, Physical Review B **48**, 9539 (1993).

[77] S. T. Bramwell, M. J. P. Gingras, and J. N. Reimers, Order by disorder in an anisotropic pyrochlore lattice antiferromagnet, Journal of Applied Physics **75**, 5523 (1994).

[78] M. Elhajal, B. Canals, R. Sunyer, and C. Lacroix, Ordering in the pyrochlore antiferromagnet due to Dzyaloshinsky-Moriya interactions, Physical Review B **71**, 094420 (2005).

[79] D. Bergman, J. Alicea, E. Gull, S. Trebst, and L. Balents, Order-by-disorder and spiral spin-liquid in frustrated diamond-lattice antiferromagnets, Nature Physics **3**, 487 (2007).

[80] G.-W. Chern, Pyrochlore antiferromagnet with antisymmetric exchange interactions: critical behavior and order from disorder, arXiv:1008.3038 [cond-mat.str-el] (2010).

[81] M. V. Gvozdikova, P.-E. Melchy, and M. E. Zhitomirsky, Magnetic phase diagrams of classical triangular and kagome antiferromagnets, Journal of Physics: Condensed Matter **23**, 164209 (2011).

[82] M. E. Zhitomirsky, P. C. W. Holdsworth, and R. Moessner, Nature of finite-temperature transition in anisotropic pyrochlore $Er_2Ti_2O_7$, Physical Review B **89**, 140403 (2014).

[83] P. A. McClarty, P. Stasiak, and M. J. P. Gingras, Order-by-disorder in the *XY* pyrochlore antiferromagnet, Physical Review B **89**, 024425 (2014).

[84] N. Francini, L. Janssen, and D. Lozano-Gómez, Higher-rank spin liquids and spin nematics from competing orders in pyrochlore magnets, Physical Review B **111**, 085140 (2025).

[85] P. Chandra and B. Doucot, Possible spin-liquid state at large *S* for the frustrated square Heisenberg lattice, Physical Review B **38**, 9335 (1988).

[86] K. Kubo and T. Kishi, Ordering Due to Quantum Fluctuations in the Frustrated Heisenberg Model, Journal of the Physical Society of Japan **60**, 567 (1991).

[87] S. Sachdev, Kagomé and triangular-lattice Heisenberg antiferromagnets: Ordering from quantum fluctuations and quantum-disordered ground states with unconfined bosonic spinons, Physical Review B **45**, 12377 (1992).

[88] A. V. Chubukov and D. I. Golosov, Quantum theory of an antiferromagnet on a triangular lattice in a magnetic field, Journal of Physics: Condensed Matter **3**, 69 (1991).

[89] A. Chubukov, Order from Disorder in a Kagomé Antiferromagnet, Physical Review Letters **69**, 832 (1992).

[90] C. L. Henley, Selection by Quantum Fluctuations of Dipolar Order in a Diamond Lattice, Physical Review Letters **73**, 2788 (1994).

[91] P. Lecheminant, B. Bernu, C. Lhuillier, and L. Pierre, $J_1 - J_2$ quantum Heisenberg antiferromagnet on the triangular lattice: A group-symmetry analysis of order by disorder, Physical Review B **52**, 6647 (1995).

[92] R. R. Sobral and C. Lacroix, Order by disorder in the pyrochlore antiferromagnets, Solid State Communications **103**, 407 (1997).

[93] J. D. M. Champion, M. J. Harris, P. C. W. Holdsworth, A. S. Wills, G. Balakrishnan, S. T. Bramwell, E. Čižmár, T. Fennell, J. S. Gardner, J. Lago, D. F. McMorrow, M. Orendáč, A. Orendáčová, D. M. Paul, R. I. Smith, M. T. F. Telling, and A. Wildes, $Er_2Ti_2O_7$: Evidence of quantum order by disorder in a frustrated antiferromagnet, Physical Review B **68**, 020401 (2003).

[94] G. Baskaran, D. Sen, and R. Shankar, Spin-S Kitaev model: Classical ground states, order from disorder, and exact correlation functions, Physical Review B **78**, 115116 (2008).

[95] J.-S. Bernier, M. J. Lawler, and Y. B. Kim, Quantum Order by Disorder in Frustrated Diamond Lattice Antiferromagnets, Physical Review Letters **101**, 047201 (2008).

[96] A. Mulder, R. Ganesh, L. Capriotti, and A. Paramekanti, Spiral order by disorder and lattice nematic order in a frustrated Heisenberg antiferromagnet on the honeycomb lattice, Physical Review B **81**, 214419 (2010).

[97] L. Savary, K. A. Ross, B. D. Gaulin, J. P. C. Ruff, and L. Balents, Order by Quantum Disorder in $Er_2Ti_2O_7$, Physical Review Letters **109**, 167201 (2012).

[98] M. E. Zhitomirsky, M. V. Gvozdikova, P. C. W. Holdsworth, and R. Moessner, Quantum Order by Disorder and Accidental Soft Mode in $Er_2Ti_2O_7$, Physical Review Letters **109**, 077204 (2012).

[99] A. L. Chernyshev and M. E. Zhitomirsky, Quantum Selection of Order in an XXZ Antiferromagnet on a Kagome Lattice, Physical Review Letters **113**, 237202 (2014).

[100] I. Rousochatzakis, J. Reuther, R. Thomale, S. Rachel, and N. B. Perkins, Phase Diagram and Quantum Order by Disorder in the Kitaev $K_1 - K_2$ Honeycomb Magnet, Physical Review X **5**, 041035 (2015).

[101] J. G. Rau, P. A. McClarty, and R. Moessner, Pseudo-Goldstone Gaps and Order-by-Quantum Disorder in Frustrated Magnets, Physical Review Letters **121**, 237201 (2018).

[102] B. Placke, R. Moessner, and O. Benton, Hierarchy of energy scales and field-tunable order by disorder in dipolar-octupolar pyrochlores, Physical Review B **102**, 245102 (2020).

[103] G. Chen and X. Wang, Electron quasi-itinerancy intertwined with quantum order by disorder in pyrochlore iridate magnetism, Physical Review Research **2**, 043273 (2020).

[104] C. Liu, C.-J. Huang, and G. Chen, Intrinsic quantum Ising model on a triangular lattice magnet $TmMgGaO_4$, Physical Review Research **2**, 043013 (2020).

[105] S. Khatua, S. Srinivasan, and R. Ganesh, State selection in frustrated magnets, Physical Review B **103**, 174412 (2021).

[106] Y. V. Fyodorov and E. F. Shender, Random-field effects in antiferromagnets with classically degenerate ground states, Journal of Physics: Condensed Matter **3**, 9123 (1991).

[107] L. Savary, E. Gull, S. Trebst, J. Alicea, D. Bergman, and L. Balents, Impurity effects in highly frustrated diamond-lattice antiferromagnets, Physical Review B **84**, 064438 (2011).

[108] V. S. Maryasin and M. E. Zhitomirsky, Triangular Antiferromagnet with Nonmagnetic Impurities, Physical Review Letters **111**, 247201 (2013).

[109] A. Andreanov and P. A. McClarty, Order induced by dilution in pyrochlore XY antiferromagnets, Physical Review B **91**, 064401 (2015).

[110] V. S. Maryasin and M. E. Zhitomirsky, Collective impurity effects in the Heisenberg triangular antiferromagnet, Journal of Physics: Conference Series **592**, 012112 (2015).

[111] A. I. Smirnov, T. A. Soldatov, O. A. Petrenko, A. Takata, T. Kida, M. Hagiwara, A. Y. Shapiro, and M. E. Zhitomirsky, Order by Quenched Disorder in the Model Triangular Antiferromagnet $RbFe(MoO_4)_2$, Physical Review Letters **119**, 047204 (2017).

[112] E. C. Andrade, J. A. Hoyos, S. Rachel, and M. Vojta, Cluster-Glass Phase in Pyrochlore *XY* Antiferromagnets with Quenched Disorder, Physical Review Letters **120**, 097204 (2018).

[113] P. M. Cônsoli and M. Vojta, Disorder effects in spiral spin liquids: Long-range spin textures, Friedel-like oscillations, and spiral spin glasses, Physical Review B **109**, 064423 (2024).

[114] K. A. Ross, Y. Qiu, J. R. D. Copley, H. A. Dabkowska, and B. D. Gaulin, Order by Disorder Spin Wave Gap in the *XY* Pyrochlore Magnet $Er_2Ti_2O_7$, Physical Review Letters **112**, 057201 (2014).

[115] P. A. McClarty, S. H. Curnoe, and M. J. P. Gingras, Energetic selection of ordered states in a model of the $Er_2Ti_2O_7$ frustrated pyrochlore XY antiferromagnet, Journal of Physics: Conference Series **145**, 012032 (2009).

[116] S. Petit, J. Robert, S. Guitteny, P. Bonville, C. Decorse, J. Ollivier, H. Mutka, M. J. P. Gingras, and I. Mirebeau, Order by disorder or energetic selection of the ground state in the *XY* pyrochlore antiferromagnet $Er_2Ti_2O_7$: An inelastic neutron scattering study, Physical Review B **90**, 060410 (2014).

[117] J. G. Rau, S. Petit, and M. J. P. Gingras, Order by virtual crystal field fluctuations in pyrochlore *XY* antiferromagnets, Physical Review B **93**, 184408 (2016).

[118] M. Elliot, P. A. McClarty, D. Prabhakaran, R. D. Johnson, H. C. Walker, P. Manuel, and R. Coldea, Order-by-Disorder from Bond-Dependent Exchange and Intensity Signature of Nodal Quasiparticles in a Honeycomb Cobaltate, Nature Communications **12**, 3936 (2021).

[119] Y. J. Kim, A. Aharony, R. J. Birgeneau, F. C. Chou, O. Entin-Wohlman, R. W. Erwin, M. Greven, A. B. Harris, M. A. Kastner, I. Y. Korenblit, Y. S. Lee, and G. Shirane, Ordering due to Quantum Fluctuations in $Sr_2Cu_3O_4Cl_2$, Physical Review Letters **83**, 852 (1999).

[120] T. Brueckel, B. Dorner, A. G. Gukasov, V. P. Plakhty, W. Prandl, E. F. Shender, and O. P. Smirnow, Dynamical interaction of antiferromagnetic subsystems: a neutron scattering study of the spinwave spectrum of the garnet $Fe_2Ca_3(GeO_4)_3$, Zeitschrift für Physik B Condensed Matter **72**, 477 (1988).

[121] C. L. Sarkis, J. G. Rau, L. D. Sanjeewa, M. Powell, J. Kolis, J. Marbey, S. Hill, J. A. Rodriguez-Rivera, H. S. Nair, D. R. Yahne, S. Säubert, M. J. P. Gingras, and K. A. Ross, Unravelling competing microscopic interactions at a phase boundary: A single-crystal study of the metastable antiferromagnetic pyrochlore $Yb_2Ge_2O_7$, Physical Review B **102**, 134418 (2020).

[122] T. Inami, Y. Ajiro, and T. Goto, Magnetization Process of the Triangular Lattice Antiferromagnets, $RbFe(MoO_4)_2$ and $CsFe(SO_4)_2$, Journal of the Physical Society of Japan **65**, 2374 (1996).

[123] A. I. Smirnov, H. Yashiro, S. Kimura, M. Hagiwara, Y. Narumi, K. Kindo, A. Kikkawa, K. Katsumata, A. Y. Shapiro, and L. N. Demianets, Triangular lattice antiferromagnet $RbFe(MoO_4)_2$ in high magnetic fields, Physical Review B **75**, 134412 (2007).

[124] T. Susuki, N. Kurita, T. Tanaka, H. Nojiri, A. Matsuo, K. Kindo, and H. Tanaka, Magnetization Process and Collective Excitations in the $S = 1/2$ Triangular-Lattice Heisenberg Antiferromagnet $Ba_3CoSb_2O_9$, Physical Review Letters **110**, 267201 (2013).

[125] K. M. Ranjith, S. Luther, T. Reimann, B. Schmidt, P. Schlender, J. Sichelschmidt, H. Yasuoka, A. M. Strydom, Y. Skourski, J. Wosnitza, H. Kühne, T. Doert, and M. Baenitz, Anisotropic field-induced ordering in the triangular-lattice quantum spin liquid $NaYbSe_2$, Physical Review B **100**, 224417 (2019).

[126] B. Lenz, M. Fabrizio, and M. Casula, Order from disorder phenomena in $BaCoS_2$, Communications Physics **7**, 1 (2024).

[127] D. Lozano-Gómez, V. Noculak, J. Oitmaa, R. R. P. Singh, Y. Iqbal, J. Reuther, and M. J. P. Gingras, Competing gauge fields and entropically driven spin liquid to spin liquid transition in non-Kramers pyrochlores, Proceedings of the National Academy of Sciences of the United States of America **121**, e2403487121 (2024).

[128] L. Zhang, J. Ren, J.-S. Wang, and B. Li, Topological magnon insulator in insulating ferromagnet, Physical Review B **87**, 144101 (2013).

[129] A. Mook, J. Henk, and I. Mertig, Magnon hall effect and topology in kagome lattices: A theoretical investigation, Physical Review B **89**, 134409 (2014).

[130] A. Mook, J. Henk, and I. Mertig, Edge states in topological magnon insulators, Physical Review B **90**, 024412 (2014).

[131] R. Chisnell, J. S. Helton, D. E. Freedman, D. K. Singh, R. I. Bewley, D. G. Nocera, and Y. S. Lee, Topological Magnon Bands in a Kagome Lattice Ferromagnet, Physical Review Letters **115**, 147201 (2015).

[132] A. L. Chernyshev and P. A. Maksimov, Damped Topological Magnons in the Kagome-Lattice Ferromagnets, Physical Review Letters **117**, 187203 (2016).

[133] A. Mook, K. Plekhanov, J. Klinovaja, and D. Loss, Interaction-Stabilized Topological Magnon Insulator in Ferromagnets, Physical Review X **11**, 021061 (2021).

[134] T. Moriya, Anisotropic Superexchange Interaction and Weak Ferromagnetism, Physical Review **120**, 91 (1960).

[135] H. Yan, O. Benton, L. Jaubert, and N. Shannon, Theory of multiple-phase competition in pyrochlore magnets with anisotropic exchange with application to $Yb_2Ti_2O_7$, $Er_2Ti_2O_7$, and $Er_2Sn_2O_7$, Physical Review B **95**, 094422 (2017).

[136] D. Coffey, T. M. Rice, and F. C. Zhang, Dzyaloshinskii-Moriya interaction in the cuprates, Physical Review B **44**, 10112 (1991).

[137] K. Riedl, D. Guterding, H. O. Jeschke, M. J. P. Gingras, and R. Valentí, Ab Initio Determination of Spin Hamiltonians with Anisotropic Exchange Interactions: The Case of the Pyrochlore Ferromagnet $Lu_2V_2O_7$, Physical Review B **94**, 014410 (2016).

[138] K. A. Ross, L. Savary, B. D. Gaulin, and L. Balents, Quantum Excitations in Quantum Spin Ice, Physical Review X **1**, 021002 (2011).

[139] J. G. Rau and M. J. P. Gingras, Frustration and anisotropic exchange in ytterbium magnets with edge-shared octahedra, Physical Review B **98**, 054408 (2018).

[140] J. G. Rau, L. S. Wu, A. F. May, L. Poudel, B. Winn, V. O. Garlea, A. Huq, P. Whitfield, A. E. Taylor, M. D. Lumsden, M. J. P. Gingras, and A. D. Christianson, Anisotropic exchange within decoupled tetrahedra in the quantum breathing pyrochlore $Ba_3Yb_2Zn_5O_{11}$, Physical Review Letters **116**, 257204 (2016).

[141] S.-i. Shamoto, T. Nakano, Y. Nozue, and T. Kajitani, Substitution Effects on Ferromagnetic Mott Insulator $Lu_2V_2O_7$, Journal of Physics and Chemistry of Solids **63**, 1047 (2002).

[142] A. Ali Biswas and Y. Jana, Crystal-Field, Exchange Interactions and Magnetism in Pyrochlore Ferromagnet $R_2V_2O_7$ (R^{3+}=Y, Lu), J. Magn. Magn. Mater. **329**, 118 (2013).

[143] D. V. Nazipov, A. E. Nikiforov, and V. A. Chernyshev, Exchange interaction in pyrochlore vanadates $Lu_2V_2O_7$ and $Y_2V_2O_7$: Ab initio approach, Physics of the Solid State **58**, 1989 (2016).

[144] D. V. Nazipov, A. E. Nikiforov, and V. A. Chernyshev, Structure, lattice dynamics, and exchange interaction in $Lu_2V_2O_7$, $Y_2V_2O_7$: an ab initio approach, Optics and Spectroscopy **121**, 544 (2016).

[145] M. Mena, R. S. Perry, T. G. Perring, M. D. Le, S. Guerrero, M. Storni, D. T. Adroja, C. Rüegg, and D. F. McMorrow, Spin-Wave Spectrum of the Quantum Ferromagnet on the Pyrochlore Lattice $Lu_2V_2O_7$, Physical Review Letters **113**, 047202 (2014).

[146] J. D. Alzate-Cardona, D. Sabogal-Suárez, R. F. L. Evans, and E. Restrepo-Parra, Optimal phase space sampling for Monte Carlo simulations of Heisenberg spin systems, Journal of Physics: Condensed Matter **31**, 095802 (2019).

[147] K. Binder and D. W. Heermann, *Monte Carlo Simulation in Statistical Physics: An Introduction* (Springer Science & Business Media, 2010).

[148] M. Creutz, Overrelaxation and Monte Carlo simulation, Physical Review D **36**, 515 (1987).

[149] J. P. Bouchaud and P. G. Zérah, Dipolar ferromagnetism: A Monte Carlo study, Physical Review B **47**, 9095 (1993).

[150] P. M. Chaikin and T. C. Lubensky, *Principles of Condensed Matter Physics* (Cambridge University Press, 2000).

[151] J. G. Rau, R. Moessner, and P. A. McClarty, Magnon interactions in the frustrated pyrochlore ferromagnet $Yb_2Ti_2O_7$, Physical Review B **100**, 104423 (2019).

[152] M. Mourigal, W. T. Fuhrman, A. L. Chernyshev, and M. E. Zhitomirsky, Dynamical structure factor of the triangular-lattice antiferromagnet, Physical Review B **88**, 094407 (2013).

[153] J. T. Chalker, P. C. W. Holdsworth, and E. F. Shender, Hidden order in a frustrated system: Properties of the Heisenberg Kagomé antiferromagnet, Physical Review Letters **68**, 855 (1992).

[154] V. S. Maryasin, M. E. Zhitomirsky, and R. Moessner, Low-field behavior of an xy pyrochlore antiferromagnet: Emergent clock anisotropies, Physical Review B **93**, 100406 (2016).

[155] C. Burgess, Goldstone and pseudo-Goldstone bosons in nuclear, particle and condensed-matter physics, Physics Reports **330**, 193 (2000).

[156] A. Aharony, Critical Behavior of Anisotropic Cubic Systems, Physical Review B **8**, 4270 (1973).

[157] M. Ferer, J. P. Van Dyke, and W. J. Camp, Effect of a cubic crystal field on the critical behavior of a 3D model with Heisenberg exchange coupling: A high-temperature series investigation, Physical Review B **23**, 2367 (1981).

[158] K. E. Newman and E. K. Riedel, Cubic N-vector model and randomly dilute Ising model in general dimensions, Physical Review B **25**, 264 (1982).

[159] J. Manuel Carmona, A. Pelissetto, and E. Vicari, N-component Ginzburg-Landau Hamiltonian with cubic anisotropy: A six-loop study, Physical Review B **61**, 15136 (2000).

[160] L. T. Adzhemyan, E. V. Ivanova, M. V. Kompaniets, A. Kudlis, and A. I. Sokolov, Six-loop ε expansion study of three-dimensional n-vector model with cubic anisotropy, Nuclear Physics B **940**, 332 (2019).

[161] D. J. Wallace, Critical behaviour of anisotropic cubic systems, Journal of Physics C: Solid State Physics **6**, 1390 (1973).

[162] I. J. Ketley and D. J. Wallace, A modified epsilon expansion for a Hamiltonian with cubic point-group symmetry, Journal of Physics A: Mathematical, Nuclear and General **6**, 1667 (1973).

[163] A. Pelissetto and E. Vicari, Critical Phenomena and Renormalization-Group Theory, Physics Reports **368**, 549 (2002).

[164] A. Hickey, D. Lozano-Gómez, and M. J. P. Gingras, Data for "Order-by-disorder without quantum zero-point fluctuations in the pyrochlore Heisenberg ferromagnet with Dzyaloshinskii-Moriya interactions", `https://osf.io/jxg8r` (2025).

[165] M. Ernzerhof, Taylor-series expansion of density functionals, Physical Review A **50**, 4593 (1994).

[166] F. London, The λ-Phenomenon of Liquid Helium and the Bose-Einstein Degeneracy, Nature **141**, 643 (1938).

[167] D. Lozano-Gómez, O. Benton, M. J. P. Gingras, and H. Yan, An Atlas of Classical Pyrochlore Spin Liquids, arXiv:2411.03547 [cond-mat.str-el] (2025).

[168] J.-Y. Chen, S. A. Kivelson, and X.-Q. Sun, Enhanced Thermal Hall Effect in Nearly Ferroelectric Insulators, Physical Review Letters **124**, 167601 (2020).

[169] K. K. Kesharpu and P. A. Maksimov, Quantum selection of order and dynamic properties of the Kitaev-Heisenberg ferromagnet on a triangular lattice, Physical Review B **112**, 054416 (2025).

[170] S. Ramchandani, S. Trebst, and C. Hickey, Constructing emergent U(1) symmetries in the Γ' model, Physical Review B **112**, 054444 (2025).

[171] A. G. D. Maestro and M. J. P. Gingras, Quantum spin fluctuations in the dipolar Heisenberg-like rare earth pyrochlores, Journal of Physics: Condensed Matter **16**, 3339 (2004).

[172] H. Watanabe and H. Murayama, Unified Description of Nambu-Goldstone Bosons without Lorentz Invariance, Physical Review Letters **108**, 251602 (2012).

[173] R. P. Feynman, Forces in Molecules, Physical Review **56**, 340 (1939).

[174] S. Coleman, There are no Goldstone bosons in two dimensions, Communications in Mathematical Physics **31**, 259 (1973).

[175] N. D. Mermin and H. Wagner, Absence of Ferromagnetism or Antiferromagnetism in One- or Two-Dimensional Isotropic Heisenberg Models, Physical Review Letters **17**, 1133 (1966).

[176] P. C. Hohenberg, Existence of Long-Range Order in One and Two Dimensions, Physical Review **158**, 383 (1967).

[177] V. L. Berezinskii, Destruction of Long-range Order in One-dimensional and Two-dimensional Systems having a Continuous Symmetry Group I. Classical Systems, Zhurnal Éksperimental'noĭ i Teoreticheskoĭ Fiziki **59**, 907 (1970), [Journal of Experimental and Theoretical Physics **32**, 493 (1971)].

[178] V. L. Berezinskii, Destruction of Long-range Order in One-dimensional and Two-dimensional Systems Possessing a Continuous Symmetry Group II. Quantum Systems, Zhurnal Éksperimental'noĭ i Teoreticheskoĭ Fiziki **61**, 1144 (1971), [Journal of Experimental and Theoretical Physics **34**, 610 (1972)].

[179] P. D. Loly, The Heisenberg ferromagnet in the selfconsistently renormalized spin wave approximation, Journal of Physics C: Solid State Physics **4**, 1365 (1971).

[180] W. T. Fuhrman, M. Mourigal, M. E. Zhitomirsky, and A. L. Chernyshev, Dynamical structure factor of quasi-two-dimensional antiferromagnet in high fields, Physical Review B **85**, 184405 (2012).

[181] R. Schick, O. Götze, T. Ziman, R. Zinke, J. Richter, and M. E. Zhitomirsky, Ground-state selection by magnon interactions in a fcc antiferromagnet, Physical Review B **106**, 094431 (2022).

[182] C. A. Gallegos and A. L. Chernyshev, Magnon interactions in the quantum paramagnetic phase of $CoNb_2O_6$, Physical Review B **109**, 014424 (2024).

[183] E. Lhotel, J. Robert, E. Ressouche, F. Damay, I. Mirebeau, J. Ollivier, H. Mutka, P. Dalmas de Réotier, A. Yaouanc, C. Marin, C. Decorse, and S. Petit, Field-induced phase diagram of the XY pyrochlore antiferromagnet $Er_2Ti_2O_7$, Physical Review B **95**, 134426 (2017).

[184] J. S. Gardner, G. Ehlers, A. Faraone, and V. G. Sakai, High-resolution neutron spectroscopy using backscattering and neutron spin-echo spectrometers in soft and hard condensed matter, Nature Reviews Physics **2**, 103 (2020).

[185] X. Lin and T. Shi, Pseudo-Goldstone Modes at Finite Temperature, arXiv:2505.07229v1 [cond-mat.str-el] (2025).

[186] B. Yan and C. Felser, Topological Materials: Weyl Semimetals, Annual Review of Condensed Matter Physics **8**, 337 (2017).

[187] S. Pancharatnam, Generalized theory of interference, and its applications, Proceedings of the Indian Academy of Sciences - Section A **44**, 247 (1956).

[188] M. V. Berry, Quantal phase factors accompanying adiabatic changes, Proceedings of the Royal Society of London. A. Mathematical and Physical Sciences **392**, 45 (1984).

[189] P. Fazekas, *Lecture Notes On Electron Correlation And Magnetism* (World Scientific Publishing Company, 1999).

[190] A. Haghighirad, C. Gross, and W. Assmus, Powder synthesis and crystal growth of $Y_2V_2O_7$ under high pressure and its physical properties, Journal of Crystal Growth **310**, 2277 (2008).

[191] L. Soderholm and J. Greedan, Relationship between crystal structure and magnetic properties of $(RE)_2V_2O_7$; RE=Lu, Yb, Tm, Materials Research Bulletin **17**, 707 (1982).

[192] S. Miyahara, A. Murakami, and N. Furukawa, Orbital ordering induced ferromagnetism in $Lu_2V_2O_7$, Journal of Molecular Structure **838**, 223 (2007).

[193] H. Ichikawa, L. Kano, M. Saitoh, S. Miyahara, N. Furukawa, J. Akimitsu, T. Yokoo, T. Matsumura, M. Takeda, and K. Hirota, Orbital Ordering in Ferromagnetic $Lu_2V_2O_7$, Journal of the Physical Society of Japan **74**, 1020 (2005).

[194] F. D. M. Haldane, Model for a Quantum Hall Effect without Landau Levels: Condensed-Matter Realization of the "Parity Anomaly", Physical Review Letters **61**, 2015 (1988).

[195] V. K. Dugaev, P. Bruno, B. Canals, and C. Lacroix, Berry phase of magnons in textured ferromagnets, Physical Review B **72**, 024456 (2005).

[196] B. A. Bernevig and T. L. Hughes, *Topological Insulators and Topological Superconductors* (Princeton University Press, 2013).

[197] P. Matl, N. P. Ong, Y. F. Yan, Y. Q. Li, D. Studebaker, T. Baum, and G. Doubinina, Hall effect of the colossal magnetoresistance manganite $La_{1-x}Ca_xMnO_3$, Physical Review B **57**, 10248 (1998).

[198] Y. Taguchi and Y. Tokura, Magnetotransport phenomena in a metallic ferromagnet on the verge of Mott transition: $Sm_2Mo_2O_7$, Physical Review B **60**, 10280 (1999).

[199] J. Ye, Y. B. Kim, A. J. Millis, B. I. Shraiman, P. Majumdar, and Z. Tešanović, Berry Phase Theory of the Anomalous Hall Effect: Application to Colossal Magnetoresistance Manganites, Physical Review Letters **83**, 3737 (1999).

[200] Y. Taguchi, Y. Oohara, H. Yoshizawa, N. Nagaosa, and Y. Tokura, Spin Chirality, Berry Phase, and Anomalous Hall Effect in a Frustrated Ferromagnet, Science **291**, 2573 (2001).

[201] Y. Lyanda-Geller, S. H. Chun, M. B. Salamon, P. M. Goldbart, P. D. Han, Y. Tomioka, A. Asamitsu, and Y. Tokura, Charge transport in manganites: Hopping conduction, the anomalous Hall effect, and universal scaling, Physical Review B **63**, 184426 (2001).

[202] K. Ohgushi, S. Murakami, and N. Nagaosa, Spin anisotropy and quantum Hall effect in the kagomé lattice: Chiral spin state based on a ferromagnet, Physical Review B **62**, R6065 (2000).

[203] S. Murakami, N. Nagaosa, and S.-C. Zhang, Dissipationless Quantum Spin Current at Room Temperature, Science **301**, 1348 (2003).

[204] C. L. Kane and E. J. Mele, Quantum Spin Hall Effect in Graphene, Physical Review Letters **95**, 226801 (2005).

[205] B. A. Bernevig, T. L. Hughes, and S.-C. Zhang, Quantum Spin Hall Effect and Topological Phase Transition in HgTe Quantum Wells, Science **314**, 1757 (2006).

[206] S. Onoda, N. Sugimoto, and N. Nagaosa, Intrinsic Versus Extrinsic Anomalous Hall Effect in Ferromagnets, Physical Review Letters **97**, 126602 (2006).

[207] N. A. Sinitsyn, A. H. MacDonald, T. Jungwirth, V. K. Dugaev, and J. Sinova, Anomalous Hall effect in a two-dimensional Dirac band: The link between the Kubo-Streda formula and the semiclassical Boltzmann equation approach, Physical Review B **75**, 045315 (2007).

[208] A. Neubauer, C. Pfleiderer, B. Binz, A. Rosch, R. Ritz, P. G. Niklowitz, and P. Böni, Topological Hall Effect in the *A* Phase of MnSi, Physical Review Letters **102**, 186602 (2009).

[209] M. Lee, W. Kang, Y. Onose, Y. Tokura, and N. P. Ong, Unusual Hall Effect Anomaly in MnSi under Pressure, Physical Review Letters **102**, 186601 (2009).

[210] N. Kanazawa, Y. Onose, T. Arima, D. Okuyama, K. Ohoyama, S. Wakimoto, K. Kakurai, S. Ishiwata, and Y. Tokura, Large Topological Hall Effect in a Short-Period Helimagnet MnGe, Physical Review Letters **106**, 156603 (2011).

[211] Y. Li, N. Kanazawa, X. Z. Yu, A. Tsukazaki, M. Kawasaki, M. Ichikawa, X. F. Jin, F. Kagawa, and Y. Tokura, Robust Formation of Skyrmions and Topological Hall Effect Anomaly in Epitaxial Thin Films of MnSi, Physical Review Letters **110**, 117202 (2013).

[212] A. A. Zyuzin and A. A. Burkov, Topological response in Weyl semimetals and the chiral anomaly, Physical Review B **86**, 115133 (2012).

[213] A. A. Burkov, Anomalous Hall Effect in Weyl Metals, Physical Review Letters **113**, 187202 (2014).

[214] S. T. Ramamurthy and T. L. Hughes, Patterns of electromagnetic response in topological semimetals, Physical Review B **92**, 085105 (2015).

[215] B. I. Halperin, Quantized Hall conductance, current-carrying edge states, and the existence of extended states in a two-dimensional disordered potential, Physical Review B **25**, 2185 (1982).

[216] Y. Hatsugai, Chern number and edge states in the integer quantum Hall effect, Physical Review Letters **71**, 3697 (1993).

[217] C. L. Kane and E. J. Mele, Z_2 Topological Order and the Quantum Spin Hall Effect, Physical Review Letters **95**, 146802 (2005).

[218] L. Fu, C. L. Kane, and E. J. Mele, Topological Insulators in Three Dimensions, Physical Review Letters **98**, 106803 (2007).

[219] M. Z. Hasan and C. L. Kane, *Colloquium*: Topological insulators, Reviews of Modern Physics **82**, 3045 (2010).

[220] X.-L. Qi and S.-C. Zhang, Topological insulators and superconductors, Reviews of Modern Physics **83**, 1057 (2011).

[221] A. A. Burkov, M. D. Hook, and L. Balents, Topological nodal semimetals, Physical Review B **84**, 235126 (2011).

[222] A. A. Burkov, Topological semimetals, Nature Materials **15**, 1145 (2016).

[223] N. P. Armitage, E. J. Mele, and A. Vishwanath, Weyl and Dirac semimetals in three-dimensional solids, Reviews of Modern Physics **90**, 015001 (2018).

[224] J. Y. Lee, J. Ahn, H. Zhou, and A. Vishwanath, Topological Correspondence between Hermitian and Non-Hermitian Systems: Anomalous Dynamics, Physical Review Letters **123**, 206404 (2019).

[225] I. Žutić, J. Fabian, and S. Das Sarma, Spintronics: Fundamentals and applications, Reviews of Modern Physics **76**, 323 (2004).

[226] Y. Kajiwara, K. Harii, S. Takahashi, J. Ohe, K. Uchida, M. Mizuguchi, H. Umezawa, H. Kawai, K. Ando, K. Takanashi, S. Maekawa, and E. Saitoh, Transmission of electrical signals by spin-wave interconversion in a magnetic insulator, Nature **464**, 262 (2010).

[227] S. D. Bader and S. S. P. Parkin, Spintronics, Annual Review of Condensed Matter Physics **1**, 71 (2010).

[228] A. V. Chumak, V. I. Vasyuchka, A. A. Serga, and B. Hillebrands, Magnon spintronics, Nature Physics **11**, 453 (2015).

[229] V. Baltz, A. Manchon, M. Tsoi, T. Moriyama, T. Ono, and Y. Tserkovnyak, Antiferromagnetic spintronics, Reviews of Modern Physics **90**, 015005 (2018).

[230] A. Hirohata, K. Yamada, Y. Nakatani, I.-L. Prejbeanu, B. Diény, P. Pirro, and B. Hillebrands, Review on spintronics: Principles and device applications, Journal of Magnetism and Magnetic Materials **509**, 166711 (2020).

[231] M. Onoda, S. Murakami, and N. Nagaosa, Hall Effect of Light, Physical Review Letters **93**, 083901 (2004).

[232] S. Raghu and F. D. M. Haldane, Analogs of quantum-Hall-effect edge states in photonic crystals, Physical Review A **78**, 033834 (2008).

[233] F. D. M. Haldane and S. Raghu, Possible Realization of Directional Optical Waveguides in Photonic Crystals with Broken Time-Reversal Symmetry, Physical Review Letters **100**, 013904 (2008).

[234] Z. Wang, Y. Chong, J. D. Joannopoulos, and M. Soljačić, Observation of unidirectional backscattering-immune topological electromagnetic states, Nature **461**, 772 (2009).

[235] P. Ben-Abdallah, Photon Thermal Hall Effect, Physical Review Letters **116**, 084301 (2016).

[236] O. Hosten and P. Kwiat, Observation of the Spin Hall Effect of Light via Weak Measurements, Science **319**, 787 (2008).

[237] C. Strohm, G. L. J. A. Rikken, and P. Wyder, Phenomenological Evidence for the Phonon Hall Effect, Physical Review Letters **95**, 155901 (2005).

[238] L. Sheng, D. N. Sheng, and C. S. Ting, Theory of the Phonon Hall Effect in Paramagnetic Dielectrics, Physical Review Letters **96**, 155901 (2006).

[239] Y. Kagan and L. A. Maksimov, Anomalous Hall Effect for the Phonon Heat Conductivity in Paramagnetic Dielectrics, Physical Review Letters **100**, 145902 (2008).

[240] A. V. Inyushkin and A. N. Taldenkov, On the phonon Hall effect in a paramagnetic dielectric, JETP Letters **86**, 379 (2007).

[241] L. Zhang, J. Ren, J.-S. Wang, and B. Li, Topological Nature of the Phonon Hall Effect, Physical Review Letters **105**, 225901 (2010).

[242] R. Süsstrunk and S. D. Huber, Classification of topological phonons in linear mechanical metamaterials, Proceedings of the National Academy of Sciences **113**, E4767 (2016).

[243] G. Go, S. K. Kim, and K.-J. Lee, Topological Magnon-Phonon Hybrid Excitations in Two-Dimensional Ferromagnets with Tunable Chern Numbers, Physical Review Letters **123**, 237207 (2019).

[244] K. Sugii, M. Shimozawa, D. Watanabe, Y. Suzuki, M. Halim, M. Kimata, Y. Matsumoto, S. Nakatsuji, and M. Yamashita, Thermal Hall Effect in a Phonon-Glass $Ba_3CuSb_2O_9$, Physical Review Letters **118**, 145902 (2017).

[245] J.-S. Wang and L. Zhang, Phonon Hall thermal conductivity from the Green-Kubo formula, Physical Review B **80**, 012301 (2009).

[246] T. Qin, J. Zhou, and J. Shi, Berry curvature and the phonon Hall effect, Physical Review B **86**, 104305 (2012).

[247] M. Mori, A. Spencer-Smith, O. P. Sushkov, and S. Maekawa, Origin of the Phonon Hall Effect in Rare-Earth Garnets, Physical Review Letters **113**, 265901 (2014).

[248] T. Yang, J. Wang, X.-P. Li, X. Wang, Z. Cheng, W. Wang, and G. Zhang, Topological nodal-point phononic systems, Matter **7**, 320 (2024).

[249] J. Romhányi, K. Penc, and R. Ganesh, Hall effect of triplons in a dimerized quantum magnet, Nature Communications **6**, 6805 (2015).

[250] D. G. Joshi and A. P. Schnyder, Topological quantum paramagnet in a quantum spin ladder, Physical Review B **96**, 220405 (2017).

[251] P. A. McClarty, F. Krüger, T. Guidi, S. F. Parker, K. Refson, A. W. Parker, D. Prabhakaran, and R. Coldea, Topological triplon modes and bound states in a Shastry-Sutherland magnet, Nature Physics **13**, 736 (2017).

[252] D. G. Joshi and A. P. Schnyder, $\mathbb{Z}_2$ topological quantum paramagnet on a honeycomb bilayer, Physical Review B **100**, 020407 (2019).

[253] K. Nawa, K. Tanaka, N. Kurita, T. J. Sato, H. Sugiyama, H. Uekusa, S. Ohira-Kawamura, K. Nakajima, and H. Tanaka, Triplon band splitting and topologically protected edge states in the dimerized antiferromagnet, Nature Communications **10**, 2096 (2019).

[254] P. S. Anisimov, F. Aust, G. Khaliullin, and M. Daghofer, Nontrivial Triplon Topology and Triplon Liquid in Kitaev-Heisenberg-type Excitonic Magnets, Physical Review Letters **122**, 177201 (2019).

[255] S. Fujimoto, Hall Effect of Spin Waves in Frustrated Magnets, Physical Review Letters **103**, 047203 (2009).

[256] S. Murakami and A. Okamoto, Thermal Hall Effect of Magnons, Journal of the Physical Society of Japan **86**, 011010 (2017).

[257] R. Shindou, R. Matsumoto, S. Murakami, and J.-i. Ohe, Topological chiral magnonic edge mode in a magnonic crystal, Physical Review B **87**, 174427 (2013).

[258] R. Shindou, J.-i. Ohe, R. Matsumoto, S. Murakami, and E. Saitoh, Chiral spin-wave edge modes in dipolar magnetic thin films, Physical Review B **87**, 174402 (2013).

[259] A. Mook, J. Henk, and I. Mertig, Tunable Magnon Weyl Points in Ferromagnetic Pyrochlores, Physical Review Letters **117**, 157204 (2016).

[260] S. K. Kim, H. Ochoa, R. Zarzuela, and Y. Tserkovnyak, Realization of the Haldane-Kane-Mele Model in a System of Localized Spins, Physical Review Letters **117**, 227201 (2016).

[261] R. Cheng, S. Okamoto, and D. Xiao, Spin Nernst Effect of Magnons in Collinear Antiferromagnets, Physical Review Letters **117**, 217202 (2016).

[262] S. A. Owerre, A first theoretical realization of honeycomb topological magnon insulator, Journal of Physics: Condensed Matter **28**, 386001 (2016).

[263] J. Fransson, A. M. Black-Schaffer, and A. V. Balatsky, Magnon Dirac materials, Physical Review B **94**, 075401 (2016).

[264] F. Y. Li, Y. D. Li, Y. B. Kim, L. Balents, Y. Yu, and G. Chen, Weyl magnons in breathing pyrochlore antiferromagnets, Nature Communications **7** (2016).

[265] V. A. Zyuzin and A. A. Kovalev, Magnon Spin Nernst Effect in Antiferromagnets, Physical Review Letters **117**, 217203 (2016).

[266] J. H. Han and H. Lee, Spin Chirality and Hall-Like Transport Phenomena of Spin Excitations, Journal of the Physical Society of Japan **86**, 011007 (2017).

[267] X. S. Wang, Y. Su, and X. R. Wang, Topologically protected unidirectional edge spin waves and beam splitter, Physical Review B **95**, 014435 (2017).

[268] K. Nakata, S. K. Kim, J. Klinovaja, and D. Loss, Magnonic topological insulators in antiferromagnets, Physical Review B **96**, 224414 (2017).

[269] K. Nakata, J. Klinovaja, and D. Loss, Magnonic quantum Hall effect and Wiedemann-Franz law, Physical Review B **95**, 125429 (2017).

[270] B. Göbel, A. Mook, J. Henk, and I. Mertig, Unconventional topological Hall effect in skyrmion crystals caused by the topology of the lattice, Physical Review B **95**, 094413 (2017).

[271] Y. Su, X. S. Wang, and X. R. Wang, Magnonic Weyl semimetal and chiral anomaly in pyrochlore ferromagnets, Physical Review B **95**, 224403 (2017).

[272] S. A. Owerre, Magnonic analogs of topological Dirac semimetals, Journal of Physics Communications **1**, 025007 (2017).

[273] R. Seshadri and D. Sen, Topological magnons in a kagome-lattice spin system with XXZ and Dzyaloshinskii-Moriya interactions, Physical Review B **97**, 134411 (2018).

[274] A. Mook, B. Göbel, J. Henk, and I. Mertig, Taking an electron-magnon duality shortcut from electron to magnon transport, Physical Review B **97**, 140401 (2018).

[275] X. S. Wang, H. W. Zhang, and X. R. Wang, Topological Magnonics: A Paradigm for Spin-Wave Manipulation and Device Design, Physical Review Applied **9**, 024029 (2018).

[276] S. S. Pershoguba, S. Banerjee, J. C. Lashley, J. Park, H. Agren, G. Aeppli, and A. V. Balatsky, Dirac Magnons in Honeycomb Ferromagnets, Physical Review X **8**, 011010 (2018).

[277] M. Kawano and C. Hotta, Thermal Hall effect and topological edge states in a square-lattice antiferromagnet, Physical Review B **99**, 054422 (2019).

[278] S. K. Kim, K. Nakata, D. Loss, and Y. Tserkovnyak, Tunable Magnonic Thermal Hall Effect in Skyrmion Crystal Phases of Ferrimagnets, Physical Review Letters **122**, 057204 (2019).

[279] S. A. Díaz, J. Klinovaja, and D. Loss, Topological Magnons and Edge States in Antiferromagnetic Skyrmion Crystals, Physical Review Letters **122**, 187203 (2019).

[280] F. Zhu, L. Zhang, X. Wang, F. J. dos Santos, J. Song, T. Mueller, K. Schmalzl, W. F. Schmidt, A. Ivanov, J. T. Park, J. Xu, J. Ma, S. Lounis, S. Blügel, Y. Mokrousov, Y. Su, and T. Brückel, Topological magnon insulators in two-dimensional van der Waals ferromagnets $CrSiTe_3$ and $CrGeTe_3$: Toward intrinsic gap-tunability, Science Advances **7**, eabi7532 (2021).

[281] Z. Cai, S. Bao, Z.-L. Gu, Y.-P. Gao, Z. Ma, Y. Shangguan, W. Si, Z.-Y. Dong, W. Wang, Y. Wu, D. Lin, J. Wang, K. Ran, S. Li, D. Adroja, X. Xi, S.-L. Yu, X. Wu, J.-X. Li, and J. Wen, Topological magnon insulator spin excitations in the two-dimensional ferromagnet $CrBr_3$, Physical Review B **104**, L020402 (2021).

[282] A. Mook, R. Hoyer, J. Klinovaja, and D. Loss, Magnons, magnon bound pairs, and their hybrid spin-multipolar topology, Physical Review B **107** (2023).

[283] S. Khatua, V. P. Kravchuk, K. V. Yershov, and J. van den Brink, Magnon topology driven by altermagnetism, arXiv:2507.17822 [cond-mat.str-el] (2025).

[284] R. Matsumoto, R. Shindou, and S. Murakami, Thermal Hall effect of magnons in magnets with dipolar interaction, Physical Review B **89**, 054420 (2014).

[285] X. Cao, K. Chen, and D. He, Magnon Hall effect on the Lieb lattice, Journal of Physics: Condensed Matter **27**, 166003 (2015).

[286] A. Mook, J. Henk, and I. Mertig, Spin dynamics simulations of topological magnon insulators: From transverse current correlation functions to the family of magnon Hall effects, Physical Review B **94**, 174444 (2016).

[287] S. A. Owerre, Topological honeycomb magnon Hall effect: A calculation of thermal Hall conductivity of magnetic spin excitations, Journal of Applied Physics **120**, 043903 (2016).

[288] P. A. McClarty, X.-Y. Dong, M. Gohlke, J. G. Rau, F. Pollmann, R. Moessner, and K. Penc, Topological magnons in Kitaev magnets at high fields, Physical Review B **98**, 060404 (2018).

[289] S. A. Owerre, Topological thermal Hall effect in frustrated kagome antiferromagnets, Physical Review B **95**, 014422 (2017).

[290] P. Laurell and G. A. Fiete, Magnon thermal Hall effect in kagome antiferromagnets with Dzyaloshinskii-Moriya interactions, Physical Review B **98**, 094419 (2018).

[291] D. G. Joshi, Topological excitations in the ferromagnetic Kitaev-Heisenberg model, Physical Review B **98**, 060405 (2018).

[292] T. Cookmeyer and J. E. Moore, Spin-wave analysis of the low-temperature thermal Hall effect in the candidate Kitaev spin liquid α-$RuCl_3$, Physical Review B **98**, 060412 (2018).

[293] K.-S. Kim, K. H. Lee, S. B. Chung, and J.-G. Park, Magnon topology and thermal Hall effect in trimerized triangular lattice antiferromagnet, Physical Review B **100**, 064412 (2019).

[294] A. Mook, J. Henk, and I. Mertig, Thermal Hall effect in noncollinear coplanar insulating antiferromagnets, Physical Review B **99**, 014427 (2019).

[295] R. R. Neumann, A. Mook, J. Henk, and I. Mertig, Thermal hall effect of magnons in collinear antiferromagnetic insulators: Signatures of magnetic and topological phase transitions, Physical Review Letters **128**, 117201 (2022).

[296] L. Soderholm and J. E. Greedan, Ferromagnetic semiconductors: Magnetic properties of the pyrochlores, $(Y_xLu_{1-x})_2V_2O_7$ and $(Sc_xLu_{1-x})_2V_2O_7$, Materials Research Bulletin **14**, 1449 (1979).

[297] H. D. Zhou, E. S. Choi, J. A. Souza, J. Lu, Y. Xin, L. L. Lumata, B. S. Conner, L. Balicas, J. S. Brooks, J. J. Neumeier, and C. R. Wiebe, Magnetic-polaron-driven magnetoresistance in the pyrochlore $Lu_2V_2O_7$, Physical Review B **77**, 020411 (2008).

[298] D. Dahlbom, H. Zhang, C. Miles, S. Quinn, A. Niraula, B. Thipe, M. Wilson, S. Matin, H. Mankad, S. Hahn, D. Pajerowski, S. Johnston, Z. Wang, H. Lane, Y. W. Li, X. Bai, M. Mourigal, C. D. Batista, and K. Barros, Sunny.jl: A Julia Package for Spin Dynamics, arXiv:2501.13095 [quant-ph] (2025).

[299] M. Lein and K. Sato, Krein-Schrödinger formalism of bosonic Bogoliubov-de Gennes and certain classical systems and their topological classification, Physical Review B **100**, 075414 (2019).

[300] K. Kawabata, K. Shiozaki, M. Ueda, and M. Sato, Symmetry and Topology in Non-Hermitian Physics, Physical Review X **9**, 041015 (2019).

[301] S. Park, N. Nagaosa, and B.-J. Yang, Thermal Hall Effect, Spin Nernst Effect, and Spin Density Induced by a Thermal Gradient in Collinear Ferrimagnets from Magnon-Phonon Interaction, Nano Letters **20**, 2741 (2020).

[302] M. Ye, L. Savary, and L. Balents, Phonon Hall Viscosity in Magnetic Insulators, arXiv:2103.04223 [cond-mat.str-el] (2021).

[303] L. Mangeolle, L. Balents, and L. Savary, Thermal conductivity and theory of inelastic scattering of phonons by collective fluctuations, Physical Review B **106**, 245139 (2022).

[304] L. Mangeolle, L. Balents, and L. Savary, Phonon Thermal Hall Conductivity from Scattering with Collective Fluctuations, Physical Review X **12**, 041031 (2022).

APPENDICES

Appendix A

Evaluation of the magnon self-energy

Here, explicit expressions for the magnon self-energy at $O(S^0)$ [Eq. (2.68)] are provided for completeness. In each case, the diagrams are evaluated using the Feynman rules for the self-energy which can be found in Ref. [53]. It will suffice to evaluate one each of the normal and anomalous blocks of the self-energy (e.g. $\boldsymbol{\Sigma}^{-+}(\boldsymbol{k}, i\omega_n)$ and $\boldsymbol{\Sigma}^{--}(\boldsymbol{k}, i\omega_n)$), as the remaining blocks are related by symmetries of the spin wave Hamiltonian.

To simplify the expressions, it is useful to define the matrix elements:

$$\begin{aligned} X^{ab}_{\boldsymbol{k},+} &\equiv Y^{ab}_{\boldsymbol{k}}, \qquad & X^{ab}_{\boldsymbol{k},-} &\equiv X^{ab}_{\boldsymbol{k}}, \\ Y^{ab}_{\boldsymbol{k},+} &\equiv \bar{X}^{ab}_{\boldsymbol{k}}, \qquad & Y^{ab}_{\boldsymbol{k},-} &\equiv \bar{Y}^{ab}_{\boldsymbol{k}}, \end{aligned} \tag{A.1}$$

where the matrices $\boldsymbol{X}_{\boldsymbol{k}}$ and $\boldsymbol{Y}_{\boldsymbol{k}}$ are defined in Eq. (2.46). This notation will allow for the evaluation of the relevant Matsubara sums in a very general manner. In each case, the sum over Matsubara frequencies is evaluated in the usual way, by defining an appropriate contour and using the residue theorem. For bosons, this reads [52]

$$k_{\mathrm{B}}T \sum_{i\omega_n} g(i\omega_n) = \frac{1}{2\pi i} \oint \mathrm{d}z \; g(z) \left[\xi + n_{\mathrm{B}}(z)\right], \tag{A.2}$$

where the contour is taken to enclose the entire imaginary axis and $\xi = 0$ ($\xi = 1$) controls the convergence of the function $g(z)$ in the right (left) half of the complex plane, and $n_{\mathrm{B}}(z) = \left(e^{Sz/k_{\mathrm{B}}T} - 1\right)^{-1}$. In particular, the relevant Matsubara sums that we make use of are evaluated to

be

$$k_{\mathrm{B}}T\sum_{i\Omega_n}(-i\Omega_n+z)^{-1}=n_{\mathrm{B}}(z), \tag{A.3}$$

$$k_{\mathrm{B}}T\sum_{i\Omega_n}(-i\Omega_n+z_1)^{-1}(-i\Omega_n+z_2)^{-1}=-\frac{n_{\mathrm{B}}(z_1)-n_{\mathrm{B}}(z_2)}{z_1-z_2}. \tag{A.4}$$

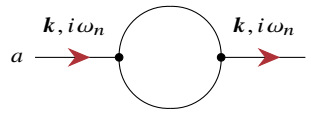
Using Eqs. (A.3)-(A.4), we define the following quantities involving the Matsubara sum of Green's functions

$$\begin{aligned}
Q^{\sigma\sigma'\rho\rho'}_{cdef}(\boldsymbol{q},\boldsymbol{k}-\boldsymbol{q},i\omega_n) &\equiv k_{\mathrm{B}}T\sum_{i\Omega_n}g^{\sigma\sigma'}_{cd}(\boldsymbol{q},i\Omega_n)g^{\rho\rho'}_{ef}(\boldsymbol{k}-\boldsymbol{q},i\omega_n-i\Omega_n)\\
&= \sum_{\ell\ell'}X^{c\ell}_{\sigma,\boldsymbol{q}}Y^{d\ell}_{\sigma',\boldsymbol{q}}X^{e\ell'}_{\rho,\boldsymbol{k}-\boldsymbol{q}}Y^{f\ell'}_{\rho',\boldsymbol{k}-\boldsymbol{q}}\left(\frac{1+n_{\mathrm{B}}(\epsilon_{\boldsymbol{q},\ell})+n_{\mathrm{B}}(\epsilon_{\boldsymbol{k}-\boldsymbol{q},\ell'})}{-i\omega_n+S\epsilon_{\boldsymbol{q},\ell}+S\epsilon_{\boldsymbol{k}-\boldsymbol{q},\ell'}}\right)\\
&\quad+\sum_{\ell\ell'}X^{c\ell}_{\sigma,\boldsymbol{q}}Y^{d\ell}_{\sigma',\boldsymbol{q}}Y^{e\ell'}_{\rho,\boldsymbol{q}-\boldsymbol{k}}X^{f\ell'}_{\rho',\boldsymbol{q}-\boldsymbol{k}}\left(\frac{n_{\mathrm{B}}(\epsilon_{\boldsymbol{q}-\boldsymbol{k},\ell'})-n_{\mathrm{B}}(\epsilon_{\boldsymbol{q},\ell})}{-i\omega_n+S\epsilon_{\boldsymbol{q},\ell}-S\epsilon_{\boldsymbol{q}-\boldsymbol{k},\ell'}}\right)\\
&\quad+\sum_{\ell\ell'}Y^{c\ell}_{\sigma,-\boldsymbol{q}}X^{d\ell}_{\sigma',-\boldsymbol{q}}X^{e\ell'}_{\rho,\boldsymbol{k}-\boldsymbol{q}}Y^{f\ell'}_{\rho',\boldsymbol{k}-\boldsymbol{q}}\left(\frac{n_{\mathrm{B}}(\epsilon_{\boldsymbol{k}-\boldsymbol{q},\ell'})-n_{\mathrm{B}}(\epsilon_{-\boldsymbol{q},\ell})}{i\omega_n+S\epsilon_{-\boldsymbol{q},\ell}-S\epsilon_{\boldsymbol{k}-\boldsymbol{q},\ell'}}\right)\\
&\quad+\sum_{\ell\ell'}Y^{c\ell}_{\sigma,-\boldsymbol{q}}X^{d\ell}_{\sigma',-\boldsymbol{q}}Y^{e\ell'}_{\rho,\boldsymbol{q}-\boldsymbol{k}}X^{f\ell'}_{\rho',\boldsymbol{q}-\boldsymbol{k}}\left(\frac{1+n_{\mathrm{B}}(\epsilon_{-\boldsymbol{q},\ell})+n_{\mathrm{B}}(\epsilon_{\boldsymbol{q}-\boldsymbol{k},\ell'})}{i\omega_n+S\epsilon_{-\boldsymbol{q},\ell}+S\epsilon_{\boldsymbol{q}-\boldsymbol{k},\ell'}}\right),
\end{aligned} \tag{A.5}$$

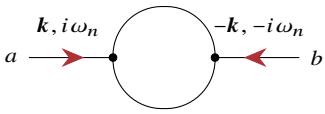
$$\begin{aligned}
\mathcal{R}^{\sigma\sigma'\rho\rho'}_{cdef}(\boldsymbol{q}) &\equiv k_{\mathrm{B}}T\sum_{i\Omega_n}g^{\sigma\sigma'}_{cd}(\boldsymbol{0},i0)g^{\rho\rho'}_{ef}(\boldsymbol{q},i\Omega_n)\\
&=\sum_{\ell\ell'}\left(\frac{X^{c\ell}_{\sigma,\boldsymbol{0}}Y^{d\ell}_{\sigma',\boldsymbol{0}}+Y^{c\ell}_{\sigma,\boldsymbol{0}}X^{d\ell}_{\sigma',\boldsymbol{0}}}{S\epsilon_{\boldsymbol{0},\ell}}\right)\left[X^{e\ell'}_{\rho,\boldsymbol{q}}Y^{f\ell'}_{\rho',\boldsymbol{q}}n_{\mathrm{B}}\left(S\epsilon_{\boldsymbol{q},\ell'}\right)+Y^{e\ell'}_{\rho,-\boldsymbol{q}}X^{f\ell'}_{\rho',-\boldsymbol{q}}\left(1+n_{\mathrm{B}}\left(S\epsilon_{-\boldsymbol{q},\ell'}\right)\right)\right],
\end{aligned} \tag{A.6}$$

$$\mathcal{W}^{\sigma\sigma'}_{cd}(\boldsymbol{q})\equiv k_{\mathrm{B}}T\sum_{i\Omega_n}g^{\sigma\sigma'}_{cd}(\boldsymbol{q},i\Omega)=\sum_{\ell}\left[X^{c\ell}_{\sigma,\boldsymbol{q}}Y^{d\ell}_{\sigma',\boldsymbol{q}}n_{\mathrm{B}}\left(S\epsilon_{\boldsymbol{q},\ell}\right)+Y^{c\ell}_{\sigma,-\boldsymbol{q}}X^{d\ell}_{\sigma',-\boldsymbol{q}}\left(1+n_{\mathrm{B}}\left(S\epsilon_{-\boldsymbol{q},\ell}\right)\right)\right]. \tag{A.7}$$

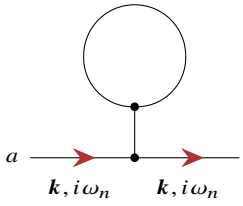
From here, the self-energy diagrams are evaluated to be



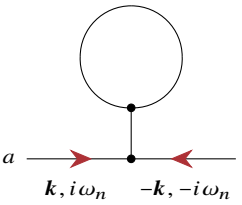
$$
\begin{aligned}
= &-\frac{S}{2N_c}\sum_{\boldsymbol{q}}\sum_{cdef} T^{cea}_{\boldsymbol{q},\boldsymbol{k}-\boldsymbol{q}}\bar{T}^{dfb}_{\boldsymbol{q},\boldsymbol{k}-\boldsymbol{q}} Q^{-+-+}_{cdef}(\boldsymbol{q},\boldsymbol{k}-\boldsymbol{q},i\omega_n) \\
&-\frac{S}{N_c}\sum_{\boldsymbol{q}}\sum_{cdef} T^{bed}_{\boldsymbol{k},\boldsymbol{q}-\boldsymbol{k}}\bar{T}^{afc}_{\boldsymbol{k},\boldsymbol{q}-\boldsymbol{k}} Q^{-++-}_{cdfe}(\boldsymbol{q},\boldsymbol{k}-\boldsymbol{q},i\omega_n) \\
&-\frac{S}{N_c}\sum_{\boldsymbol{q}}\sum_{cdef} \bar{T}^{aec}_{\boldsymbol{k},\boldsymbol{q}-\boldsymbol{k}}\bar{T}^{dfb}_{\boldsymbol{q},\boldsymbol{k}-\boldsymbol{q}} Q^{-+++}_{cdef}(\boldsymbol{q},\boldsymbol{k}-\boldsymbol{q},i\omega_n) \\
&-\frac{S}{N_c}\sum_{\boldsymbol{q}}\sum_{cdef} T^{cea}_{\boldsymbol{q},\boldsymbol{k}-\boldsymbol{q}} T^{bfd}_{\boldsymbol{k},\boldsymbol{q}-\boldsymbol{k}} Q^{-+--}_{cdef}(\boldsymbol{q},\boldsymbol{k}-\boldsymbol{q},i\omega_n) \\
&-\frac{S}{N_c}\sum_{\boldsymbol{q}}\sum_{cdef} \bar{T}^{aec}_{\boldsymbol{k},\boldsymbol{q}-\boldsymbol{k}} T^{bdf}_{\boldsymbol{k},-\boldsymbol{q}} Q^{--++}_{cdef}(\boldsymbol{q},\boldsymbol{k}-\boldsymbol{q},i\omega_n)
\end{aligned}
\tag{A.8}
$$



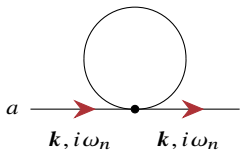
$$
\begin{aligned}
= &-\frac{S}{2N_c}\sum_{\boldsymbol{q}}\sum_{cdef} T^{cea}_{\boldsymbol{q},\boldsymbol{k}-\boldsymbol{q}} T^{dfb}_{-\boldsymbol{q},\boldsymbol{q}-\boldsymbol{k}} Q^{----}_{cdef}(\boldsymbol{q},\boldsymbol{k}-\boldsymbol{q},i\omega_n) \\
&-\frac{S}{N_c}\sum_{\boldsymbol{q}}\sum_{cdef} \bar{T}^{ace}_{\boldsymbol{k},-\boldsymbol{q}}\bar{T}^{fbd}_{\boldsymbol{k}-\boldsymbol{q},-\boldsymbol{k}} Q^{+--+}_{cdef}(\boldsymbol{q},\boldsymbol{k}-\boldsymbol{q},i\omega_n) \\
&-\frac{S}{N_c}\sum_{\boldsymbol{q}}\sum_{cdef} T^{cea}_{\boldsymbol{q},\boldsymbol{k}-\boldsymbol{q}}\bar{T}^{bdf}_{-\boldsymbol{k},\boldsymbol{q}} Q^{-+--}_{cdef}(\boldsymbol{q},\boldsymbol{k}-\boldsymbol{q},i\omega_n) \\
&-\frac{S}{N_c}\sum_{\boldsymbol{q}}\sum_{cdef} \bar{T}^{ace}_{\boldsymbol{k},-\boldsymbol{q}} T^{dfb}_{-\boldsymbol{q},\boldsymbol{q}-\boldsymbol{k}} Q^{+---}_{cdef}(\boldsymbol{q},\boldsymbol{k}-\boldsymbol{q},i\omega_n) \\
&-\frac{S}{N_c}\sum_{\boldsymbol{q}}\sum_{cdef} \bar{T}^{eac}_{\boldsymbol{q}-\boldsymbol{k},\boldsymbol{k}}\bar{T}^{fbd}_{\boldsymbol{k}-\boldsymbol{q},-\boldsymbol{k}} Q^{--++}_{cdef}(\boldsymbol{q},\boldsymbol{k}-\boldsymbol{q},i\omega_n),
\end{aligned}
\tag{A.9}
$$



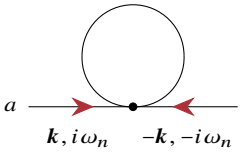
$$
\begin{aligned}
= &- \frac{S}{2N_c} \sum_{\boldsymbol{q}} \sum_{cdef} \left[T^{bca}_{\boldsymbol{k},\boldsymbol{0}} T^{efd}_{\boldsymbol{q},-\boldsymbol{q}} \mathcal{R}^{-+--}_{cdef}(\boldsymbol{q}) + \bar{T}^{acb}_{\boldsymbol{k},\boldsymbol{0}} \bar{T}^{efd}_{-\boldsymbol{q},\boldsymbol{q}} \mathcal{R}^{+-++}_{cdef}(\boldsymbol{q}) \right] \\
&- \frac{S}{2N_c} \sum_{\boldsymbol{q}} \sum_{cdef} \left[T^{efd}_{\boldsymbol{q},-\boldsymbol{q}} \bar{T}^{acb}_{\boldsymbol{k},\boldsymbol{0}} \mathcal{R}^{++--}_{cdef}(\boldsymbol{q}) + \bar{T}^{fed}_{\boldsymbol{q},-\boldsymbol{q}} T^{bca}_{\boldsymbol{k},\boldsymbol{0}} \mathcal{R}^{--++}_{cdef}(\boldsymbol{q}) \right] \\
&- \frac{S}{N_c} \sum_{\boldsymbol{q}} \sum_{cdef} \left[T^{cba}_{\boldsymbol{0},\boldsymbol{k}} \bar{T}^{dfe}_{\boldsymbol{0},\boldsymbol{q}} \mathcal{R}^{-+-+}_{cdef}(\boldsymbol{q}) + \bar{T}^{cab}_{\boldsymbol{0},\boldsymbol{k}} T^{def}_{\boldsymbol{0},\boldsymbol{q}} \mathcal{R}^{-+-+}_{cdef}(\boldsymbol{q}) \right] \\
&- \frac{S}{N_c} \sum_{\boldsymbol{q}} \sum_{cdef} \left[\bar{T}^{fde}_{\boldsymbol{q},\boldsymbol{0}} \bar{T}^{acb}_{\boldsymbol{k},\boldsymbol{0}} \mathcal{R}^{++-+}_{cdef}(\boldsymbol{q}) + T^{edf}_{\boldsymbol{q},\boldsymbol{0}} T^{bca}_{\boldsymbol{k},\boldsymbol{0}} \mathcal{R}^{---+}_{cdef}(\boldsymbol{q}), \right]
\end{aligned}
\tag{A.10}
$$



$$
\begin{aligned}
= &- \frac{S}{2N_c} \sum_{\boldsymbol{q}} \sum_{cdef} \left[T^{efd}_{\boldsymbol{q},-\boldsymbol{q}} \bar{T}^{abc}_{\boldsymbol{k},-\boldsymbol{k}} \mathcal{R}^{-+--}_{cd,ef}(\boldsymbol{q}) + \bar{T}^{fed}_{\boldsymbol{q},-\boldsymbol{q}} \bar{T}^{abc}_{\boldsymbol{k},-\boldsymbol{k}} \mathcal{R}^{--++}_{cdef}(\boldsymbol{q}) \right] \\
&- \frac{S}{N_c} \sum_{\boldsymbol{q}} \sum_{cdef} \left[T^{edf}_{\boldsymbol{q},\boldsymbol{0}} \bar{T}^{abc}_{\boldsymbol{k},-\boldsymbol{k}} \mathcal{R}^{---+}_{cdef}(\boldsymbol{q}) + \bar{T}^{abc}_{\boldsymbol{k},-\boldsymbol{k}} \bar{T}^{dfe}_{\boldsymbol{0},\boldsymbol{q}} \mathcal{R}^{-+-+}_{cdef}(\boldsymbol{q}) \right],
\end{aligned}
\tag{A.11}
$$



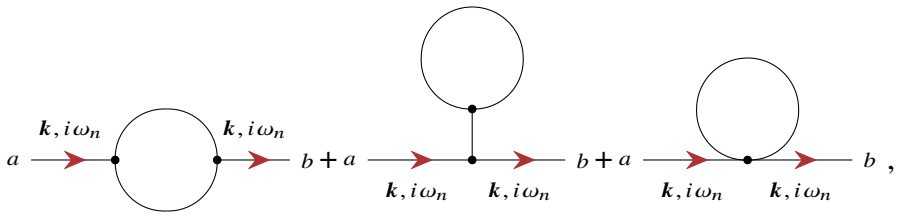
$$
\begin{aligned}
= &\frac{1}{N_c} \sum_{\boldsymbol{q}} \sum_{cd} V^{adcb}_{\boldsymbol{k},\boldsymbol{q},\boldsymbol{0}} \mathcal{W}^{-+}_{cd}(\boldsymbol{q}) \\
&+ \frac{1}{2N_c} \sum_{\boldsymbol{q}} \sum_{cd} \left[D^{bcda}_{\boldsymbol{k},-\boldsymbol{q},\boldsymbol{q}} \mathcal{W}^{--}_{cd}(\boldsymbol{q}) + \bar{D}^{acdb}_{\boldsymbol{k},-\boldsymbol{q},\boldsymbol{q}} \mathcal{W}^{++}_{cd}(\boldsymbol{q}) \right],
\end{aligned}
\tag{A.12}
$$



$$= \frac{1}{N_c} \sum_{\boldsymbol{q}} \sum_{cd} \left[\bar{D}^{abdc}_{\boldsymbol{k},-\boldsymbol{k},\boldsymbol{q}} \mathcal{W}^{-+}_{cd}(\boldsymbol{q}) + \frac{1}{2} V^{abdc}_{\boldsymbol{q},-\boldsymbol{q},\boldsymbol{k}-\boldsymbol{q}} \mathcal{W}^{--}_{cd}(\boldsymbol{q}) \right]. \tag{A.13}$$

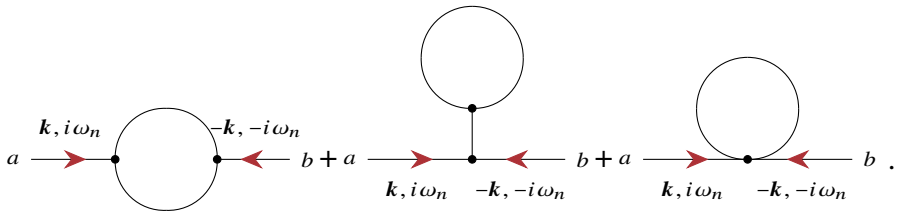
Using the expressions in Eqs. (A.5)-(A.13), the normal and anomalous components of the imaginary-time self-energy may then be computed as

$$\Sigma^{-+}_{ab}(\boldsymbol{k}, i\omega_n) =$$



, (A.14)

$$\Sigma^{--}_{ab}(\boldsymbol{k}, i\omega_n) =$$



. (A.15)

The remaining blocks can be computed by noting that

$$\boldsymbol{\sigma}_3 \boldsymbol{\Sigma}(\boldsymbol{k}, i\omega_n) \boldsymbol{\sigma}_3 = \boldsymbol{\Sigma}(-\boldsymbol{k}, -i\omega_n)^{\intercal}, \tag{A.16}$$

$$\boldsymbol{\Sigma}(\boldsymbol{k}, i\omega_n)^{\dagger} = \boldsymbol{\Sigma}(\boldsymbol{k}, -i\omega_n), \tag{A.17}$$

which implies the following relationship between the blocks of the self-energy

$$\Sigma^{+-}_{ab}(\boldsymbol{k}, i\omega_n) = \Sigma^{-+}_{ba}(-\boldsymbol{k}, -i\omega_n), \tag{A.18}$$

$$\Sigma^{++}_{ab}(\boldsymbol{k}, i\omega_n) = \bar{\Sigma}^{--}_{ab}(-\boldsymbol{k}, i\omega_n). \tag{A.19}$$

The real-time retarded and advanced self-energies may then be computed using analytic continuation

$$\boldsymbol{\Sigma}^{R(A)}(\boldsymbol{k}, \omega) = \boldsymbol{\Sigma}(\boldsymbol{k}, i\omega_n \to \omega \pm i0^{+}). \tag{A.20}$$

Appendix B

Non-linear spin wave theory of the Heisenberg ferromagnet

In this appendix, some calculations of the self-energy are provided as a simple application of non-linear spin wave theory.

Isotropic model

The starting point will be a nearest-neighbour Heisenberg ferromagnet in three dimensions

$$H = -J \sum_{\langle i,j \rangle} \boldsymbol{S}_i \cdot \boldsymbol{S}_j, \tag{B.1}$$

where $J > 0$. We assume without loss of generalization that the ground state is polarized along the global $\hat{\boldsymbol{z}}$ direction. Using the Holstein-Primakoff transformation, the Hamiltonian to $O(S^0)$ is given by

$$H = NS^2\epsilon_{\text{cl}} + S \sum_{\boldsymbol{k}} \epsilon_{\boldsymbol{k}} a^\dagger_{\boldsymbol{k}} a_{\boldsymbol{k}} + \frac{1}{4N} \sum_{\boldsymbol{k},\boldsymbol{q},\boldsymbol{Q}} V_{\boldsymbol{k},\boldsymbol{q},\boldsymbol{Q}}\ a^\dagger_{\boldsymbol{k}+\boldsymbol{Q}} a^\dagger_{\boldsymbol{q}-\boldsymbol{Q}} a_{\boldsymbol{q}} a_{\boldsymbol{k}} + O(S^{-1}). \tag{B.2}$$

where $\epsilon_{\text{cl}} \equiv -Jz/2$ is the classical ground state energy, $\epsilon_{\boldsymbol{k}} \equiv Jz\left(1 - \gamma_{\boldsymbol{k}}\right)$ is the linear spin-wave dispersion, and we have defined $\gamma_{\boldsymbol{k}} \equiv z^{-1} \sum_{\boldsymbol{\delta}} e^{i\boldsymbol{k}\cdot\boldsymbol{\delta}}$ with the sum taken over all nearest-neighbour vectors $\boldsymbol{\delta}$. The symmetrized four-body interaction in this case is found to be

$$V_{\boldsymbol{k},\boldsymbol{q},\boldsymbol{Q}} \equiv \frac{Jz}{2}\left(\gamma_{\boldsymbol{k}+\boldsymbol{Q}} + \gamma_{\boldsymbol{q}-\boldsymbol{Q}} + \gamma_{\boldsymbol{q}} + \gamma_{\boldsymbol{k}} - 2\gamma_{\boldsymbol{k}+\boldsymbol{q}+\boldsymbol{Q}} - 2\gamma_{\boldsymbol{Q}}\right). \tag{B.3}$$

Magnetization in linear spin-wave theory

Here, we calculate the low temperature magnetization in linear spin-wave theory, going beyond the lowest order correction proportional to $T^{3/2}$ expected from Bloch's law. The asymptotic expansion method used in this section to calculate the magnetization loosely follows the derivation in Ref. [38]. Keeping only terms to $O(S^1)$ in Eq. (B.1), the bulk magnetization can be calculated as

$$\frac{m(T)}{m(0)} = 1 - \frac{1}{NS}\sum_{\boldsymbol{k}} \left\langle a_{\boldsymbol{k}}^\dagger a_{\boldsymbol{k}} \right\rangle . \tag{B.4}$$

The thermal expectation value of the magnon number operator can be expressed conveniently as a geometric series

$$\left\langle a_{\boldsymbol{k}}^\dagger a_{\boldsymbol{k}} \right\rangle = \frac{1}{e^{\beta S \epsilon_{\boldsymbol{k}}} - 1} = \sum_{n=1}^{\infty} e^{-\beta n S \epsilon_{\boldsymbol{k}}} . \tag{B.5}$$

Assuming a simple cubic lattice of unit volume ($a = 1$), the magnetization in the thermodynamic limit is

$$\begin{aligned} \frac{m(T)}{m(0)} &= 1 - \frac{1}{S}\sum_{n=1}^{\infty} e^{-6n\beta JS} \left(\int_{-\pi}^{\pi} \frac{\mathrm{d}k_x}{2\pi}\, e^{2n\beta JS\cos k_x} \right)^3 \\ &= 1 - \frac{1}{S}\sum_{n=1}^{\infty} e^{-6n\beta JS} \left[I_0(2n\beta JS) \right]^3 , \end{aligned} \tag{B.6}$$

where $I_\ell(x) = \frac{1}{\pi}\int_0^\pi \mathrm{d}\theta\ e^{x\cos\theta}\cos(\ell\theta) - \frac{\sin(\ell\pi)}{\pi}\int_0^\infty \mathrm{d}\theta\ e^{-x\cosh\theta - \ell\theta}\cos(\ell\theta)$ is the modified Bessel function of the first kind, of order ℓ. In the low-temperature limit ($T \ll 2JS$), we may use the asymptotic expansion of $I_0(x)$

$$\begin{aligned} I_0(x) &= \frac{e^x}{\sqrt{2\pi}} \left(\frac{1}{x^{1/2}} + \frac{1}{8x^{3/2}} + \frac{9}{128x^{5/2}} + \frac{75}{1024x^{7/2}} + O\left(x^{-9/2}\right) \right), \\ \left[I_0(x) \right]^3 &= \frac{e^{3x}}{(2\pi)^{3/2}} \left(\frac{1}{x^{3/2}} + \frac{3}{8x^{5/2}} + \frac{33}{128x^{7/2}} + O\left(x^{-9/2}\right) \right). \end{aligned} \tag{B.7}$$

This leads to a series expansion of the magnetization

$$\frac{m(T)}{m(0)} = 1 - \frac{\zeta\left(\frac{3}{2}\right)}{8\ S} \left(\frac{T}{\pi JS} \right)^{3/2} - \frac{3\pi\zeta\left(\frac{5}{2}\right)}{128S} \left(\frac{T}{\pi JS} \right)^{5/2} - \frac{33\pi^2\zeta\left(\frac{7}{2}\right)}{4096S} \left(\frac{T}{\pi JS} \right)^{7/2} - O\left(T^{9/2}\right). \tag{B.8}$$

Self-energy corrections

Next, we evaluate the self-energy to $O(S^0)$ to obtain the leading order correction to the magnon dispersion (and magnetization) due to interactions. In the absence of three-body interactions, the self-energy only contains the static Hartree-Fock term

$$\Sigma_{\boldsymbol{k}} = \frac{1}{N}\sum_{\boldsymbol{q}} V_{\boldsymbol{k},\boldsymbol{q},\boldsymbol{0}}\, n_{\mathrm{B}}(\epsilon_{\boldsymbol{q}}) = -\frac{Jz}{N}\sum_{\boldsymbol{q}}\left(1+\gamma_{\boldsymbol{k}-\boldsymbol{q}}-\gamma_{\boldsymbol{q}}-\gamma_{\boldsymbol{k}}\right)\, n_{\mathrm{B}}(\epsilon_{\boldsymbol{q}}). \tag{B.9}$$

Note that this is equivalent to taking the thermal expectation value of the four-body interaction in Eq. (B.1) and contracting over all single-magnon propagators using Wick's theorem. For a simple cubic lattice, the self-energy in the thermodynamic limit is then

$$\begin{aligned}
\Sigma_{\boldsymbol{k}} &= -2J\sum_{\mu}\left(1-\cos k_\mu\right)\sum_{n=1}^{\infty} e^{-6n\beta JS}\int\frac{\mathrm{d}^3q}{(2\pi)^3}\left(1-\cos q_\mu\right)e^{2n\beta JS\sum_\nu\cos q_\nu}\\
&= -2J\sum_{\mu}\left(1-\cos k_\mu\right)\sum_{n=1}^{\infty} e^{-6n\beta JS}\left(\int_{-\pi}^{\pi}\frac{\mathrm{d}q_x}{2\pi}\, e^{2n\beta JS\cos q_x}\right)^2\int_{-\pi}^{\pi}\frac{\mathrm{d}q_y}{2\pi}\,\left(1-\cos q_y\right)e^{2n\beta JS\cos q_y}\\
&= -\epsilon_{\boldsymbol{k}}\sum_{n=1}^{\infty} e^{-6n\beta JS}\left[I_0(2n\beta JS)\right]^2\left[I_0(2n\beta JS)-I_1(2n\beta JS)\right].
\end{aligned} \tag{B.10}$$

The fact that the first-order self-energy is proportional to the linear-spin wave dispersion is peculiar to this model and will not hold at all orders of perturbation theory. This contribution is strictly real, and simply renormalizes the magnon spectrum, with the renormalized dispersion given by

$$\tilde{\epsilon}_{\boldsymbol{k}} \equiv \epsilon_{\boldsymbol{k}} + S^{-1}\Sigma_{\boldsymbol{k}} = \epsilon_{\boldsymbol{k}}\left(1-\frac{\alpha(T)}{S}\right). \tag{B.11}$$

To calculate the low-temperature expansion of $\alpha(T)$, we make use of the asymptotic expansion for $I_1(x)$

$$I_1(x) = \frac{e^x}{\sqrt{2\pi}}\left(\frac{1}{x^{1/2}}-\frac{3}{8x^{3/2}}-\frac{15}{128x^{5/2}}-\frac{105}{1024x^{7/2}}+O\left(x^{-9/2}\right)\right). \tag{B.12}$$

Combining this with Eq. (B.7), we find

$$\alpha(T) = \frac{\pi\zeta\left(\frac{5}{2}\right)}{32}\left(\frac{T}{\pi JS}\right)^{5/2}+\frac{5\pi^2\zeta\left(\frac{7}{2}\right)}{512}\left(\frac{T}{\pi JS}\right)^{7/2}+O(T^{9/2}). \tag{B.13}$$

At low temperature $\alpha(T) > 0$, implying the renormalized magnon dispersion is lower than the unperturbed one. In this sense, the effect of temperature is to make the spin-wave excitations

"softer". The $O(S^0)$ correction to the magnetization can be calculated by simply repeating the calculation in Eq. (B.6) with the renormalized magnon dispersion $\epsilon_{\boldsymbol{k}} \to \tilde{\epsilon}_{\boldsymbol{k}}$ (or equivalently, mapping $J \to (1 - \frac{\alpha}{S})J$ in Eq. (B.8)), resulting in the series

$$\begin{aligned}\frac{m(T)}{m(0)} = 1 &- \frac{\zeta\left(\frac{3}{2}\right)}{8\,S}\left(\frac{T}{\pi JS}\right)^{3/2} - \frac{3\pi\zeta\left(\frac{5}{2}\right)}{128S}\left(\frac{T}{\pi JS}\right)^{5/2} \\ &- \frac{33\pi^2\zeta\left(\frac{7}{2}\right)}{4096S}\left(\frac{T}{\pi JS}\right)^{7/2} - \frac{3\pi\zeta\left(\frac{3}{2}\right)\zeta\left(\frac{5}{2}\right)}{512\,S^2}\left(\frac{T}{\pi JS}\right)^{4} + O\left(T^{9/2}\right).\end{aligned} \tag{B.14}$$

The last term, proportional to T^4, was first obtained by Dyson [39] and represents the leading correction to the spontaneous magnetization of a ferromagnet due to spin-wave interactions.

Anisotropic Ferromagnet

Next, we generalize the low-temperature expansion to include both an external magnetic field and an easy-axis anisotropy, given by the terms

$$H' = -h\sum_i S_i^z - D\sum_i \left(S_i^z\right)^2, \tag{B.15}$$

with $h, D \geq 0$. Taken together with Eq. (B.1), the spin-wave theory takes the same form as Eq. (B.2), with modified coefficients

$$\epsilon_{\text{cl}} = -\left(\frac{Jz}{2} + D + \frac{h}{S}\right) \tag{B.16}$$

$$\epsilon_{\boldsymbol{k}} = \frac{h}{S} + \left(2 - \frac{1}{S}\right)D + Jz\left(1 - \gamma_{\boldsymbol{k}}\right) \tag{B.17}$$

$$V_{\boldsymbol{k},\boldsymbol{q},\boldsymbol{Q}} = -4D + \frac{Jz}{2}\left(\gamma_{\boldsymbol{k}+\boldsymbol{Q}} + \gamma_{\boldsymbol{q}-\boldsymbol{Q}} + \gamma_{\boldsymbol{q}} + \gamma_{\boldsymbol{k}} - 2\gamma_{\boldsymbol{k}+\boldsymbol{q}+\boldsymbol{Q}} - 2\gamma_{\boldsymbol{Q}}\right). \tag{B.18}$$

Magnetization in linear spin-wave theory

Assuming a simple cubic lattice of unit volume ($a = 1$), the magnetization in the thermodynamic limit is then

$$\begin{aligned}\frac{m(T)}{m(0)} &= 1 - \frac{1}{S}\sum_{n=1}^{\infty} e^{-n\beta S\Delta_0} e^{-6n\beta JS} \left(\int_{-\pi}^{\pi} \frac{\mathrm{d}k_x}{2\pi}\, e^{2n\beta JS\cos k_x}\right)^3 \\ &= 1 - \frac{1}{S}\sum_{n=1}^{\infty} e^{-n\beta S\Delta_0} e^{-6n\beta JS} \left[I_0(2n\beta JS)\right]^3, \end{aligned} \tag{B.19}$$

where $S\Delta_0 \equiv S\epsilon_{\mathbf{0}} = h + (2S-1)D$ is the spin-wave gap at $O(S^1)$. Using the asymptotic expansion for $I_0(x)$ in Eq. (B.7), the magnetization in linear spin-wave theory is then given by

$$\begin{aligned}\frac{m(T)}{m(0)} = 1 &- \frac{\mathrm{Li}_{\frac{3}{2}}\left(e^{-\beta S\Delta_0}\right)}{8S}\left(\frac{T}{\pi JS}\right)^{3/2} \\ &- \frac{3\pi \mathrm{Li}_{\frac{5}{2}}\left(e^{-\beta S\Delta_0}\right)}{128S}\left(\frac{T}{\pi JS}\right)^{5/2} - \frac{33\pi^2 \mathrm{Li}_{\frac{7}{2}}\left(e^{-\beta S\Delta_0}\right)}{4096S}\left(\frac{T}{\pi JS}\right)^{7/2} - O\left(T^{9/2}\right), \end{aligned} \tag{B.20}$$

where $\mathrm{Li}_s(x) = \sum_{n=1}^{\infty} \frac{x^n}{n^s}$ is the polylogarithm of order s. Note that this expression is identical to Eq. (B.8) when the spin-wave gap vanishes, as $\mathrm{Li}_s(1) = \zeta(s)$ is the Riemann-zeta function. For $T \ll S\Delta_0$, it follows that

$$\frac{m(T)}{m(0)} = 1 - e^{-S\Delta_0/T}\left[\frac{1}{8S}\left(\frac{T}{\pi JS}\right)^{3/2} - \frac{3\pi}{128S}\left(\frac{T}{\pi JS}\right)^{5/2} - \frac{33\pi^2}{4096S}\left(\frac{T}{\pi JS}\right)^{7/2} - O\left(T^{9/2}\right)\right]. \tag{B.21}$$

Self-energy corrections

Next, we evaluate the self-energy to $O(S^0)$ to obtain the leading order correction to the magnon dispersion (and magnetization) due to interactions in the presence of anisotropy. The first-order self-energy is

$$\Sigma_{\boldsymbol{k}} = \frac{1}{N}\sum_{\boldsymbol{q}} V_{\boldsymbol{k},\boldsymbol{q},\mathbf{0}}\, n_{\mathrm{B}}(\epsilon_{\boldsymbol{q}}) = -\frac{Jz}{N}\sum_{\boldsymbol{q}}\left(1 + \gamma_{\boldsymbol{k}-\boldsymbol{q}} - \gamma_{\boldsymbol{q}} - \gamma_{\boldsymbol{k}}\right)\, n_{\mathrm{B}}(\epsilon_{\boldsymbol{q}}) - \frac{4D}{N}\sum_{\boldsymbol{q}}\, n_{\mathrm{B}}(\epsilon_{\boldsymbol{q}}). \tag{B.22}$$

For a simple cubic lattice, the self-energy in the thermodynamic limit is

$$\begin{aligned}\Sigma_{\boldsymbol{k}} &= -2J\sum_{\mu}\left(1-\cos k_{\mu}\right)\sum_{n=1}^{\infty}e^{-n\beta S\Delta_0}e^{-6n\beta JS}\int\frac{\mathrm{d}^3q}{(2\pi)^3}\left(1-\cos q_{\mu}\right)e^{2n\beta JS\sum_{\nu}\cos q_{\nu}}\\ &\quad-4D\sum_{n=1}^{\infty}e^{-n\beta S\Delta_0}e^{-6n\beta JS}\int\frac{\mathrm{d}^3q}{(2\pi)^3}e^{2n\beta JS\sum_{\nu}\cos q_{\nu}}\\ &= -6J\left(1-\gamma_{\boldsymbol{k}}\right)\sum_{n=1}^{\infty}e^{-n\beta S\Delta_0}e^{-6n\beta JS}\left[I_0(2n\beta JS)\right]^2\left[I_0(2n\beta JS)-I_1(2n\beta JS)\right]\\ &\quad-4D\sum_{n=1}^{\infty}e^{-n\beta S\Delta_0}e^{-6n\beta JS}\left[I_0(2n\beta JS)\right]^3. \end{aligned}\tag{B.23}$$

Expanding the modified Bessel functions in an asymptotic series ($\beta J\to\infty$), we find for the self-energy to $O(e^{-S\Delta_0/T}T^{7/2})$

$$\begin{aligned}\Sigma_{\boldsymbol{k}} &= -6J\left(1-\gamma_{\boldsymbol{k}}\right)\left[\frac{\pi\mathrm{Li}_{\frac{5}{2}}\left(e^{-\beta S\Delta_0}\right)}{32}\left(\frac{T}{\pi JS}\right)^{5/2}+\frac{5\pi^2\mathrm{Li}_{\frac{7}{2}}\left(e^{-\beta S\Delta_0}\right)}{512}\left(\frac{T}{\pi JS}\right)^{7/2}\right]\\ &\quad-4D\left[\frac{\mathrm{Li}_{\frac{3}{2}}\left(e^{-\beta S\Delta_0}\right)}{8}\left(\frac{T}{\pi JS}\right)^{3/2}+\frac{3\pi\mathrm{Li}_{\frac{5}{2}}\left(e^{-\beta S\Delta_0}\right)}{128}\left(\frac{T}{\pi JS}\right)^{5/2}+\frac{33\pi^2\mathrm{Li}_{\frac{7}{2}}\left(e^{-\beta S\Delta_0}\right)}{4096}\left(\frac{T}{\pi JS}\right)^{7/2}\right]\\ &= -e^{-S\Delta_0/T}\left[\frac{D}{2}\left(\frac{T}{\pi JS}\right)^{3/2}+\frac{\pi}{32}\left[6J\left(1-\gamma_{\boldsymbol{k}}\right)+3D\right]\left(\frac{T}{\pi JS}\right)^{5/2}\right.\\ &\quad\left.+\frac{\pi^2}{1024}\left[60J\left(1-\gamma_{\boldsymbol{k}}\right)+33D\right]\left(\frac{T}{\pi JS}\right)^{7/2}\right], \end{aligned}\tag{B.24}$$

where the last line uses the asymptotic form of the polylogarithm $\mathrm{Li}_s\left(e^{-x}\right)\to e^{-x}$, valid when $T\ll\Delta_0$. The renormalized dispersion is then given by $\tilde{\epsilon}_{\boldsymbol{k}}\equiv\epsilon_{\boldsymbol{k}}+S^{-1}\Sigma_{\boldsymbol{k}}$. It is useful to separate the self-energy into a dispersive part $\alpha(T)$ and a momentum-independent gap $\Delta(T)$, such that

$$\tilde{\epsilon}_{\boldsymbol{k}}=\Delta(T)+6J(1-\gamma_{\boldsymbol{k}})\left(1-\frac{\alpha(T)}{S}\right),\tag{B.25}$$

where

$$\alpha(T)\equiv\frac{\pi}{32}\mathrm{Li}_{\frac{5}{2}}\left(e^{-\beta S\Delta_0}\right)\left(\frac{T}{\pi JS}\right)^{5/2}+\frac{5\pi^2}{512}\mathrm{Li}_{\frac{7}{2}}\left(e^{-\beta S\Delta_0}\right)\left(\frac{T}{\pi JS}\right)^{7/2}+O(T^{9/2}),\tag{B.26}$$

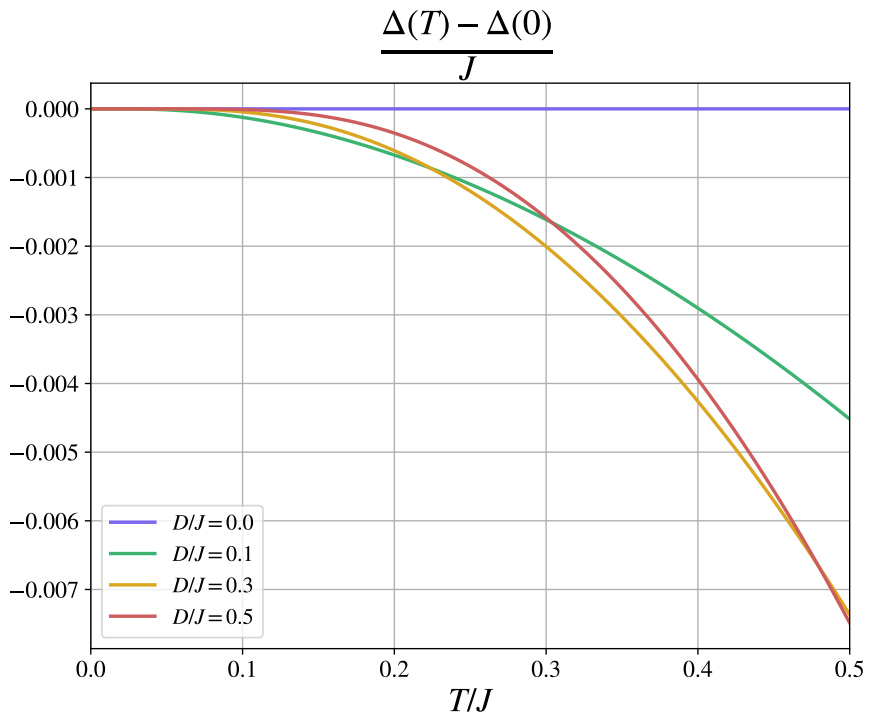


Figure B.1: Relative spin-wave gap of the simple cubic Heisenberg ferromagnet with single-ion anisotropy, in zero-field ($h = 0$), calculated using Eq. (B.27) with $S = 1$. The gap is calculated to $O(S^0)$ and $O(T^{7/2})$ in non-linear spin-wave theory.

and

$$\Delta(T) \equiv \tilde{\epsilon}_{\mathbf{0}} = \Delta_0 - \frac{D}{S}\left[\frac{1}{2}\mathrm{Li}_{\frac{3}{2}}\left(e^{-\beta S\Delta_0}\right)\left(\frac{T}{\pi JS}\right)^{3/2} + \frac{3\pi}{32}\mathrm{Li}_{\frac{5}{2}}\left(e^{-\beta S\Delta_0}\right)\left(\frac{T}{\pi JS}\right)^{5/2} + \frac{33\pi^2}{1024}\mathrm{Li}_{\frac{7}{2}}\left(e^{-\beta S\Delta_0}\right)\left(\frac{T}{\pi JS}\right)^{7/2}\right]. \tag{B.27}$$

The calculation of the spin-wave gap for several representative values of D/J is depicted in Fig. B.1. We see that thermal effects at leading order tend to slightly reduce the gap due to anisotropy.

The magnetization is calculated in the same way as the linear spin-wave theory using the renormalized dispersion. This amounts to replacing $J \to (1 - \frac{\alpha}{S})J$ and $\Delta_0 \to \Delta(T)$ in Eq. (B.20),

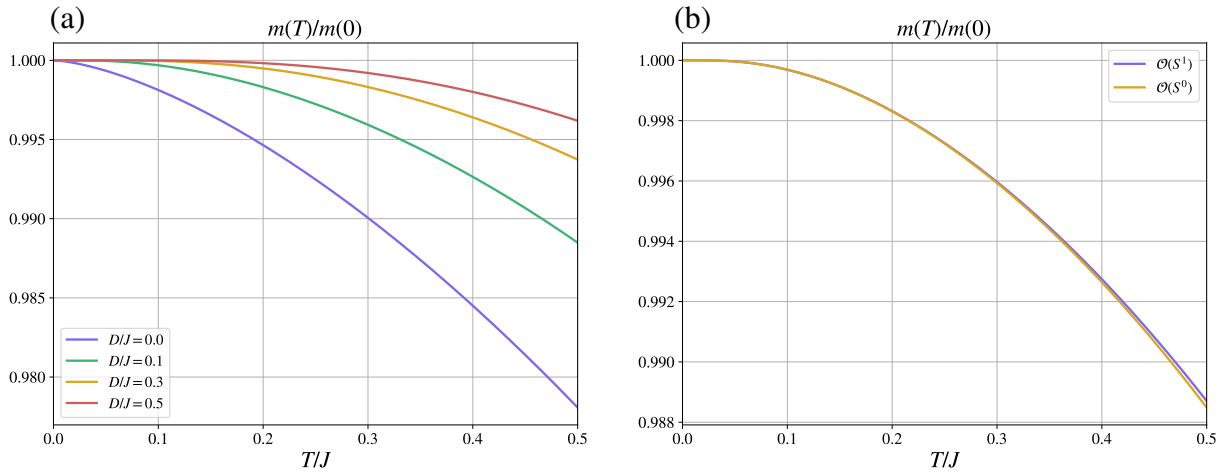


Figure B.2: Spontaneous magnetization of the simple cubic Heisenberg ferromagnet with single-ion anisotropy, in zero-field ($h = 0$), with $S = 1$. Panel (a) depicts the magnetization for several representative values of D/J, using Eq. (B.28). Panel (b) compares the linear spin-wave calculation (Eq. (B.20)) to the leading non-linear spin-wave correction (Eq. (B.28)) for $D/J = 0.1$.

leading to

$$\begin{aligned}\frac{m(T)}{m(0)} = 1 &- \frac{\mathrm{Li}_{\frac{3}{2}}\left(e^{-\Delta(T)/T}\right)}{8S}\left(\frac{T}{\pi JS}\right)^{3/2}\left(1-\frac{\alpha(T)}{S}\right)^{-3/2} \\ &- \frac{3\pi\mathrm{Li}_{\frac{5}{2}}\left(e^{-\Delta(T)/T}\right)}{128S}\left(\frac{T}{\pi JS}\right)^{5/2}\left(1-\frac{\alpha(T)}{S}\right)^{-5/2} \\ &- \frac{33\pi^2\mathrm{Li}_{\frac{7}{2}}\left(e^{-\Delta(T)/T}\right)}{4096S}\left(\frac{T}{\pi JS}\right)^{7/2}\left(1-\frac{\alpha(T)}{S}\right)^{-7/2} - O\left(T^{9/2}\right). \end{aligned} \tag{B.28}$$

The spontaneous magnetization in zero-field is depicted in Fig. B.2(a) for several values of D/J. Fig. B.2(b) compares the magnetization calculated in both linear and non-linear spin-wave theory for D/J; we see that the correction due to interactions is effectively negligible for this model.